



UNIVERSIDADE FEDERAL DO CEARÁ
CENTRO DE CIÊNCIAS
DEPARTAMENTO DE FÍSICA
PROGRAMA DE PÓS-GRADUAÇÃO EM FÍSICA



UNIVERSITEIT ANTWERPEN
FACULTEIT WETENSCHAPPEN
DEPARTEMENT FYSICA

Diego Rabelo da Costa

Transportes e confinamento em monocamada e bicamada de nanoestruturas de grafeno com diferentes bordas, interfaces e potenciais

Transport and confinement in monolayer and bilayer graphene nanostructures with different edges, interfaces and potentials

Transport en opsluiting in monolaag en bilaag grafeen nanostructuren met verschillende randen, interfaces en potentialen

Diego Rabelo da Costa

Transportes e confinamento em monocamada e bicamada de nanoestruturas de grafeno com diferentes bordas, interfaces e potenciais

Transport and confinement in monolayer and bilayer graphene nanostructures with different edges, interfaces and potentials

Transport en opsluiting in monolaag en bilaag grafeen nanostructuren met verschillende randen, interfaces en potentialen

Tese apresentada ao Curso de Pós-graduação em Física da Universidade Federal do Ceará como parte dos requisitos necessários para a obtenção do título de Doutor em Física.

Orientador:

Prof. Dr. Gil de Aquino Farias

Co-orientadores:

Prof. Dr. Andrey Chaves

Prof. Dr. François M. Peeters

DOUTORADO EM FÍSICA
DEPARTAMENTO DE FÍSICA
PROGRAMA DE PÓS-GRADUAÇÃO EM FÍSICA
CENTRO DE CIÊNCIAS
UNIVERSIDADE FEDERAL DO CEARÁ

Fortaleza - CE

26 de novembro de 2014

Dados Internacionais de Catalogação na Publicação
Universidade Federal do Ceará
Biblioteca do Curso de Física

C871t Costa, Diego Rabelo da
Transportes e confinamento em monocamada e bicamada de nanoestruturas de grafeno com diferentes bordas, interfaces e potenciais / Diego Rabelo da Costa. - Fortaleza, 2014.
201 f.:il. algumas color. enc.; 30 cm.

Tese (Doutorado em Física) - Universidade Federal do Ceará, Centro de Ciências, Departamento de Física, Programa de Pós-Graduação em Física, Fortaleza, 2014.

Orientação: Prof. Dr. Gil de Aquino Farias.

Coorientação: Prof. Dr. Andrey Chaves.

Coorientação: Prof. Dr. François M. Peeters.

Área de concentração: Física da Matéria Condensada.

Inclui índice.

1. Nanotecnologia. 2. Multicamadas de grafeno. 3. Sistemas de baixa dimensionalidade. 4. Propriedades de transporte. 5. Propriedades eletrônicas. I. Farias, Gil de Aquino. II. Chaves, Andrey. III. Peeters, François M. IV. Título.

CDD 530.41

DIEGO RABELO DA COSTA

Transportes e confinamento em monocamada e bicamada de nanoestruturas de grafeno com diferentes bordas, interfaces e potenciais

Transport and confinement in monolayer and bilayer graphene nanostructures with different edges, interfaces and potentials

Transport en opsluiting in monolaag en bilaag grafeen nanostructuren met verschillende randen, interfaces en potentialen

Tese de doutorado apresentada ao Curso de Pós-graduação em Física da Universidade Federal do Ceará como parte dos requisitos necessários para a obtenção do título de Doutor em Física.

Aprovada em: 26/11/2014.

BANCA EXAMINADORA

Prof. Dr. Gil de Aquino Farias (Orientador)
Departamento de Física – UFC

Prof. Andrey Chaves (Co - orientador)
Departamento de Física – UFC

Prof. François Maria Leopold Peeters (Co - orientador)
Departamento de Física – UFC
Department of Physics – University of Antwerp

Prof. Robson Ferreira
Laboratoire Pierre Aigrain
Ecole Normale Supérieure

Prof. Nilson Sena de Almeida
Departamento de Física
Universidade do Estado do Rio Grande do Norte - UERN

*To my parents,
close relatives
and friends.*

Acknowledgments

First, I warmly thank God and my family, especially my parents *Costa Neto* and *Maria Vilaneide*, and my brothers *Thays Rabelo* and *Thiago Rabelo*. I would like to express my sincere gratitude to them for everything that they did for me, giving me the opportunity to study, supporting me and helping me during my whole life. I also wish to express my heartfelt thanks to my fiancée *Deri* for her continuous love, support and encouragement.

I would like to thank Prof. *Gil de Aquino Farias* for his support, guidance, continuous encouragement during my PhD study and for giving me the great opportunity of being part of his group.

My deep appreciation to my co-promoter Prof. *Andrey Chaves* that during the my whole academic process gave me fruitful and constructive teachings, but particularly I am grateful for his patience and continuous support along these years. These numerous and essential knowledges were very important to the preparation of this thesis.

Equally important was the support and collaboration of Prof. *François Peeters* during the period that I worked at University of Antwerp, where I learned a lot physics with him about the subjects worked.

I thank Prof. *Milton Pereira* for the support, attention and advices that were given to me during these last years, and specially his patient explanations.

I would like to thank my collaborators *Mohmmad Zarenia* and *Lucian Covaci* for their guidance and support during my stay in Antwerp, and also my colleagues at the CMT group for their friendship and the nice time that we had together, in particular, *Victor*, *William*, *Belisa*, *Eduardo*, *Yierpan*, *Massoud*, *Davoud*, *Ben*, *Khosrow*, *Mehdi*, *Slavisa* (...). I must thank also to Ben for translating the abstract of my thesis in Dutch.

I thank the other members of the jury, Prof. *Nilson Almeida* and Prof. *Robson Ferreira*, for the time spent reviewing this work, as well as for their very important comments, corrections and suggestions that made possible to improve the quality of the final version of this thesis.

In view of my academic background, I appreciate the discussions and exchanges of views to all professors of the Department of Physics at UFC, by contributing directly to

my scientific progress.

Certainly the merits of my academic background are also due to my friends, because without their support I would not have gotten, in particular: *Abraão Cefas, Ariel Adorno, Bruno Gondim, Daniel Gomes, Daniel Marchesi, Davi Dantas, David Figueiredo, Davi Monteiro, Diego Franklin “UHUU”, Diego Lucena, Diego Ximenes, Estefferson torres, Felipe Moreira, Felipe Munarin, Heitor Credidio, Hygor Piaget, Hudson Pacheco, Igor de Brito, Jorge Kapuan, Jorge Luiz, Jorge Roberto, José Gadelha, Josias Valentin, Júlio César, Kauã Monteiro, Leandro Jader, Levi Leite, Luci Pinheiro, Rafael Alencar, Rilder de Sousa, Saulo Dantas, Thiago de Melo, Vagner Bessa, Victor Santos, (...)*. To my colleagues of the GTMC group: *André Borba, Danilo, Diego Frota, Duarte José, Gabriel Oliveira, Heitor Alves, Ícaro Rodrigues, Jessé Pereira, Luan Vieira, Marcelo Montanha* and *Jonas Nascimento*.

I would like to thank all the agencies that gave me financial support for carrying out my projects and also for presenting them at conferences: CAPES Foundation under the process number BEX 7178/13-1, CNPq under contract NanoBioEstruturas 555183/2005-0, PRONEX / FUNCAP, the Flemish Science Foundation (FWO-VI), the European Science Foundation (ESF) under the EUROCORES program Euro-GRAPHENE (project CONGRAN), the Bilateral programme between CNPq and FWO-VI, and the Brazilian Program Science Without Borders (CsF).

Finally, I thank all those who helped me directly or indirectly, for the preparation and conclusion of this work.

“A noble spirit embiggens the smallest man.”
Jebediah Springfield

Resumo

Grafeno, uma rede bidimensional de átomos de carbono, tem sido amplamente estudado durante os últimos anos. O interesse por este material não é apenas devido às suas possíveis aplicações tecnológicas futuras, mas também porque oferece a possibilidade de investigar fenômenos interessantes previstos pelas teorias quânticas de campo, que vão desde o tunelamento de Klein e outros efeitos quasi-relativísticos à existência de novos tipos de graus de liberdade do elétron, ou seja, o *pseudo-spin*, e a existência de dois vales eletrônicos não-equivalentes na vizinhança dos pontos sem *gap* do seu espectro de energia. Várias das propriedades exóticas observadas no grafeno originam-se do facto de que dentro da aproximação de baixas energias para o Hamiltoniano *tight-binding* do grafeno, elétrons se comportam como férmions de Dirac sem massa, com uma dispersão de energia linear. Assim como no caso de uma monocamada de grafeno, o espectro eletrônico de baixas energias para uma bicamada de grafeno é sem *gap*, mas, neste caso, é dominado pela dispersão parabólica. No entanto, uma característica interessante é compartilhada por ambas monocamada e bicamada de grafeno: o grau de liberdade de vale.

Nesta tese, nós investigamos teoricamente: (i) as propriedades dinâmicas em mono e bicamadas de grafeno, realizando um estudo sistemático do espalhamento de pacotes de onda em diferentes formas de interfaces, bordas e potenciais; e, além disso, (ii) os níveis de energia de sistemas confinados no grafeno na presença ou ausência de campos magnéticos e elétricos externos. Na primeira parte do trabalho, nós utilizamos a abordagem *tight-binding* para estudar o espalhamento de um pacote de onda Gaussiano nas bordas de uma monocamada de grafeno (*armchair* e *zigzag*) na presença de campos magnéticos reais e pseudo-magnéticos (induzidos por tensão) e também calculamos as probabilidades de transmissão de um pacote de onda Gaussiano através de um contato de ponto quântico definido por potenciais eletrostáticos em bicamadas de grafeno. Estes cálculos numéricos são baseados na solução da equação de Schrödinger dependente do tempo para o Hamiltoniano do modelo *tight-binding*, usando a técnica *Split-operator*. Nossa teoria permite investigar espalhamento no espaço recíproco, e dependendo do tipo de borda do grafeno, nós observamos espalhamento dentro do mesmo vale, ou entre diferentes vales. Na presença de um campo magnético externo, as bem conhecidas órbitas *skipping orbits* são observadas. No entanto, nossos resultados demonstram que, no caso de um campo pseudo-magnético induzido por uma tensão não-uniforme, o espalhamento por uma borba *armchair* resulta em um estado de borda não-propagante. Nós também propomos um sistema de filtragem de vales muito eficiente através de um sistema de contato de ponto quântico definido por portas eletrostáticas em uma bicamada de grafeno. Para o sistema de bicamadas sugerido, nós investigamos a forma de melhorar a eficiência do sistema como um filtro de vales por diferentes parâmetros, como comprimento, largura e amplitude do potencial aplicado.

Na segunda parte da tese, nós apresentamos um estudo sistemático dos espectros de

energia de anéis quânticos de grafeno com diferentes geometrias e tipos de borda, na presença de um campo magnético perpendicular. Nós discutimos quais características obtidas por meio de um modelo simplificado de Dirac podem ser recuperadas quando os auto-estados de anéis quânticos de grafeno são comparados com os resultados do modelo *tight-binding*. Além disso, nós também investigamos os estados confinados em dois sistemas híbridos diferentes de monocamada - bicamada, identificando estados localizados dentro do ponto e estados de borda para as estruturas de confinamento em bicamadas sugeridas, assim como vamos estudar o comportamento dos níveis de energia em função do tamanho do ponto e sob um campo magnético externo aplicado. Finalmente, usando o modelo contínuo de Dirac de quatro bandas, nós também derivamos uma expressão geral para a condição de contorno de massa infinita em bicamada de grafeno, a fim de aplicar essa condição de contorno para calcular analiticamente os estados confinados e as correspondentes funções de onda em um ponto quântico em uma bicamada de grafeno na ausência e na presença de um campo magnético perpendicular. Nossos resultados analíticos apresentam boa concordância quando comparados com os resultados *tight-binding*.

Abstract

Graphene, a two-dimensional lattice of carbon atoms, has been widely studied during the past few years. The interest in this material is not only due to its possible future technological applications, but also because it provides the possibility to probe interesting phenomena predicted by quantum field theories, ranging from Klein tunneling and other quasi-relativistic effects to the existence of new types of electron degrees of freedom, namely, the pseudo-spin, and the existence of two inequivalent electronic valleys in the vicinity of the gapless points of its energy spectrum. Several of the exotic properties observed in graphene originate from the fact that within the low energy approximation for the tight-binding Hamiltonian of graphene, electrons behave as massless Dirac fermions, with a linear energy dispersion. Just like in single layer graphene, the low-energy electronic spectrum in bilayer graphene is gapless, but in this case it is dominated by the parabolic dispersion. Nevertheless, one interesting feature is shared by both monolayer and bilayer graphene: the valley degree of freedom.

In this thesis, we theoretically investigate: (i) the dynamic properties in mono and bilayer graphene, performing a systematic study of wave packet scattering in different interface shapes, edges and potentials; and furthermore (ii) the energy levels of confined systems in graphene in the presence or absence of external magnetic and electric fields. In the first part of the work, we use the tight-binding approach to study the scattering of a Gaussian wave packet on monolayer graphene edges (armchair and zigzag) in the presence of real and pseudo (strain induced) magnetic fields and also calculate the transmission probabilities of a Gaussian wave packet through a quantum point contact defined by electrostatic gates in bilayer graphene. These numerical calculations are based on the solution of the time-dependent Schrödinger equation for the tight-binding model Hamiltonian, using the Split-operator technique. Our theory allows us to investigate scattering in reciprocal space, and depending on the type of graphene edge we observe scattering within the same valley, or between different valleys. In the presence of an external magnetic field, the well known skipping orbits are observed. However, our results demonstrate that in the case of a pseudo-magnetic field, induced by non-uniform strain, the scattering by an armchair edge results in a non-propagating edge state. We propose also a very efficient valley filtering through a quantum point contact system defined by electrostatic gates in bilayer graphene. For the suggested bilayer system, we investigate how to improve the efficiency of the system as a valley filter by varying parameters, such as length, width and amplitude of the applied potential.

In the second part of the thesis, we present a systematic study of the energy spectra of graphene quantum rings having different geometries and edge types, in the presence of a perpendicular magnetic field. We discuss which features obtained through a simplified Dirac model can be recovered when the eigenstates of graphene quantum rings are compared with the tight-binding results. Furthermore, we also investigate the confined

states in two different hybrid monolayer - bilayer systems, identifying dot-localized states and edge states for the suggested bilayer confinement structures, as well as we will study the behavior of the energy levels as a function of dot size and under an applied external magnetic field. Finally, using the four-band continuum Dirac model, we also derive a general expression for the infinite-mass boundary condition in bilayer graphene in order to apply this boundary condition to calculate analytically the confined states and the corresponding wave functions in a bilayer graphene quantum dot in the absence and presence of a perpendicular magnetic field. Our analytic results exhibit good agreement when compared with the tight-binding ones.

Abstract

Grafeen, een twee-dimensionaal rooster van koolstof atomen, vormt de laatste jaren een zeer intens onderzoeksgebied. De interesse in dit materiaal is niet enkel dankzij zijn mogelijke technologische toepassingen, maar ook omdat het een mogelijkheid voorziet om interessante nieuwe kwantum fenomenen te observeren. Dit gaande van Klein tunneling en andere quasirelativistische verschijnselen tot het bestaan van nieuwe types van elektronische vrijheidsgraden, namelijk de pseudospin en het bestaan van twee niet equivalente elektronische valleien in de nabijheid van punten waarin het energiespectrum geen bandkloof heeft. Verschillende exotische eigenschappen in grafeen hebben hun oorsprong in het feit dat binnen de lage energie benadering voor de "tight-binding" Hamiltoniaan van grafeen de elektronen zich gedragen als massaloze Dirac fermionen en dus een lineaire energie dispersie hebben. Net als in monolaag grafeen is het energiespectrum in bilaag grafeen kloofloos, maar in dit geval heeft het een parabolische dispersie. Desalniettemin delen deze twee materialen de vallei vrijheidsgraad.

In deze thesis onderzoeken we theoretische: (i) de dynamische eigenschappen in mono- en bilaag grafeen door een systematische studie uit te voeren van golfpakket verstrooiing aan verschillende vormen van interface, rand en potentiaal; verder (ii) onderzoeken we de energie niveaus van gebonden systemen in grafeen in de nabijheid of afwezigheid van externe magnetische en elektrische velden. In het eerste deel van het werk gebruiken we de tight-binding beschrijving om de verstrooiing van een Gaussisch golfpakket aan monolaag grafeen randen (zig-zag en "armchair") te bestuderen in een echt en pseudo (vervorming geïnduceerd) magneetveld en berekenen ook de transmissie waarschijnlijkheden van een Gaussisch golfpakket door een kwantum punt contact bepaald door elektrostatische poorten in bilaag grafeen. Deze numerieke berekeningen zijn gebaseerd op de oplossingen van de tijdsafhankelijke Schrodinger vergelijking voor de tight-binding model Hamiltoniaan gebruikmakend van de split-operator techniek. onze theorie laat ons toe om de verstrooiing te bestuderen in reciproke ruimte. Afhankelijk van het type grafeen rand observeren we verstrooiing binnen dezelfde vallei of tussen verschillende valleien. In de nabijheid van een extern magneetveld zien we de welbekende springende cirkelbanen. Onze resultaten tonen echter dat in het geval dat een pseudomagneet veld geïnduceerd wordt door niet uniforme vervorming, de verstrooiing bij een armchair rand resulteert in een niet propagerende randtoestand. We stellen ook een zeer efficiënte vallei filter door een kwantum punt contact gevormd door een elektrostatische poort voor in bilaag grafeen. Voor dit bilaag systeem onderzoeken we hoe de efficiency van het systeem als valleifilter kan worden geoptimaliseerd door verschillende parameters te variëren zoals de lengte, breedte of amplitude van de aangelegde potentiaal.

In het tweede deel van de thesis stellen we een systematische studie voor van de energie spectra van grafeen kwantumringen met verschillende geometriën en rand types voor in de nabijheid van een loodrecht magneetveld. We bespreken welke eigenschappen verk-

laard kunnen worden door middel van een vereenvoudigd Dirac model kunnen worden verklaard wanneer de eigentoestanden van de grafeen kwantum ring vergeleken worden et de tight-binding resultaten. Verder onderzoeken we ook de gebonden toestanden in twee verschillende hybride monolaag-bilaag systemen en identificeren we puntgelocaliseerde toestanden en randtoestanden voor de voorgestelde bilaag gebonden structuren. Daarenboven bespreken we het gedrag van de energieniveaus als functie van de grootte van het punt en onder een extern magneetveld. Ten slotte leiden we ook een algemene uitdrukking af voor de oneindige massa randvoorwaarde in bilaag grafeen om de gebonden toestanden en de overeenstemmende eigentoestanden analytisch te kunnen berekenen in de vierbandshamiltoniaan van het bilaag grafeen kwantum punt. Dit doen we met en zonder een extern magneetveld. Onze analytische resultaten stemmen goed overeen met de numerieke resultaten die we verkregen via tight-binding.

Contents

List of Figures	xviii
List of Tables	xxx
List of abbreviations	xxxi
List of nomenclatures	xxxii
1 Introduction	34
1.1 A brief history: carbon materials	34
1.2 The carbon atom and its hybridizations	37
1.2.1 sp hybridization	38
1.2.2 sp^2 hybridization	40
1.2.3 sp^3 hybridization	41
1.3 Allotropes of carbon	45
1.4 Fabrication techniques	47
1.4.1 Exfoliation from graphite	48
1.4.2 Epitaxial growth on SiC	49
1.4.3 Chemical vapor deposition	50
1.5 Applications	52
1.5.1 Flexible graphene for displays	53
1.5.2 Coating with graphene	55
1.5.3 Graphene photodetector	56
1.5.4 Challenges in graphene commercialization	58
1.5.5 Granted investments to graphene	59
1.6 Organization of the thesis	62
2 Theoretical framework and methodology	64
2.1 Graphene	64

2.2	Bilayer graphene	68
2.3	Influence of an external perpendicular magnetic field	73
2.3.1	Classical picture	73
2.3.2	Landau levels in a monolayer graphene	74
2.3.3	Landau levels in a bilayer graphene	76
2.4	Boundary conditions	79
2.4.1	Zigzag boundary condition	81
2.4.2	Armchair boundary condition	81
2.4.3	Infinite-mass boundary condition	82
2.5	<i>Split-operator</i> method	84
2.5.1	<i>Tight-binding</i> Hamiltonian	86
2.5.2	Dirac Hamiltonian	88
3	Geometry and edge effects on the energy levels of graphene quantum rings a comparison between tight-binding and simplified Dirac models	90
3.1	Motivation	90
3.2	Tight-Binding model	92
3.3	Continuum model	94
3.4	Results and discussion	96
3.4.1	Comparison between tight-binding and Dirac models	96
3.4.2	Geometry, edge types, and n -fold energy bands	107
3.5	Conclusion	111
4	Analytical study of the energy levels in bilayer graphene quantum dots	115
4.1	Motivation	115
4.2	Infinite-mass boundary condition	117
4.3	Energy levels: Zero magnetic field	121
4.4	Energy levels: Perpendicular magnetic field	124
4.5	Cyclotron resonance	128
4.6	Conclusion	129
5	Monolayer-bilayer graphene quantum dots	131
5.1	Motivation	131
5.2	Numerical Method	133
5.3	Results and discussion	134
5.3.1	Zero magnetic field	134
5.3.2	In the presence of a perpendicular magnetic field	139
5.4	Conclusion	146

6	Wave packet scattering on graphene edges in the presence of a (pseudo) magnetic field	149
6.1	Motivation	149
6.2	Edge-dependent scattering	151
6.3	Skipping orbits	154
6.4	Probability density current calculations	158
6.5	Conclusion	161
7	Valley filtering using electrostatic potentials in bilayer graphene	162
7.1	Motivation	162
7.2	Split-operator technique for the bilayer graphene Hamiltonian	163
7.3	Results and discussion	167
7.4	Conclusion	173
8	Conclusions and perspectives	174
Appendix A		
	Multilayer graphene in AA stacking	177
Appendix B		
	Publications related to this thesis	178
	Bibliography	181
	Index	199

List of Figures

- 1.1 Ingredients to find out graphene: two good researchers, scotch tape and graphite. Photographs taken when Geim and Novoselov were attending the 2010 Nobel Prize ceremony (December 8, 2010) at Aula Magna, Stockholm University. 36
- 1.2 Process to derive sp hybridization in carbon atoms. Electronic distribution for carbon is presented from left to right in the ground state, excited state, after the promotion of one electron to one of the $2p$ orbitals, and the last stage is the sp hybridized state. The yellow background in the excited stage comprises the two orbitals involved to make hybridization happen. The energy level of the two sp orbitals is smaller than the two $2p$ pure orbitals and greater than $2s$ orbital in ground state. In the final process, one has two sp hybridized states. 39
- 1.3 Schematic view of the sp hybridization showing the linear combination between the s and p_x orbitals to form the two $|sp_a\rangle$ and $|sp_b\rangle$ hybrid states, according to Eqs. (1.5) and (1.6), respectively. The color directions denote the positive (blue) and negative (orange) amplitude of the wave function. Only positive lobes are presented in illustration of $|sp\rangle$ state. 40
- 1.4 Process to derive sp^2 hybridization in carbon atoms. Electronic distribution for carbon is presented from left to right in the ground state, excited state, after the promotion of one electron to one of the $2p$ orbitals, and the last stage is the sp^2 hybridized state. The yellow background in the excited stage comprises the three orbitals involved to make hybridization happen. The energy level of the three sp^2 orbitals is smaller than the single $2p$ pure orbital and greater than $2s$ orbital in ground state. In the final process, one has three sp^2 hybridized states. 42

- 1.5 Schematic view of the sp^2 hybridization showing the linear combination between the s , p_x and p_y orbitals to form the three $|sp_a^2\rangle$, $|sp_b^2\rangle$ and $|sp_c^2\rangle$ hybrid states, according to Eqs. (1.9a), (1.9b, and (1.9c), respectively. The color directions denote the positive (blue) and negative (orange) amplitude of the wave function. Only positive lobes are presented in illustration of $|sp^2\rangle$ state. 42
- 1.6 Process to derive sp^3 hybridization in carbon atoms. Electronic distribution for carbon is presented from left to right in the ground state, excited state, after the promotion of one electron to one of the $2p$ orbitals, and the last stage is the sp^3 hybridized state. The yellow background in the excited stage comprises the four orbitals involved to make hybridization happen. The energy level of the four sp^3 orbitals is smaller than the $2p$ orbital and greater than $2s$ orbital of ground state. In the final process, one has four sp^3 hybridized states. 44
- 1.7 Schematic view of the sp^3 hybridization showing the linear combination between the s , p_x , p_y and p_z orbitals to form the four $|sp_a^3\rangle$, $|sp_b^3\rangle$, $|sp_c^3\rangle$ and $|sp_d^3\rangle$ hybrid states, according to Eqs. (1.12a), (1.12b, (1.12c) and (1.12d), respectively. The color directions denote the positive (blue) and negative (orange) amplitude of the wave function. This hybridization originates molecules with a tetrahedral shape. 44
- 1.8 Crystal structures of different allotropes of carbon according to their dimensionality. Three-dimensional (a) diamond and (b) carbon amorphous ($3D$); two-dimensional (c) graphite and (d) graphene ($2D$); one-dimensional (e) carbon nanotube ($1D$); and zero-dimensional fullerenes ($0D$): (f) C_{60} , (g) C_{540} , (h) C_{70} and (i) C_{84} . The idea is taken from Refs. [7] and [29]. 46
- 1.9 (a) Graphite flakes on adhesive tape to isolate graphene through scotch-tap method. (b) and (c) are optical images of few-layer graphene obtained by micromechanical exfoliation from graphite. In (b) one has thin graphite and (c) FLG and a single layer graphene shown in lighter purple contrast on a $\approx 300\text{nm}$ SiO_2 layer. The colors are related with local thickness of the sample. Yellowish color indicates thicker samples while bluish and lighter contrast indicates thinner samples. Adapted from Refs. [33] and [34]. 48
- 1.10 (a) Schematic illustration of the process of thermal decomposition of SiC for graphene synthesis. (b) and (c) are AFM measurements showing respectively silicon (0001) and carbon ($000\bar{1}$) surfaces after graphene growth. Adapted from Refs. [32] and [36]. 50

- 1.11 (a) Graphene growth process using a Ni film and its different stages (1-3):
 1. The Ni film deposited on SiO₂/Si is heated to 900°C and annealed for 20 minutes under flowing H₂ and Ar. 2. Exposure to H₂ and CH₄ for 5 minutes. CH₄ is decomposed catalytically and the carbon produced is incorporated into Ni film. 3. The substrate is cooled down from 1000⁰ to 500⁰C under Ar, H₂. At 500⁰C, the sample is taken out of the furnace and cooled rapidly to room temperature. (b)-(e) Two types of graphene films with different densities and their characterization. (b) and (d) are optical images of the graphene films on Ni, (c) and (e) are optical images of the graphene films transferred to SiO₂/Si. The transference to SiO₂/Si substrate enables thickness analysis by optical contrast. (f) Photograph of a large graphene film (blue film on the purple substrate of SiO₂/Si) with ≈ 87 percent of its area covered by 1 and 2 layers of graphene. Adapted from Ref. [42] 51
- 1.12 (a) Transmittance versus wavelength into the visual spectrum for different transparent conductors: graphene, single-walled carbon nanotubes (SWNTs), indium tin oxide (ITO), ZnO/Ag/Zno and TiO₂/Ag/TiO₂. (b) Transmittance versus sheet resistance plots for different transparent conductive films, including CVD graphene and theoretical calculation of graphene. (c) Transmittance for an increasing number of layers, which show that graphene and bilayer graphene are highly transparent and that graphene absorbs only 2.3% of light for a very large range of wavelengths. (d) Graphene-based touchscreen panel (top, left) showing outstanding flexibility (bottom, left), a transparent ultralarge-area graphene film transferred on a 30-inch sheet fabricated by Samsung company (top, right) and possible applications in bendable mobile devices (bottom, right). Adapted from Refs. [52], [54], [55] and [56]. 54
- 1.13 (a) Illustration depicting a graphene sheet as a chemically inert diffusion barrier, preventing the reactive agent from ever reaching the metal underneath. (b) Photograph showing graphene coated (upper) and uncoated (lower) penny after H₂O₂ treatment (30%, 2 min). (c) Photographs of Cu and Cu/Ni foil with and without graphene coating taken before and after annealing in air (200 °C, 4 h). Adapted from Ref. [61]. 55
- 1.14 Schematic view of the metal-graphene-metal photodetector, where the electrodes are composed by palladium (Pd) and titanium (Ti) located on the top of a piece of multilayered or single-layered graphene. V_G is the gate bias. Adapted from Ref. [62]. 57

1.15	Some graphene applications for three main types of graphene product: graphene films, graphene oxide (GO) flakes and graphene nanoplatelets (GNPs), in which they are classified by technology readiness level. Adapted from Ref. [70].	59
1.16	Number of (a) publications and (b) patent applications per year up to 2010 for three carbon allotropes: carbon nanotubes, graphene and fullerenes. The publications in graphene are accelerating faster than the buzz that surrounded carbon nanotubes in the 1990s, whereas the number of patent applications involving graphene just mathed those citing nanotubes. (c) The development of the total number of graphene-related patents over the past few years together with selected scientific publications on the preparation and application of graphene. Adapted from Refs. [20] and [72].	61
2.1	(a) Hexagonal lattice structure of graphene represented by two interpenetrating triangular lattices A and B , whose primitive vectors are \vec{a}_1 and \vec{a}_2 , and $\vec{\delta}_i$, with $i = 1, 2$ and 3 , are the vectors that locate the nearest neighbors. The area in yellow shows the unit cell. (b) The first two Brillouin zones and the points of high symmetry of the reciprocal lattice (\vec{b}_1, \vec{b}_2) are also shown. The Dirac cones are located at the K and K' points.	65
2.2	(a) Electronic dispersion relation of graphene with a zoom in the energy bands, showing the conical relationship nearby K and K' Dirac points. (b) Contour plot of the conduction band on the first Brillouin zone.	66
2.3	(a) The crystal structure of bilayer graphene in Bernal stacking with the various hopping parameters. The bottom (top) layer is represented by dashed (solid) lines with triangular sublattices formed by A_1 (yellow) and B_1 (brown) (A_2 (black) and B_2 (green)) sites. γ_0 is the inter-layer hopping energy and $\gamma_{1,3,4}$ are the intra-layer hopping energies. (b) Perspective and (c) top views of crystalline structure of bilayer graphene, emphasizing the $A_1 - B_2$ connections and the middle position of the A_2 sites with respect to the carbon hexagons in bottom layer. $a \approx 1.42 \text{ \AA}$ and $d \approx 3.35 \text{ \AA}$ are the inter-atomic and intra-layer distances between the two closer carbon atoms in the same layer and between the two layers, respectively.	68
2.4	Drawing of the electronic band of (a) unbiased $\Delta U = 0$ and (b) biased bilayer graphene $\Delta U = U_1 - U_2 \neq 0$. (c) Energy spectrum of bilayer graphene for four different potential configurations, being $U_1 = U_2 = U = 0$ (black solid curve), $U_1 = -U_2 = U = 0.1 \text{ eV}$ (red dashed curve), $U_1 = -U_2 = U = 0.2 \text{ eV}$ (blue dotted curve) and $U_1 = -U_2 = U = 0.4 \text{ eV}$ (green short-dotted curve).	71

- 2.5 (a) Scheme of a charged particle with charge q and mass m performing a circular motion due to the influence of an external perpendicular magnetic field. The orientation of the vectors velocity \vec{v} and magnetic force \vec{F} are presented. (b) Classical skipping orbits experienced by a charge particle under a perpendicular magnetic field. 73
- 2.6 Landau levels as a function of the magnetic flux $\left(\frac{\phi}{\phi_0} = \frac{3\sqrt{3}a^2eB_0}{2h}\right)$ for (a) monolayer graphene $E_n = \pm\hbar v_F \sqrt{\frac{8\pi n}{3\sqrt{3}a^2} \frac{\phi}{\phi_0}}$, (b) unbiased bilayer graphene, and (c) biased bilayer graphene with gate potentials $U_1 = -U_2 = 100$ meV. 78
- 2.7 (a) The lattice structure of a graphene sheet denoting the zigzag and armchair type edge terminations. Top and bottom are armchair edges, left and right are zigzag edges. (b) In the zigzag case, each edge is built from atoms of one sublattice only. Following the dashed green lines forming a regular zigzag hexagon, one notice that the sublattice switches at every side. (c) In the armchair case, both sublattices are present at each edge forming dimer with $A - B$ or $B - A$ termination with respect to the tangential direction. 79
- 2.8 Surface S with an outward unit normal vector \vec{n} used to describe how to find the infinity-mass boundary condition used in order to confine carriers in a monolayer graphene. $\alpha(s)$ is the angle between the outward unit vector at the edges and the x -axis. Δ is the mass-related potential, which it is zero inside the arbitrary graphene quantum dot and infinity at its edges [93]. 84
- 3.1 Sketch of (a, c, e) armchair and (b, d, f) zigzag rings, with hexagonal, triangular and rhombus geometries respectively, as well as (g, h) circular rings, considered in this work. The first six geometries are characterized by the number of carbon rings $N_E(N_I)$ in their outer (inner) edge. Circular rings are characterized by their width W and average radius R . (g) Circular ring defined by cutting the graphene lattice. (h) Circular graphene ring defined by a smooth ring-shaped staggered potential M_i , where the color scale goes from $M_i = -M_0$ (red) to $M_i = +M_0$ (blue), and the $M_i = 0$ region inside the ring is represented in green. The atoms belonging to sublattices A and B have different colors because of the staggered potential profile. 93
- 3.2 Energy levels of armchair rhombus quantum rings, schematically shown in Fig. 1(e), as a function of the magnetic flux through a single carbon hexagon for two ring widths: (a) $N_E = 17$, $N_I = 12$ and (b) $N_E = 17$, $N_I = 11$. As shown in the insets, the energy spectrum does not have a zero-energy state: states close to $E = 0$ are rather similar to the first states above and below this energy, which are composed by branches of two oscillating energy states. 97

- 3.3 Energy levels of armchair hexagonal quantum rings, schematically shown in Fig. 1(a), as a function of the magnetic flux through a single carbon hexagon for two ring widths: (a) $N_E = 15$, $N_I = 10$ and (b) $N_E = 15$, $N_I = 3$. The spectrum is symmetric with respect to $E = 0$ 98
- 3.4 Current density profile for an armchair hexagonal quantum ring corresponding to magnetic flux indicated by (I) and (II) in Fig. 3.3(a). The results for the current density are numerically calculated based on the method discussed in Refs. [130], [142] and reproduced in the present manuscript. 100
- 3.5 (a) Rhombus armchair quantum ring (blue polygon figure) considered in the TB calculation, with $N_E = 17$ and $N_I = 12$, along with the one-dimensional $R \approx 32.3\text{\AA}$ ring (red circle) considered in the simplified model. (b) Energy spectra, obtained from the simplified (solid lines) and TB (dashed lines) models, as a function of the magnetic flux threading the red circle illustrated in (a). Curves with different colors represent different angular momentum index l . (c) The results from the TB model with a background mass term $M = 0.5E_0$ are also compared to those from the simplified model in this case. 102
- 3.6 (a) Hexagonal armchair quantum ring (blue polygon figure) considered in the TB calculation, with $N_E = 15$ and $N_I = 10$, along with the one-dimensional $R \approx 47\text{\AA}$ ring (red circle) considered in the simplified model. (b) Energy spectra, obtained from the simplified (solid lines) and TB (dashed lines) models, as a function of the magnetic flux threading the red circle illustrated in (a). Curves with different colors represent different angular momentum index l . (c) The results from the TB model with a background mass term $M = 0.5E_0$ are also compared to those from the simplified model in this case. 103
- 3.7 Energy levels of armchair hexagonal quantum ring, obtained from the simplified (solid) and TB (dashed) models, as function of ring radius R , calculated assuming an average radius given by $R = \left(\frac{3\sqrt{3}}{2\pi} \left(\frac{|L_E + L_I|}{2} \right)^2 \right)^{1/2}$ and mass term $M = 0.1$ eV, for different values of the magnetic flux Φ/Φ_0 . Curves with green, red and blue colors represent angular momentum index l zero, negative and positive, respectively. The spectrum is symmetric with respect to $E = 0$ 104
- 3.8 Energy levels as a function of the magnetic flux through a single carbon hexagon for (a) the circular graphene ring schematically shown in Fig. 3.1(g), and (b) a quantum ring formed by a site-dependent potential given by Eq. (3.2) and schematically shown in Fig. 3.1(h), with smoothness $S = 10$ \AA and height $M_0 = 1$ eV. In both cases, the average radius of the ring is $R = 80$ \AA and the width is 60 \AA . The spectrum is symmetric with respect to $E = 0$ 106

3.9	Energy spectrum, obtained by the continuum model for K (red solid) and K' (blue dashed), as a function of the magnetic flux for a graphene quantum ring defined by an infinite mass boundary, with the same average radius and width as the ring in Fig. 3.8(b). The spectrum is symmetric with respect to $E = 0$	107
3.10	Energy levels of zigzag hexagonal quantum rings, schematically shown in Fig. 1(b), as a function of the magnetic flux through a single carbon hexagon for two ring widths: (a) $N_E = 15$, $N_I = 10$ and (b) $N_E = 15$, $N_I = 9$. In the (former) latter the inner and outer zigzag edges are (anti-) aligned, as sketched in the insets.	109
3.11	Energy levels of zigzag rhombus quantum rings, schematically shown in Fig. 1(f), as a function of the magnetic flux through a single carbon hexagon for two ring widths: (a) $N_E = 17$, $N_I = 11$ and (b) $N_E = 17$, $N_I = 9$. For both widths, the energy spectrum does not have a zero-energy state, they are three pairs of oscillating states as shown in the insets.	110
3.12	Energy levels of zigzag triangular quantum rings, schematically shown in Fig. 1(d), as a function of the magnetic flux through a single carbon hexagon for two ring widths: (a) $N_E = 17$, $N_I = 12$ and (b) $N_E = 15$, $N_I = 10$. For both widths, the energy spectrum has a zero-energy state.	111
3.13	Energy levels of armchair triangular quantum rings, schematically shown in Fig. 1(c), as a function of the magnetic flux through a single carbon hexagon for two ring widths: (a) $N_E = 15$, $N_I = 10$ and (b) $N_E = 15$, $N_I = 9$. The spectrum is symmetric with respect to $E = 0$	112
4.1	An illustration of a circular quantum dot of radius R made of bilayer graphene. The dot is surrounded by an infinity mass potential $\Delta \rightarrow \infty$	116
4.2	Schematic picture of the mass potential profile for a (a) ring-shaped barrier and (b) dot barrier divided into three and two regions, respectively. The width of the barrier, i.e. $\delta \ll 1$, is shown by the yellow region and the radius of the dot and ring is set to 1.	118
4.3	Energy levels of a circular BLG quantum dot as a function of angular momentum label m for $R = 70$ nm and in the absence of a magnetic field. The energy levels corresponding to the K and K' valleys are shown by the blue crosses and the red dashed	122
4.4	Energy levels of a circular BLG quantum dot as a function of the dot radius with $m = 1$ (a, b), $m = 0$ (c, d) and $m = -1$ (e, f). Left and right panels correspond, respectively, to zero magnetic field and $B_0 = 5$ T. The energy levels corresponding to the K and K' valleys are shown by the blue dashed and the red solid curves respectively.	123

- 4.5 Energy spectrum of a circular BLG quantum dot as a function of a perpendicular magnetic field with $R = 70$ nm and for $-4 \leq m \leq 4$. The energy levels corresponding to the K and K' valleys are shown by the blue dashed and the red solid curves, respectively. The black dotted lines are the three first LLs of BLG. The inset shows an enlargement of the low energy levels at small magnetic fields. 126
- 4.6 Energy spectrum of a circular BLG quantum dot as a function of a perpendicular magnetic field with $R = 10$ nm obtained within (a) the continuum model taking $-22 \leq m \leq 22$ and (b) the tight-binding model. The energy levels corresponding to the K and K' valleys are shown in (a) by the blue dashed and the red solid curves, respectively. The green dashed lines are the three first LLs of bulk BLG. Figures (c) and (d) show the squared total wave function ($|\Psi_{TB}|^2$) for the states indicated by (c) $\epsilon \approx 0.5348$ and (d) $\epsilon \approx 0.6746$ in figure (b), respectively. Blue (red, black) color is low (high, very high) density. The mass potential region is shadowed by the gray color. 127
- 4.7 Contour plot of the electron probability density as a function of the normalized magnetic field β and the dot radius ρ for the lowest states of the K valley and with (a, b) $m = 0$, (c, d) $m = 1$, and (e, f) $m = -1$. Left and right panels show respectively $|\phi_A|^2 + |\phi_B|^2$ and $|\phi_{A'}|^2 + |\phi_{B'}|^2$ corresponding to the density in the different layers. 129
- 4.8 (a) Transition energies and (b) the corresponding transition rates as a function of the normalized magnetic field for a QD with radius $R = 70$ nm. The label ($m \rightarrow m'$) indicates the angular momentum of the initial m and the final m' states. The results corresponding to the K and K' valleys are respectively shown by the solid and dashed curves. 130
- 5.1 (Color online) Sketches of the studied systems in this work composed by hexagonal shaped quantum dots of size L in bilayer graphene created by (a) cutting out atoms in the inner region of the top layer and (b) with the top layer being smaller than the bottom one. In both cases (a) and (b), the outer edges are taken armchair forming a hexagonal dot with a larger size. A cross-section view of the dots are presented at the bottom of each system. The distance between the layers is d , that was taken as ≈ 100 Å. . 132
- 5.2 (Color online) Energy spectrum of hexagonal BLG quantum dots with zigzag edges as a function of dot size L in the presence of a symmetric electrical bias with $V_0 = 0.1$ eV for the system represented in Fig. 5.1(a). A zoom of the yellow region is shown to emphasize the behaviour around the anti-crossing of different states. 135

- 5.3 (Color online) Squared total wave function ($|\psi|^2 = |\psi_1|^2 + |\psi_2|^2$) for the states labeled in Fig. 5.2 as (a) 1, 2, 3, (b) 4, 5, 11, 12, (c) 6, 7, 9, 10, (d) 8, 13, 14 and (e) 15. The wave functions corresponding to the states represented in each item from (a) to (d) have the same symmetry, but they have a phase difference such that are rotated as related to each other. Small (large) circle with blue (red) color represents low (high) density. The bilayer region is shadowed by the gray color. 136
- 5.4 (Color online) Energy spectrum of hexagonal BLG quantum dots with armchair edges as a function of dot size L in the presence of electrical bias with $V_0 = 0.1$ eV for the system represented in Fig. 5.1(a). 136
- 5.5 (Color online) Squared total wave function $|\psi|^2$ and contribution from each layer: bottom $|\psi_1|^2$ and up $|\psi_2|^2$ for the states indicated by 1 and 2 in Fig. 5.4. Small (large) circle with blue (red) color represents low (high) density. The bilayer region is shadowed by the gray color. 137
- 5.6 (Color online) Energy spectrum of hexagonal BLG quantum dots with (a) zigzag and (b) armchair edges as a function of dot size L for the system represented in Fig. 5.1(b). The dashed lines are the energy levels of the monolayer system that has the same dimension as the bottom layer for the bilayer system sketched in Fig. 5.1(b). 138
- 5.7 (Color online) Squared total wave function $|\psi|^2$ for the states indicated by (a) 1 and (b) 2 in Fig. 5.6(a) for the zigzag (zz) case and (c) 3 and (d) 4 in Fig. 5.6(b) for the armchair (ac) case. Small (large) circle with blue (red) color represents low (high) density. The bilayer region is shadowed by the gray color. 139
- 5.8 (Color online) Energy spectrum of hexagonal BLG quantum dots with (a, b) armchair and (c, d) zigzag edges as a function of magnetic flux in the absence of electrical bias for the system represented in Fig. 5.1(a). The red lines in (a) and (c) correspond to the first six Landau levels of an unbiased bilayer graphene. (b) and (d) show a zoom closer around $E = 0$ 140
- 5.9 (Color online) Squared total wave function $|\psi|^2 = |\psi_1|^2 + |\psi_2|^2$ in each layer: bottom $|\psi_1|^2$ and upper $|\psi_2|^2$ for the states indicated by 1 and 2 in Fig. 5.8(a). Small (large) circle with blue (red) color represents low (high) density. The bilayer region is shadowed by the gray color. 142
- 5.10 (Color online) Energy spectrum of hexagonal BLG quantum dots with (a, b) armchair and (c, d) zigzag edges as a function of magnetic flux in the presence of electrical bias with $V_0 = 0.1$ eV for the system represented in Fig. 5.1(a). The red lines in (a) and (c) correspond to the first six Landau levels of a biased bilayer graphene. (b) and (d) show a zoom closer around $E = 0$ to emphasize the points 1 – 10 and the opening of the energy levels around the zero energy. 143

- 5.11 (Color online) Squared total wave function $|\psi|^2$ for the states indicated in Fig. 5.10(b) for the system sketched in Fig. 5.1(a) with armchair edges, such as the points 1 – 6 correspond to the plots (a) 1, (b) 2 and 5, (c) 3 and 4 and (d) 6. Small (large) circle with blue (red) color represents low (high) density. The bilayer region is shadowed by the gray color. 145
- 5.12 (Color online) Squared total wave function $|\psi|^2$ for the states indicated in Fig. 5.10(d) for a system sketched in Fig. 5.1(a) with zigzag edges, such as the points 7 – 10 correspond to the plots (a) 7, (b) 8, (c) 9 and (d) 10. Small (large) circle with blue (red) color represents low (high) density. The bilayer region is shadowed by the gray color. 146
- 6.1 (a) Dirac cones of graphene, along with an illustrative scheme of the inter-(green circles) and intra-(gray circles) valley scattering. (b) Sketch of the strained graphene sample considered in this work, where the (open green) full black circles represent the (un)strained case. The upper boundary is set as the $y = 0$ axis for convenience. 150
- 6.2 Average position of a gaussian wave packet of width $d = 300 \text{ \AA}$ in an unstrained graphene flake, in the absence of external magnetic fields, as a function of time. (a) Horizontal propagation of a wave packet with $\vec{k} = (0.03\text{\AA}^{-1}, 4\pi/3\sqrt{3}a)$, and its consequent reflection by a zigzag edge. In this case the origin of the system is shifted, so that the right zigzag edge is set as the $x = 0$ axis. The wave packet starts at $(x_0, y_0) = (-600\text{\AA}, -600\text{\AA})$, and exhibits also a slow drag towards the upper edge, due to Zitterbewegung effects. (b) Vertical propagation of a wave packet with $\vec{k} = (0, 4\pi/3\sqrt{3}a + 0.02\text{\AA}^{-1})$, starting at $(0, -600\text{\AA})$, exhibiting reflection by the upper armchair border. In this case, the sample is not shifted, *i.e.* the upper edge is at the $y = 0$ axis, as sketched in Fig. 6.1(b). 152
- 6.3 Time evolution of the wave packet in reciprocal space corresponding to the situations shown in Fig. 6.2. (a) Illustrative scheme of the lines in reciprocal space along which Fourier transform of the wave functions are taken. For the propagation in the horizontal direction (see Fig. 6.2(a)), we consider $\vec{k} = (0.03\text{\AA}^{-1}, 4\pi/3\sqrt{3}a)$. The time evolution of the wave function along the (i) – (ii) line of reciprocal space is shown in (b) as contour plots. For vertical propagation (see Fig. 6.2(b)), we consider $\vec{k} = (0, 4\pi/3\sqrt{3}a + 0.02\text{\AA}^{-1})$. The time evolution of the wave function along the (iii) – (iv) line of reciprocal space is shown as contour plots in (c) and (d), corresponding to different ranges of k_y^{iii-iv} 154

- 6.4 Trajectories drawn by $\langle x \rangle$ and $\langle y \rangle$ for a gaussian wave packet in the presence of an external magnetic field ≈ 5 T, propagating close to the edges in a rectangular graphene flake, within a $t = 2000$ fs propagation time. The arrows indicate the direction of propagation. Different values of the initial wave packet width d are considered. The edges of this panel are placed at the positions of the actual edges of the sample. (b) Average values of the wave packet position $\langle x \rangle$ and $\langle y \rangle$ as a function of time for the trajectories drawn in (a). Different parts of the trajectory in (a) were labeled from (I) to (V), and the time intervals where they occur are delimited by the vertical lines in (b). 155
- 6.5 (a) Trajectories drawn by $\langle x \rangle$ and $\langle y \rangle$ for a $t = 2000$ fs time evolution of a wave packet, which propagates close to the upper (armchair) border of a bent rectangular graphene sample, for two values of wave packet width d . The radius of the circular distortion is $R = 10^4 \text{ \AA}$, corresponding to an almost uniform ≈ 5 T pseudo-magnetic field. The horizontal dashed line represents the upper edge of the sample. (b) Average values of the wave packet position $\langle x \rangle$ and $\langle y \rangle$ as a function of time for the trajectories drawn in (a). 156
- 6.6 Contour plots of the time evolution of the wave packet in reciprocal space corresponding to the propagation shown in Fig. 6.5, *i.e.* for a strained graphene sample. The Fourier transform of the wave packet is taken in the vicinity of the (a) K and (b) K' points of the reciprocal space illustrated in Fig. 6.3(a), along the $k_x = -0.06 \text{ \AA}^{-1}$ ($k_x = 0.045 \text{ \AA}^{-1}$) vertical axis for K (K'). 157
- 6.7 Integrated probability density currents as a function of time for the situations proposed in Figs. 6.4 and 6.5, namely, (a) for an unstrained graphene sample in the presence of an external 5 T magnetic field, and (b) in a circularly bent graphene sample, which produces an almost uniform ≈ 5 T pseudo-magnetic field. The curves (symbols) represent the component of the current in the x (y)-direction, *i.e.* j_x (j_y). Two different values of wave packet width are considered: $d = 100 \text{ \AA}$ (black solid - circles) and 300 \AA (red dashed - triangles) The regions delimited in (a) are the same as in Fig. 6.4. 160
- 7.1 Sketch of the QPC structure, forming a channel with length L and width W , with (a) aligned and (b) anti-aligned bias. The actual sample used in our numerical calculation is rectangular with 3601×1000 atoms in each layer that corresponds to a size $\approx 213 \times 443 \text{ nm}^2$ 163

- 7.2 Band structure for the two potential configurations sketched in Fig. 7.1, namely, (a) aligned and (b) anti-aligned potential barriers. Results are presented for $V_0 = 200$ meV and three values for the quantum well width $W = 5$ (black solid), 10 (red dashed) and 20 nm, (blue dotted). 168
- 7.3 Transmission probability as a function of wave packet energy for aligned potentials with $V_0 = 100$ meV (closed symbols) and $V_0 = 200$ meV (open symbols). The value for width of the QPC was considered $W = 10$ nm. The square and circular symbols correspond to the lengths $L = 5$ and 20 nm, respectively. 169
- 7.4 The same as Fig. 7.3, but for anti-aligned potentials and with initial wave packet in K valley (a) and in K' valley (b). 170
- 7.5 Transmission probability (top panels) and valley polarization (bottom panels) as a function of the electrostatic bias V_0 in the case of anti-aligned potentials with initial wave packet energy $E = 30$ meV and three different values of L : (a, b) 5 nm, (c, d) 10 nm and (e, f) 20 nm. The opened (closed) square-like, circular and triangular symbols correspond to $W = 5$, 10 and 20 nm, for the K (K') valley, respectively in panels (a), (c) and (e). The black solid, red dashed and blue dotted lines show the polarization for $W = 5$, 10 and 20 nm, respectively in panels (b), (d) and (f). 171
- 7.6 (a, c) Transmission probability and (b, d) the polarization as a function of width W of the QPC for anti-aligned potentials with $V_0 = 100$ meV (left side panels) and $V_0 = 200$ meV (right side panels). The average wave packet energy was $E = 30$ meV. The opened (closed) square-like, circular and triangular symbols correspond to $L = 5$, 10 and 20 nm, for the K (K') valley, respectively in Figs. (a) and (c). The black solid, red dashed and blue dotted curves show the polarization for $L = 5$, 10 and 20 nm, respectively in Figs. (b) and (d). 172

List of Tables

1.1	Carbon hybridization.	45
1.2	Allotropes made of carbon [27].	45
1.3	Comparative table of growth/deposition techniques to isolate/produce few graphene layers. Adapted from Refs. [33] and [41].	52

List of abbreviations

<i>0D</i>	Zero-dimensional
<i>1D</i>	One-dimensional
<i>2D</i>	Two-dimensional
<i>3D</i>	Three-dimensional
AB	Aharonov-Bohm
AFM	Atomic force microscopy
BLG	Bilayer graphene
CNTs	Carbon nanotubes
CVD	Chemical vapor deposition
DOS	Density of states
fcc lattice	Face-center-cubic lattice
FLG	Few-layer graphene
(G)QDs	(Graphene) quantum dots
h-BN	Hexagonal boron nitride
HOPG	Highly oriented pyrolytic graphite
LCDs	Liquid crystal displays
LEDs	Light emitting diodes
LL(s)	Landau Level(s)
MLG	Monolayer graphene
MWNTs	Multi-wall carbon nanotubes
PAH	Polycyclic aromatic hydrocarbon
QPC	Quantum point contact
SWNTs	Single-wall carbon nanotubes
STM	Scanning tunneling microscopy
TB(M)	Tight-binding (model)

List of nomenclatures

v_f	Fermi velocity
τ, γ_i	Hopping parameters
$\Psi_A(\Psi_B)$	The probability of finding the electron on sublattice A and B
e	Elementary electron charge
\vec{A}	Vector potential
\vec{B}	Magnetic field
l_B	Magnetic length
ϕ_0	Magnetic quantum flux
m	Angular momentum label
\vec{p}	Momentum vector
I	Identity matrix
M	Mass-term matrix
Δ	Mass potential
\hat{U}	Time evolution operator
T	Kinetic operator
V	Potential operator
\vec{a}_i	Real lattice vector i
\vec{b}_i	Reciprocal lattice vector i
\vec{F}	Force
H	Hamiltonian
H_D	Dirac Hamiltonian
\mathbf{a}_i^\dagger	Creation operator of electrons on the site i of the sublattice A
\mathbf{a}_i	Annihilation operator of electrons on the site i of the sublattice A
\mathbf{b}_i^\dagger	Creation operator of electrons on the site i of the sublattice B
\mathbf{b}_i	Annihilation operator of electrons on the site i of the sublattice B

$g(\vec{k})$	Structure factor of the crystal
$Y_l^m(\theta, \phi)$	Spherical harmonics
$J_m(\kappa\rho)$	The Bessel function of the first kind
$\widetilde{M}(A_{\pm}, B, \widetilde{\rho})$	The regularized confluent hypergeometric function
$\mathcal{H}_n(x)$	Hermite polynomials
\hbar	Plank constant
K	Dirac cone K
K'	Dirac cone K'
ϵ_i	Self-energy on site i
d	Width of initial gaussian wave packet
W	Quantum point contact width
L	Quantum point contact length
R	Radius of the quantum dot and ring
$N_{E(I)}$	Number of carbon rings in the outer (inner) edge
$\vec{\rho}$	Density matrix operator
j	The probability current
P	The valley polarization
$T_{K(K')}$	The transmission probability for a wave packet starting in the K (K') cone
k	The modulus of the wave vector
θ	Incident angle
Γ	Gamma point, center of first Brillouin zone
$\vec{\sigma}_i$	Pauli matrix i
a	Lattice parameter
E	Energy
E_g	Gap energy

In this chapter, we will explore some basic properties of the chemical element carbon, which is responsible for the existence of a wide variety of materials in nature. Initially, we will expose a brief history of obtaining isolated graphene, talking about the reasons for delay in making this “discovery”. We also discuss the different allotropes of carbon and the hybridizations that generate them. We will relate the physical properties, such as dimensionality, with its crystalline forms and its hybridizations. Finally, we present three ways of obtaining few-layer graphene (FLG).

1.1 A brief history: carbon materials

During the last twenty years, the scientific community has focused its attention to research involving nanomaterials, especially for the study and exploration of properties of those materials consisting only of carbon atoms, among which is graphene¹.

Although some of the allotropes of carbon are known for many years, such as diamond and graphite², the invention/isolation of graphene, even being considered the mother of all these different forms, was somehow very delayed. The reasons are due to the fact that (i) studies of two-dimensional crystal structures have been guided by the idea that such atomic arrangements would be thermodynamically unstable at finite temperatures, and that (ii) there could be some graphene among the pencil debris, but there were no experimental tools to search for one-atom-thick flakes there[1].

The idea that two-dimensional atomic crystals do not exist and are thermodynamically unstable under ambient conditions is based on the physical theory of Peierls, Landau, Lifshitz and Mermin [3, 4, 5, 6], which states that thermal fluctuations existing at any finite temperature should make the low dimensional crystal lattices undergo atomic displacements comparable to interatomic distances such that this lattice would collapse. This

¹Graphene is the name given to a polycyclic aromatic hydrocarbon (PAH) with carbon rings formed by six carbon atoms, which extend infinitely in the $2D$ plane.

²Graphite has been known as a mineral for nearly 500 years and has been used in a pencil for at least 440 years [1, 2].

statement is described in Mermin-Wagner theorem [6, 7]. Since the conventional methods to synthesize crystal growth heretofore developed and used (before the graphene isolation) were all based on temperature variations, and coupled with the Mermin-Wagner theorem, such a synthesis was not feasible. Furthermore, it is known that the melting temperature of a thin film decreases with its thickness. Thus, when some graphite layers are subjected to high temperatures, it results in the formation of islands or in the decomposition of the film, making it unstable. This led to the idea that the two-dimensional crystal lattices could only exist as part of a three-dimensional system or on top of non-crystalline substrates [8].

However, the discovery of new carbon allotropes in the last thirty years made reemerge the interest in carbon materials. First, the fullerenes were discovered in 1985 by a team from Rice University and University of Sussex, composed by R. F. Curl, H. W. Kroto and R. E. Smalley [9], who were awarded the Nobel Prize in chemistry in 1996 “*for their discovery of fullerenes*” [10]. And latter, in 1991 it is attributed to S. Iijima the discovery of carbon nanotubes, where in his publication S. Iijima reported about multi-wall carbon nanotubes (MWNTs) [11]. Two years latter in 1993, a single-wall carbon nanotubes (SWNTs) was observed simultaneously by S. Iijima and D. S. Bethune and published in the same issue of *Nature* [12, 13]. These discoveries have opened new perspectives for innovations in the electronics industry based on carbon.

Until then, graphene was considered only as a “physics toy” [2] and an “academic material” [8]. Its theory was developed by P. R. Wallace in 1947 [14], who explained how the band structure of graphene is and showed the unusual semimetallic behavior in this material even before it was found experimentally. This theory is used for describing properties of fullerenes and carbon nanotubes and it is one of the reasons that graphene is considered the mother of carbon materials.

After many experimental attempts of various research groups in condensed matter to obtain graphene, in 2004, a group of physicists from Manchester University (UK) led by Andre Geim and Kostya Novoselov finally succeeded in isolating films consisting of few layers of graphene. This study by Geim’s group began in 2002/2003. The initial goal was to obtain around 100-layer graphite and to study it with the hope of finding problems similar to those in the carbon nanotube world [15]. This search to make graphite films as thin as possible was part of the experiments performed by Geim and his collaborators only for fun, without any strict commitment with the quality of results. They devoted ten percent of their time to so-called “Friday evening” experiments and the graphene business started as one of these Fridays [16]. In the experimental process to obtain thin films of graphite, they employed a widely used procedure for the surface cleaning of graphite for analysis in scanning tunneling microscope (STM), which consists only in sticking ordinary adhesive tape in the graphite and then pull it, repeating this operation several times. At the end, very thin flakes are left attached to the tape. After this stage, the researchers needed to deposit the resulting thin films on a particular substrate previously unknown

to analyze the films on tape. Luckily, they deposited on an oxidized silicon substrate (Si/SiO_2) (the only available substrate in the initial week of testing), and thus one could notice that some films had only one layer [17]. Thus, in 2004, it was announced by Geim and Novoselov the formal obtainment/“discovery” of graphene in an isolated and stable form at room temperature³ [18], and in 2010 they were already awarded the Nobel Prize in Physics “for groundbreaking experiments regarding the two-dimensional material graphene” [19].

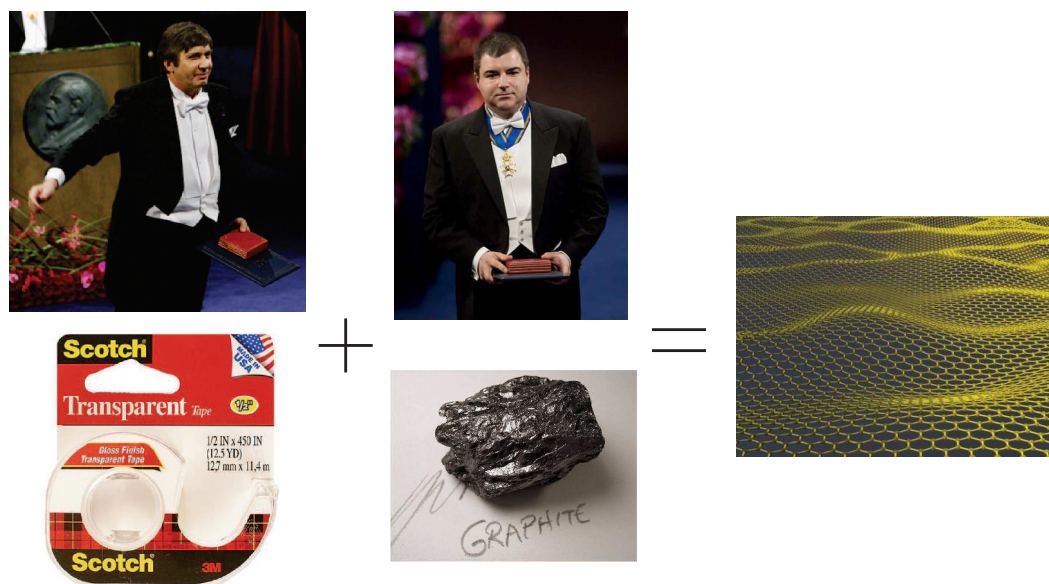


Figure 1.1: Ingredients to find out graphene: two good researchers, scotch tape and graphite. Photographs taken when Geim and Novoselov were attending the 2010 Nobel Prize ceremony (December 8, 2010) at Aula Magna, Stockholm University.

The following years after the discovery of graphene were marked by numerous publications that have consolidated this $2D$ nanomaterial in the scenario of scientific research. This hot topic has received a lot of attention from the science community [20] due to its importance in basic science [21, 22] and its unique electronic properties, which make it an excellent and promising option for the industry to create new devices such as simple molecular gas sensor, ballistic transistors and spintronic devices [8, 23]. The atypical properties of charge carriers in graphene are due to its linear dispersion relation at low energies ($E < 1\text{eV}$). Displaying a gapless energy spectrum with a conic format [21], the low-energy electrons behave like zero-mass relativistic particles with an effective velocity of the order of 10^6 m/s. Thus, the motion of these charge carriers is governed by the massless Dirac fermions equation, which leads to several interesting phenomena such as, for example, ambipolar electric field effect, minimum conductivity, anomalous quantum Hall effect and Klein tunneling [1, 24].

These results stated the existence of thermodynamically stable two-dimensional crystals, *i. e.*, the few layers of graphene isolated, and with the improvement in experimental

³In fact, what Geim’s group found was still graphite, about 10-layers thick [15].

techniques in the last years, they opened the doors to study other $2D$ atomic crystals, such as molybdenum disulphide (MoS_2) and hexagonal boron nitride (h-BN) [25]. Thus, it is possible that the research area in $2D$ crystals remains as a hot topic for many years, just like the semiconductor physics is still widely studied until today.

1.2 The carbon atom and its hybridizations

Carbon, an unique chemical element, composes the elementary building block of all organic molecules. In this way, it is also responsible for life on Earth, as well as constitutes plenty of inorganic materials. This element is the fourth most abundant chemical element in the universe by mass, losing only to hydrogen, helium, and oxygen, being abundant in the Sun, stars, comets, and in the atmosphere of most planets.

The carbon atom is a member of group 14 and the sixth element on the periodic table, neighbor to Boron and Nitrogen. Its atom has six electrons distributed in the ground state according the configuration $1s^2 2s^2 2p^2$. The $1s$ orbital is occupied by two electrons strongly bound to the nucleus, such that they are irrelevant for chemical bounds. These electrons, together with the nucleus, are called the core of the atom. On the other hand, the other four electrons, the so-called valence electrons that occupy the $2s$ and $2p$ orbitals, are more weakly bound. Therefore, they have an effective participation in chemical reactions. Since carbon has two half-filled orbitals, valence electrons open the possibility to form at least two bonds with other atoms.

Let us start from the context of the hydrogen-like atom to understand how the wave function is written for multi-electronic atoms. It is known that the eigenfunctions for the hydrogen-like atom are called atomic orbitals, where the state corresponding to each orbital is described as $|nlm\rangle$, or, in spectroscopic notation, as $|nx^m\rangle$, with $x = s, p, d, f, g, h\dots$ related to $l = 0, 1, 2, 3, 4, 5\dots$, respectively, and $-l \leq m \leq l$. These eigenfunctions $|nlm\rangle$ (or Ψ_{nlm}) are given in terms of the product of spherical harmonics $Y_l^m(\theta, \phi)$ and a function $F(r)$ that depends on the radial direction, related to the central potential $V_c(r)$. Since only orbitals s and p are considered in the carbon atom interactions, corresponding to l values equal to 0 and 1, then the $Y_l^m(\theta, \phi)$ functions concerned are

$$Y_0^0(\theta, \phi) = \frac{1}{2\sqrt{\pi}}, \quad (1.1a)$$

$$Y_1^{\pm 1}(\theta, \phi) = \frac{\mp 1}{2} \sqrt{\frac{3}{2\pi}} \sin \theta e^{\pm i\phi}, \quad (1.1b)$$

$$Y_1^0(\theta, \phi) = \frac{1}{2} \sqrt{\frac{3}{\pi}} \cos \theta, \quad (1.1c)$$

showing that the wave function for the s orbital is always real and has a spherical shape, since Y_0^0 is constant. For p states that carry complex values in the $|nlm\rangle$ basis, it is

convenient to make a transformation in order to obtain always orbitals that assume real values. Using the linear combination of the states with $m = \pm 1$ we have

$$|np_x\rangle = \frac{1}{\sqrt{2}} (|np^1\rangle - |np^{-1}\rangle), \quad (1.2a)$$

$$|np_y\rangle = \frac{1}{i\sqrt{2}} (|np^1\rangle + |np^{-1}\rangle), \quad (1.2b)$$

$$|np_z\rangle = |np^0\rangle. \quad (1.2c)$$

These p orbitals are plotted in Figs. 1.3, 1.5 and 1.7, and have the shape of two spheres touching each other forming a dumbbell. The colors blue and orange represent, respectively, the positive and negative signs of the wave function⁴.

Although the inclusion of electron-electron interactions makes it impossible to have the exact solution for multi-electron atoms, we can still extend the concept of orbital for an approximation of independent electrons to many-electron atoms. Thus, we use the concept of orbitals of hydrogen-like atoms to describe the bounds between many-electron atoms.

Despite the $2s$ orbital to be approximately 4 eV less energetic than the $2p$ orbitals, this energy difference is smaller as compared to the binding energies involving the carbon atom. Thus, for the ground state, it is more energetically favorable to keep two electrons in the $2s$ orbital and two in the $2p$ orbitals, whereas in the presence of other atoms it is favorable to promote one of the two electrons in $2s$ orbital to the third $2p$ orbital, that was previously empty, as shown in Figs. 1.2, 1.4 and 1.6 on excited states. Therefore, one has, after the process of electron promotion, four half-filled orbitals that can easily form covalent bonds with the linear combination of states $|2s\rangle$, $|2p_x\rangle$, $|2p_y\rangle$ and $|2p_z\rangle$. This mixing of the state $|2s\rangle$ and n states $|2p_j\rangle$, with $j = 1, 2$ and 3 , that enhances the binding energy between the carbon and its neighboring atoms, is called hybridization, where the superposition of a single $2s$ electron with n $2p$ electrons is named as sp^n hybridization [27].

We are now going to describe how the three types of hybridization happen on carbon, showing which states get into to form the hybrid orbitals sp , sp^2 and sp^3 .⁵

1.2.1 sp hybridization

In the process of sp hybridization, after the promotion of one electron to $2p$ orbital, as we can see in Fig. 1.2, the $2s$ orbital and one of the $2p$ orbitals, $2p_x$ for example, are

⁴The orbital figures were made using the Orbital Viewer program, available for free in [26].

⁵There are other kind of hybridization involving more energetic orbitals with other atoms, for example sp^3d hybridization, that composes the bounds in PF_5 , SF_4 and BrF_3 molecules, exhibiting a triangular bipyramidal shape, and sp^3d^2 hybridization, that composes the bounds in SF_6 , ClF_5 and XeF_4 molecules, exhibit an octahedral shape [28].

combined. This mixing results in two $2sp$ hybridized orbitals and two $2p$ non-hybridized orbitals. From this linear combination between $|2s\rangle$ and $|2p_x\rangle$ orbitals, arise two hybrids states

$$|sp_a\rangle = C_1 |2s\rangle + C_2 |2p_x\rangle, \quad (1.3a)$$

$$|sp_b\rangle = C_3 |2s\rangle + C_4 |2p_x\rangle, \quad (1.3b)$$

that obey the orthonormality conditions

$$\langle sp_a | sp_a \rangle = \langle sp_b | sp_b \rangle = 1, \quad (1.4a)$$

$$\langle sp_a | sp_b \rangle = \langle sp_b | sp_a \rangle = 0. \quad (1.4b)$$

The fact that the probability of $2s$ orbital to be occupied in $|sp_a\rangle$ and $|sp_b\rangle$ combinations should be 1, *i. e.* $C_1^2 + C_3^2 = 1$, implies that $C_1 = C_2 = C_3 = -C_4 = \frac{1}{\sqrt{2}}$. With all these conditions we find the two hybrid states

$$|sp_a\rangle = \frac{1}{\sqrt{2}} (|2s\rangle + |2p_x\rangle), \quad (1.5)$$

$$|sp_b\rangle = \frac{1}{\sqrt{2}} (|2s\rangle - |2p_x\rangle). \quad (1.6)$$

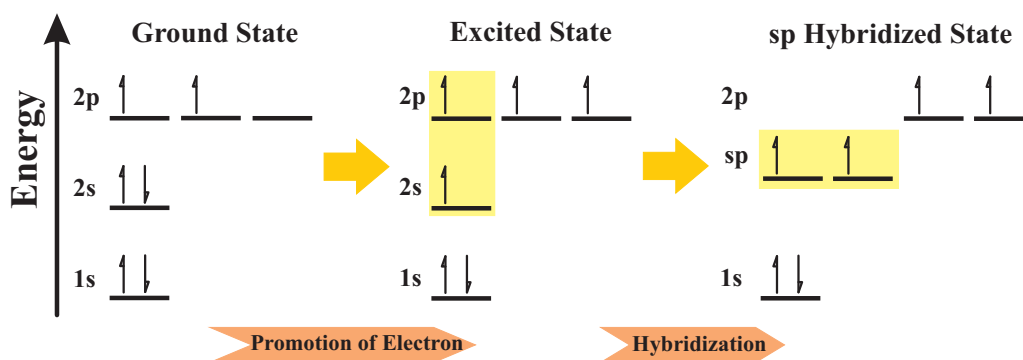


Figure 1.2: Process to derive sp hybridization in carbon atoms. Electronic distribution for carbon is presented from left to right in the ground state, excited state, after the promotion of one electron to one of the $2p$ orbitals, and the last stage is the sp hybridized state. The yellow background in the excited stage comprises the two orbitals involved to make hybridization happen. The energy level of the two sp orbitals is smaller than the two $2p$ pure orbitals and greater than $2s$ orbital in ground state. In the final process, one has two sp hybridized states.

In Fig. 1.3 we present a schematic view of how the sp hybridization forms the two hybrid states. We can see that the two hybrid orbitals have their large positive lobes

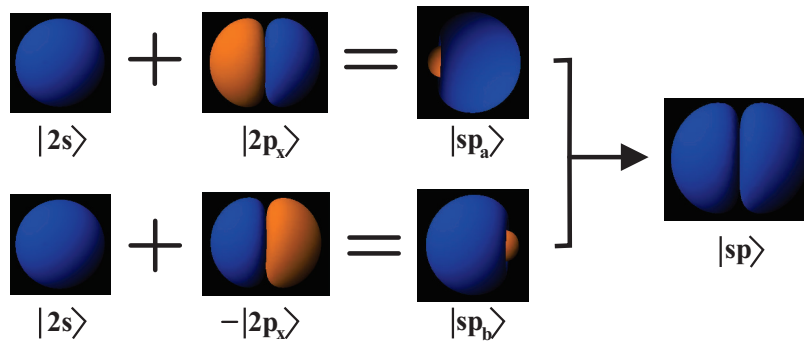


Figure 1.3: Schematic view of the sp hybridization showing the linear combination between the s and p_x orbitals to form the two $|sp_a\rangle$ and $|sp_b\rangle$ hybrid states, according to Eqs. (1.5) and (1.6), respectively. The color directions denote the positive (blue) and negative (orange) amplitude of the wave function. Only positive lobes are presented in illustration of $|sp\rangle$ state.

oriented at an angle of 180° with respect to each other, with $|sp_a\rangle$ ($|sp_b\rangle$) elongated in positive (negative) x -direction, being a favorable orbital to form covalent σ bonds with neighbor atoms connected to the carbon. The other two p pure orbitals not hybridized are perpendicular to the axis that passes through the chain and are responsible to form π bonds. An example of structure formed by carbon that presents this sp hybridization is the acetylene ($\text{HC}\equiv\text{CH}$). This molecule is linear and has a triple bond between its two carbon atoms, which corresponds to a stronger σ bond and two additional π bonds, which are weaker than the former.

1.2.2 sp^2 hybridization

Now, the mixing of orbitals involves the $2s$ orbital and two $2p$ orbitals, for example $2p_x$ and $2p_y$ orbitals, as schematically represented in Fig. 1.4. This process is responsible for the emergence of orbitals propitious to three identical and coplanar connections equally spaced, making a 120° angle with each carbon atom. Mathematically, the origin of the three hybrid states can be written as a linear combination of $|2s\rangle$, $|2p_x\rangle$ and $|2p_y\rangle$ orbitals, such as

$$|sp_a^2\rangle = C_1 |2s\rangle + C_2 |2p_x\rangle + C_3 |2p_y\rangle, \quad (1.7a)$$

$$|sp_b^2\rangle = C_4 |2s\rangle + C_5 |2p_x\rangle + C_6 |2p_y\rangle, \quad (1.7b)$$

$$|sp_c^2\rangle = C_7 |2s\rangle + C_8 |2p_x\rangle + C_9 |2p_y\rangle. \quad (1.7c)$$

Given the fact that the sp^2 hybridization gives rise to three identical bonds in xy -plane, that the $2s$ orbital is also symmetrically spherical and that the probability of being occupied should be 1 in $|sp_a^2\rangle$, $|sp_b^2\rangle$ and $|sp_c^2\rangle$ hybrid states, one has $C_1^2 + C_4^2 + C_7^2 = 1$, leading

to $C_1 = C_4 = C_7 = C$. In addition to these facts, in order to find the other C_i 's constant values, we have that only $2p$ orbitals are relevant to define the preferential direction of hybrid states and that these directions of the orbitals are $(0, -1, 0)$, $(\sqrt{3}/2, 1/2, 0)$ and $(-\sqrt{3}/2, 1/2, 0)$, which implies that

$$|sp_a^2\rangle = C |2s\rangle + \sqrt{1 - C^2} [-|2p_y\rangle], \quad (1.8a)$$

$$|sp_b^2\rangle = C |2s\rangle + \sqrt{1 - C^2} \left[\frac{\sqrt{3}}{2} |2p_x\rangle + \frac{1}{2} |2p_y\rangle \right], \quad (1.8b)$$

$$|sp_c^2\rangle = C |2s\rangle + \sqrt{1 - C^2} \left[-\frac{\sqrt{3}}{2} |2p_x\rangle + \frac{1}{2} |2p_y\rangle \right]. \quad (1.8c)$$

Similarly to what was done to the sp hybridization (Eqs. (1.4a) and (1.4b)), we are going to use the orthonormality conditions to find C : using the fact that $\langle sp_i^2 | sp_j^2 \rangle = \delta_{ij}$, we have $C = 1/\sqrt{3}$. Consequently, Eqs. (1.8a)-(1.8c) become

$$|sp_a^2\rangle = \frac{1}{\sqrt{3}} |2s\rangle - \sqrt{\frac{2}{3}} |2p_y\rangle, \quad (1.9a)$$

$$|sp_b^2\rangle = \frac{1}{\sqrt{3}} |2s\rangle + \frac{1}{\sqrt{2}} |2p_x\rangle + \frac{1}{\sqrt{6}} |2p_y\rangle, \quad (1.9b)$$

$$|sp_c^2\rangle = \frac{1}{\sqrt{3}} |2s\rangle - \frac{1}{\sqrt{2}} |2p_x\rangle + \frac{1}{\sqrt{6}} |2p_y\rangle, \quad (1.9c)$$

where the sum to form the hybrid orbitals is shown in Fig. 1.5. Only the lobes part are presented in $|sp^2\rangle$ state.

Therefore, the three equivalent sp^2 orbitals will arrange themselves in a trigonal planar configuration, oriented in the xy -plane. The remaining non-hybridized $2p_z$ orbital is perpendicular to the plane. Such hybridization occurs in graphite, graphene and in chains of polyacetylene, for example the ethylene ($\text{H}_2\text{C}=\text{CH}_2$) [27, 28].

1.2.3 sp^3 hybridization

When one superposes the $2s$ and all three $2p$ orbitals, this mixing provides the sp^3 hybridization (see Fig. 1.6 to understand how this happens). It forms four identical bonds symmetrically distributed in space and placed with the maximum separation possible, *i. e.* making a $109^\circ 28'$ angle between each bonding and resulting in a tetrahedral shape for the molecule.

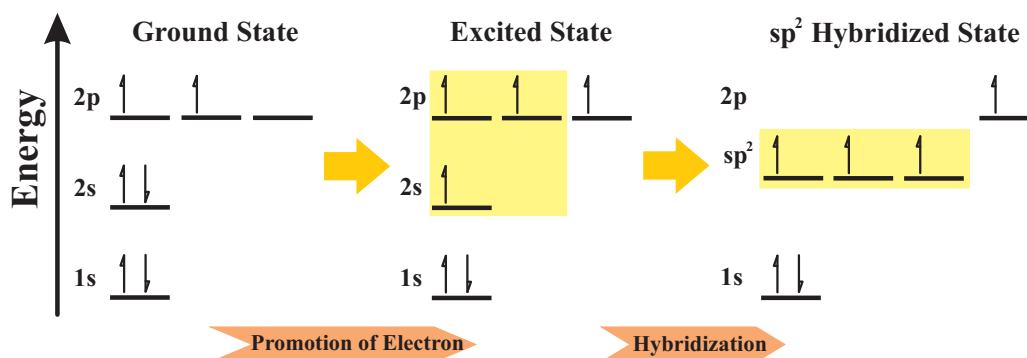


Figure 1.4: Process to derive sp^2 hybridization in carbon atoms. Electronic distribution for carbon is presented from left to right in the ground state, excited state, after the promotion of one electron to one of the $2p$ orbitals, and the last stage is the sp^2 hybridized state. The yellow background in the excited stage comprises the three orbitals involved to make hybridization happen. The energy level of the three sp^2 orbitals is smaller than the single $2p$ pure orbital and greater than $2s$ orbital in ground state. In the final process, one has three sp^2 hybridized states.

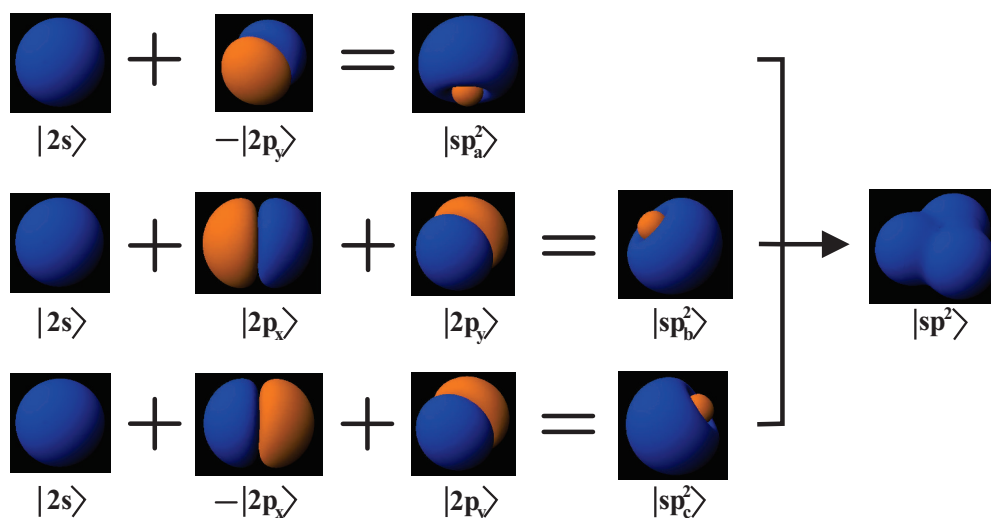


Figure 1.5: Schematic view of the sp^2 hybridization showing the linear combination between the s , p_x and p_y orbitals to form the three $|sp_a^2\rangle$, $|sp_b^2\rangle$ and $|sp_c^2\rangle$ hybrid states, according to Eqs. (1.9a), (1.9b), and (1.9c), respectively. The color directions denote the positive (blue) and negative (orange) amplitude of the wave function. Only positive lobes are presented in illustration of $|sp^2\rangle$ state.

Analogously to previous cases, we can write the four hybrid states as a linear combination of $|2s\rangle$, $|2p_x\rangle$, $|2p_y\rangle$ and $|2p_z\rangle$ orbitals

$$|sp_a^3\rangle = C_1 |2s\rangle + C_2 |2p_x\rangle + C_3 |2p_y\rangle + C_4 |2p_z\rangle, \quad (1.10a)$$

$$|sp_b^3\rangle = C_5 |2s\rangle + C_6 |2p_x\rangle + C_7 |2p_y\rangle + C_8 |2p_z\rangle, \quad (1.10b)$$

$$|sp_c^3\rangle = C_9 |2s\rangle + C_{10} |2p_x\rangle + C_{11} |2p_y\rangle + C_{12} |2p_z\rangle, \quad (1.10c)$$

$$|sp_d^3\rangle = C_{13} |2s\rangle + C_{14} |2p_x\rangle + C_{15} |2p_y\rangle + C_{16} |2p_z\rangle. \quad (1.10d)$$

As each $|sp_i^3\rangle$ orbital, with $i = a, b, c$ and d , is aligned to the axes of tetrahedron, then we can build the four orbitals along the $(1, 1, 1)$, $(-1, -1, 1)$, $(-1, 1, -1)$ and $(1, -1, 1)$ directions. From this, we obtain a set of equations similar to Eqs. (1.8a)-(1.8c)

$$|sp_a^3\rangle = C |2s\rangle + (\sqrt{1 - C^2}) \frac{1}{\sqrt{3}} [|2p_x\rangle + |2p_y\rangle + |2p_z\rangle], \quad (1.11a)$$

$$|sp_b^3\rangle = C |2s\rangle + (\sqrt{1 - C^2}) \frac{1}{\sqrt{3}} [-|2p_x\rangle - |2p_y\rangle + |2p_z\rangle], \quad (1.11b)$$

$$|sp_c^3\rangle = C |2s\rangle + (\sqrt{1 - C^2}) \frac{1}{\sqrt{3}} [-|2p_x\rangle + |2p_y\rangle - |2p_z\rangle], \quad (1.11c)$$

$$|sp_d^3\rangle = C |2s\rangle + (\sqrt{1 - C^2}) \frac{1}{\sqrt{3}} [|2p_x\rangle - |2p_y\rangle + |2p_z\rangle]. \quad (1.11d)$$

Finally, using the orthonormality conditions, we obtain that $C = 1/2$. Replacing it in Eqs. (1.11a)-(1.11d),

$$|sp_a^3\rangle = \frac{1}{2} [|2s\rangle + |2p_x\rangle + |2p_y\rangle + |2p_z\rangle], \quad (1.12a)$$

$$|sp_b^3\rangle = \frac{1}{2} [|2s\rangle - |2p_x\rangle - |2p_y\rangle + |2p_z\rangle], \quad (1.12b)$$

$$|sp_c^3\rangle = \frac{1}{2} [|2s\rangle - |2p_x\rangle + |2p_y\rangle - |2p_z\rangle], \quad (1.12c)$$

$$|sp_d^3\rangle = \frac{1}{2} [|2s\rangle + |2p_x\rangle - |2p_y\rangle + |2p_z\rangle]. \quad (1.12d)$$

This sum is represented in Fig. 1.7. Chemical examples for this carbon hybridization are methane (CH_4) and diamond. We summarize the kind of structure, hybridization, geometry and angle between each bond in Table 1.1.

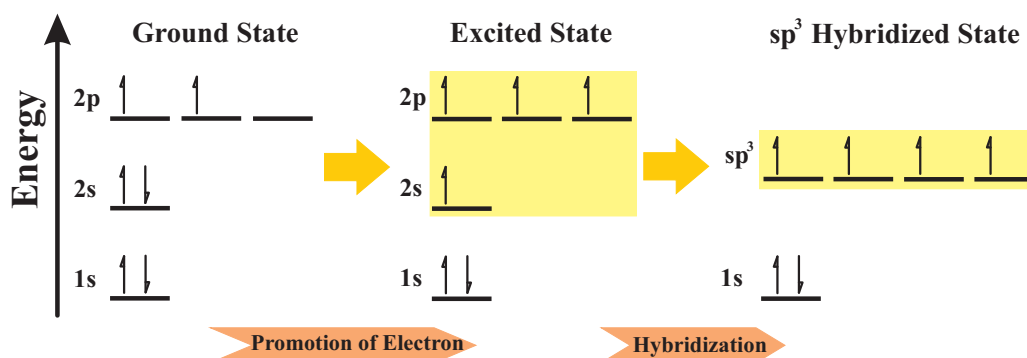


Figure 1.6: Process to derive sp^3 hybridization in carbon atoms. Electronic distribution for carbon is presented from left to right in the ground state, excited state, after the promotion of one electron to one of the $2p$ orbitals, and the last stage is the sp^3 hybridized state. The yellow background in the excited stage comprises the four orbitals involved to make hybridization happen. The energy level of the four sp^3 orbitals is smaller than the $2p$ orbital and greater than $2s$ orbital of ground state. In the final process, one has four sp^3 hybridized states.

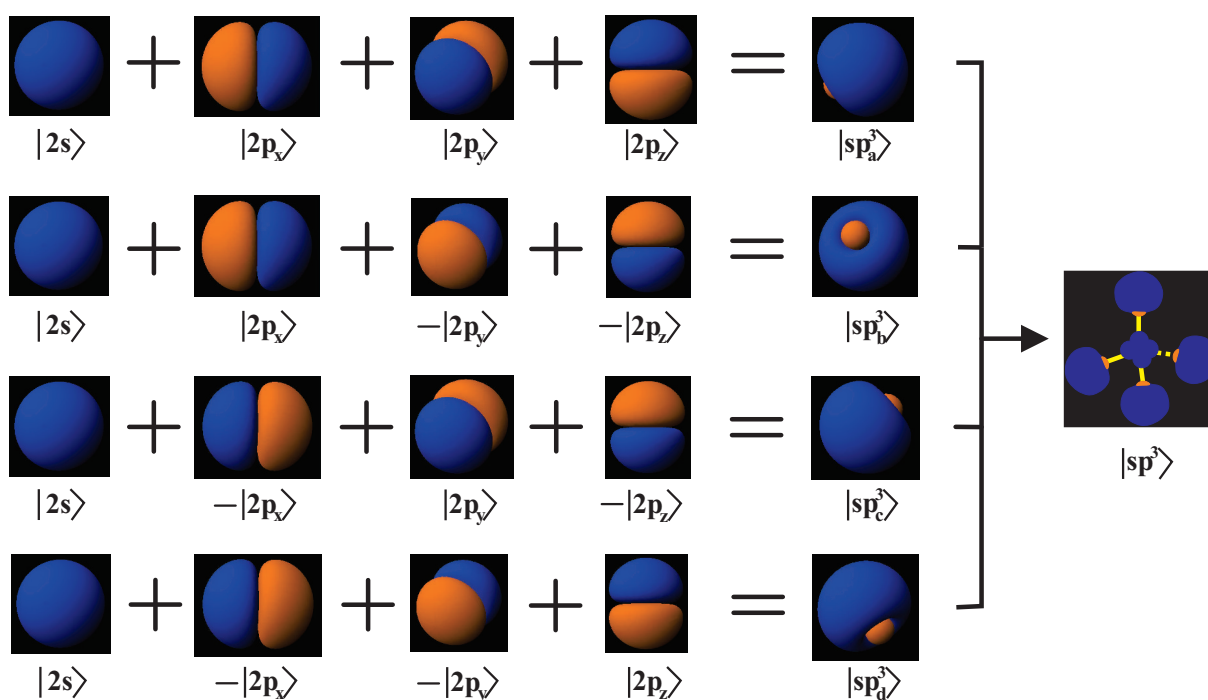
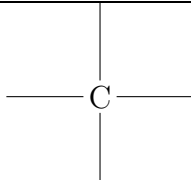
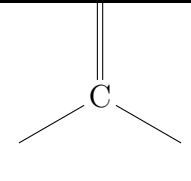
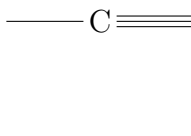
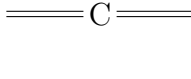


Figure 1.7: Schematic view of the sp^3 hybridization showing the linear combination between the s , p_x , p_y and p_z orbitals to form the four $|sp_a^3\rangle$, $|sp_b^3\rangle$, $|sp_c^3\rangle$ and $|sp_d^3\rangle$ hybrid states, according to Eqs. (1.12a), (1.12b), (1.12c) and (1.12d), respectively. The color directions denote the positive (blue) and negative (orange) amplitude of the wave function. This hybridization originates molecules with a tetrahedral shape.

Table 1.1: Carbon hybridization.

Structure	Hybridization Type	Geometry	Angle	Binding Type
	sp^3	tetrahedral	$109^{\circ}28'$	Four single bonds (σ)
	sp^2	trigonal planar	120°	A double bond (1π and 1σ) and two single bonds
	sp	linear	180°	A triple (2π and 1σ) and a single (σ) bond
				Two double bonds (1π and 1σ)

1.3 Allotropes of carbon

Due to different kinds of sp^n hybridization in carbon atom, this chemical element assumes several structural forms, as shown in Fig. 1.8. The different hybridizations give rise to a plethora of organic and inorganic compounds, forming an unlimited number of structures with a wide variety of physical and chemical properties. Most of these properties are crucial to determine the dimensionality of the structures. Table 1.2 shows some relatively well-known allotropes of carbon and a couple of their features, for example, their dimensionality, that varies from 0D to 3D. From Table 1.2, one can see that the carbon material which has a n dimensionality will have a sp^n hybridization type.

Table 1.2: Allotropes made of carbon [27].

Dimension	0D	1D	2D	3D
Allotrope	Fullerene, C_{60}	Nanotube, Carbyne	Graphite, Fiber, Graphene	Diamond, Amorphous
Hybridization	sp^2	sp^2 (sp)	sp^2	sp^3
Density (g/cm^3)	1.72	1.2 – 2.0	2.26	3.52
Bond Length (\AA)	1.40 (C=C) 1.46 (C—C)	1.44 (C=C)	1.42 (C=C)	1.54 (C=C)
Electronic Properties	Semiconductor $E_g = 1.9$ eV	Semiconductor or Metal	Semimetal	Insulating $E_g = 5.47$ eV

Let us now comment these structures. We start with an amorphous structure (Fig. 1.8 (b)). The amorphous carbon form is a non-crystalline and irregular three-dimensional ar-

arrangement, which looks like graphite but not held in a crystalline macrostructure, namely, it has a disordered arrangement. It appears in nature in a glassy state as a powder, and constitutes materials such as charcoal and activated carbon. Both sp^2 and sp^3 hybridization are randomly present on amorphous carbon [27].

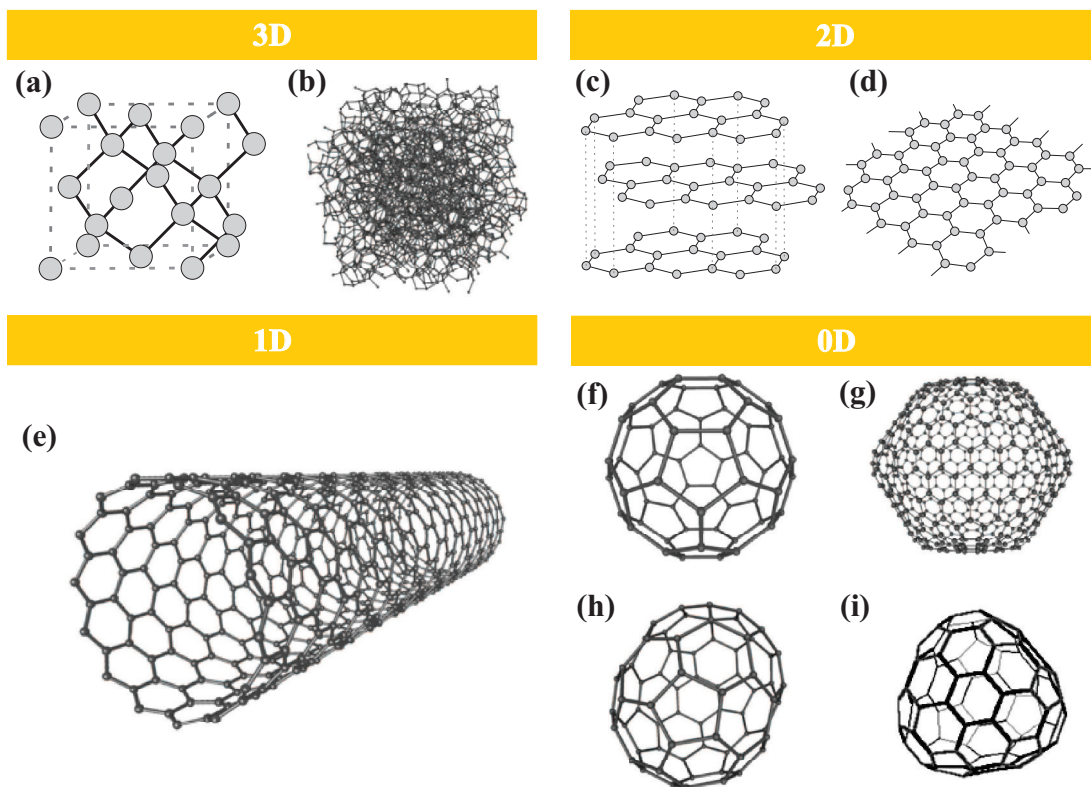


Figure 1.8: Crystal structures of different allotropes of carbon according to their dimensionality. Three-dimensional (a) diamond and (b) carbon amorphous ($3D$); two-dimensional (c) graphite and (d) graphene ($2D$); one-dimensional (e) carbon nanotube ($1D$); and zero-dimensional fullerenes ($0D$): (f) C_{60} , (g) C_{540} , (h) C_{70} and (i) C_{84} . The idea is taken from Refs. [7] and [29].

The graphite is formed by carbon sheets that are stacked, bonded through weak van der Waals forces (Fig. 1.8 (c)). The adjacent surfaces interact with each other through the π electrons that populate the $2p_z$ orbital perpendicular to sheet planes. These bonds are weaker than the covalent σ bonds in plane. The atoms in each sheet are disposed in a hexagonal network, such as each atom is bonded trigonally to three others, presenting a sp^2 hybridization. The distance ($C=C$) in each sheet is 1.42 \AA , while the displacement between the layers is of 3.33 \AA . Due to the weak interplanar connections between the layers, graphite plans can move easily over each other forming a good solid lubricant and making such material to behave like a $2D$ material. Although this topic will be still explained further in more details when we discuss about graphene (Fig. 1.8 (d)), which is the allotrope of interest in the following Chapters, we can already mention that graphene is a single graphite sheet, arranged as a honeycomb lattice of atoms. Each carbon atom

in this structure has a sp^2 hybridization and is very strongly bound through σ bonds with three other neighboring atoms. The π electrons in half-filled $2p_z$ orbital are responsible for the unusual electronic transport properties in graphene [30].

The diamond (Fig. 1.8 (a)), that is rather wished by many people, together with graphite are the two allotropic forms that historically have been the most popular. Under high pressure, carbon forms diamond, that is the most compact carbon allotrope. Its 3D lattice consists of two interpenetrating face-center-cubic (fcc) lattices, such as each atom is bonded to four others nearest neighbors, forming a tetrahedron that possess a sp^3 hybridization. The lattice spacing in (C—C) links are of 1.54 Å. Diamond is the hardest mineral in nature, because all four bonds are covalent σ bonds. This fact is the reason for diamond to be an insulator with a large gap of 5.47 eV [31]. Counter intuitively, the diamond is thermodynamically unstable under normal conditions and when exposed to some perturbations it transforms back into graphite, but at room temperature this process is extremely slow [27].

Another allotropic form of carbon is the fullerene (Fig. 1.8 (f)-(i)). In this structure, carbon atoms are packed in a spherical or oval surface, forming hexagons and pentagons or even heptagons of carbons. These latter are responsible for the curvature of the structure in spheroid shapes. The fullerenes are large molecules in which carbon atoms are bonded trigonally and possess a sp^2 hybridization. The best-known fullerene is the soccerball-shaped C_{60} buckminsterfullerene, that has twelve pentagons and twenty hexagons and is also called *buckyball*. It has the same symmetry of a regular icosahedron and it forms a 0D system in confinement sense [9].

Carbon nanotubes (CNTs) are one dimensional structures that can be understood as a curved graphene sheet forming a hollow cylinder with a diameter of several nanometers, depending on the number of walls (see Fig. 1.8 (e)).

1.4 Fabrication techniques

Since the 1960's, many researchers have done many attempts to obtain a single isolated sheet of graphite. Although they have failed, the techniques used in such attempts have gained new perspectives with Geim and Novoselov results [18], which boosted the search for other new methods of synthesis of graphene and the improvement of existing techniques, aiming the development of very effective and inexpensive methods of graphene production on a large industrial scale. In this way, even though this is a theoretical thesis, it is important to discuss, in general lines, about the most commonly employed growth/deposition methods used to obtain graphene: exfoliation from graphite, epitaxial growth on silicon carbide (SiC) and catalytic growth on metal by chemical vapor deposition (CVD).

1.4.1 Exfoliation from graphite

Although there are two kinds of exfoliation techniques, namely, mechanical and chemical⁶ exfoliation, both are based in the same principle, that consists in breaking down the Van der Waals forces between the graphite layers.

Mechanical exfoliation was developed first, hence, it is the most popular method for producing graphene. Its procedure has two main steps: “peeling” and “rubbing”. In the first step, one starts with highly oriented pyrolytic graphite (HOPG), which is sandwiched between adhesive tapes to peel off layers from a graphite flake. This is done successively, so that in each time the graphite is sliced into two parts, and each part is thinner than the original one. After several cycles, the second step is performed, when the tape is pressed down against a substrate, formed by silicon oxide (SiO_2), to deposit a sample. This process is very similar to what happens when we write with a pencil, except for the level of purity of the used graphite. Due to the use of tapes, this technique is also called “scotch-tape” method. As the inter-layer Van der Waals interaction energy is of about 2 eV/nm^2 , then the order of magnitude of the force required to exfoliate graphite is about $300 \text{ nN}/\mu\text{m}^2$ [33].

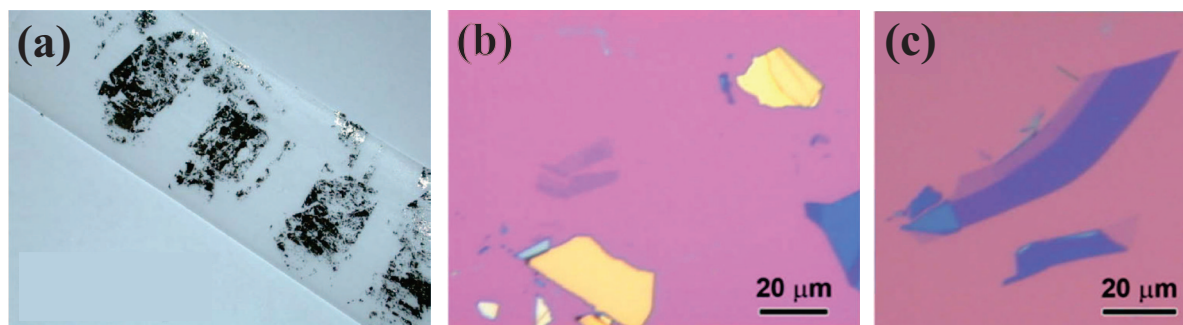


Figure 1.9: (a) Graphite flakes on adhesive tape to isolate graphene through scotch-tape method. (b) and (c) are optical images of few-layer graphene obtained by micromechanical exfoliation from graphite. In (b) one has thin graphite and (c) FLG and a single layer graphene shown in lighter purple contrast on a $\approx 300\text{nm}$ SiO_2 layer. The colors are related with local thickness of the sample. Yellowish color indicates thicker samples while bluish and lighter contrast indicates thinner samples. Adapted from Refs. [33] and [34].

The graphene produced by this method has a perfect crystallinity and a high electrical quality, once that this process is performed with a single crystalline graphite source and does not undergo any intrusive procedure or equipment. However, the produced flakes reach only $100 \mu\text{m}^2$ [2] and are obtained in the wafer form isolated or mixed with few-layer graphene, which does not allow its application on a large scale. Thus, graphene

⁶This technique was widely used in the 70’s and consists of reducing the Van der Waals forces between the atomic planes of graphite by inserting chemical species between the planes in order to expand the bonds. For more details, see Refs. [2] and [32].

synthesized by mechanical exfoliation is suitable only for basic research and demonstration devices.

As the resulting flakes are composed by a mixing of FLG, then to visualize single flakes, peeled HOPG should be placed on 300 nm thick SiO₂ to enhance the optical contrast under white light illumination in a optical microscope. Fig. 1.9 shows a sample of thin films of graphite, where the different colors are related to the number of graphene layers. The SiO₂ substrate with a thickness of 300 nm has a violet coloration when observed by optical microscope. With the increasing in thickness due to FLG presence, one can observe a change in color to blue in the region where the films are located. The thinner the films are, more tenuous is the change in coloration, until films with a thickness smaller than 1.5 nm are no longer visible by this method.

1.4.2 Epitaxial growth on SiC

Even before the isolation of a single layer of graphite, it was known since the 70's that layers of graphene could be grown epitaxially on solid substrates using thermal decomposition of carbides [1, 33]. The most popular epitaxial process uses a silicon carbide substrate. In fact this experimental method is actually a hybrid epitaxial and thermal decomposition process of a crystal of SiC at high temperature.

The thermal treatment consists in the sublimation of the silicon atoms at the top of the crystal, that are desorbed, leaving a carbon-enriched surface. As the silicon atoms are sublimated, the remaining carbon atoms reorganize themselves forming graphitic structures. This stage is also called "graphitization". This epitaxial growth requires temperatures around 1300°C and ultra high vacuum [35].

The number of layers and the physical properties of these graphitic layers are controlled parameters in this growth technique. The accuracy in the number of layers can be controlled by the growth time or by the temperature used in the heating treatment, while the quality of the samples depends on the chosen SiC surface used for their growth. There are two surface terminations: Si-terminated surface (0001) and C-terminated surface (000 $\bar{1}$). In the case of C-terminated surface, the graphitization process is slow, so that one may control more accurately how many layers are formed, and thus produce fewer layers. The resulting electron mobility is rather low in such a way that this kind of surface orientation is less chosen for samples used in transport measurements. On the other hand, the epitaxial-thermal process using Si-terminated surface is very fast, producing a large number of graphene layers. In this last termination, the electron mobility is rather high [1, 35]. This formation process is schematically illustrated in Fig. 1.10, using Si- and C-terminated surfaces.

An important point in this synthesis is that the SiC substrate must be considered as an integral part of whole system. This implies that the electronic properties can change along the sample, indicating a certain degree of inhomogeneity after graphene growth. The interaction between substrate and the obtained FLG is stronger at the first graphite

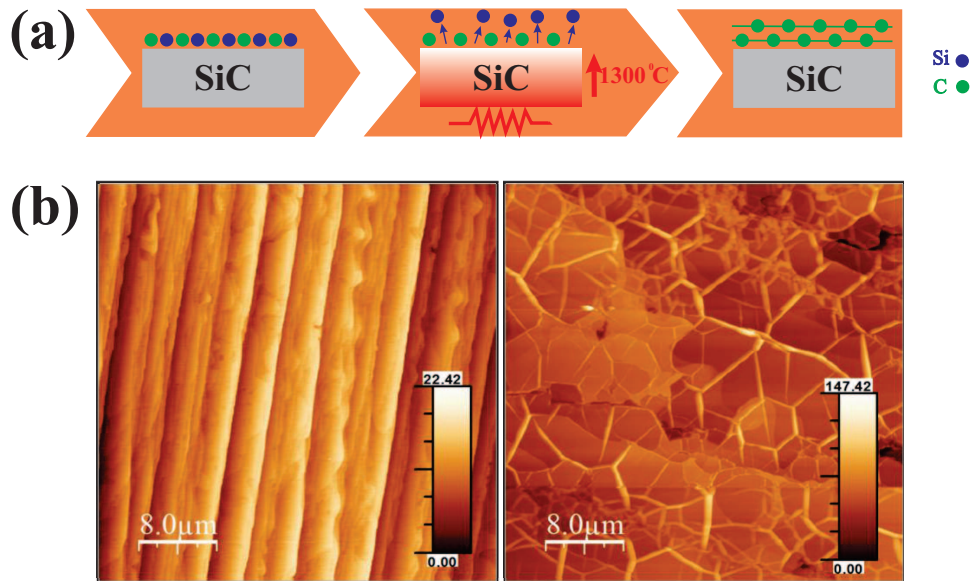


Figure 1.10: (a) Schematic illustration of the process of thermal decomposition of SiC for graphene synthesis. (b) and (c) are AFM measurements showing respectively silicon (0001) and carbon (000 $\bar{1}$) surfaces after graphene growth. Adapted from Refs. [32] and [36].

layers. It is so tightly bound to the SiC substrate that the distance of the first carbon layer directly on top of the substrate ($\approx 2 \text{ \AA}$) is smaller than the distance between graphene sheets in crystalline graphite ($\approx 3.4 \text{ \AA}$), whereas the distance between the above layers are bigger than the ones in crystalline graphite [37]. Furthermore, the graphene layers produced in this experimental method are heavily doped, due to the charge transfer from the substrate to graphene layers, leading the sample to exhibit a metallic character [1]. This excess of charges due to electronic doping moves the Fermi level away from the graphene Dirac point, therefore changing the graphene properties [38].

1.4.3 Chemical vapor deposition

Another well-known possibility of synthesizing graphene on a substrate is by means of the method called Chemical Vapor Deposition (CVD). This technique has many advantages that made it become the most promising method for the production of graphene on a large scale. Some of these advantages can be listed, as for example: the possibility of synthesizing thin films of graphene with high uniformity, the fact that it can be transferred easily to other substrates, the relatively low cost and the rapidity and simplicity of the process [33, 39, 40].

The process of graphene synthesis using CVD involves sputtering of an initial thin metal film. It happens by the exposure of the transition metals to a carbon rich atmosphere at high temperatures. In general, this gaseous flow of hydrocarbons is composed by methane (CH_4) or ethyne (C_2H_2). The gas molecules are deposited on the substrate,

usually a Si/SiO₂ wafer, on which a thin film of transition metal is deposited. The transition metal acts as a catalyst, thermally decomposing the molecules and providing the necessary conditions for the formation of graphitic structures on the substrate surface. The solubilization of carbon in the thin film after the thermal decomposition of hydrocarbons gases occurs due to the fact that transition metals have specific characteristics of melting and boiling points, along with the fact that these transition metals have a great number of half-filled electronic orbitals which facilitate the breaking of the molecular bonds, since in the catalyzation process, a compound interacts with the metal by electrons donating such as the anti-bonding orbitals are populated, assisting the breaking of the bonds. Thus, after heating and exposing stages, the sample is subjected to cooling stage. It is during cool-down that the solubility of the carbon in the metal decreases, resulting in crystallization of graphene on the surface [32, 41].

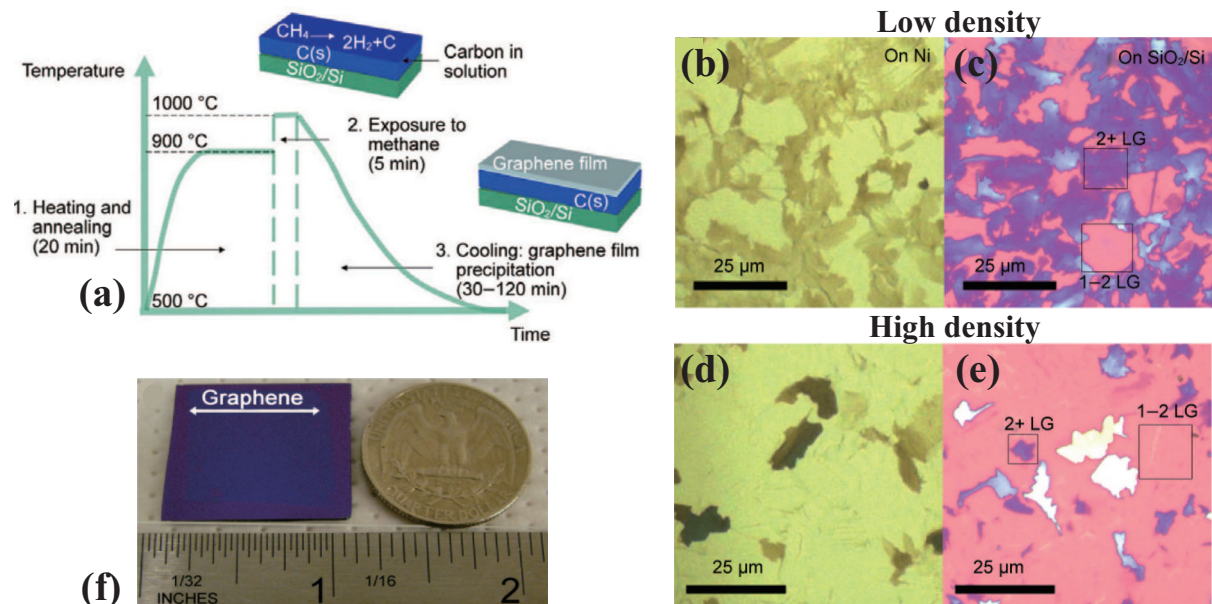


Figure 1.11: (a) Graphene growth process using a Ni film and its different stages (1-3): 1. The Ni film deposited on SiO₂/Si is heated to 900⁰C and annealed for 20 minutes under flowing H₂ and Ar. 2. Exposure to H₂ and CH₄ for 5 minutes. CH₄ is decomposed catalytically and the carbon produced is incorporated into Ni film. 3. The substrate is cooled down from 1000⁰ to 500⁰C under Ar, H₂. At 500⁰C, the sample is taken out of the furnace and cooled rapidly to room temperature. (b)-(e) Two types of graphene films with different densities and their characterization. (b) and (d) are optical images of the graphene films on Ni, (c) and (e) are optical images of the graphene films transferred to SiO₂/Si. The transference to SiO₂/Si substrate enables thickness analysis by optical contrast. (f) Photograph of a large graphene film (blue film on the purple substrate of SiO₂/Si) with ≈ 87 percent of its area covered by 1 and 2 layers of graphene. Adapted from Ref. [42]

Recent studies addressing the synthesis of graphene by CVD have used different tran-

sition metals such as nickel (Ni) [39, 42, 43], iron (Fe) [44], copper (Cu) [45, 46], ruthenium (Ru) [47], iridium (Ir) [48] and others. The most investigated ones are those involving growth with nickel and copper as catalysts. As an example of CVD synthesis employing one of these most used transition metals, the growth cycle using thin films of nickel is schematically illustrated in Fig. 1.11.

As we can see in Fig 1.11(f), with this technique, one can cover an entire wafer with graphene. However, these films (Figs. 1.11(b)-1.11(d)) can not be used directly in electronic applications, due to the conducting substrate. Therefore, it is necessary to transfer them to a substrate like SiO₂/Si (Figs. 1.11(c)-1.11(e)) [41, 42].

In summary, all these three presented techniques have each one their specificities. Thus, depending on the desired application, one may choose one or another technique which may be more attractive. Table 1.3 briefly lists advantages and disadvantages of each method to isolate and to produce few graphene layers.

Table 1.3: Comparative table of growth/deposition techniques to isolate/produce few graphene layers. Adapted from Refs. [33] and [41].

Method	Description	Advantages	Disadvantages
Exfoliation from graphite	Graphene peeled from HOPG using scotch tape	<ul style="list-style-type: none"> · Highest quality · Low-cost · No special equipment needed 	<ul style="list-style-type: none"> · Random (shape, size, location) · Does not scale
Epitaxial growth on SiC	SiC annealed ($\approx 1300^{\circ}\text{C}$) → Si sublimation	<ul style="list-style-type: none"> · Good control over number of layers · Large domains 	<ul style="list-style-type: none"> · Expensive substrates · High temperature · Surface steps
Catalytic growth on metal (CVD)	Catalyst film heated and hydrocarbon supplied	<ul style="list-style-type: none"> · No limit of substrate size · Low temperature · Rapid process · Straightforward up scaling · Versatile handling of the suspension 	<ul style="list-style-type: none"> · Synthesized graphene have high electrical resistance · Fragile stability of the colloidal dispersion · Reduction to graphene is only partial

1.5 Applications

Graphene possess unusual electronic, mechanical and optical properties that make this material a promising candidate for future electronic application, as already mentioned in

the previous section [49], as well as an exceptional material to replace all the devices and technology based on silicon [50]. According to Andre Geim, as reported in the BBC news [51] on May 21th 2011, he said that “Graphene does not just have one application” and also in the same issue of this journal Jari Kinaret, professor of technology at Chalmers University in Sweden, mentioned that “It can open completely new applications in transparent electronics, in flexible electronics and electronics that are much faster than today”. Thus, graphene and its derivatives offer the promise to significantly improve existing products and to enable the design of materials and devices with novel functionalities. We will mention here a few examples of graphene materials and devices. Some of these applications they are in a more mature stage, in the sense that are closer to be implemented in the list of commercial devices, while the other ones in different areas are in a more conceptual stage.

1.5.1 Flexible graphene for displays

Graphene has emerged as an ideal candidate for transparent and flexible electrodes. This is one of the most practical applications for graphene in electronics, which is based on three important properties, two optical and one mechanical: (i) graphene can be used as a very thin transparent conducting film, (ii) it presents low resistivity [52] and, in addition, (iii) it has the smallest bending radius among all flexible transparent conductors characterized so far [53] (see Figs. 1.12(a) and 1.12(b)). It has been also shown that plastic can become conductive by adding only 1% of graphene while it will remain transparent and that graphene is highly transparent even for the visual spectrum [52, 54] (see Fig. 1.12(c)). In this way, transparent conducting films based on graphene can be used in many applications such as touchscreen, smart windows, mobile phones, TVs, solar cells, Light Emitting Diodes (LEDs) and Liquid Crystal Displays (LCDs), as illustrated by Fig. 1.12(d).

Nowadays, the transparent electrodes are typically made from indium tin oxide (ITO), because of its relatively good conductivity and optical transparency, as shown in a comparative way with graphene in Figs. 1.12(a) and 1.12(b). But Indium is very expensive and toxic, moreover ITO has poor mechanical properties, such that it tends to crack when bent or stretched [55]. Hence, graphene has a realistic chance to be used in the manufacture of flexible components needed in flexible and transparent electrodes, since it has been already demonstrated that graphene is mechanically robust and its synthesis by CVD consumes only tiny amounts of carbon gases and does not need rare mineral resources such as indium or silver, thus becoming, cheaper than ITO.

Many companies have been increasingly struggling to achieve reasonable and optimized results to be able to apply those experimental techniques on the mass production of graphene. An example of the biggest investors in the development of new technologies using graphene is the Samsung company, being one of various results obtained by the team supported by this company illustrated in Fig. 1.12(d), that is a large sample of graphene

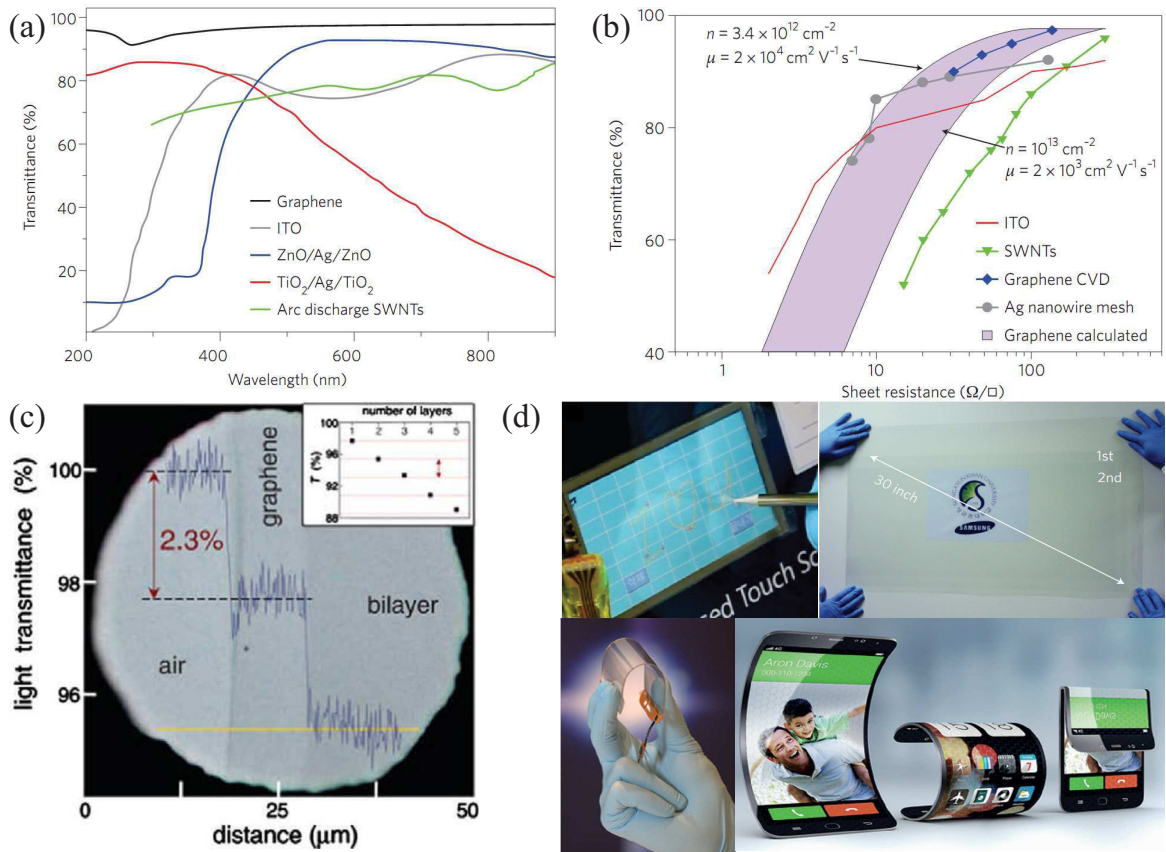


Figure 1.12: (a) Transmittance versus wavelength into the visual spectrum for different transparent conductors: graphene, single-walled carbon nanotubes (SWNTs), indium tin oxide (ITO), ZnO/Ag/ZnO and TiO₂/Ag/TiO₂. (b) Transmittance versus sheet resistance plots for different transparent conductive films, including CVD graphene and theoretical calculation of graphene. (c) Transmittance for an increasing number of layers, which show that graphene and bilayer graphene are highly transparent and that graphene absorbs only 2.3% of light for a very large range of wavelengths. (d) Graphene-based touchscreen panel (top, left) showing outstanding flexibility (bottom, left), a transparent ultralarge-area graphene film transferred on a 30-inch sheet fabricated by Samsung company (top, right) and possible applications in bendable mobile devices (bottom, right). Adapted from Refs. [52], [54], [55] and [56].

film developed in June 2010 by Samsung company using the roll-to-roll production and wet-chemical doping of predominantly monolayer 30-inch graphene grown by chemical vapour deposition onto flexible copper substrates [54].

1.5.2 Coating with graphene

Another very interesting graphene application is related to preventing corrosion of metals such as steel. In this purpose, graphene is used to coating the metals against corrosion process, which is one of the greatest challenges faced by the metal industry, since this effect occurs in a natural way, triggered by environmental factors, as the presence of water, oxygen and electrolytes.

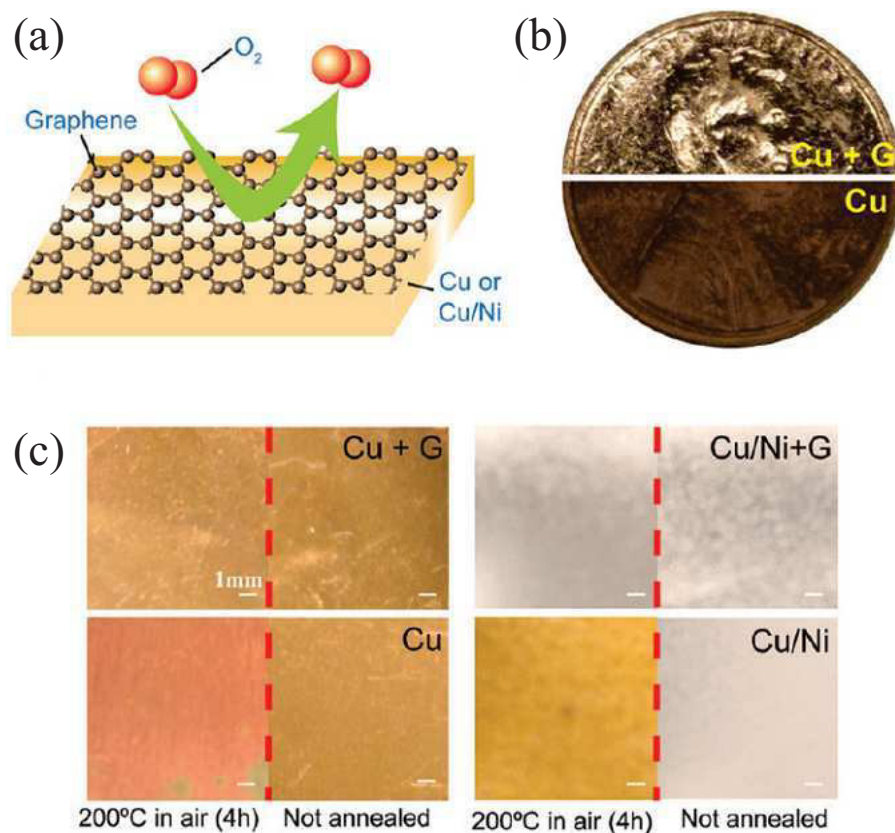


Figure 1.13: (a) Illustration depicting a graphene sheet as a chemically inert diffusion barrier, preventing the reactive agent from ever reaching the metal underneath. (b) Photograph showing graphene coated (upper) and uncoated (lower) penny after H₂O₂ treatment (30%, 2 min). (c) Photographs of Cu and Cu/Ni foil with and without graphene coating taken before and after annealing in air (200 °C, 4 h). Adapted from Ref. [61].

Because of many adverse effects on human and environment health brought with the usage of Chromium and Zinc as anticorrosive materials for metal coatings, different corrosion protections have been sought in order to reduce production costs and the adverse side effects [57]. In this direction, graphene has attracted attention of the steel industry because it has a more efficient, innovative and cheaper technology to overcome corrosion

issues, making a preventive and protective work against corrosion. The two properties that provide graphene as a good anticorrosion mechanism are: (i) the impermeability of pristine graphene, so that graphene coatings can make the path of permeating water more tortuous, acting as an excellent barrier to water, oxygen and other corrosive materials, and the fact that (ii) graphene has a higher electrical conductivity than steel.

Recent approaches in the production process have proposed graphene-based coatings, which are composed by functionalized graphene incorporated into organic coatings [58]. It has been shown that these graphene hybrid nanocomposites demonstrate an excellent corrosion inhibition capability when compared with current chromate-free anticorrosion technology, and comparable performance to chromate-based anticorrosion technology [59]. Thus these graphene-based coatings can be used as inhibitors in protective coatings to prevent oxidation of underlying metals in oxidizing chemicals, water or air for longer period [60, 61] and for bipolar plates in fuel cells, which are stainless steel components that separate individual cells in a stack and aid in the distribution of fuel and oxidant, water management and current collection [57].

As an illustrative example that thin layers of graphene in the top of metal surface serve as impermeable coatings, we show in Fig. 1.13 photograph images of two metal surfaces, Nickel (Ni) and Copper (Cu), both graphene-coated and uncoated, after air anneals and exposure to liquid etchant. In all showed cases, the graphene-coated metal surfaces exhibit very little visible change, as opposed to the uncoated metals whose surfaces change appearance dramatically. Thus, the use of graphene in coating process reduce the oxidation of the metals and in addition it does not alter their conductivity [61].

1.5.3 Graphene photodetector

The unique physical properties of graphene make it suitable for detecting light, since that: (i) electrons and holes move much faster through graphene than through other materials and (ii) it is very good at absorbing light over a very wide range of wavelengths, ranging from the visible to the infrared, whereas thin layers of III-V semiconductors do not absorb many infrared frequencies. The knowledge of these benefits opens the possibility to exploit graphene for optoelectronics using graphene sheets to make photodetectors.

Photodetectors are electronic components that measure photon flux or optical power by converting the absorbed photon energy (optical signals) into electrical current. They are widely used in a range of common devices, such as remote controls, televisions, DVD players and receivers in fiber optic networks where they return the light information to the form of an electric signal [52]. The modern light detectors are typically made using III-V semiconductors, such as silicon or gallium arsenide. When light strikes these materials, each photon absorbed creates an electron-hole pair, which are then separated in an electrical field, which leads to an electrical current. This electrical field usually is generated by an external voltage applied to the component.

The photoelectrical response of graphene was first investigated by the IBM researchers

team led by Phaedon Avouris (see Fig. 1.14), that made use of the internal electric field that exists at the interface of graphene and metal [62]. Through a sophisticated combination of palladium (Pd) and titanium (Ti) electrodes they created a photodetector that does not rely on external current. They did this by placing palladium or titanium electrodes on top of a piece of multilayered or single-layered graphene. The metal contacts produce electric fields at the interface between the electrodes and graphene. This electric field separates the electrons and holes in a very efficient way, and thus a photocurrent is produced when light is shone onto the device. Using this specific arrangement, the IBM team overcame the problem of quick carrier recombination of the electrons and holes generated by incoming photons and, moreover, allowed to eliminate unwanted noise at the same time, once that it does not need to apply a bias voltage for the device to operate. Normally this pair combination in graphene happens within tens of picoseconds, leaving no free electrons for current [62, 63].

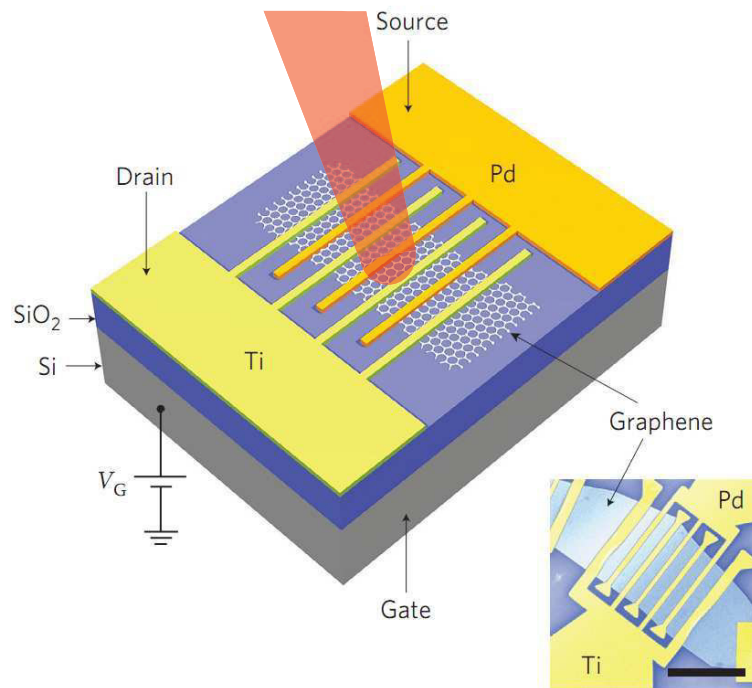


Figure 1.14: Schematic view of the metal-graphene-metal photodetector, where the electrodes are composed by palladium (Pd) and titanium (Ti) located on the top of a piece of multilayered or single-layered graphene. V_G is the gate bias. Adapted from Ref. [62].

Thereby, graphene-based devices can be also used in optical communications, remote sensing, environmental monitoring, terahertz detection, and surveillance. This brings a significant impact on mainstream optical applications into photonics, specially due to the fact that graphene photodetectors can operate with an internal quantum efficiency of 15 – 30%, despite its gapless nature and, in addition, it enables an ultrawide range of operational wavelengths [64].

1.5.4 Challenges in graphene commercialization

Despite the plenty of possible advantages that graphene could bring with its usage as a base-compound for electronics, photoelectronics, spintronics and valleytronics, many considerable challenges must be overcome to integrate this material into the commercial devices, even for the graphene researches that are in high progress level. It follows some hindrances in the attempt to make graphene become useful for realistic applications, which includes the development and the improvement of [55]:

- a low-cost and large-scale synthesis method for high-quality graphene [55];
- manufacturing techniques with guaranteed of uniformity and reproducibility [65];
- defect- and residue-free transfer method that is compatible with conventional device manufacturing processes [66];
- doping processes that can assure stable, high electrical conductivity over long periods [67];
- methods to insure the environmental stability of graphene electrodes against moisture and chemicals in the air [68];
- methods to decrease the contact resistance between electrodes and active materials [69].

Limited material availability and material cost to produce in quality are the two of the most significant factors that could affect the speed of commercial deployment of graphene. Although there are diverse methods to produce different types of graphene material, the development of graphene manufacturing methods still need achieve a experience degree to outstrip demand for quality, quantity, reliability, consistency and price. The choice of production process depends on the required graphene properties and the targeted application, which it turn will define the volume and price requirements, *i. e.* the material cost required to enable commercialization is application-dependent. In the other words, one can see that the large-scale manufacturing method for the industry needs standardization and industrialization, otherwise it may slow the commercial adoption of graphene in the industry [70].

Another critical market barrier that could affect the speed of adoption of graphene is the resistance produced by incumbent materials and technologies. For example, if the graphene turn out to indeed replace silicon in electronics, then all sectors of industrial chain must undergo a transformation to suit their methods of graphene production. Thus, certainly graphene should feel a resistance by existing suppliers in an attempt to slow down or prevent a switch to this new material [70].

To illustrate the level of some graphene applications and in which stages they are up to now, we present in Fig. 1.15 a block diagram showing the applications related to three

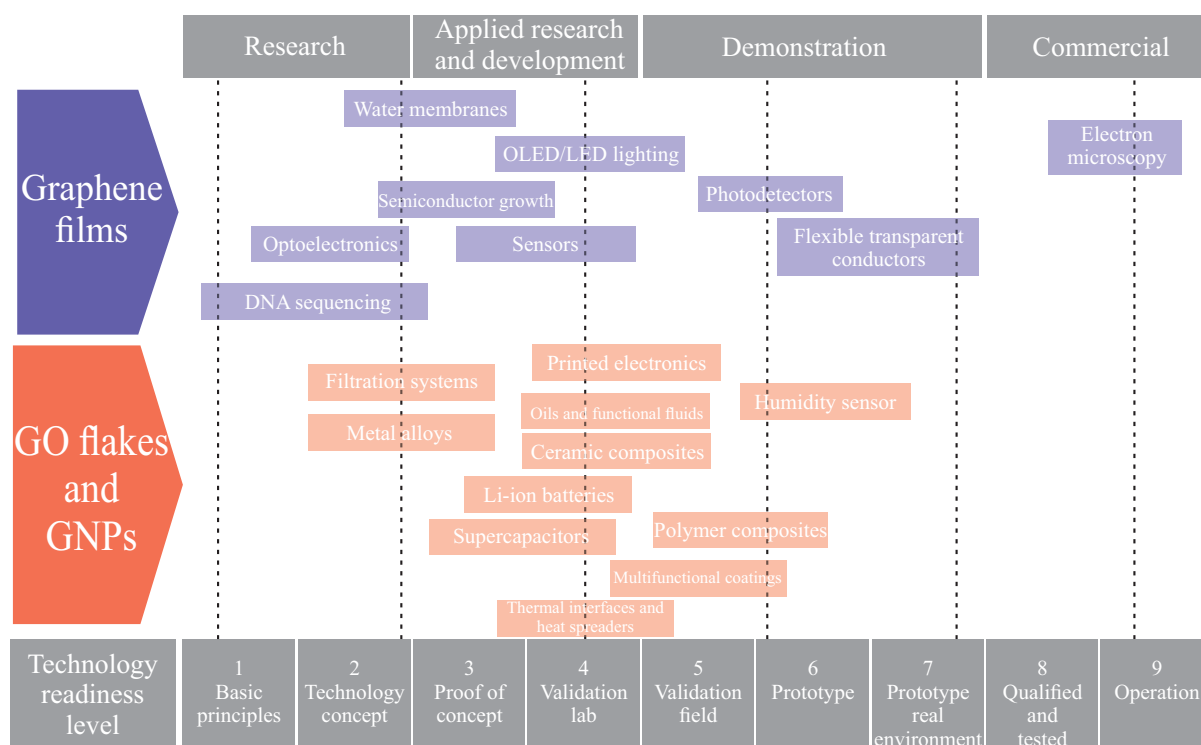


Figure 1.15: Some graphene applications for three main types of graphene product: graphene films, graphene oxide (GO) flakes and graphene nanoplatelets (GNPs), in which they are classified by technology readiness level. Adapted from Ref. [70].

main types of graphene product: graphene films, graphene oxide (GO) flakes and graphene nanoplatelets, in which they are classified by technology readiness level from 1 (basic principles) to 9 (operation). As one can realize, the discussed applications in previous section using graphene as a based to photodetectors, flexible and transparent devices and coating are placed respectively in the stage of applied research and development and demonstration. It shows that these applications are niche applications that present low barriers to adoption and are close to commercialization. According to some experts in emerging technologies field, the number of organizations developing graphene applications and the number of patents filed may suggest an opportunity for a further acceleration of graphene commercialization, such as expressed in the following quote: “Judging from the progress to date, the resources mobilized worldwide and the level of industry awareness, graphene might be on track to become a commercial reality in less than 20 years from the first attempts at commercialization.”, said by the researchers A. Zurutuza and C. Marinelli that work at Graphenea and at Applied Graphene Materials [70].

1.5.5 Granted investments to graphene

Since the graphene isolation in 2004 [18] and the first series of published papers that triggered a sharp rise in the level of graphene research efforts worldwide, many companies have been attracted attention to the possible graphene applications. It has been esti-

mated that more than 44 companies currently active are now involved in research around graphene [70]. This wave of investments around the world heading toward a new technological revolution has been fuelled by both public and private investments, composed for example by European Commission, UK and Korean governments and by the private ventures from Samsung, IBM and Nokia. To have an idea of how much substantial is being invested nowadays, we will cite now the amount by three mentioned governments. In 2013, the European Commission elected graphene to be one of Europe's 10-year 1 billion euro Future Emerging Technology flagships. This program is called as Graphene Flagship⁷ and coordinates 76 academic and industrial research groups in 17 European countries. Another examples are South Korea, that has invested US\$ 200 million in graphene research since 2012, where significant contributions come from private industries like Samsung, and the United Kingdom, that has invested a more modest amount of 50 million euro at the beginning of 2012 [71]. These investments indicate an important involvement of the companies worldwide with graphene, proving it to be a very promising market. In 2013, the size of the graphene market was estimated to be around US\$12 million [70], and the market projections for the next years indicate significant expansion and revenue increase. The IDTechEx⁸, that has provided independent market research, business intelligence and events on emerging technology to clients in over 80 countries, has been closely tracking the graphene market for over two years and realized that: "Graphene markets will grow from around \$20 million in 2014 to more than \$390 million in 2024 at the material level. The market will be split across many application sectors; each attracting a different type of graphene manufactured using different means. The market today remains dominated by research interest but the composition will change as other sectors such as energy storage and composites grow."

Other indexes that reflect the progress in the commercialization and research development in graphene are the number of patents and publications in this field. These data are shown in Fig. 1.16 for (a) the number of publications and (b) patent applications per year for three carbon allotropes: carbon nanotubes, graphene and fullerenes, and (c) patents yearly from both corporations and academic institutions. In all graphics in Fig. 1.16, it is presented some historical points about the research evolution in the timeline. One can realize the expressive amount of publications and patents involving graphene, that seems to increase more and more leading a positive effect in the speed of commercial deployment of graphene. Just in 2010, about 3000 papers were published on graphene, reflecting a shift in research away from carbon nanotubes. Associating the representative scientific discoveries and the number of patents in Fig. 1.16(c), one can notice that around 2007 graphene became more widely known in the science and industrial research communities such as a spike in numbers of patent applications both from corporations and academic

⁷For more information visit the official website from Graphene Flagship: <http://graphene-flagship.eu/>.

⁸Read more at: <http://www.idtechex.com/research/reports/graphene-markets-technologies-and-opportunities-2014-2024-000390.asp?viewopt=showall>

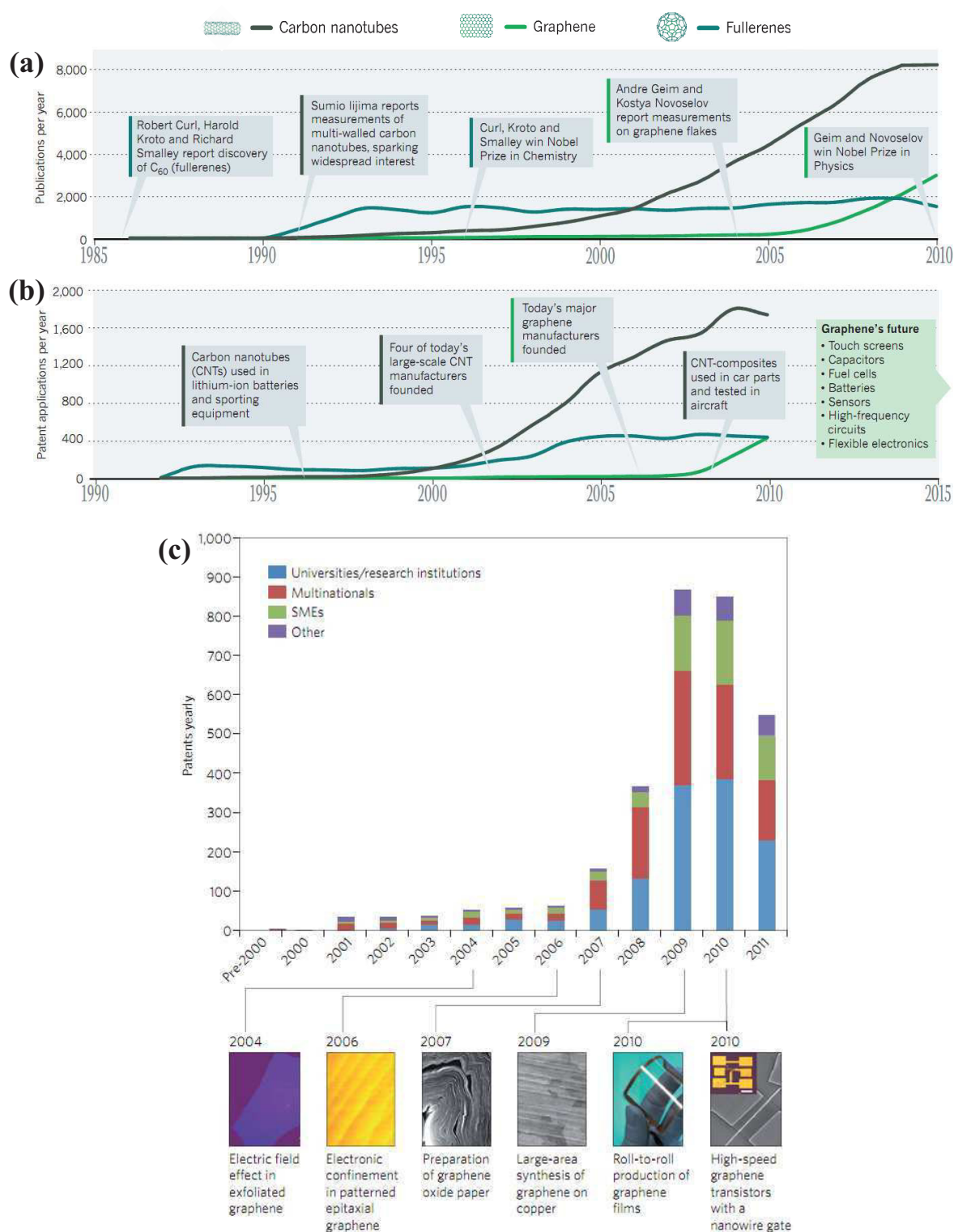


Figure 1.16: Number of (a) publications and (b) patent applications per year up to 2010 for three carbon allotropes: carbon nanotubes, graphene and fullerenes. The publications in graphene are accelerating faster than the buzz that surrounded carbon nanotubes in the 1990s, whereas the number of patent applications involving graphene just mathed those citing nanotubes. (c) The development of the total number of graphene-related patents over the past few years together with selected scientific publications on the preparation and application of graphene. Adapted from Refs. [20] and [72].

institutions is observed.

All indices presented here are indicators of commercial potential of graphene, *i. e.* the large number of companies, academies, publications and patents involved with graphene represent a positive direction of viable commercial solutions based on graphene.

1.6 Organization of the thesis

In this thesis we will present a theoretical study of: (i) the dynamic properties in multilayers graphene, performing a systematic study of the wave packets scattering in different interface shapes, edges and potentials; and furthermore of (ii) the energy levels of confined systems in graphene under the presence or absence of external magnetic and electric fields.

In the next Chapter 2 we will develop the mathematical tools used to explain the basic properties of mono and bilayer graphene indexbilayer graphene. We will start from Tight-binding model, and under some approximations, we will achieve the Dirac continuum model. We will also calculate the energy spectra of both monolayer and bilayer graphene under the influence of an external perpendicular magnetic field, showing thus the Landau levels. In addition to the models to compute the electronic structure of graphene, we will also present the Split-operator technique for a Tight-binding Hamiltonian and for the Dirac Hamiltonian.

In Chapter 3, we will present a systematic study of the energy spectra of graphene quantum rings having different geometries and edge types, in the presence of a perpendicular magnetic field. Four kinds of geometry will be considered: triangle, rhombus, hexagon and circle, with two edge types: armchair and zigzag. The results will be obtained within both the tight-binding and Dirac models, in order to compare and discuss which features can be recovered by using the approximations imposed by Dirac model.

In Chapter 4, we will derive a general expression for the infinite-mass boundary condition in bilayer graphene using the four-band continuum model. This new boundary condition can be used for any kind of circular confined structure, as a bilayer quantum dot or a bilayer quantum ring. In this Chapter we will apply this boundary condition to calculate analytically the confined states and the corresponding wave functions in a bilayer graphene quantum dot in the absence and presence of a perpendicular magnetic field. We will discuss the kinds of symmetry present in the studied system and also show some of its properties, such as its cyclotron resonance.

In Chapter 5, we will investigate the confined states in two different hybrid monolayer - bilayer systems. They are defined as: (i) a hexagonal anti-dot in bilayer graphene under perpendicularly applied electric field and (ii) a hexagonal bilayer graphene dot surrounded by a hexagonal region of monolayer graphene. Using the tight-binding model, we will study the behavior of the energy levels as a function of dot size and under an applied external magnetic field. We will also identify which states are dot-localized states, or

edge states or even mixed states.

In Chapter 6, we will numerically study the influence of the graphene edges in the scattering of a Gaussian wave packet. Furthermore, we will investigate the skipping orbits when an external magnetic field is applied and also what happens when the sample is submitted to a pseudo-magnetic field induced by non-uniform strain.

In Chapter 7, we will calculate the transmission probabilities of a Gaussian wave packet through a quantum point contact defined by electrostatic gates in bilayer graphene. Two kinds of the potential alignment will be considered, in order to provide a bias between the layers. In one of the cases, the gates will be set such that on both sides of the contact will produce the same bias and so an energy gap. It is similar as in an usual quantum point contact. In the other case, the bias will be inverted on one of the sides of the quantum point contact, although still forming the same energy gap at both sides. It will be done to allow only electrons belonging to one of the Dirac valleys to pass. Thus we will provide which parameters improve the efficiency of proposed bilayer system as a valley filtering, such as length, width and amplitude of the applied potential.

Finally, the thesis is concluded in Chapter 8, where we summarize the main results and we give some suggestions for future works.

Theoretical framework and methodology

In the solution to the problems proposed in this thesis for the study of nano-graphene structures, we shall use the tight-binding model and Dirac equation, which we will detail below. Another mathematical tool that was computationally implemented and also used in the development of this thesis is the Split-operator technique, which will also be presented as follows in this Chapter.

2.1 Graphene

We start with the microscopic definition of graphene to obtain latter, in the low-energy approximation, the continuum model for charge carriers dynamics. But first, let us discuss how this material has been studied in recent years [8].

Graphene is a two-dimensional crystal formed by carbon atoms arranged in a honeycomb lattice. This structure can be viewed as two superposed triangular sublattices shifted one from each other, **A** and **B**, or as a single lattice with two atoms per unit cell, as shown in Fig. 2.1.

The lattice vectors can be written as

$$\vec{a}_1 = \frac{3a}{2}\hat{x} + \frac{\sqrt{3}a}{2}\hat{y} \quad \vec{a}_2 = \frac{3a}{2}\hat{x} - \frac{\sqrt{3}a}{2}\hat{y}, \quad (2.1)$$

where $a \approx 1.42 \text{ \AA}$ is the lattice parameter, *i. e.*, the smallest distance between two carbon atoms that forms the C=C bond. The reciprocal lattice vectors are given by

$$\vec{b}_1 = \frac{2\pi}{3a}\hat{x} + \frac{2\sqrt{3}\pi}{3a}\hat{y} \quad \vec{b}_2 = \frac{2\pi}{3a}\hat{x} - \frac{2\sqrt{3}\pi}{3a}\hat{y}. \quad (2.2)$$

In the second quantization formalism, we have that the tight-binding Hamiltonian for electrons in graphene, considering only the first neighbors terms, is given by

$$H = \sum_i (\epsilon_i + M_i)(\mathbf{a}_i^\dagger \mathbf{a}_i + \mathbf{b}_i^\dagger \mathbf{b}_i) + \sum_{\langle i,j \rangle} (\tau_{i,j} \mathbf{a}_i^\dagger \mathbf{b}_j + \tau_{i,j}^* \mathbf{b}_j^\dagger \mathbf{a}_i), \quad (2.3)$$

where \mathbf{a}_i^\dagger and \mathbf{a}_i are creation and annihilation operators, respectively, for electrons on the site i , with self-energy ϵ_i , for the sublattice **A**, while \mathbf{b}_i^\dagger and \mathbf{b}_i are the same operators for

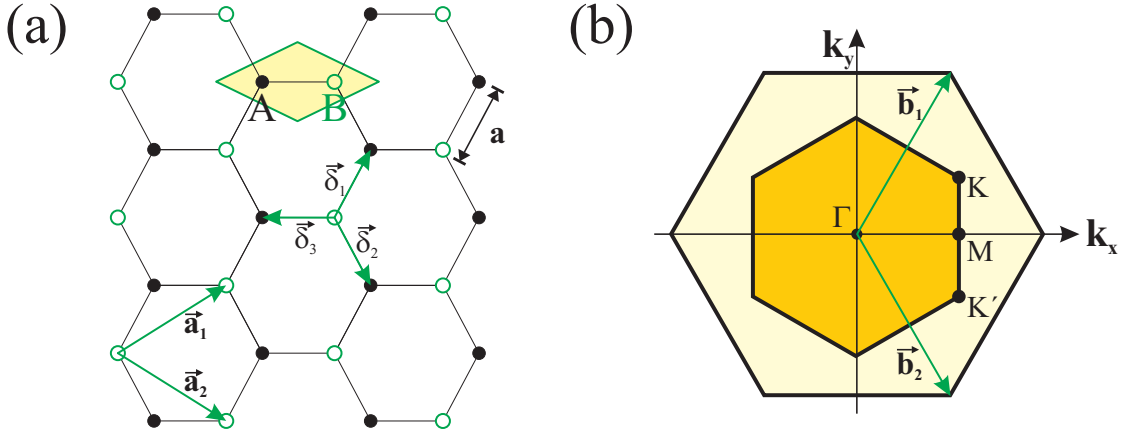


Figure 2.1: (a) Hexagonal lattice structure of graphene represented by two interpenetrating triangular lattices A and B , whose primitive vectors are \vec{a}_1 and \vec{a}_2 , and $\vec{\delta}_i$, with $i = 1, 2$ and 3 , are the vectors that locate the nearest neighbors. The area in yellow shows the unit cell. (b) The first two Brillouin zones and the points of high symmetry of the reciprocal lattice (\vec{b}_1, \vec{b}_2) are also shown. The Dirac cones are located at the K and K' points.

the sublattice \mathbf{B} , and $\tau_{i,j}$ is the hopping parameter. In order to consider the presence of an external magnetic field in the tight-binding model, one should include a phase on hopping parameters, taking a Peierls transformation [1, 73] described as $\tau_{ij} \rightarrow \tau_{ij} \exp \left[i \frac{e}{\hbar} \int_j^i \vec{A} \cdot d\vec{l} \right]$, where \vec{A} is the vector potential related to the external magnetic field. A strain field would lead to a variation of the interatomic distances and, consequently, of the hopping energy between sites, leading to changes such as $\tau_{i,j} \rightarrow \tau_{i,j} (1 + 2\Delta a_{i,j}/a_0)$ with $\Delta a_{i,j} = a_{i,j} - a_0$, where $a_{i,j}$ is the distance between the atoms after the application of strain field [74, 75, 76]. The M_i term appears as a mass-related term in the continuum model, as we will demonstrate further on. This term is a staggered site-dependent potential, which is positive (negative) if the i -site belongs to the lattice \mathbf{A} (\mathbf{B}). Due to this property, such potential is normally used to simulate confining structures in graphene, such as quantum dots and rings [77], where it leads to a gap.

Without loss of generality, we omit for simplicity the first sum of the Hamiltonian (2.3) whose only effect is to shift the Fermi energy level of the system. Let us also consider that all the hopping energies are equal to $t \approx 2.8$ eV [1]. Thus we have that¹

$$H = - \sum_{\langle i,j \rangle} t (\mathbf{a}_i^\dagger \mathbf{b}_j + \mathbf{b}_j^\dagger \mathbf{a}_i). \quad (2.4)$$

By considering an infinite lattice, we can make a Fourier transform of the creation and annihilation operators presented in Hamiltonian (2.4):

$$\mathbf{a}_i = \frac{1}{\sqrt{N}} \sum_k e^{i\vec{k} \cdot \vec{r}_i} \mathbf{a}_k \quad \mathbf{a}_i^\dagger = \frac{1}{\sqrt{N}} \sum_k e^{-i\vec{k} \cdot \vec{r}_i} \mathbf{a}_k^\dagger \quad (2.5)$$

¹The symbol $\langle \rangle$ below of the summation means that the sum is performed only for the nearest neighbors.

$$\mathbf{b}_j = \frac{1}{\sqrt{N}} \sum_{k'} e^{i\vec{k}' \cdot \vec{r}_j} \mathbf{b}_{k'} \quad \mathbf{b}_j^\dagger = \frac{1}{\sqrt{N}} \sum_{k'} e^{-i\vec{k}' \cdot \vec{r}_j} \mathbf{b}_{k'}^\dagger. \quad (2.6)$$

Replacing Eqs. (2.5) and (2.6) in Hamiltonian (2.4), and also considering only the interactions with the first three nearest neighbors, we obtain that

$$H = -t \sum_k [g(\vec{k}) \mathbf{a}_k^\dagger \mathbf{b}_k + g^*(\vec{k}) \mathbf{b}_k^\dagger \mathbf{a}_k], \quad (2.7)$$

where

$$g(\vec{k}) = e^{ik'_x a} + 2 \cos(k'_y \sqrt{3}a/2) e^{-ik'_x a/2} \quad (2.8)$$

is the structure factor of the crystalline lattice.

Since we can write $H = \sum_k \langle \Psi_k | H_k | \Psi_k \rangle$, where $|\Psi_k\rangle = (\mathbf{a}_k, \mathbf{b}_k)^T$ and H_k are, respectively, the electronic states and the Hamiltonian for a particular \vec{k} , therefore we now write the Hamiltonian (2.7) in a matrix form

$$H_k = \begin{pmatrix} 0 & -tg(\vec{k}) \\ -tg^*(\vec{k}) & 0 \end{pmatrix}. \quad (2.9)$$

By diagonalization on the Hamiltonian (2.9) we obtain that the eigenvalues are

$$E_{\pm k} = \pm t |g(\vec{k})| = \pm t \sqrt{3 + f(\vec{k})}, \quad (2.10)$$

where $f(\vec{k}) = 4 \cos(3k_x a/2) \cos(\sqrt{3}k_y a/2) + 2 \cos(\sqrt{3}k_y a)$.

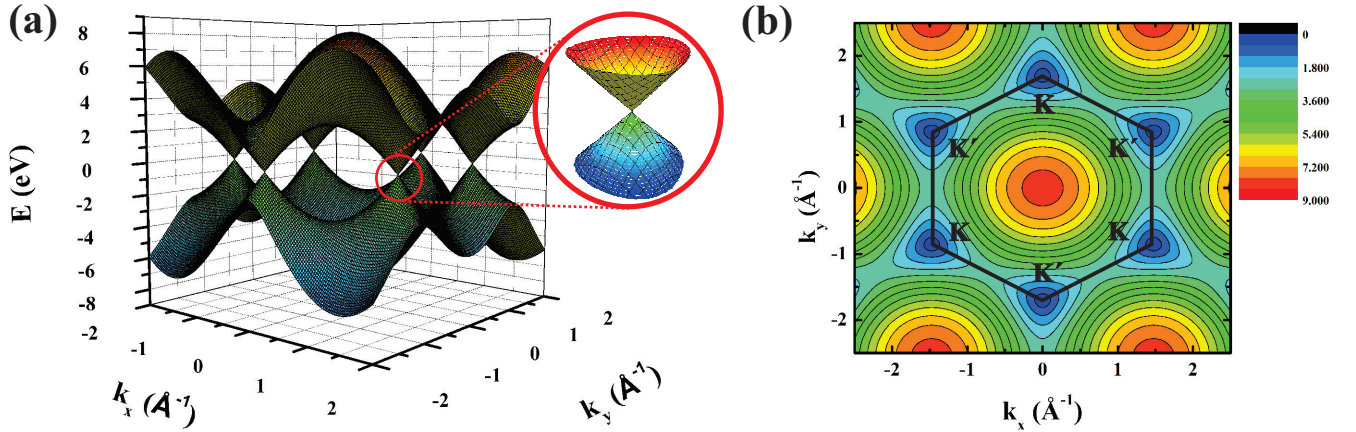


Figure 2.2: (a) Electronic dispersion relation of graphene with a zoom in the energy bands, showing the conical relationship nearby K and K' Dirac points. (b) Contour plot of the conduction band on the first Brillouin zone.

As it can be seen from Fig. 2.2, the band structure of graphene is gapless at six points, known as the Dirac points. In the vicinity of these points, one observes that there is a conical electronic dispersion, suggesting that the electron in these nearby of the reciprocal space should behave as a massless quasiparticle described by the Dirac equation, which

also has a linear dependence with energy. Only two of the six cones are not equivalent, whose positions in reciprocal space are given by the vectors

$$\vec{K} = \left(\frac{2\pi}{3a}, \frac{2\pi}{3\sqrt{3}a} \right) \quad \vec{K}' = \left(\frac{2\pi}{3a}, -\frac{2\pi}{3\sqrt{3}a} \right). \quad (2.11)$$

Until the present moment, we have described the electronic behavior in a microscopic approach given by the Hamiltonian (2.9). Reducing the model to the study of the electronic behavior only in the vicinity of the Dirac points, we achieve the continuum model. To do this, we will expand the non-zero terms of Hamiltonian (2.9) in a Taylor series around these \vec{K} e \vec{K}' points. Thus, retaining just the first-order terms of $g(\vec{k})$, we get:

- For K :

$$g(\vec{k}) = \frac{3a}{2}(k'_x - ik'_y)e^{-i\frac{5\pi}{6}}. \quad (2.12)$$

- For K' :

$$g(\vec{k}) = \frac{3a}{2}(-k'_x - ik'_y)e^{-i\frac{\pi}{6}}. \quad (2.13)$$

The complex exponentials in Eqs. (2.12) and (2.13) may be included in the wave functions without any changes to the physical system, once that the quadratic norms of these terms are 1. Including Eqs. (2.12) and (2.13) in Hamiltonian (2.9) we get

$$H_k = \hbar v_f \begin{pmatrix} 0 & \pm k'_x - ik'_y \\ \pm k'_x + ik'_y & 0 \end{pmatrix}, \quad (2.14)$$

where $v_f = 3at/2\hbar$ is the Fermi velocity and the signs + and - are related to the low-energy electrons around K and K' points, respectively. In a more compact form, we can write

$$H_k = v_f \vec{\sigma} \cdot \vec{p}. \quad (2.15)$$

The Hamiltonian (2.14) is the bidimensional Dirac Hamiltonian that describes relativistic electrons with a zero mass and with the light velocity c replaced by the Fermi velocity v_f . For this reason, it is usual to say that the electrons in graphene behave like massless relativistic fermions.

In the presence of external magnetic fields \vec{B} and potentials V and M , the Hamiltonian from Eq. (2.15) can be generalized in the form

$$H_D = v_f \vec{\sigma} \cdot (\vec{p} + e\vec{A}) + V(x, y)\mathbf{I} + \tau M(x, y)\sigma_z, \quad (2.16)$$

where \mathbf{I} is the identity matrix 2×2 , $\tau = 1(-1)$ for the cone $K(K')$, $M(\vec{r})$ is a site-dependent potential related to the mass term, as previously mentioned in Eq. (2.3) being used to create a gap in the energy spectrum and simulate electronic confinements [77, 78], and the eigenstates are pseudospinors $\Psi = [\Psi_A, \Psi_B]^T$, where $\Psi_{A(B)}$ gives the probability of finding the electron in sublattice $A(B)$.² In the next sections we shall comment more

²The presented Hamiltonian one refers to the K point. For the K' point one should replace $\vec{\sigma}$ by $\vec{\sigma}^*$.

about the influence of magnetic field on the energy spectrum of monolayer and bilayer graphene, and we shall discuss the Hamiltonian (2.15) in more details in the Chapter 3 as well.

With these two basic tools for the study of electrons in graphene, we can develop theories for finite systems, based on tight-binding model, and for low-energy electrons in infinite systems, through the Dirac model.

2.2 Bilayer graphene

As a natural extension of the model used for monolayer graphene, as given in the previous section, we shall introduce in this section the commonly-used tight-binding model for bilayer graphene, as well its band and crystal structures. The tight-binding framework for bilayer graphene deals with a higher complexity due to the introduction of various inter-layer hopping elements that were not considered in monolayer case. Although there are these additional contributions, we shall treat here only the simplest generalization of bilayer description under some approximations. The external bias potential shall be also investigated.

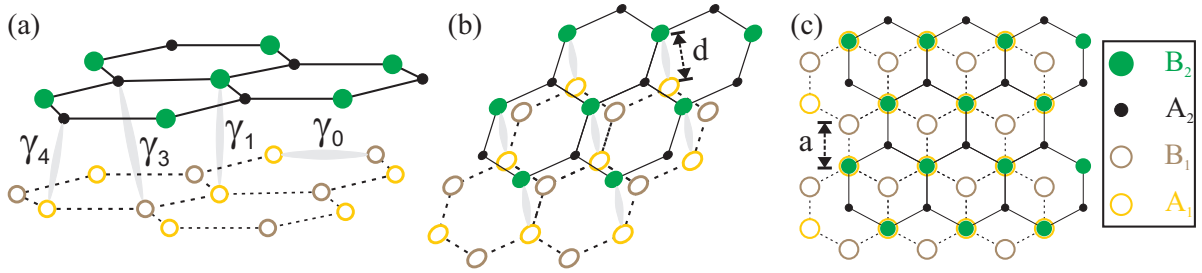


Figure 2.3: (a) The crystal structure of bilayer graphene in Bernal stacking with the various hopping parameters. The bottom (top) layer is represented by dashed (solid) lines with triangular sublattices formed by A_1 (yellow) and B_1 (brown) (A_2 (black) and B_2 (green)) sites. γ_0 is the inter-layer hopping energy and $\gamma_{1,3,4}$ are the intra-layer hopping energies. (b) Perspective and (c) top views of crystalline structure of bilayer graphene, emphasizing the $A_1 - B_2$ connections and the middle position of the A_2 sites with respect to the carbon hexagons in bottom layer. $a \approx 1.42 \text{ \AA}$ and $d \approx 3.35 \text{ \AA}$ are the inter-atomic and intra-layer distances between the two closer carbon atoms in the same layer and between the two layers, respectively.

The bilayer graphene (BLG) consists of two coupled graphene layers linked by Van-der-Waals bounds with a separation distance of $d \approx 3.35 \text{ \AA}$. These two parallel layers are formed by carbon atoms and arranged each one with a honeycomb arrangement, as in a monolayer. The most typical arrangement considered for the bilayer structure is the Bernal stacked bilayer graphene, also called AB -stacked bilayer graphene, although AA

stacking³ is also possible but not as stable [7]. In AB stacking, one layer is rotated by 60° with respect to the other. It implies that the layers are positioned so that the sublattice B of upper layer lies exactly on top of the sublattice A of the lower layer, whereas the sublattice A of upper layer (A_2) are located on the middle of the carbon hexagons of the lower layer⁴. Figure 2.3 shows the crystal structure of bilayer graphene in Bernal stacking configuration in different views.

The tight-binding Hamiltonian that describes π electrons in a AB -stacked bilayer graphene can be written as [1, 79, 80]

$$\begin{aligned}
 H_{BLG} = & \sum_{i,j} \sum_{n=1}^2 \left(E_{A_n} \mathbf{a}_{i;n}^\dagger \mathbf{a}_{i;n} + E_{B_n} \mathbf{b}_{j;n}^\dagger \mathbf{b}_{j;n} \right) \\
 & - \gamma_0 \sum_{i,j} \sum_{n=1}^2 \left(\mathbf{a}_{i;n}^\dagger \mathbf{b}_{j;n} + \mathbf{b}_{j;n}^\dagger \mathbf{a}_{i;n} \right) \\
 & - \gamma_1 \sum_{i,j} \left(\mathbf{a}_{i;1}^\dagger \mathbf{b}_{j;2} + \mathbf{b}_{j;2}^\dagger \mathbf{a}_{i;1} \right) \\
 & - \gamma_3 \sum_{i,j} \left(\mathbf{a}_{i;2}^\dagger \mathbf{b}_{j;1} + \mathbf{b}_{j;1}^\dagger \mathbf{a}_{i;2} \right) \\
 & - \gamma_4 \sum_{i,j} \left(\mathbf{a}_{i;1}^\dagger \mathbf{a}_{j;2} + \mathbf{a}_{j;2}^\dagger \mathbf{a}_{i;1} + \mathbf{b}_{i;1}^\dagger \mathbf{b}_{j;2} + \mathbf{b}_{j;2}^\dagger \mathbf{b}_{i;1} \right),
 \end{aligned} \tag{2.17}$$

$$\tag{2.18}$$

where $a_{i;n}(a_{i;n}^\dagger)$ annihilates (creates) an electron on the site i of sublattice A of layer n , while $a_{i;n}(a_{i;n}^\dagger)$ act likewise on the site j of sublattice B . Thus, we can understand each contribution of the Hamiltonian through the hopping parameters as in graphite nomenclature, such as [1]: (i) the first term of the Hamiltonian represents the on-site energy of the sublattices A_n and B_n for each layer n ; (ii) the intra-layer contributions between the atoms of the same layer n are described by the second part of the Hamiltonian, once that $\gamma_0 = t \approx 2.8$ eV is the in-plane hopping energy ($A_1 - B_1$ and $A_2 - B_2$); (iii) the third part of the Hamiltonian that contains the term $\gamma_1 = t_\perp \approx 0.4$ eV describes the most important inter-layer coupling, since there is no projection of the vector connecting the dimer bond between the two lattice sites A_1 and B_2 on the xy -plane ($A_1 - B_2$); (iv) the inter-layer coupling $\gamma_3 \approx 0.3$ eV corresponds to the hopping between the sites B_1 and A_2 ; and (v) the last term of the Hamiltonian is linked to the hopping energy due to the bounds between the sites A_1 and A_2 .

In the simplest case, we can approximate the Hamiltonian (2.17) considering only inter-layer coupling t_\perp , which connects the two atoms stacked right on top of each other,

³For more details[81] about the Hamiltonian described using the AA stacking to see Appendix A.

⁴The unit cell for the bilayer problem has four atoms, being a pair A_1, B_1 (A_2, B_2) from the lower (upper) layer, instead of just two as in monolayer case. The primitive lattice vectors for bilayer lattice are the same as for monolayer graphene \vec{a}_1 and \vec{a}_2 , as well as the area in the $x - y$ plane of the unit cell, as shown in Fig. 2.1(a). Thus, since the unit cell of bilayer graphene contains four atoms, and, if the tight-binding model includes one p_z orbital per atomic site, there will be four bands near zero energy, instead of the two bands in monolayer graphene, as showed in Fig. 2.4.

and the nearest-neighbour in-plane hopping parameter t . Following the same scheme as for the monolayer as discussed in section 2.1 and considering only the p_z electrons which form the π bands, there are this way four orbital wave functions and consequently the tight-binding Hamiltonian is now a 4×4 matrix given by

$$H_k = \begin{pmatrix} 0 & -tg(\vec{k}) & t_\perp & 0 \\ -tg^*(\vec{k}) & 0 & 0 & 0 \\ t_\perp & 0 & 0 & -tg^*(\vec{k}) \\ 0 & 0 & -tg(\vec{k}) & 0 \end{pmatrix}. \quad (2.19)$$

It consists of two single-layer Hamiltonian on the diagonal, similar as Eq. (2.9), with $g(\vec{k})$ from Eq. (2.8). The off-diagonal 2×2 blocks describe the inter-layer coupling. The above matrix can be diagonalized resulting in the corresponding spectrum [7]

$$E_{\pm k}^\pm = \pm \frac{t_\perp}{2} \pm \sqrt{\frac{t_\perp^2}{4} + t|g(\vec{k})|^2}, \quad (2.20)$$

formed by four eigenvalues and consequently four bands. These four energy bands are composed by two conduction bands and two valence bands. The bilayer graphene spectrum seems like the the band structure of monolayer graphene, except for the fact that each monolayer band split into two by an energy approximately equal to the inter-layer coupling t_\perp , *i. e.* the gap separation between the two non-touching bands around the K and K' points is $2t_\perp$ being these two upper bands with energies $E_+^+ \geq t_\perp$ and $E_-^- \leq -t_\perp$. But in contrast to the band structure of monolayer graphene, bilayer graphene spectrum turns out to be a gapless semiconductor with parabolic band. An illustration of the electronic band of the bilayer graphene in the absence of external bias potential is shown in Fig. 2.4(a).

Repeating the same procedure performed for the single-layer case to obtain the effective Hamiltonian in the form as expressed in Eq. (2.14), *i. e.* using continuum model for the low-energy approximation close to the K and K' points, we can construct, in analogy, the following effective Hamiltonian for bilayer graphene

$$H_{BLG} = \begin{pmatrix} 0 & \pi & t_\perp & 0 \\ \pi^\dagger & 0 & 0 & 0 \\ t_\perp & 0 & 0 & \pi^\dagger \\ 0 & 0 & \pi & 0 \end{pmatrix}, \quad (2.21)$$

where $\pi = v_F(\tau p_x + ip_y)$ and $\pi^\dagger = v_F(\tau p_x - ip_y)$, with $\tau = +1$ or $\tau = -1$ to denote the Hamiltonian that corresponds to the K or K' valleys, and $p_{x,y} = \hbar k_{x,y}$. The corresponding K and K' four component wave functions for the Hamiltonian (2.21) are assumed as

$$\Psi_K = \begin{pmatrix} \varphi_A \\ \varphi_B \\ \varphi_{B'} \\ \varphi_{A'} \end{pmatrix} \quad \text{and} \quad \Psi_{K'} = \begin{pmatrix} \varphi_B \\ \varphi_A \\ \varphi_{A'} \\ \varphi_{B'} \end{pmatrix}. \quad (2.22)$$

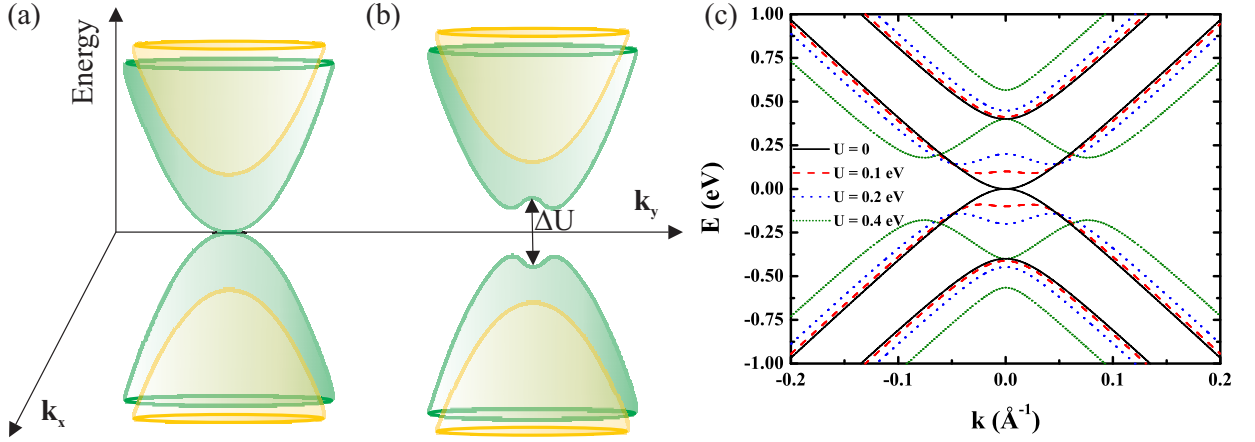


Figure 2.4: Drawing of the electronic band of (a) unbiased $\Delta U = 0$ and (b) biased bilayer graphene $\Delta U = U_1 - U_2 \neq 0$. (c) Energy spectrum of bilayer graphene for four different potential configurations, being $U_1 = U_2 = U = 0$ (black solid curve), $U_1 = -U_2 = U = 0.1$ eV (red dashed curve), $U_1 = -U_2 = U = 0.2$ eV (blue dotted curve) and $U_1 = -U_2 = U = 0.4$ eV (green short-dotted curve).

In order to obtain the spectrum of a free particle, solving $H\Psi = E\Psi$ for the Hamiltonian Eq. (2.21) and the wave function Eq. (2.22), we can write the following set of equations

$$(k_x - ik_y) \varphi_B = \epsilon \varphi_A - t'_\perp \varphi_{B'}, \quad (2.23a)$$

$$(k_x + ik_y) \varphi_A = \epsilon \varphi_B, \quad (2.23b)$$

$$(k_x + ik_y) \varphi_{A'} = \epsilon \varphi_{B'} - t'_\perp \varphi_A, \quad (2.23c)$$

$$(k_x - ik_y) \varphi_{B'} = \epsilon \varphi_{A'}, \quad (2.23d)$$

where it was considered the dimensionless units $\epsilon = E/\hbar v_F$ and $t'_\perp = t_\perp/\hbar v_F$. Using the definition of the wave vector $k = \sqrt{k_x^2 + k_y^2}$, the above equations result in a simple decoupled equation to φ_A such as $[\epsilon^4 - (2k^2 + t_\perp'^2) \epsilon^2 + k^4] \varphi_A = 0$. It can be readily seen that the solution yields a spectrum

$$\epsilon = \pm \sqrt{k^2 + \frac{t_\perp'^2}{2} \pm t'_\perp \sqrt{\left(\frac{t_\perp'}{2}\right)^2 + k^2}}, \quad (2.24)$$

formed by four energy bands, as already expect by Eq. (2.20). The four valley degenerate bands given be above equation is plotted in Fig. 2.4(c) in black solid curve.

The presence of a perpendicularly applied external electric field produces a breaking of the inversion symmetry, implying in opening of a band gap in the bilayer graphene spectrum. The gap between the conduction and valence bands at the K (K') point induced by external gates are possible in the bilayer graphene, since the sublattices A_1/B_2 that correspond to the inter-layer hopping energies t_\perp lie on different layers⁵. To understand the effect of external bias potential on the energy spectrum of bilayer graphene, we

⁵In monolayer graphene, breaking the A/B sublattice symmetry in a controllable way is very difficult,

investigate this tunable gap due to the application of a voltage V perpendicular to the carbon planes. In the present case, the Hamiltonian (2.19) becomes

$$H_k = \begin{pmatrix} V/2 & -tg(\vec{k}) & t_\perp & 0 \\ -tg^*(\vec{k}) & V/2 & 0 & 0 \\ t_\perp & 0 & -V/2 & -tg^*(\vec{k}) \\ 0 & 0 & -tg(\vec{k}) & -V/2 \end{pmatrix}, \quad (2.25)$$

and the eigenvalues is now given by [7]

$$E_{\pm k}^\pm = \pm \sqrt{\frac{t_\perp^2}{2} + \frac{V^2}{4} + t^2 |g(\vec{k})|^2} \pm \sqrt{\frac{t_\perp^4}{4} + (t_\perp^2 + V^2) t^2 |g(\vec{k})|^2}. \quad (2.26)$$

This spectrum with an applied bias potential is illustrated in Fig. 2.4(b). As V can be externally controlled, this model predicts that biased bilayer graphene should be a tunable-gap semiconductor. Notice that the gap does not reach a minimum at the K point (it has a maximum at $k = 0$) due to the ‘‘Mexican-hat’’ dispersion at low energies.

Using continuum model and expanding the Hamiltonian around to the K and K' Dirac cones, we obtain in a similar manner to the procedure performed from Eq. (2.21) to Eq. (2.24), the energy spectrum for the problem of a bilayer graphene under application of electrostatic potentials U_1 and U_2 , respectively, on the upper and lower layers. This can be included by adding an extra potential term on the diagonal of the Hamiltonian (2.21) as

$$H_{BLG} \rightarrow H_{BLG} + \begin{pmatrix} U_1 \mathbf{I} & 0 \\ 0 & U_2 \mathbf{I} \end{pmatrix}, \quad (2.27)$$

being \mathbf{I} the 2×2 unity matrix. Assuming the wave functions as Eq. (2.22) and doing $H\Psi = E\Psi$, it results that the free particle spectrum is obtained as solution of the following equation

$$[(\epsilon - u_1)^2 - k^2] [(\epsilon - u_2)^2 - k^2] - t_\perp'^2 (\epsilon - u_1) (\epsilon - u_2) = 0, \quad (2.28)$$

being the dimensionless units $\epsilon = E/\hbar v_F$, $t'_\perp = t_\perp/\hbar v_F$ and $u_{1,2} = U_{1,2}/\hbar v_F$, which it gives

$$\epsilon = \frac{u_1 + u_2}{2} \pm \frac{1}{2} \sqrt{\left(t'_\perp \pm \sqrt{t_\perp'^2 + 4k^2 + 4(u_1 - u_2)^2 \frac{k^2}{t_\perp'^2}} \right)^2 + \left(1 - 4 \frac{k^2}{t_\perp'^2} \right) (u_1 - u_2)^2}. \quad (2.29)$$

It can be easily seen that for $u_1 = u_2 = u$, the energy spectrum (2.29) recovers the previous dispersion format as expressed by Eq. (2.26). The two lowest bands with a ‘‘Mexican hat’’ format correspond to the signs inside the square being negative ($-$). Figure 2.4(c) shows the spectrum for four different potential configurations, being the black solid, dashed red, dotted blue and green short-dotted curves corresponding respectively because it would require a special periodic (staggered) potential, since the sites A and B are identical and adjacent on the same layer.

to values $U_1 = U_2 = U = 0$, $U_1 = -U_2 = U = 0.1$ eV, $U_1 = -U_2 = U = 0.2$ eV and $U_1 = -U_2 = U = 0.4$ eV. One can realize that as $|U|$ is made larger, the “Mexican hat” shaped band gap becomes more pronounced.

These results for the bias bilayer graphene suggest a route to new nanoelectronic devices. By combination of top and bottom gates, one can control the gap in the bilayer spectrum and hence define confinement structures, which are even able to localize electrons.

2.3 Influence of an external perpendicular magnetic field

Let us now investigate the influence of a perpendicular magnetic field \vec{B} on the energy levels of monolayer and bilayer graphene. We will obtain discrete energy levels (so called *Landau levels* (LLs)) of two-dimensional electrons in the presence of an external magnetic field. But first, we will discuss briefly the classical case.

2.3.1 Classical picture

In classical electrodynamics, a charged particle q with mass m under the influence of a external magnetic field \vec{B} experiences a magnetic force described by following equation

$$\vec{F} = q (\vec{v} \times \vec{B}), \quad (2.30)$$

where \vec{v} is the charge velocity. An illustration is present in Fig. 2.5(a), where it is pointed the orientation of each these vectors.

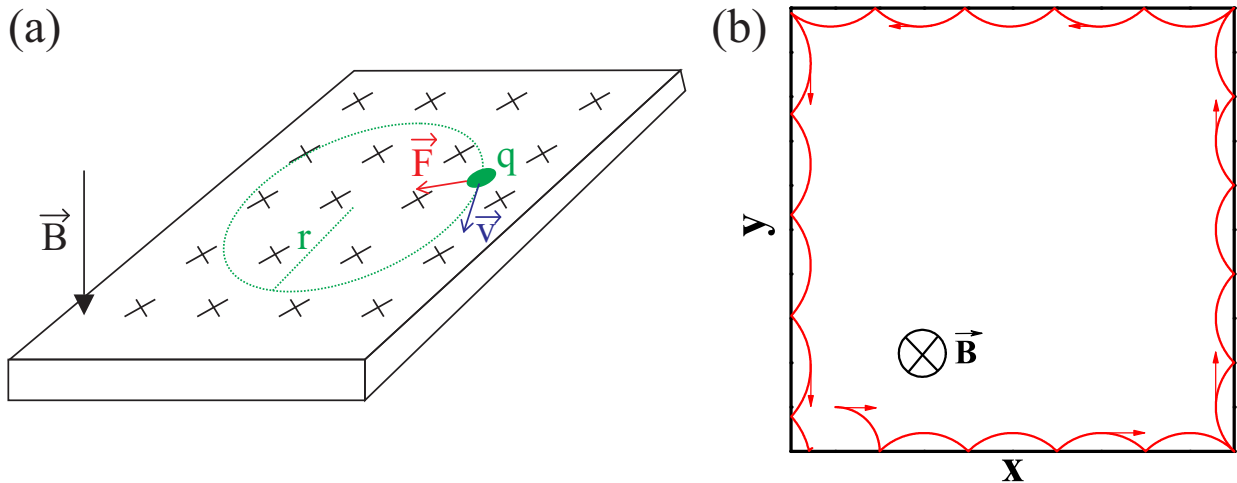


Figure 2.5: (a) Scheme of a charged particle with charge q and mass m performing a circular motion due to the influence of an external perpendicular magnetic field. The orientation of the vectors velocity \vec{v} and magnetic force \vec{F} are presented. (b) Classical skipping orbits experienced by a charge particle under a perpendicular magnetic field.

Considering that a particle moves within an uniform magnetic field and there are no other external forces in addition to the magnetic field, then if the initial particle velocity

is perpendicular to the magnetic field with magnitude qvB , one has that in each instant the magnitude of the velocity remains constant, once that at each moment the force is perpendicular to the velocity. This results in a uniform circular motion, such as $mv^2/r = qvB$. The path is consequently a circular orbit, so called cyclotron orbit, with radius $r = mv/qB$ and angular velocity $w = qB/m$. An example of the charged particle moving close to the edges of a certain material under the presence of a uniform and perpendicular magnetic field is shown in Fig. 2.5(b). Notice that the particle performs semi-circular orbits. These orbits are called as skipping orbits, since that each time that the particle reaches the edge, the direction of its momentum is changed.

2.3.2 Landau levels in a monolayer graphene

The Hamiltonian that describes a free electron in a single-layer graphene with a perpendicular applied magnetic field can be written as

$$H = v_F \vec{\sigma} \cdot \vec{\Pi} \quad (2.31)$$

where we performed the transformation $\vec{p} \rightarrow \vec{\Pi} = \vec{p} + e\vec{A}$ in Eq. (2.15), being \vec{A} the vector potential that generates the magnetic field $\vec{B} = \nabla \times \vec{A}$ and e the elementary charge. This transformation for electrons on a lattice in the presence of magnetic field is valid for the case that the magnetic length

$$l_B = \sqrt{\frac{eB}{\hbar}} \quad (2.32)$$

is much larger than the interatomic distance a . As a is in the order of 1.42 \AA and any experimentally available fields produced in the labs are less than $B \ll 10^4 \text{ T}$, then the approximation involved in this transformation is not violated. Considering the Landau gauge $\vec{A} = (0, B_0x, 0)$ defined by a uniform magnetic field $\vec{B} = B_0\hat{z}$, we can write Eq. (2.31) explicitly as

$$H = -i\hbar v_f \begin{pmatrix} 0 & \frac{\partial}{\partial x} - i\frac{\partial}{\partial y} + \frac{eB_0}{\hbar}x \\ \frac{\partial}{\partial x} + i\frac{\partial}{\partial y} - \frac{eB_0}{\hbar}x & 0 \end{pmatrix}. \quad (2.33)$$

The two-component wave function $\Psi(x, y)$ can be assumed as the following form

$$\Psi(x, y) = \begin{pmatrix} \psi_A(x, y) \\ \psi_B(x, y) \end{pmatrix} = e^{ik_y y} \begin{pmatrix} \psi_A(x) \\ \psi_B(x) \end{pmatrix}, \quad (2.34)$$

since that, for the chosen gauge, the y -coordinate does not appear in the Hamiltonian, the Hamiltonian commutes with p_y , *i. e.* $[H, p_y] = 0$, being p_y this way a constant of motion. This implies that the eigenstates of the p_y should be also eigenstates of the Hamiltonian, with eigenvalue given by $\hbar v_F k_y$. Solving the eigenvalue problem $H\Psi(x, y) = E\Psi(x, y)$

results in two coupled differential equations

$$\left[\frac{\partial}{\partial x} + k_y + \frac{x}{l_B^2} \right] \psi_B = \frac{iE}{\hbar v_F} \psi_A, \quad (2.35a)$$

$$\left[\frac{\partial}{\partial x} - k_y - \frac{x}{l_B^2} \right] \psi_A = \frac{iE}{\hbar v_F} \psi_B. \quad (2.35b)$$

Inserting one equation into another, we can decouple the equations as

$$\left[\frac{\partial^2}{\partial \bar{x}^2} - (k_y l_B + \bar{x})^2 + 1 + \left(\frac{E l_B}{\hbar v_F} \right)^2 \right] \psi_B = 0, \quad (2.36)$$

where it was considered the dimensionless unit $\bar{x} = x/l_B$. The above second-order differential equation seems like [82]

$$\psi_n''(x) + (2n + 1 - x^2) \psi_n(x) = 0, \quad (2.37)$$

which solutions are the well-known Hermite polynomials $\mathcal{H}_n(x)$, with $\psi(x)_n = e^{-x^2/2} \mathcal{H}_n(x)$. Thus comparing Eqs. (2.36) and (2.37), we obtain a discrete spectrum given by

$$E_n = \pm \frac{\hbar v_F}{l_B} \sqrt{2n}, \quad (2.38)$$

with $n = 0, 1, 2, \dots$, where E_n are the Landau levels for a monolayer graphene. The positive values correspond to electrons (conduction band), while the negative values correspond to holes (valence band). Repeating the same procedure but now decoupling for the ψ_A component, one obtains that

$$\left[\frac{\partial^2}{\partial \bar{x}^2} - (k_y l_B + \bar{x})^2 - 1 + \left(\frac{E l_B}{\hbar v_F} \right)^2 \right] \psi_A = 0, \quad (2.39)$$

such that now, comparing Eqs. (2.37) and (2.39), the energy levels are given by

$$E_n = \pm \frac{\hbar v_F}{l_B} \sqrt{2(n+1)}. \quad (2.40)$$

which, comparing to the previous results Eq. (2.38), lacks the level with $E = 0$. The existence of a zeroth Landau level $E_0 = 0$ is a direct consequence of the zero gap in the energy spectrum for Dirac fermions in graphene. This zeroth Landau level has twice smaller degeneracy as compared with the other Landau levels. Another important remark about Eqs. (2.38) and (2.40) is that the Landau levels are independent of the valley index. Thus, the zeroth Landau level has actually four-fold degeneracy, being two-fold associated with the electron-hole symmetry and the another two-fold because of valley symmetry. A consequence of different dependence of the energy levels for sublattices A ($E_A \propto \sqrt{2(n+1)}$) and B ($E_B \propto \sqrt{2n}$), which must differ in the index n for 1 to yield the same energy eigenvalue for both, results in a different occupation of the sublattices A and B . This means that the wave function at the Landau level $n = 0$ should have non-zero

amplitude only on B (A) sublattice for valley K (K'), while at the Landau level $n \neq 0$ should always have non-zero amplitudes on both sublattices A and B .

According to Eq. (2.37), the eigenfunctions can be written as

$$\begin{pmatrix} \psi_A(x) \\ \psi_B(x) \end{pmatrix} \propto e^{-(k_y l_B + \bar{x})^2/2} \begin{pmatrix} \mathcal{H}_{n_A}(k_y l_B + \bar{x}) \\ \mathcal{H}_{n_B}(k_y l_B + \bar{x}) \end{pmatrix}, \quad (2.41)$$

with $n_B = \frac{1}{2} \left(\frac{El_B}{\hbar v_F} \right)^2$ and $n_A = n_B - 1$, being the wave functions not normalized.

Comparing the obtained Landau levels by Eqs. (2.38) and (2.40) with Landau levels for a conventional electron gas within the Schrödinger equation, one can notice that the latter has equidistant energy levels $E_n = \hbar e B / m (n + 1/2)$, which is due to the parabolic dispersion law of free electron, and a linear dependence on the magnetic field $E_n \propto (n + 1/2) B$, whereas the Landau levels in graphene are not equally spaced and follow a square root dependence on the magnetic field $E_n \propto \sqrt{2nB}$. The largest energy separation is between the zeroth and first Landau levels, as one can see in Fig. 2.6(a). Experimental results about the Landau levels in graphene have been reported in Refs. [83], [84] and [85].

2.3.3 Landau levels in a bilayer graphene

The single particle Hamiltonian for bilayer graphene in the continuum approximation, in the vicinity of the K point and in the presence of applied bias potentials U_1 and U_2 , respectively for the upper and lower layer, is the 4×4 matrix

$$H = \begin{pmatrix} U_1 & \pi & t & 0 \\ \pi^\dagger & U_1 & 0 & 0 \\ t & 0 & U_2 & \pi^\dagger \\ 0 & 0 & \pi & U_2 \end{pmatrix}, \quad (2.42)$$

where it was considered only nearest-neighbor hopping $t \approx 400$ meV that couples the A and B' sites at the two layers. In the presence of an external magnetic field $\vec{B} = B_0 \hat{z}$ perpendicular to the bilayer graphene sheet, π and π^\dagger are given by

$$\pi = -i\hbar v_F \left[\frac{\partial}{\partial x} + i \left(\frac{\partial}{\partial y} + i \frac{eB_0}{\hbar} x \right) \right], \quad (2.43a)$$

$$\pi^\dagger = -i\hbar v_F \left[\frac{\partial}{\partial x} - i \left(\frac{\partial}{\partial y} + i \frac{eB_0}{\hbar} x \right) \right], \quad (2.43b)$$

where we used the Landau gauge for the vector potential $\vec{A} = (0, B_0 x, 0)$. In a similar way as for the Dirac Hamiltonian Eq. (2.33), the Hamiltonian for bilayer graphene Eq. (2.42) commutes with p_y and therefore is a conserved quantity. As $[H, p_y] = 0$, then one

can write the four-component wave function as

$$\Psi(x, y) = e^{-ik_y y} \begin{pmatrix} \varphi_A(x) \\ \varphi_B(x) \\ \varphi_{B'}(x) \\ \varphi_{A'}(x) \end{pmatrix}. \quad (2.44)$$

Solving $H\Psi(x, y) = E\Psi(x, y)$, we obtain the following set of equations

$$-i\hbar v_F \left[\frac{\partial}{\partial x} - k_y - \frac{eB_0}{\hbar} x \right] \varphi_B = (E - U_1) \varphi_A - t\varphi_{B'}, \quad (2.45a)$$

$$-i\hbar v_F \left[\frac{\partial}{\partial x} + k_y + \frac{eB_0}{\hbar} x \right] \varphi_A = (E - U_1) \varphi_B, \quad (2.45b)$$

$$-i\hbar v_F \left[\frac{\partial}{\partial x} + k_y + \frac{eB_0}{\hbar} x \right] \varphi_{A'} = (E - U_2) \varphi_{B'} - t\varphi_A, \quad (2.45c)$$

$$-i\hbar v_F \left[\frac{\partial}{\partial x} - k_y - \frac{eB_0}{\hbar} x \right] \varphi_{B'} = (E - U_2) \varphi_{A'}. \quad (2.45d)$$

Considering the dimensionless units $\bar{x} = k_y l_B + x/l_B$, $u_{1,2} = U_{1,2} l_B / \hbar v_F$, $\epsilon = El_B / \hbar v_F$, $t' = tl_B / \hbar v_F$, $u_0 = (u_1 + u_2)/2$, $\Delta u = u_1 - u_2$, $\alpha = \epsilon - u_0$ and $\delta = \Delta u/2$, and replacing them into the set of differential equation Eq. (2.45), yields

$$-i \left[\frac{\partial}{\partial \bar{x}} - \bar{x} \right] \varphi_B = (\alpha - \delta) \varphi_A - t' \varphi_{B'}, \quad (2.46a)$$

$$-i \left[\frac{\partial}{\partial \bar{x}} + \bar{x} \right] \varphi_A = (\alpha - \delta) \varphi_B, \quad (2.46b)$$

$$-i \left[\frac{\partial}{\partial \bar{x}} + \bar{x} \right] \varphi_{A'} = (\alpha + \delta) \varphi_{B'} - t' \varphi_A, \quad (2.46c)$$

$$-i \left[\frac{\partial}{\partial \bar{x}} - \bar{x} \right] \varphi_{B'} = (\alpha + \delta) \varphi_{A'}. \quad (2.46d)$$

We can reduce the above equations Eqs. (2.46)(a) - (2.46)(d) to a single differential equation. Decoupling for φ_A ,

$$\left[\frac{\partial}{\partial \bar{x}^2} - \bar{x}^2 + \alpha^2 + \delta^2 \right]^2 \varphi_A = [t'^2(\alpha^2 - \delta^2) + (1 - 2\alpha\delta)^2] \varphi_A. \quad (2.47)$$

The solution for the above equation should also satisfy the following ansatz

$$\left[-\frac{\partial}{\partial \bar{x}^2} + \bar{x}^2 \right] \varphi_A = \gamma_{\pm} \varphi_A, \quad (2.48)$$

where $\gamma_{\pm} = \alpha^2 + \delta^2 \pm \sqrt{t'^2(\alpha^2 - \delta^2) + (1 - 2\alpha\delta)^2}$. Assuming $\varphi_A(\bar{x}) = f_A(\bar{x})e^{-\bar{x}^2/2}$ to solve Eq. (2.48), in order to eliminate the \bar{x}^2 , we have that

$$\frac{\partial^2 f_A}{\partial \bar{x}^2} - 2\bar{x} \frac{\partial f_A}{\partial \bar{x}} + (\gamma_{\pm} - 1)f_A = 0, \quad (2.49)$$

whose solutions can be obtained in terms of Hermite polynomials $\mathcal{H}_n(\bar{x})$, that satisfies the differential Hermite equation $u'' - 2xu' + 2nu = 0$. Comparing the format of Eq. (2.49) and Hermite equation, we can see that the eigenvalues obey the relation $\gamma_{\pm} = 2n + 1$, where n is a non-negative integer. After some straightforward algebra, we finally find that the discrete spectrum of Landau levels will correspond to the solutions of the following fourth-order algebraic equation

$$[(\alpha + \delta)^2 - 2(n + 1)] [(\alpha - \delta)^2 - 2n] = (\alpha^2 - \delta^2) t'^2. \quad (2.50)$$

For an unbiased bilayer, *i. e.* $u_{1,2} = 0$ and consequently $\delta = 0$, Eq. (2.50) results in

$$\epsilon = \pm \left[\frac{t'^2}{2} + 2n + 1 \pm \sqrt{\frac{t'^4}{4} + (2n + 1)t'^2 + 1} \right]^{1/2}. \quad (2.51)$$

A special case is when both the inter-hopping and the potential tend to zero, *i. e.* $t' \rightarrow 0$ and $\delta \rightarrow 0$. For this case, the spectrum is given by $\epsilon = \pm\sqrt{2n + 1 \pm 1}$, that corresponds to two uncoupled layers of graphene⁶.

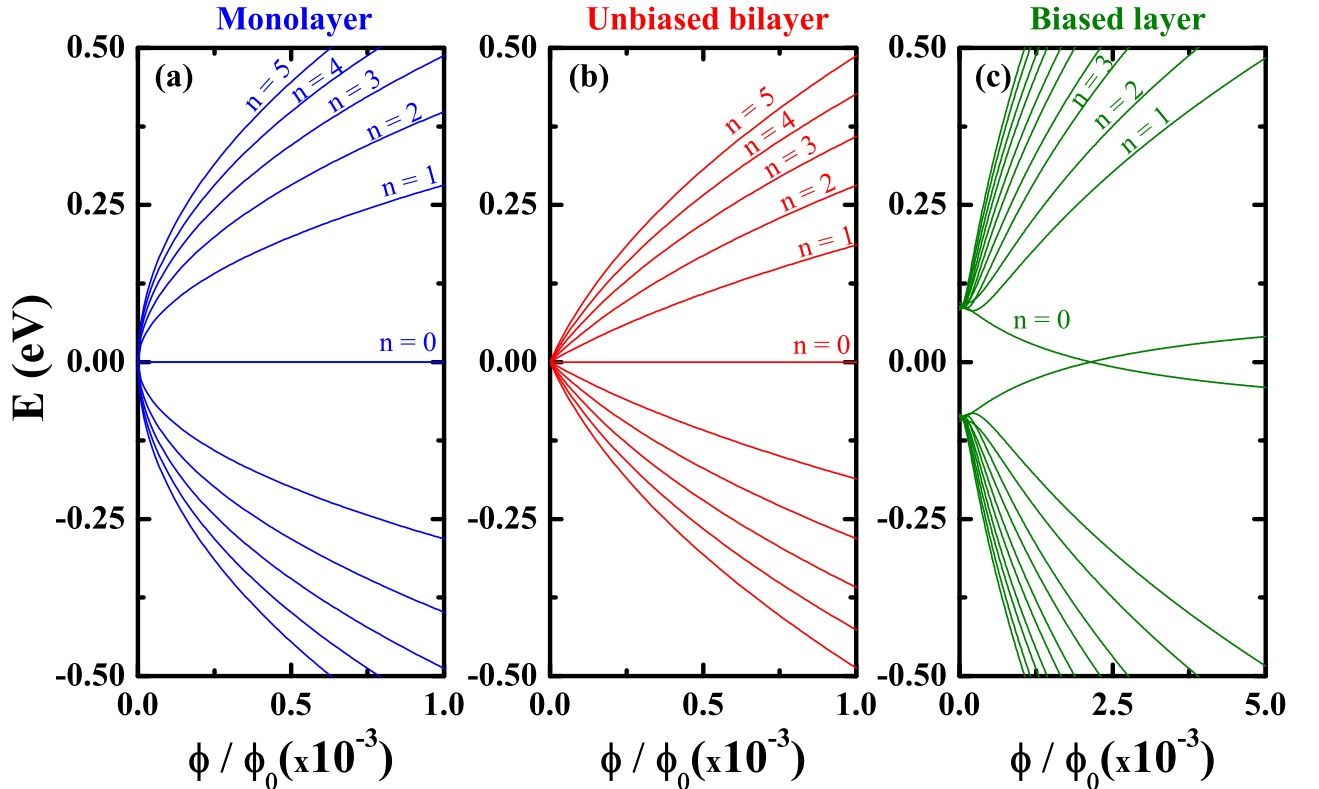


Figure 2.6: Landau levels as a function of the magnetic flux ($\frac{\phi}{\phi_0} = \frac{3\sqrt{3}a^2eB_0}{2h}$) for (a) monolayer graphene $E_n = \pm\hbar v_F \sqrt{\frac{8\pi n}{3\sqrt{3}a^2} \frac{\phi}{\phi_0}}$, (b) unbiased bilayer graphene, and (c) biased bilayer graphene with gate potentials $U_1 = -U_2 = 100$ meV.

⁶For more details about the Landau levels and the wave functions which are solutions of the both biased and unbiased bilayer graphene see Ref. [86].

In an illustrative way, we show in Figs. 2.6(b) and 2.6(c) the Landau levels respectively for unbiased and biased bilayer graphene. For the biased case, we considered the gate potentials as being $U_1 = -U_2 = 100$ meV.

2.4 Boundary conditions

As it has been already demonstrated in the literature [27], the electronic states of the carbon systems depend strongly on its size and geometry. For instance, in the case of carbon nanotubes, the geometry dependence is strongly influenced by the bipartite character of the graphene lattice and the wrapping direction imposes different boundary conditions on the wave function in the different sublattices, which determine whether the system is semiconducting or metallic [87]. For graphene nanoribbons, Brey & Fertig have been reported in Refs. [88] and [89] that the electronic energies and states of graphene nanoribbons with different atomic terminations may be understood in terms of eigenvalues and eigenvectors of the Dirac Hamiltonian with correct boundary conditions. They have focused in the two more conventional graphene edges terminations: zigzag and armchair edges, as illustrated in Fig. 2.7(a). Akhmerov & Beenakker have derived in Ref. [90] the boundary condition for the Dirac equation corresponding to a tight-binding model on two-dimensional honeycomb lattice terminated along an arbitrary direction. They have shown that the boundary condition for intermediate case (a mixed boundary condition) remains orientations of the zigzag form, so that the armchair boundary condition is only reached for a discrete set of orientations.

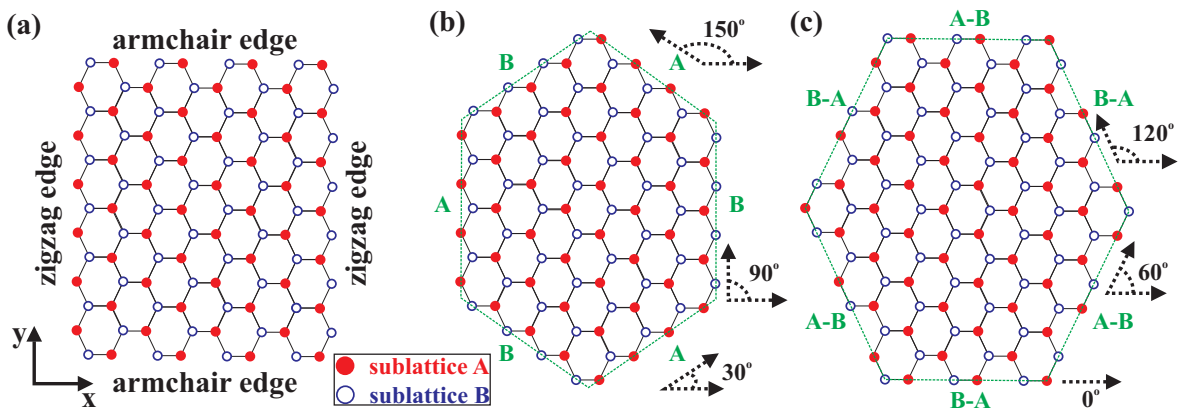


Figure 2.7: (a) The lattice structure of a graphene sheet denoting the zigzag and armchair type edge terminations. Top and bottom are armchair edges, left and right are zigzag edges. (b) In the zigzag case, each edge is built from atoms of one sublattice only. Following the dashed green lines forming a regular zigzag hexagon, one notice that the sublattice switches at every side. (c) In the armchair case, both sublattices are present at each edge forming dimer with $A - B$ or $B - A$ termination with respect to the tangential direction.

Other important topic in the understanding of the boundary conditions is related to electron confinement in nanostructured systems. It is known that in conventional two-dimensional electron gases, as realized in semiconductor heterostructures, the charge carriers can be confined by the application of side or top gate voltages, such that these voltages shift the Fermi energy locally from the conduction or valence band into the gap of the spectrum. This can be achieved by defining an effective system boundary where electrons are reflected from, and hence are confined. In the same way, the importance in the studying of the boundary conditions in graphene nanostructures lies in the possibility of confining carriers. Electrostatic potentials do, however, not necessarily confine massless Dirac electrons in graphene, as their corresponding energy spectrum does not have a gap. Instead, the Fermi energy can only be shifted from the conduction band into the valence band or vice versa, such that electrons can be transmitted into the gated region. It is due to well-known Klein tunneling [1], in which under normal incidence a perfect transmission is allowed. Because of this (partial) transparency of electrostatic barriers for charge carriers in graphene, electrons and holes in graphene nanostructures or flakes are expected to scatter only from the edges that eventually terminate the graphene lattice [91].

Since the physical properties of a carbon system are affected by its format and edge terminations, we investigate in the following three subsections how are the boundary conditions depending on the crystallographic orientation of the boundary and how to implement it in the continuum model in a appropriate way. We focus our attention only on the simplest and the most commonly considered boundary conditions for graphene formed by zigzag edges, armchair edges and with infinite-mass term outside of the confinement structure, described in the effective Dirac Hamiltonian.

Before presenting the appropriated boundary conditions for each edge termination, we shall briefly derive the effective 4×4 Hamiltonian to describe the quasiparticle dynamics in graphene at low energies, *i. e.* close to the two inequivalent K and K' Dirac points, being the Hamiltonian for each valley given by Eq. (2.15). Thus, the Hamiltonian for massless Dirac fermions can be written as

$$H = \begin{pmatrix} H_K & 0 \\ 0 & H_{K'} \end{pmatrix}, \quad (2.52)$$

where H_K ($H_{K'}$) is the 2×2 Hamiltonian in the K (K') valley, which are given by

$$H_K = v_f \vec{\sigma} \cdot \vec{p} \quad \text{and} \quad H_{K'} = v_f \vec{\sigma}^* \cdot \vec{p}, \quad (2.53)$$

with $\vec{\sigma} = (\sigma_x, \sigma_y)$ being the Pauli matrices and $\vec{\sigma}^* = (\sigma_x, \sigma_y)$ denotes the complex conjugate of the matrix $\vec{\sigma}$.

The wave functions can be expressed via the $\vec{k} \cdot \vec{p}$ approximation, in terms of envelope functions $[\varphi_A(\vec{r}), \varphi_B(\vec{r})]$ and $[\varphi_{A'}(\vec{r}), \varphi_{B'}(\vec{r})]$ for states near the K and K' points, respectively. These states can be conveniently combined into a four-vector $\Psi(\vec{r}) =$

$[\varphi_A(\vec{r}), \varphi_B(\vec{r}), \varphi_{A'}(\vec{r}), \varphi_{B'}(\vec{r})]$. Thus, we can write the wave function in the real space for the sublattice A as

$$\Psi_A(\vec{r}) = e^{i\vec{K}\cdot\vec{r}}\varphi_A(\vec{r}) + e^{i\vec{K}'\cdot\vec{r}}\varphi_{A'}(\vec{r}), \quad (2.54)$$

and for sublattice B as

$$\Psi_B(\vec{r}) = e^{i\vec{K}\cdot\vec{r}}\varphi_B(\vec{r}) + e^{i\vec{K}'\cdot\vec{r}}\varphi_{B'}(\vec{r}), \quad (2.55)$$

with \vec{K} and \vec{K}' given by Eq. (2.11).

2.4.1 Zigzag boundary condition

Let us consider the orientation of the lattice structure of a graphene sheet as presented in Fig. 2.7(a). We have that the resulting type termination are zigzag edges when the graphene lattice is terminated along a line including the angles given by 30° , 90° and 150° with respect to the x -axis, as demonstrated in Fig. 2.7(b). As one can notice, the outermost row of atoms under the green dashed lines that surrounds the hexagon contains solely atoms of either A - or B -type, such that the orientation of the edge determines the sublattice. Let us assume that a piece of graphene has a zigzag edge along the boundary curve denoted by s with $\vec{r} = \vec{r}_B(s)$. If the last atoms at the boundary are from sublattice B , then the microscopic boundary condition is that the tight-binding wave function vanishes on the (missing) A -type sites of the outermost atoms, which we understand as being the line of lattice sites that would lie just above or below the system if the bonds had not been cut to form the edge. Then the boundary condition reads

$$\varphi_A(\vec{r}_B(s)) = \varphi_{A'}(\vec{r}_B(s)) = 0 \quad (2.56)$$

with the wave function set to zero on a single sublattice, while φ_B and $\varphi_{B'}$ are not determined and not directly affected by the boundary condition. Actually, since the effective Dirac equation couples the sublattice when we solve $H\Psi = E\Psi$, we have therefore that φ_B and $\varphi_{B'}$ are affected indirectly. Similarly, when the zigzag edges are terminated by the A atoms, one has in this case that φ_B and $\varphi_{B'}$ have to vanish individually, whereas φ_A and $\varphi_{A'}$ are not determined.

In summary, the correct boundary condition for zigzag edges requires the wave function to vanish on a single sublattice at each edge. In addition, it has been shown in Ref. [88] that there are surface states strongly localized near the edges which are non-vanishing only on a single sublattice. These states are called as zigzag edge states. They exist for very low energies and present an exponential decay of the wave function away from the edge.

2.4.2 Armchair boundary condition

For the considered lattice orientation as illustrated in Fig. 2.7(a), we have that the armchair edge is achieved when the terminations of the atoms lie along the one of the

green dashed lines that surround the hexagon. This type of termination is obtained for the angle positions given by 0° , 60° and 120° with respect to the x -axis, as depicted in Fig. 2.7(c). This means that every armchair orientation lies exactly between two successive zigzag orientations and vice versa. Note that in the case of armchair boundaries the number of carbon atoms in each side is an even number. In contrast to the zigzag case, now both sublattices are present at an armchair edge; more precisely, the edge atoms consist of a line of $A - B$ dimers, with one A - and one B -atom each. Therefore, as a natural consequence, the boundary condition is that the tight-binding wave function amplitude have to vanish on both sublattices (A - and B - wave function components should be zero). From Eqs. (2.54) and (2.55) for $\Psi_A = 0$ and $\Psi_B = 0$, the armchair boundary conditions become

$$\varphi_A(\vec{r}_B(s)) = -e^{i(\vec{K}' - \vec{K}) \cdot \vec{r}_B} \varphi_{A'}(\vec{r}_B(s)), \quad (2.57a)$$

$$\varphi_B(\vec{r}_B(s)) = -e^{i(\vec{K}' - \vec{K}) \cdot \vec{r}_B} \varphi_{B'}(\vec{r}_B(s)), \quad (2.57b)$$

where \vec{r} is taken at the position of the edge \vec{r}_B .

Notice that this relates the contributions from both K and K' points to each other, in other words, the armchair edge does couple the valleys, mixing the wave functions in K and K' Dirac points.

2.4.3 Infinite-mass boundary condition

As it was presented in previous subsections, the boundary conditions for zigzag and armchair type edges are derived from microscopic lattice termination for an abruptly terminated boundary due to the cutting atoms from the system. On the other hand, we can also think about a new type of boundary in such way that Dirac electrons can be confined by means of a potential. It is well known that semiconductor nanostructures, like quantum dots, rings and wires, are realized by using scalar potentials that are produced by voltage gates. However, for massless Dirac fermions it is in principle not possible to confine them in a restricted region with any configuration of a purely electrostatic (scalar) potential. As mentioned before, the reason is the lack of a gap in the bulk band structure and the resulting Klein tunneling.

A confining structure can be obtained by gap opening. This requires a violation of the equivalence of the sublattices. Therefore, if instead of a scalar potential $V(x, y)$ we consider a potential in a form

$$m(x, y) = \tau M(x, y) \sigma_z, \quad (2.58)$$

which has a different sign on each of the two sublattices due to the Pauli matrix σ_z , where $\tau = 1(-1)$ for the K (K') Dirac point, the energy spectrum indeed has a gap wherever $m(x, y)$ is non-zero. Physically, such a staggered potential can result from certain substrates, like boron nitride (h-BN) and SiC, that couple differently to A and

B sites [78, 92], *i. e.* this term represents a difference of potential energy between the A and B sites⁷. Considering the most simple case for a constant staggered potential, such as $M(x, y) = \Delta = \text{constant}$, then we have that the Hamiltonian (2.16) can be easily diagonalized resulting in the following energy spectrum, given by

$$E(\vec{k}) = \pm \sqrt{\hbar^2 v_F^2 k^2 + \Delta^2}. \quad (2.59)$$

One can notice that the above spectrum describe massive Dirac particles with a rest mass of Δ . This is the reason why this kind of potential, as described by Eq. (2.58), is called *mass term* or *mass potential*. Note that the including of this staggered potential leads to a gap of $2|\Delta|$ in the energy spectrum and, consequently, opens the possibility of its usage to effectively confine Dirac particles.

Let us now consider a surface S with outward unit normal vector $\vec{\mathbf{n}}$ as shown in Fig. 2.8 to deal with a more complicated mass term. The infinity-mass boundary condition in a monolayer graphene system is obtained when one considers mass as zero (infinity) inside (outside) of the confinement region. This model was developed by Berry & Mondragon even long before the discovery of graphene in order to describe confined neutrinos using the 2D Dirac equation [93]. Consequently, it is achieved when the local current must be such that there is no outward current at any point of the surface edge. This condition reads as

$$\vec{\mathbf{n}}(s) \cdot \vec{\mathbf{u}}(r) = 0, \quad (2.60)$$

where $\vec{\mathbf{n}}(s) = (\cos \alpha, \sin \alpha)$ and the local current $\vec{\mathbf{u}}(r)$ in state $\Psi = [\psi_A, \psi_B]^T$ is defined as the local expectation value of the current operator

$$\hat{\mathbf{u}} = \nabla_p H = v_F \vec{\sigma}. \quad (2.61)$$

The above equation can be rewritten after some algebraic manipulations as

$$\vec{\mathbf{u}}(r) = v_F (\psi_A^*, \psi_B^*) \vec{\sigma} \begin{pmatrix} \psi_A \\ \psi_B \end{pmatrix} = 2v_F [\Re\{\psi_A^* \psi_B\} \hat{x} + \Im\{\psi_A^* \psi_B\} \hat{y}]. \quad (2.62)$$

Using the Eqs. (2.60) and (2.62), and the definition of $\vec{\mathbf{n}}(s)$, we have that

$$\cos \alpha \Re\{\psi_A^* \psi_B\} + \sin \alpha \Im\{\psi_A^* \psi_B\} = 0. \quad (2.63)$$

We can split the above Eq. (2.63) as

$$\begin{aligned} \cos \alpha \Re\{\psi_A^* \psi_B\} &= -C \sin \alpha \cos \alpha, \\ \sin \alpha \Im\{\psi_A^* \psi_B\} &= C \sin \alpha \cos \alpha, \end{aligned} \quad (2.64)$$

leading to $\psi_A^* \psi_B = iC e^{i\alpha(s)}$. Since that C is an arbitrary constant, we can assume that $\psi_A^* \psi_B = i\psi_A^* \psi_A \tau e^{i\alpha(s)}$. Therefore, we finally find

$$\psi_B / \psi_A = i\tau e^{i\alpha(s)}, \quad (2.65)$$

⁷We have already mentioned briefly at the end of Sec. 2.1 about the staggered mass-related potential in Eq. (2.16).

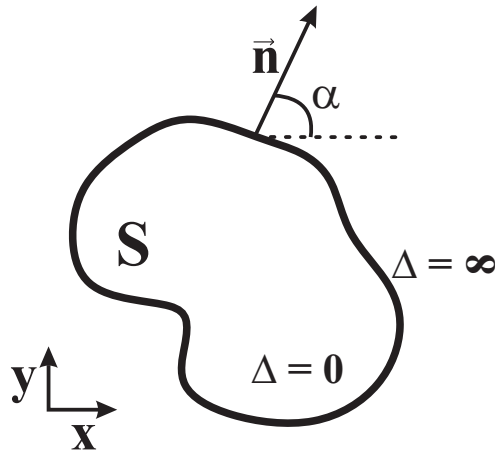


Figure 2.8: Surface S with an outward unit normal vector $\vec{\mathbf{n}}$ used to describe how to find the infinity-mass boundary condition used in order to confine carriers in a monolayer graphene. $\alpha(s)$ is the angle between the outward unit vector at the edges and the x -axis. Δ is the mass-related potential, which it is zero inside the arbitrary graphene quantum dot and infinity at its edges [93].

that is the infinity-mass boundary condition for monolayer graphene. Note that this boundary condition couples the A and B sublattices and moreover it is not invariant under the time-reversal operation [93]. τ is $1(-1)$ for the K (K') Dirac point. Due to the simplicity of implementation and possibility of obtaining analytical solutions, this infinite-mass boundary condition has been used in the study of circular graphene quantum dots [77] and rings [94, 95] in the absence and presence of a external perpendicularly magnetic field. Other different geometries, as triangular and hexagonal formats, have been already reported [96]. It is possible, because when using this infinite-mass boundary condition, the Klein tunneling effect at the interface between the internal and external regions of the confinement structure can be avoided and this way charge carriers can be confined.

2.5 *Split-operator method*

In the dynamic description of a particle by a Hamiltonian H , ones has the time-dependence of an initial wave function $\Psi(\vec{r}, t_0)$ given by

$$\Psi(\vec{r}, t) = \hat{U}(t, t_0)\Psi(\vec{r}, t_0), \quad (2.66)$$

where $\hat{U}(t, t_0)$ is known as the time evolution operator [97]. For the case in which the Hamiltonian does not depend explicitly of the time [97, 98], we have

$$\hat{U}(t, t_0) = \exp \left[-\frac{i}{\hbar} H(t - t_0) \right]. \quad (2.67)$$

In general, the exponential of Hamiltonian operator can not be solved exactly. Besides, in order to calculate the exponential of an operator which is given by sum of two or more

operators that do not commute with each other, one can not just rewrite the exponential as the product of exponentials of these operators, *i. e.*, $\exp[\hat{A} + \hat{B}] = \exp(\hat{A}) \exp(\hat{B})$ if and only if $[\hat{A}, \hat{B}] = 0$. Therefore, to address this problem, we will use the Split-operator technique [99, 100, 101, 102], that combines the separation between the Hamiltonian operators in exponentials that depend only on one of these operators, given by Masuo Suzuki [103] as

$$\exp \left[\epsilon \sum_{j=1}^q \hat{A}_j \right] = f_m(\hat{A}_1, \hat{A}_2, \hat{A}_3, \dots, \hat{A}_q) + \mathcal{O}(\epsilon^{m+1}), \quad (2.68)$$

and by the Cayley relation

$$\exp \left[\epsilon \hat{A} \right] = \left[1 - \frac{\epsilon \hat{A}}{2} \right]^{-1} \left[1 + \frac{\epsilon \hat{A}}{2} \right] + \mathcal{O}(\epsilon^4), \quad (2.69)$$

where $\mathcal{O}(\epsilon^m)$ represents the neglected terms, which have an error of order ϵ^m . The approximants functions f_m to $m = 1$ and 2 are:

$$f_1(\hat{A}_1, \hat{A}_2) = \exp[\epsilon \hat{A}_1] \exp[\epsilon \hat{A}_2], \quad (2.70)$$

$$f_2(\hat{A}_1, \hat{A}_2) = \exp \left[\frac{\epsilon \hat{A}_1}{2} \right] \exp[\epsilon \hat{A}_2] \exp \left[\frac{\epsilon \hat{A}_1}{2} \right], \quad (2.71)$$

$$f_1(\hat{A}_1, \hat{A}_2, \hat{A}_3) = \exp[\epsilon \hat{A}_1] \exp[\epsilon \hat{A}_2] \exp[\epsilon \hat{A}_3], \quad (2.72)$$

$$f_2(\hat{A}_1, \hat{A}_2, \hat{A}_3) = \exp \left[\frac{\epsilon \hat{A}_1}{2} \right] \exp \left[\frac{\epsilon \hat{A}_3}{2} \right] \exp[\epsilon \hat{A}_2] \exp \left[\frac{\epsilon \hat{A}_3}{2} \right] \exp \left[\frac{\epsilon \hat{A}_1}{2} \right]. \quad (2.73)$$

Applying this technique to Hamiltonians that do not involve spin, but only the terms of kinetic T and potential V energies ($H = T + V$), where T and V do not commute with each other, we find that

$$\exp \left[-\frac{i}{\hbar} H \Delta t \right] \cong \exp \left[-\frac{i}{2\hbar} V \Delta t \right] \exp \left[-\frac{i}{\hbar} T \Delta t \right] \exp \left[-\frac{i}{2\hbar} V \Delta t \right], \quad (2.74)$$

where the terms of $\mathcal{O}(\Delta t^3)$ order were neglected by considering a small time step Δt . Let us now discretize all involved functions in the space in order to implement this computationally (the potential V_i and the wave function Ψ_i). In this manner, we can multiply point-by-point the terms of the potential energy with the wave function, obtaining

$$\xi_i(r_i, t + \Delta t) = \exp \left[-\frac{i}{2\hbar} V_i \Delta t \right] \Psi_i(r_i, t). \quad (2.75)$$

Having ξ_i , the next step is to perform an operation involving kinetic energy term, to then obtain a new function η_i . To do this, maybe the most accessible way should be to take a Fourier transform of ξ_i , bringing this function to reciprocal space. But in fact, the most convenient one is to use Cayley form, Eq. (2.69), obtaining

$$\left(1 + \frac{i}{2\hbar} T \Delta t \right) \eta_i = \left(1 - \frac{i}{2\hbar} T \Delta t \right) \xi_i, \quad (2.76)$$

and then to discretize the derivatives of kinetic term by Crank-Nicolson form [104]. The resulting problem becomes a tridiagonal matrix equation that can be solved numerically through the TRIDAG subroutine [104]. Now, having in hands the η_i 's, then we can again multiply point-by-point the exponential that has the potential term, by the column matrix of the η_i 's.

Therefore, for problems with more than one dimension, one has just products of tridiagonal matrices, once that the potential energy terms can be directly multiplied and the total kinetic energy term can be divided into the product of exponential terms of its components. Performing this procedure several times in increments of Δt , we obtain the time evolution of the wave function for a particular proposed system.

This technique is computationally easy to apply and has been widely used in studies of wave packet propagation in semiconductor [105] and extended to the case of graphene structures by A. Chaves *et al.* [106]. We shall show briefly in the following sections the expansion of this technique for the Tight-binding and Dirac Hamiltonians.

2.5.1 *Tight-binding* Hamiltonian

A simple mathematical approach that has all the important aspects for the description of a lattice of atoms is known as *Kronig-Penney model* [107, 108, 109]. In this model, one approaches the potential of the crystal by a succession of rectangular potential wells and barriers with a periodicity that is identical to the lattice. Each well is this way an approximate representation of the potential produced by an ion.

For a one-dimensional lattice, we have that the periodic potential is formed as being many one-dimensional potential wells equally spaced. If the wells are infinitely deep, a particle would be completely located in one of the wells. Assuming that the particle is located in the i -th well, denoting the state by $|\Psi_i\rangle$, then $|\Psi_i\rangle$ is an eigenstate of the system with eigenvalue E_0 , such that $H|\Psi_i\rangle = E_0|\Psi_i\rangle$. As all the potential wells are identical and do not interact with each other, they all have the same energy values. Therefore E_0 would be an infinitely degenerate state. Otherwise, if the wells are finite, then the system eigenstate will be a linear combination of all $|\Psi_i\rangle$'s, because, since the barriers are finite, the particles have a finite tunneling probability. By completely neglecting the elements of H which are related to distant wells and just considering the influence of the nearest neighbors, we obtain the approximation known as *tight-binding* [97], *i. e.*

$$\langle\Psi_j|H|\Psi_i\rangle \neq 0, \quad \text{only if } j = i \text{ or } j = i \pm 1, \quad (2.77)$$

and

$$\langle\Psi_{i\pm 1}|H|\Psi_i\rangle = \tau_{i,i\pm 1}, \quad (2.78)$$

where τ_i (the hopping parameter) is the binding energy of the electron between the wells i and j . In this way, one obtains

$$H|\Psi_i\rangle \cong \tau_{i-1}|\Psi_{i-1}\rangle + E_0|\Psi_i\rangle + \tau_{i+1}|\Psi_{i+1}\rangle. \quad (2.79)$$

Let us now expand the tight-binding model for the description of a two-dimensional crystal. To do this, we will consider respectively i and j as the row and column indexes to locate a particular site in the lattice. So, one finds that

$$H|\Psi_{i,j}\rangle \cong (E_0 + V_{i,j})|\Psi_{i,j}\rangle + \tau_{i-1,j}|\Psi_{i-1,j}\rangle + \tau_{i+1,j}|\Psi_{i+1,j}\rangle + \tau_{i,j-1}|\Psi_{i,j-1}\rangle + \tau_{i,j+1}|\Psi_{i,j+1}\rangle. \quad (2.80)$$

Outlining the Hamiltonian obtained from one-dimensional and two-dimensional lattice in matrix form, we see that they will be represented by tridiagonal and pentadiagonal matrices in blocks, respectively. Thus, one can see the importance of using the Split-Operator technique in the numerical simplification of the problem for the case of graphene, since this structure is a two-dimensional crystal, which now can be dealt only with tridiagonal matrices, thus avoiding pentadiagonal matrices.

Finally, let us now develop the Split-operator method for systems described by tight-binding Hamiltonians in two dimensions. According to the procedure developed at the beginning of this section, we shall split the Hamiltonian to transform the problem of a pentadiagonal matrix in blocks to one problem involving only products of tridiagonal matrices, so that we can rewrite the Eq. (2.80) as follows

$$H|\Psi_{i,j}\rangle = H_i|\Psi_{i,j}\rangle + H_j|\Psi_{i,j}\rangle, \quad (2.81)$$

where the operators H_i and H_j are defined as

$$H_i|\Psi_{i,j}\rangle = \left(\frac{E_0 + V_{i,j}}{2} \right) |\Psi_{i,j}\rangle + \tau_{i,j-1}|\Psi_{i,j-1}\rangle + \tau_{i,j+1}|\Psi_{i,j+1}\rangle \quad (2.82)$$

and

$$H_j|\Psi_{i,j}\rangle = \left(\frac{E_0 + V_{i,j}}{2} \right) |\Psi_{i,j}\rangle + \tau_{i-1,j}|\Psi_{i-1,j}\rangle + \tau_{i+1,j}|\Psi_{i+1,j}\rangle. \quad (2.83)$$

Rewriting the time evolution operator in the same way as done in Eq. (2.74), we have that

$$\exp \left[-\frac{i}{\hbar} H \Delta t \right] = \exp \left[-\frac{i}{2\hbar} H_j \Delta t \right] \exp \left[-\frac{i}{\hbar} H_i \Delta t \right] \exp \left[-\frac{i}{2\hbar} H_j \Delta t \right] + \mathcal{O}(\Delta t^3). \quad (2.84)$$

The wave function at time step $t + \Delta t$ is then given by

$$|\Psi_{i,j}\rangle_{t+\Delta t} \cong \exp \left[-\frac{i}{2\hbar} H_j \Delta t \right] \exp \left[-\frac{i}{\hbar} H_i \Delta t \right] \exp \left[-\frac{i}{2\hbar} H_j \Delta t \right] |\Psi_{i,j}\rangle_t, \quad (2.85)$$

which can be developed in three steps

$$\eta_{i,j} = \exp \left[-\frac{i}{2\hbar} H_j \Delta t \right] |\Psi_{i,j}\rangle_t, \quad (2.86)$$

$$\xi_{i,j} = \exp \left[-\frac{i}{\hbar} H_i \Delta t \right] \eta_{i,j}, \quad (2.87)$$

$$|\Psi_{i,j}\rangle_{t+\Delta t} = \exp \left[-\frac{i}{2\hbar} H_j \Delta t \right] \xi_{i,j}, \quad (2.88)$$

where on the intersection of each step we will use the Cayley equation (Eq. (2.69))

$$\left(1 + \frac{i}{4\hbar}H_j\Delta t\right)\eta_{i,j} = \left(1 - \frac{i}{4\hbar}H_j\Delta t\right)|\Psi_{i,j}\rangle_t, \quad (2.89)$$

$$\left(1 + \frac{i}{4\hbar}H_i\Delta t\right)\xi_{i,j} = \left(1 - \frac{i}{4\hbar}H_i\Delta t\right)\eta_{i,j}, \quad (2.90)$$

$$\left(1 + \frac{i}{4\hbar}H_j\Delta t\right)|\Psi_{i,j}\rangle_{t+\Delta t} = \left(1 - \frac{i}{4\hbar}H_j\Delta t\right)\xi_{i,j}. \quad (2.91)$$

Thus, as already mentioned, the problem becomes simpler because now we should deal only with tridiagonal matrices.

2.5.2 Dirac Hamiltonian

As already presented earlier in section 2.1, the Dirac Hamiltonian, which describes the low-energy electronic states near the Dirac points (K and K') as massless Dirac fermions, is described by a Hamiltonian given in terms of Pauli matrices $\vec{\sigma}_i$ as given by Eq. (2.15), and in a more general way by Eq. (2.16).

The kinetic part of the Dirac Hamiltonian belongs to a special class of Hamiltonians that depend on the Pauli matrices in the form

$$H = \vec{S} \cdot \vec{\sigma}. \quad (2.92)$$

The main idea in this case to implement the Split-operator technique is split H_D into two terms such that, one of them should depend only on the coordinates of the real space, whereas the other should contains reciprocal space terms. Thus, for the more general Hamiltonian (2.16) we shall divide H_D in H_k , that has terms that depend only on the wave vector k , and in H_r , that contains only terms of real space coordinates, respectively given by:

$$H_k = \hbar v_f \vec{\sigma} \cdot \vec{k}, \quad (2.93)$$

and

$$H_r = -v_f e \vec{\sigma} \cdot \vec{A} + V \mathbf{I} + M \sigma_z. \quad (2.94)$$

However, rewriting the time evolution operator for the Hamiltonian H_D and performing the same procedure as done in Eqs. (2.74) and (7.7), we obtain

$$\exp\left[-\frac{i}{\hbar}H_D\Delta t\right] = \exp\left[-\frac{i}{2\hbar}H_r\Delta t\right] \exp\left[-\frac{i}{\hbar}H_k\Delta t\right] \exp\left[-\frac{i}{2\hbar}H_r\Delta t\right] + \mathcal{O}(\Delta t^3), \quad (2.95)$$

since H_k and H_r do not commute. Expanding each term in the exponential form

$$\exp\left[-i\vec{S} \cdot \vec{\sigma}\right] = \sum_n \frac{(-i\vec{S} \cdot \vec{\sigma})^n}{n!} = \sum_k \frac{(-1)^k (\vec{S} \cdot \vec{\sigma})^{2k}}{2k!} - i \sum_k \frac{(-1)^k (\vec{S} \cdot \vec{\sigma})^{2k+1}}{(2k+1)!}, \quad (2.96)$$

and using the following properties of Pauli matrices

$$\sigma_i \sigma_j = \mathbf{I} \quad [\sigma_i, \sigma_j] = 0, \quad (2.97)$$

it readily easy to see that

$$(\vec{S} \cdot \vec{\sigma})^{2k} = S^{2k} \mathbf{I} \quad (\vec{S} \cdot \vec{\sigma})^{2k+1} = S^{2k} (\vec{S} \cdot \vec{\sigma}). \quad (2.98)$$

Therefore, we can rewrite the expansion of the exponential, Eq. (2.96), in the form

$$\exp[-i\vec{S} \cdot \vec{\sigma}] = \begin{pmatrix} \cos(S) & 0 \\ 0 & \cos(S) \end{pmatrix} - i \frac{\sin(S)}{S} \begin{pmatrix} S_z & S_x - iS_y \\ S_x + iS_y & -S_z \end{pmatrix}. \quad (2.99)$$

Using the above expression for each exponential term of Eq. (2.95), it yields

$$\mathcal{M}_r = \exp\left[-\frac{i}{2\hbar} H_r \Delta t\right] = \begin{pmatrix} \cos(\varrho) & 0 \\ 0 & \cos(\varrho) \end{pmatrix} - i \frac{\sin(\varrho)}{\varrho} \begin{pmatrix} \mathbf{M} & A_x - iA_y \\ A_x + iA_y & -\mathbf{M} \end{pmatrix} e^{-\frac{i}{2\hbar} V \Delta t} \quad (2.100)$$

$$\mathcal{M}_k = \exp\left[-\frac{i}{2\hbar} H_k \Delta t\right] = \begin{pmatrix} \cos(\kappa) & 0 \\ 0 & \cos(\kappa) \end{pmatrix} - i \frac{\sin(\kappa)}{\kappa} \begin{pmatrix} 0 & \kappa_x - i\kappa_y \\ \kappa_x + i\kappa_y & 0 \end{pmatrix}, \quad (2.101)$$

where $\kappa = |\vec{\kappa}| = \Delta t v_f |\vec{k}|$, $\varrho = |\vec{\varrho}| = |(A_x, A_y, M)|$, $\vec{A} = \Delta t v_f e \vec{A} / 2\hbar$ and $\mathbf{M} = \Delta t M / 2\hbar$ are dimensionless units.

Finally, we can obtain the expression for the time evolution of the wave packet $\Psi_D(x, y) = [\phi_A, \phi_B]^T \Psi(x, y)$. As you can see, it is computed simply through matrix multiplications

$$\Psi(\vec{r}, t + \Delta t) = \mathcal{M}_r \cdot \mathcal{M}_k \cdot \mathcal{M}_r \Psi(\vec{r}, t) + \mathcal{O}(\Delta t^3). \quad (2.102)$$

In the matrix multiplication of the term \mathcal{M}_k , one must perform a Fourier transform of the functions in order to take the system in the reciprocal space.

Geometry and edge effects on the energy levels of graphene quantum rings a comparison between tight-binding and simplified Dirac models

We present a systematic study of the energy spectra of graphene quantum rings having different geometries and edge types, in the presence of a perpendicular magnetic field. Results are obtained within the tight-binding (TB) and Dirac models and we discuss which features of the former can be recovered by using the approximations imposed by the latter. Energy levels of graphene quantum rings obtained by diagonalizing the TB Hamiltonian are demonstrated to be strongly dependent on the rings geometry and the microscopical structure of the edges. This makes it difficult to recover those spectra by the existing theories that are based on the continuum (Dirac) model. Nevertheless, our results show that both approaches (i. e. TB and Dirac model) may provide similar results, but only for very specific combinations of ring geometry and edge types. The results obtained by a simplified model describing an infinitely thin circular Dirac ring show good agreement with those obtained for hexagonal and rhombus armchair graphene rings within the TB model. Moreover, we show that the energy levels of a circular quantum ring with an infinite mass boundary condition obtained within the Dirac model agree with those for a ring defined by a ring-shaped staggered potential obtained within the TB model.

3.1 Motivation

Graphene, a two-dimensional lattice of carbon atoms [18], has been a subject of great interest during the past few years. This interest is not only due to its possible future technological applications, but also because it provides the possibility to probe interesting phenomena predicted by quantum field theories. Several of the exotic properties originate from the fact that low energy electrons in graphene obey the zero mass Dirac equation. (for a review, see e. g. Ref. [1])

Previous works have demonstrated interesting features coming from ring- and dot-like confinement in graphene.[96, 110, 111, 112, 113, 114, 115] Theoretical studies have

predicted Aharonov-Bohm (AB) oscillations in both the conductance [116] and the energy spectrum [117] of graphene quantum rings. In fact, AB conductance oscillations were observed in recent experiments on several circular rings fabricated in few-layer graphene. [118] Luo et al. [119] demonstrated theoretically that the energy spectrum of armchair quantum rings exhibits signatures of an effective time-reversal symmetry breaking, where a gap around zero energy, which can be removed by applying an external magnetic field, is observed.

From the point of view of the continuum model, where electrons are described as massless Dirac fermions, several models have been suggested for studying the confined states of graphene quantum rings. For instance, Recher et al. [94] have used the Dirac model to show that the combined effects of a ring shaped mass-related potential and an external magnetic field can be used to break the valley degeneracy in graphene. A similar effect was also found by Wurm et al. [120], where it was theoretically demonstrated that the splitting of the valley degeneracy by a magnetic field in such a system can also be observed in the transport properties of rings that are weakly coupled to leads. The analytical solution for the graphene ring proposed in Ref. [94] was used latter by Abergel et al. [95] to study the interplay between valley polarization and electron-electron interactions on some measurable quantities in such a structure, where they observe, e. g., extra steps in the persistent current as a function of an external magnetic field. A recent paper [121] proposed a simplified model for obtaining energy levels in graphene quantum rings, based on an idea widely used for semiconductor quantum rings, [122] where the radial component of the momentum of the confined particle is assumed to be zero, so that the effective Hamiltonian of the system depends only on the angular coordinate. This model has been recently used, e. g. for the study of wave packet revivals in monolayer and bilayer graphene rings. [123]

Notice that the continuum model for graphene is developed by considering a periodic honeycomb lattice of carbon atoms of infinite size and by analysing only the low energy sector of the corresponding tight-binding Hamiltonian. However, the experimentally obtained graphene quantum rings reported in the literature are normally fabricated by cutting out the graphene flake into a finite size ring shaped structure. In order to take the finite size effects into account within the Dirac theory, the above mentioned previous papers have usually considered either infinite mass boundary conditions, or a “frozen” radial motion of the particles. But it is questionable that these conditions are really sufficient in order to describe a real graphene ring sample. If so, what are the limits of such approximations? Answering these questions is the main purpose of this paper, where we use the tight-binding model (TBM) to calculate the energy spectrum of graphene quantum rings with different geometries and different type of edges. We then discuss the main qualitative features of the obtained spectra in terms of the continuum (Dirac) approximation, making a comparison between the results obtained by such an approximation and those obtained by the TBM. Our results from tight-binding calculations

show that the energy spectra of these systems strongly depend on the detailed structure of the edges, which makes it difficult to find analytical solutions for the energy states in these systems within the continuum model. Circular rings cut out of a graphene sheet exhibit mixed armchair and zigzag edges, and the latter leads to strongly confined edge states, which significantly affects its energy spectrum. The AB oscillations in the energy spectra for other geometries of quantum rings, where one can obtain uniform edge type, exhibit geometry-specific n -fold energy sub-bands, and in some cases, the qualitative features of the spectrum are shown to depend even on the alignment between inner and outer edges of the ring. Even so, we demonstrate that under specific conditions, one can still use the proposed simplified model [121] to obtain analytically the main qualitative features of the energy spectra of armchair rings, or use the analytical solution proposed in Ref. [94] to observe some features exhibited by the energy spectrum obtained by the tight-binding model for a mass-related ring confinement, as we will discuss in further detail in the following sections.

The present paper is organized as follows. In Sec. 3.2 we briefly present an outline of the TBM and the investigated graphene rings. An approximate analytical solution is obtained for a simplified model within the Dirac approach in Sec. 3.3. Our numerical results from TBM and the analytical ones from the simplified Dirac model are shown in Sec. 3.5. A summary and concluding remarks are reported in Sec. 3.5.

3.2 Tight-Binding model

Graphene consists of a honeycomb lattice of carbon atoms, which can be described by the Hamiltonian

$$H_{TB} = \sum_i (\epsilon_i + M_i) c_i^\dagger c_i + \sum_{\langle i,j \rangle} \left(\tau_{ij} c_i^\dagger c_j + \tau_{ij}^* c_i c_j^\dagger \right), \quad (3.1)$$

where c_i (c_i^\dagger) annihilates (creates) an electron in site i , with on-site energy ϵ_i , and the sum is taken only between the nearest neighbors sites i and j , with hopping energy τ_{ij} . Due to the Klein tunnelling effect in graphene, it is hard to confine electrons by applying an external potential. [124, 125] On the other hand, a staggered site-dependent potential M_i , which is positive (negative) if i belongs to the sublattice A (B), [126] opens a gap in the energy spectrum of graphene. Due to this property, such a potential is normally used to simulate confining structures in graphene, such as quantum dots [77] and rings [94], within the Dirac model, where it appears as a mass-related term. Recent papers have suggested a way to realize such a potential experimentally, namely, by depositing the graphene lattice over specific substrates. [78, 92, 127] The effect of an external magnetic field can be introduced in the TB model by including a phase in the hopping parameters according to the Peierls substitution $\tau_{ij} \rightarrow \tau_{ij} \exp \left[i \frac{e}{\hbar} \int_j^i \vec{A} \cdot d\vec{l} \right]$, where \vec{A} is the vector potential describing the magnetic field. [128, 129] In the presence of a perpendicular magnetic field

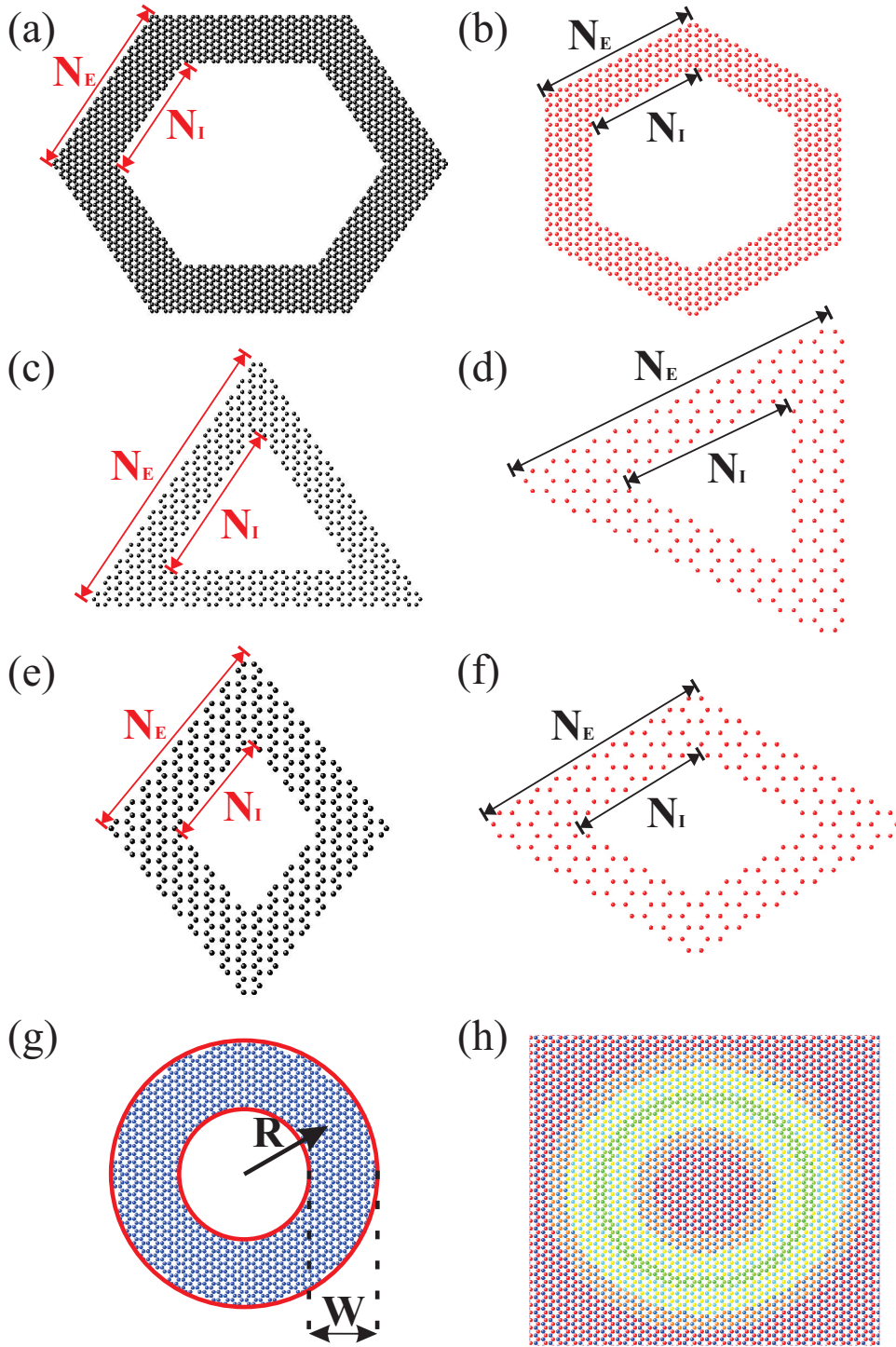


Figure 3.1: Sketch of (a, c, e) armchair and (b, d, f) zigzag rings, with hexagonal, triangular and rhombus geometries respectively, as well as (g, h) circular rings, considered in this work. The first six geometries are characterized by the number of carbon rings $N_E(N_I)$ in their outer (inner) edge. Circular rings are characterized by their width W and average radius R . (g) Circular ring defined by cutting the graphene lattice. (h) Circular graphene ring defined by a smooth ring-shaped staggered potential M_i , where the color scale goes from $M_i = -M_0$ (red) to $M_i = +M_0$ (blue), and the $M_i = 0$ region inside the ring is represented in green. The atoms belonging to sublattices A and B have different colors because of the staggered potential profile.

$\vec{B} = B\hat{z}$, we conveniently choose the Landau gauge $\vec{A} = (0, Bx, 0)$, so that the Peierls phase becomes zero in the x -direction and $\exp\left[i\frac{2\pi x}{3a}\frac{\Phi}{\Phi_0}\right]$ in the y -direction, where $a = 1.42 \text{ \AA}$ is the lattice parameter of graphene, $\Phi_0 = h/e$ is the magnetic quantum flux and $\Phi = 3\sqrt{3}a^2B/2$ is the magnetic flux through a carbon hexagon.

We write the Hamiltonian (3.1) in matrix form, diagonalize it numerically and obtain the energy spectrum for the different ring geometries schematically shown in Fig. 1: hexagonal, triangular and rhombus-shaped rings, with (a, c, e) armchair and (b, d, f) zigzag edges. We also consider circular rings defined by cutting the graphene lattice (g), or by considering a circular-shaped staggered potential (h). The edges of such circular rings exhibit an admixture of zigzag and armchair regions and are not singly defined. The ring-shaped staggered potential in Fig. 1(h) is given by

$$M_i(r_i) = \pm M_0[2 + \tanh(r_i^+) + \tanh(r_i^-)] \quad (3.2)$$

where $r_i^+ = (r_i - R - W/2)/S$ and $r_i^- = (-r_i + R - W/2)/S$, S is the width of the smooth region and $r_i = \sqrt{x_i^2 + y_j^2}$ is the position of the i -th site of the lattice. Such a staggered potential goes smoothly to zero (M_0) inside (outside) the ring region, avoiding edge-related effects.

Probability density currents within the TB model are numerically calculated based on the method developed in Ref. [130], where one defines the probability current \vec{j} in terms of the continuity equation and, after some calculations, obtain the current components in x and y directions for each site, which is defined by its line (n) and column (m) position in the lattice (see Ref. [131]), as

$$j_x(n, m) = \pm \frac{a}{\hbar} \left\{ 2\Im [\Psi_{n,m} \Psi_{n,m\pm 1}^* \tau_{n,m\pm 1}] - \Im [\Psi_{n,m} \Psi_{n-1,m}^* \tau_{n-1,m}] - \Im [\Psi_{n,m} \Psi_{n+1,m}^* \tau_{n+1,m}] \right\} \quad (3.3)$$

and

$$j_y(n, m) = \frac{\sqrt{3}a}{\hbar} \left\{ \Im [\Psi_{n,m} \Psi_{n+1,m}^* \tau_{n+1,m}] - \Im [\Psi_{n,m} \Psi_{n-1,m}^* \tau_{n-1,m}] \right\} \quad (3.4)$$

where the \mp sign in j_x will be positive (negative) if the (n, m) -site belongs to the sublattice A (B), and $\tau_{n,m}$ is the hopping parameter which, in the presence of a magnetic field, includes an additional phase according to the Peierls substitution.

3.3 Continuum model

The energy spectrum of an infinite graphene sheet in the absence of external potentials and magnetic field, as obtained from the TBM Hamiltonian (3.1), is gapless in six points of the reciprocal space, from which only two are inequivalent, labelled as K and K' .

[1, 132] In the vicinity of each of these points, the energy depends linearly on the wave vector \vec{k} and the electron behaves as a quasi-particle described by the Dirac Hamiltonian

$$H_D = \left[v_F \vec{\sigma} \cdot (\vec{\mathbf{p}} + e\vec{A}) + V(\vec{r})\mathbf{I} + \gamma M(\vec{r})\sigma_z \right], \quad (3.5)$$

where $v_F = 3\tau a_0/2\hbar$ is the Fermi velocity, \vec{A} is the electromagnetic vector potential, $V(x, y)$ is an external potential, \mathbf{I} is the identity matrix and $\vec{\sigma}_i$ denotes the components of the Pauli matrices. The eigenstates of the Hamiltonian (3.5) are the two-component spinors $\Psi = [\Psi_A, \Psi_B]^T$, where $\Psi_{A(B)}$ are the envelop functions associated with the electron probabilities in $A(B)$ sublattices.

The site-dependent staggered potential M_i in the TB Hamiltonian (3.1) contributes to the Dirac Hamiltonian as a mass-related potential $M(\vec{r})$, which is multiplied by a factor $\gamma = 1$ (-1) for the K (K') Dirac point in Eq. (3.5). Considering the mass as zero (infinity) inside (outside) of the confinement region yields the infinity-mass boundary condition $\Psi_B(\vec{r})/\Psi_A(\vec{r}) = i\gamma e^{i\theta}$, where θ is the angle between the outward unit vector at the boundaries and \vec{r} (i. e. $\theta = 0$ ($\theta = \pi$) at outer (inner) boundaries of the ring). [93]

Let us now consider a simplified model of a circular graphene ring in order to find an approximate analytical solution for the energy spectrum of graphene quantum rings that agrees with those obtained within the TBM. In the absence of an external potential and around the K point ($\gamma = 1$), [133] the Hamiltonian (3.5) in polar coordinates reads

$$H_D = \hbar v_F \begin{bmatrix} \frac{M}{\hbar v_F} & -i \left(\Pi_r^* + e^{-i\phi} \frac{\pi r B}{\Phi_0} \right) \\ -i \left(\Pi_r - e^{i\phi} \frac{\pi r B}{\Phi_0} \right) & -\frac{M}{\hbar v_F} \end{bmatrix}, \quad (3.6)$$

where $\Pi_r = e^{i\phi} \left(\frac{\partial}{\partial r} + \frac{i}{r} \frac{\partial}{\partial \phi} \right)$. We assume that the width of the ring approaches zero and therefore the momentum should be frozen in the radial direction. From the definition of the radial momentum operator [134] in cylindrical coordinates

$$\mathbf{p}_r = \frac{1}{2}(\mathbf{p}_r \cdot \hat{\mathbf{r}} + \hat{\mathbf{r}} \cdot \mathbf{p}_r) = \frac{\partial}{\partial r} + \frac{1}{2R}, \quad (3.7)$$

where $\hat{\mathbf{r}}$ is the unitary vector in the radial direction and R is the ring radius, we obtain $\partial/\partial r \rightarrow -1/2R$, as $\hat{p}_r \rightarrow 0$ and $r \rightarrow R$. Then, the simplified Hamiltonian for the graphene quantum ring is

$$H_D = \begin{bmatrix} \bar{M} & -e^{-i\phi} \left(\frac{d}{d\phi} + i \frac{\Phi_R}{\Phi_0} - \frac{i}{2} \right) \\ e^{i\phi} \left(\frac{d}{d\phi} + i \frac{\Phi_R}{\Phi_0} + \frac{i}{2} \right) & -\bar{M} \end{bmatrix}, \quad (3.8)$$

where $\Phi_R = \pi R^2 B$ is the magnetic flux through the quantum ring, the energy is in units of $E_0 = \hbar v_F/R$ and $\bar{M} = M/E_0$.

Notice that the definition of the radial momentum in Eq. (3.7) was first used by Aronov and Lyanda-Geller [135] in 1993 for the study of Schrödinger electrons in a quantum ring with Rashba spin-orbit interaction. [1] However, they mistakenly defined the radial

momentum as $\mathbf{p}_r = \frac{\partial}{\partial r}$, which leads to $\frac{\partial}{\partial r} \rightarrow 0$ as the radial momentum approaches zero. Due to this wrong assumption, they ended up with a non-Hermitian Hamiltonian for this system. The non-Hermiticity of this Hamiltonian was eliminated *artificially* in sub-sequent papers, [136, 137] by assuming an additional term $-1/2R$ in the off-diagonals of the Hamiltonian. A physical explanation for such a term was given almost ten years later in a work by Meijer et al. [122], where the authors split the Hamiltonian into two parts, one for the radial confinement and the other for the Rashba interaction, and used the eigenfunctions of the radial part to show that the average value of the radial first derivative term in the Rashba Hamiltonian is $\langle \partial/\partial r \rangle = -1/2R$. However, this is not the most general way to explain this term and such an explanation does not help for the graphene ring Hamiltonian (3.6), since in this case we cannot split the Hamiltonian and obtain a separate radial confinement term. Using Eq. (3.7), on the other hand, one obtains the result found by Meijer et al. in a more natural way, showing that the identity $\langle \partial/\partial r \rangle = -1/2R$ is actually a consequence of the zero radial momentum. Our derivation of the graphene ring Hamiltonian in Eqs. (3.6-6.6) shows that if one simply defines the radial momentum properly, the correct expression for the radial derivatives and, consequently, an Hermitian Hamiltonian will appear naturally from the derivation. It is straightforwardly seen that the same happens in the derivation of the Rashba interaction Hamiltonian for quantum rings.

The eigenstates of the Hamiltonian (6.6) are found as $\Psi_l = [A_l e^{il\phi}, iB_l e^{i(l+1)\phi}]^T$, with eigenenergies

$$E = \pm \sqrt{\left(l + \frac{\Phi_R}{\Phi_0} + 1\right) \left(l + \frac{\Phi_R}{\Phi_0}\right) + \frac{1}{4} + \bar{M}^2}, \quad (3.9)$$

where l is the angular momentum index.

3.4 Results and discussion

3.4.1 Comparison between tight-binding and Dirac models

Firstly, let us investigate the energy spectrum of graphene quantum rings, with various shapes and edge types, obtained by the TBM, focusing on the search for energy spectra that can be satisfactorily described by the continuum model. With this purpose, we first demonstrate that for a rhombus-shaped ring with armchair edges, a strong dependence of the energy spectrum on the edge alignment is observed in Fig. 3.2 for $N_E = 17$, considering $N_I = 12$ (a), where the inner and outer edges are anti-aligned, and $N_I = 11$ (b), where the edges are aligned. In the former case, one obtains very regular oscillations as the magnetic field increases, for a wide range of energies. High and irregular energy differences between the excited states are found in the latter (aligned) case, as compared to the smaller and more regular separations between energies of the eigenstates of the system with anti-aligned edges. In both cases, the spectrum exhibits two-fold bands of

oscillating energies, separated by anti-crossings, even in the higher energy region, as shown in the insets.

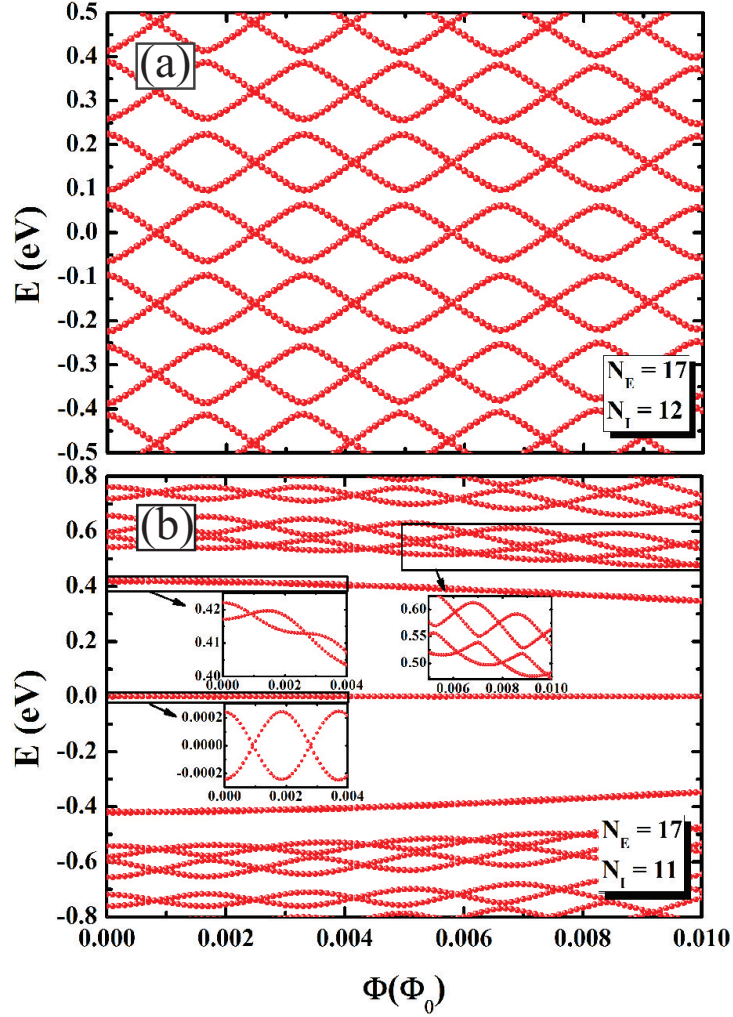


Figure 3.2: Energy levels of armchair rhombus quantum rings, schematically shown in Fig. 1(e), as a function of the magnetic flux through a single carbon hexagon for two ring widths: (a) $N_E = 17$, $N_I = 12$ and (b) $N_E = 17$, $N_I = 11$. As shown in the insets, the energy spectrum does not have a zero-energy state: states close to $E = 0$ are rather similar to the first states above and below this energy, which are composed by branches of two oscillating energy states.

Figure 3.3 shows that hexagonal armchair quantum rings also share the same kind of spectrum as the anti-aligned armchair rhombus-shaped ring in Fig. 3.2(a), though in the hexagonal case, the spectrum does not depend on the edges alignment, but only on the ring width. The spectra exhibit crossings and anti-crossings, which separate them into six-fold energy bands. A similar spectrum was also obtained in Ref. [138], but the focus of this previous work was on the inner and outer edge distribution of the eigenfunctions, so that details of the spectrum, e.g. its dependence on the ring width and the persistent current profile of the energy states at non-zero magnetic field, were not investigated.

Notice that changing the number of carbon hexagons in the inner edge N_I and keeping N_E fixed, one effectively changes the width of the ring. Considering a larger ring width, with $N_E = 15$ and $N_I = 3$, as shown in Fig. 3.3(b), the energy spectrum is more strongly affected by the magnetic field, so that the regular set of crossings and anti-crossings in Fig. 3.3 (a) is no longer observed in this case. Nevertheless, the qualitative features observed in Fig. 3.3(a), including the gap around $E = 0$ for zero magnetic field, are present for all ring widths. This is surprising, since in armchair nanoribbons, the character of the system oscillates between metallic and insulating as the width changes. [88] Although the armchair ring in Fig. 3.3(a) is made just by connecting six armchair nanoribbons, the qualitative features of such ribbons are not directly transferable to the quantum ring case, which suggests that the ring geometry and the ribbons connections are playing a major role in these systems. [119]

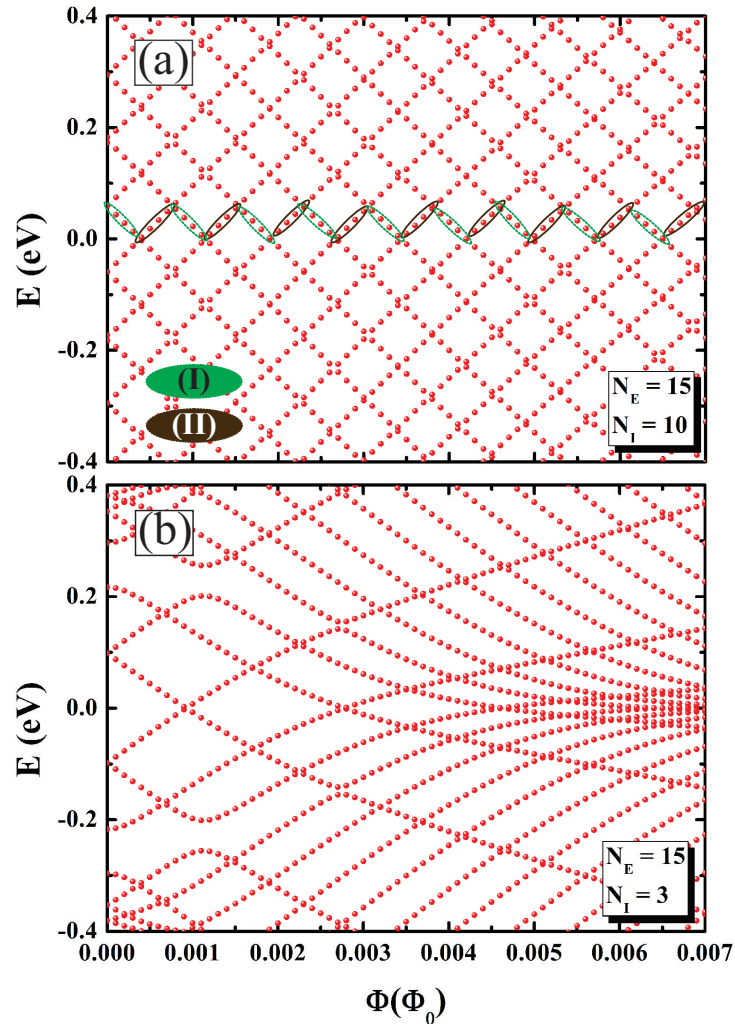


Figure 3.3: Energy levels of armchair hexagonal quantum rings, schematically shown in Fig. 1(a), as a function of the magnetic flux through a single carbon hexagon for two ring widths: (a) $N_E = 15$, $N_I = 10$ and (b) $N_E = 15$, $N_I = 3$. The spectrum is symmetric with respect to $E = 0$.

Notice that the energy spectra obtained by the TBM either in the case of a rhombus-shaped armchair ring with anti-aligned edges in Fig. 3.2(a), or for hexagonal armchair rings, specially the one with smaller width in Fig. 3.3(a), resembles the AB oscillations for ideal quantum rings reported, e. g. in Fig. 3(a) of Ref. [121]. These structures are then good candidates to be well described by the simplified Dirac model for quantum rings, developed in Sec. II of the present paper and in Ref. [121].

Thus, let us investigate the spectra in Figs. 3.2(a) and 3.3(a) with more details. Notice that both spectra exhibit a gap around $E = 0$ in the absence of a magnetic field, but the $E = 0$ states are found for specific values of the magnetic flux, which are almost equally spaced in flux. This is reminiscent of the energy spectrum for Schrödinger electrons confined in quantum rings under perpendicular magnetic fields, [139, 140, 141] where the energy oscillates periodically with the magnetic flux, due to the Aharonov-Bohm effect. Similar to the AB effect in semiconductor quantum rings, the energy oscillations in Fig. 3.3(a) can also be linked to transitions between states with clockwise and counter-clockwise persistent currents, as one can observe in the probability density current plots in Fig. 3.4. The current for the lowest energy state with decreasing (increasing) energy as the magnetic field increases, which are marked by green (brown) ellipses labelled as I (II) in Fig. 3.3(a), are found to be in (counter-)clockwise direction in Fig. 3.4.

As a matter of fact, assuming a Dirac fermion constrained to move in a circle that is thread by the same magnetic flux as the rhombus or the hexagon, i. e. that encloses the same area as these geometries, as illustrated in Figs. 3.5(a) and 3.6(a), respectively, and performing the analytical calculations for AB oscillations in the continuum model proposed in Sec. III, one obtains almost the same spectra as obtained by the TBM for the respective structures. This is demonstrated in Figs. 3.5(b) and 3.6(b) for the rhombus-shaped and hexagonal rings, respectively, where the dashed lines are obtained by the TBM, whereas the solid lines are for a massless Dirac fermion in a circle of radius R . By comparing both models, one observes that: i) the energy gap reaches a maximum value $E = \hbar v_F/R$ at $\Phi_R = n\Phi_0$ (n integer) and ii) the system is gapless for $\Phi_R = (n + 1/2)\Phi_0$. Better agreement between the models is observed for lower energies and magnetic fields, where the effects of the curvature of the energy bands and the finite width of the TBM sample are less important.

The main advantage of the simplified analytical model for these systems is to predict effects and results just by analysing the solutions of the model, without effectively solving the TBM equation, which may require high computational costs. Let us then consider the case of a ring deposited over a substrate that provides a constant mass-related potential $M = 0.5E_0$. Notice that this is still not the case proposed in Fig. 3.1(h), since in the present case we have a constant mass term M , instead of the space-dependent potential $M_i(r_i)$ of Eq. (3.2). The simplified model for a $M = 0.5E_0$ in a circle of radius R predicts that such a mass term is responsible for a minimum gap of E_0 in the energy spectrum at $\Phi_R = (n + 1/2)\Phi_0$, as shown by the solid lines in Figs. 3.5(c) and 3.6(c) for the

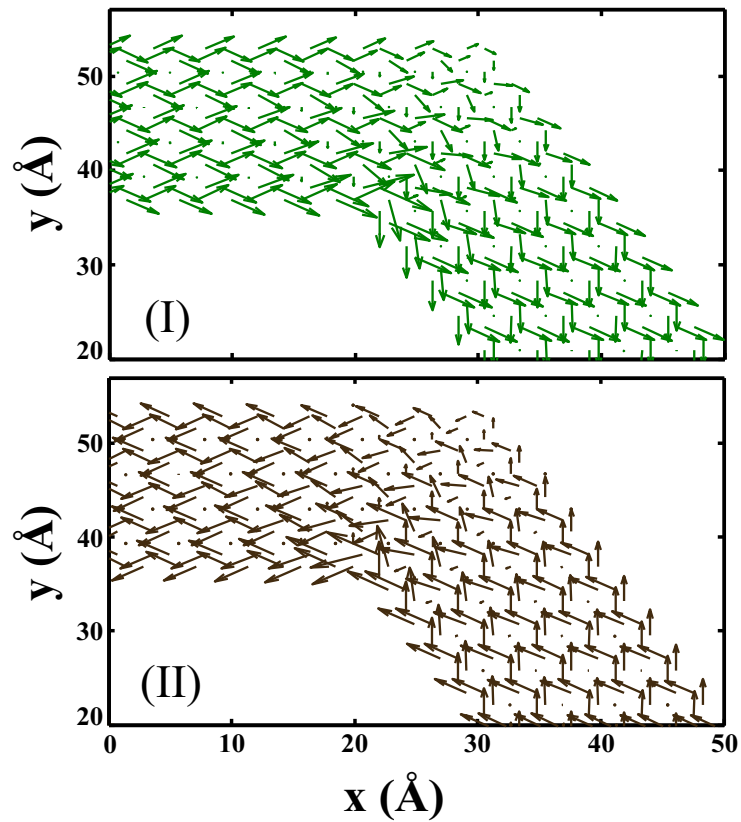


Figure 3.4: Current density profile for an armchair hexagonal quantum ring corresponding to magnetic flux indicated by (I) and (II) in Fig. 3.3(a). The results for the current density are numerically calculated based on the method discussed in Refs. [130], [142] and reproduced in the present manuscript.

rhombus-shaped and hexagonal rings, respectively. Such prediction is indeed confirmed by the results from the TBM (dashed lines) for the respective site-dependent potentials, which exhibit very good agreement with the continuum model results.

The simplified continuum model also predicts that, in the absence of magnetic field, the energy levels converge to \bar{M} as the ring radius is enlarged, and diverge as $E \approx v_F \hbar |l + 1/2|/R$ for small radii, which can be inferred from Eq. (3.9). However, for non-zero magnetic field, the energies are expected to increase almost linearly with the radius, since Eq. (3.9) can be approximated by $E = \sqrt{(\alpha R)^2 + M^2}$, with $\alpha = v_F e B / 2$, as $R \rightarrow \infty$ in this case. This is illustrated by the solid lines in Fig. 3.7, which represent the energy levels, obtained by the simplified continuum model, as a function of the ring radius, for a circular ring with a substrate induced potential $M = 0.1$ eV, considering different values of magnetic flux. The results obtained by the TBM for an armchair hexagonal ring are computed by varying the number of external carbon rings N_E , but keeping the ring width constant ($N_I = N_E - 5$), we obtain the dimensions $L_E = (3N_E - 2)a$ and $L_I = (3N_I - 1)a$ and the average radius $R = \left(\frac{3\sqrt{3}}{2\pi} \left(\frac{|L_E + L_I|}{2} \right)^2 \right)^{1/2}$, such that we can relate to the radius of the simplified model. The TB results are shown by the dashed lines and exhibit almost perfect agreement with the analytical results, both qualitatively and quantitatively. In both models, the ground state energy would converge to $E = 0$ for large radius if it were not for the gap opened by a background mass term considered in this case, which keeps electron and hole bands from touching each other even for larger radii.

It is however important to point out that the comparison between the models in Figs. 3.4-3.7 is performed for narrow widths of the quantum ring. As previously mentioned, Fig. 3.3(b) demonstrates that larger ring width leads to a stronger dependence of the energy spectrum on the magnetic field, which harms the similarities between the energy spectra obtained by the TBM and the Dirac model. Indeed, the armchair nature of the edges helps the electron to stay in the middle of the rings arms, since this kind of edge type does not allow for edge states, while the narrow width of the ring leads to the “frozen” motion in the radial direction, which makes systems with such narrow width more suitable to be described as an ideal ring in the simplified Dirac model proposed here.

Finally, let us now discuss how the Dirac model compares to the TBM for a finite width circular graphene ring. The difficulty in this case lies in the fact that one must consider the appropriate boundary conditions in order to properly describe the zigzag and armchair edges in this structure. [90] For the circular ring cut out from a graphene sheet, as shown in Fig. 3.1(g), although the circular symmetry provides an easy way to study the problem by a one-dimensional (radial) equation, the boundary conditions are still too complicated for an analytical treatment of this system, since they are an admixture of zigzag and armchair edges. The energy spectrum obtained by the TBM for the circular ring schematically illustrated in Fig. 3.1(g) is presented in Fig. 3.8(a) as a function of the magnetic flux $\Phi_R = \pi R^2 B$ threading the average ring radius $R = 80$ Å. Due to the circular symmetry, the energy bands are two-folded and exhibit AB oscillations as the

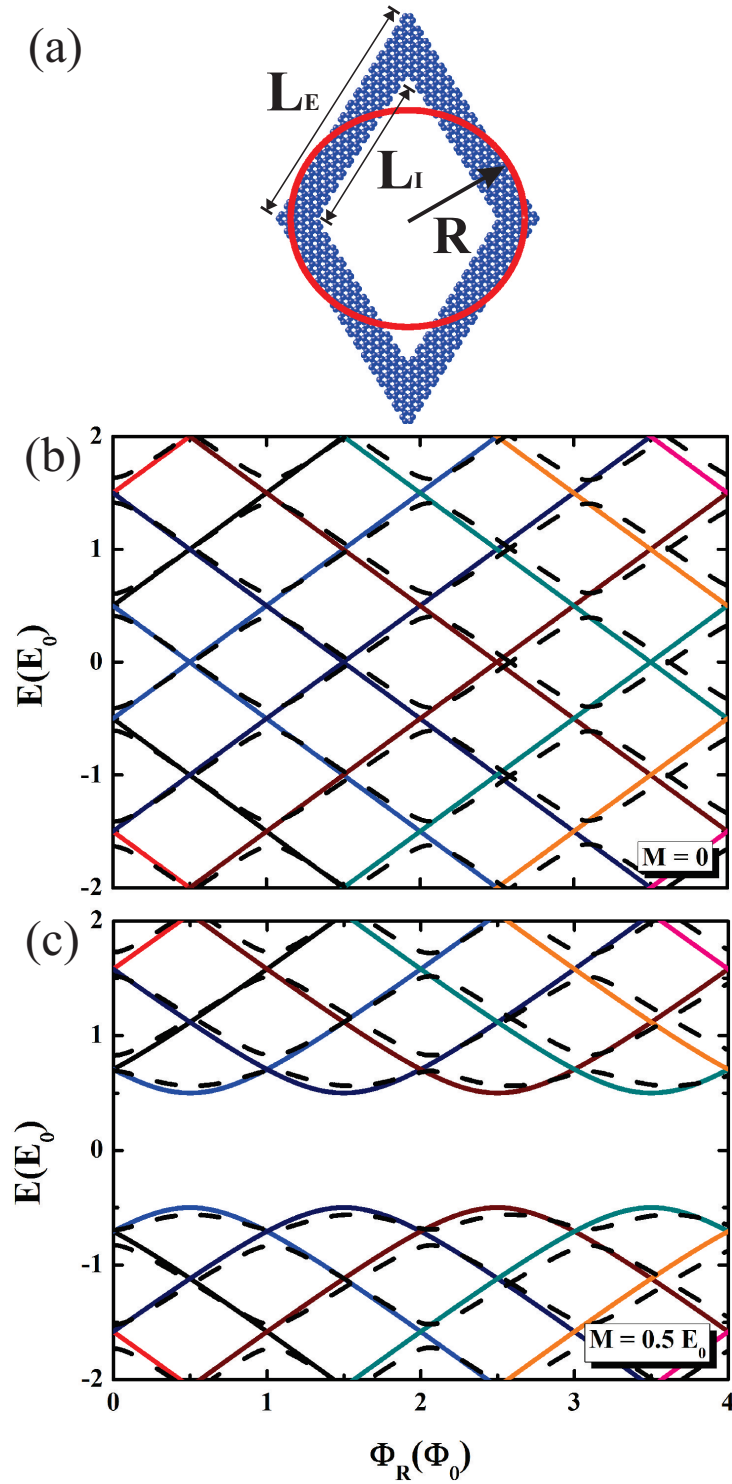


Figure 3.5: (a) Rhombus armchair quantum ring (blue polygon figure) considered in the TB calculation, with $N_E = 17$ and $N_I = 12$, along with the one-dimensional $R \approx 32.3\text{\AA}$ ring (red circle) considered in the simplified model. (b) Energy spectra, obtained from the simplified (solid lines) and TB (dashed lines) models, as a function of the magnetic flux threading the red circle illustrated in (a). Curves with different colors represent different angular momentum index l . (c) The results from the TB model with a background mass term $M = 0.5E_0$ are also compared to those from the simplified model in this case.

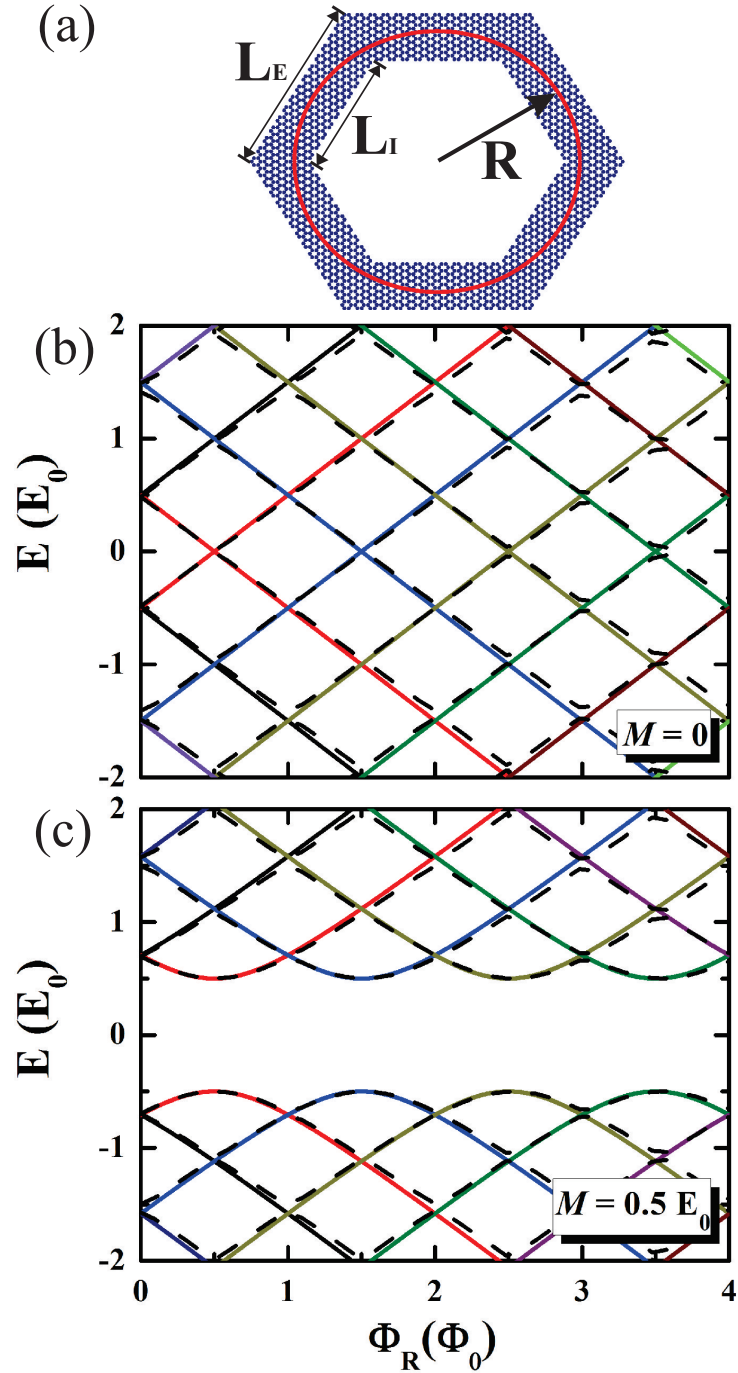


Figure 3.6: (a) Hexagonal armchair quantum ring (blue polygon figure) considered in the TB calculation, with $N_E = 15$ and $N_I = 10$, along with the one-dimensional $R \approx 47\text{\AA}$ ring (red circle) considered in the simplified model. (b) Energy spectra, obtained from the simplified (solid lines) and TB (dashed lines) models, as a function of the magnetic flux threading the red circle illustrated in (a). Curves with different colors represent different angular momentum index l . (c) The results from the TB model with a background mass term $M = 0.5E_0$ are also compared to those from the simplified model in this case.

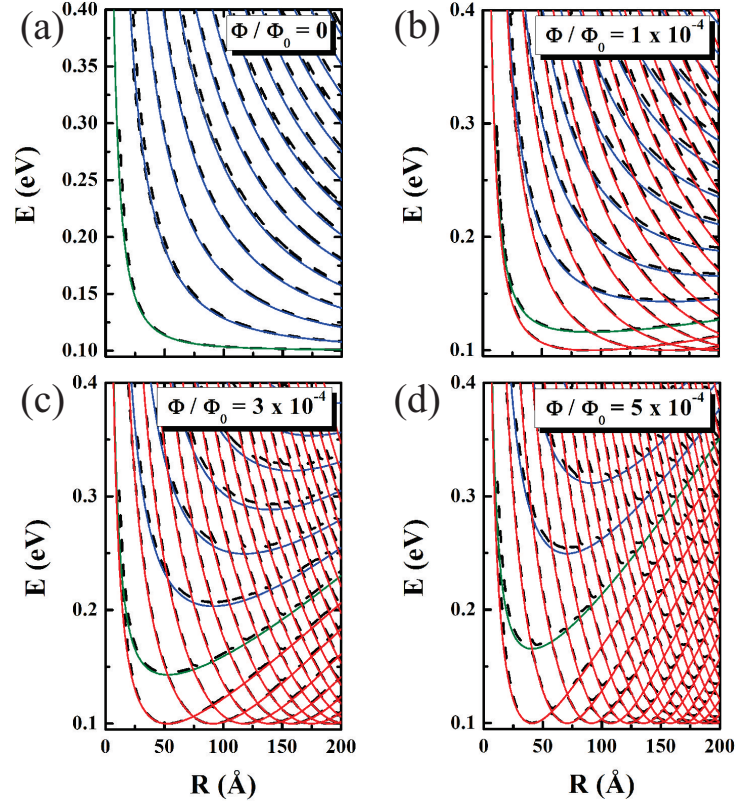


Figure 3.7: Energy levels of armchair hexagonal quantum ring, obtained from the simplified (solid) and TB (dashed) models, as function of ring radius R , calculated assuming an average radius given by $R = \left(\frac{3\sqrt{3}}{2\pi} \left(\frac{|L_E + L_I|}{2} \right)^2 \right)^{1/2}$ and mass term $M = 0.1$ eV, for different values of the magnetic flux Φ/Φ_0 . Curves with green, red and blue colors represent angular momentum index l zero, negative and positive, respectively. The spectrum is symmetric with respect to $E = 0$.

magnetic flux increases, which are not perfectly periodic in Φ_R due to the finite width $W = 60 \text{ \AA}$ of the system. The energy spectrum for a similar system was investigated in Ref. [138], but there, the two-fold bands are absent, which is due to the fact that the system considered in this previous work was not perfectly symmetric with respect to the y -axis, as one can verify by a rigorous analysis of Fig. 7(b) in this reference. In Fig. 3.8(b), we present results for the mass defined circular quantum ring [94, 95, 117] sketched in Fig. 3.1(h), considering a potential height $M_0 = 1 \text{ eV}$ and a smooth interface $S = 10 \text{ \AA}$, for a ring with the same average radius and width as in Fig. 3.8(a). The spectrum in this case exhibits a $\approx 170 \text{ meV}$ gap, that decreases as the magnetic field increases, and a degenerate ground state. The magnetic field lifts the ground state degeneracy and clear AB oscillations are observed. Surprisingly, none of the spectra found for the two circular structures investigated here within the TBM resembles the one obtained by the simplified Dirac model of a circular ring. Actually, the results from the simplified model in the presence of a background mass (see e. g. Figs. 3.5(b) and 3.6(b)) looks qualitatively closer to the one observed in Fig. 3.8(b) for the mass defined ring, but some evident disparities are clearly observed, such as the strong dependence of the gap on the magnetic field, and the existence of two sets of oscillating energies, one that increases and the other that decreases as the magnetic field increases, which will be explained further on. In the case of the cut out ring (Fig. 3.1(g)), the different edge types play such an important role that the only evidence of the circular character of the system on the energy spectrum lies in its weak AB oscillations, and no resemblance with the simplified model spectrum for circular rings can be realized in the TBM spectrum for such a system.

On the other hand, Recher et al. [94] have shown that when the ring confinement is provided by a gap opened in its inner and outer regions due to an infinite mass term, an analytical solution within the Dirac model can be obtained. This solution was repeated in subsequent papers, [95, 117] where it was shown that the ground state energy oscillates periodically with the magnetic flux and is degenerate in the absence of a magnetic field. As the analytical solution was discussed previously in Refs. [94], [95] and [117], we will not repeat them here, and will restrict ourselves to the discussion of the obtained results within this model. Figure 3.9 shows the energy spectrum, obtained within the Dirac model, for the mass defined ring in Fig. 3.1(h), considering the same parameters as in Fig. 3.8(b). The results in this case agree very well with those in Fig. 3.8(b), which were obtained within the TBM. Moreover, a better understanding of the TBM results is now provided by this Dirac model - the two sets of energy states that increase and decrease with the magnetic field, which are clearly observed in the TBM results in Fig. 3.8(b), are now demonstrated to come from the contributions of K (red solid) and K' (blue dashed) branches of the spectrum, and such a lifting of valley degeneracy may be important for future valley-tronic devices. Hence, the development of a Dirac model that agrees well with the TBM results in this case now proves its great importance, as there would be no way to recognize such valley dependence of the energy branches only within the TBM

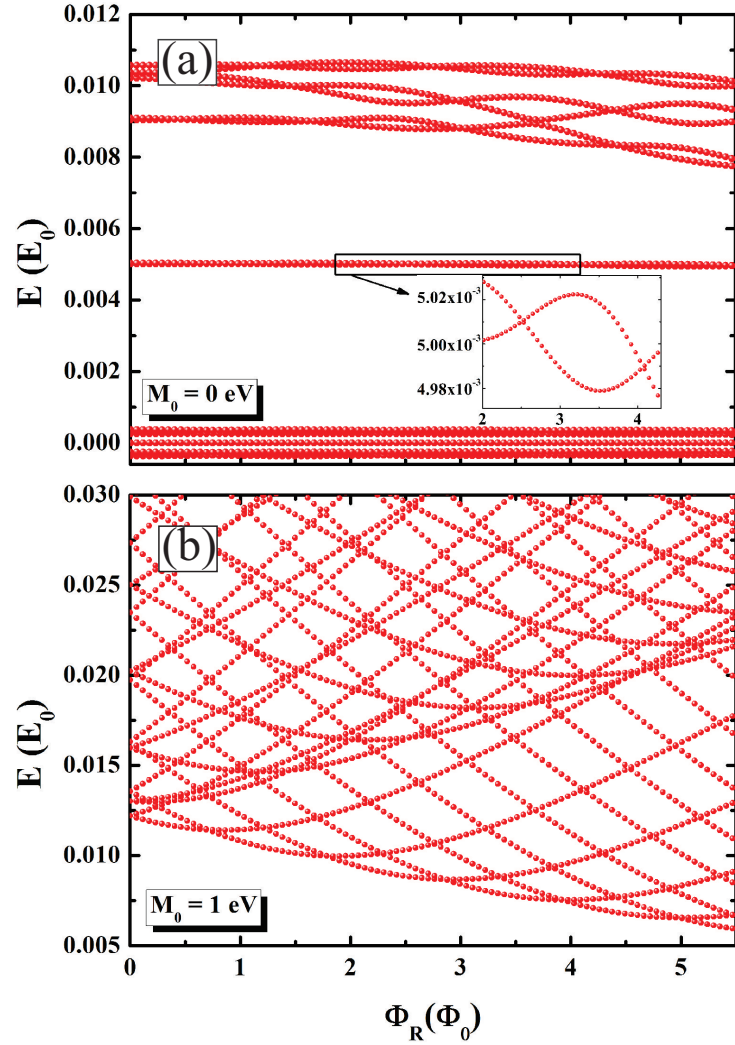


Figure 3.8: Energy levels as a function of the magnetic flux through a single carbon hexagon for (a) the circular graphene ring schematically shown in Fig. 3.1(g), and (b) a quantum ring formed by a site-dependent potential given by Eq. (3.2) and schematically shown in Fig. 3.1(h), with smoothness $S = 10 \text{ \AA}$ and height $M_0 = 1 \text{ eV}$. In both cases, the average radius of the ring is $R = 80 \text{ \AA}$ and the width is 60 \AA . The spectrum is symmetric with respect to $E = 0$.

approach.

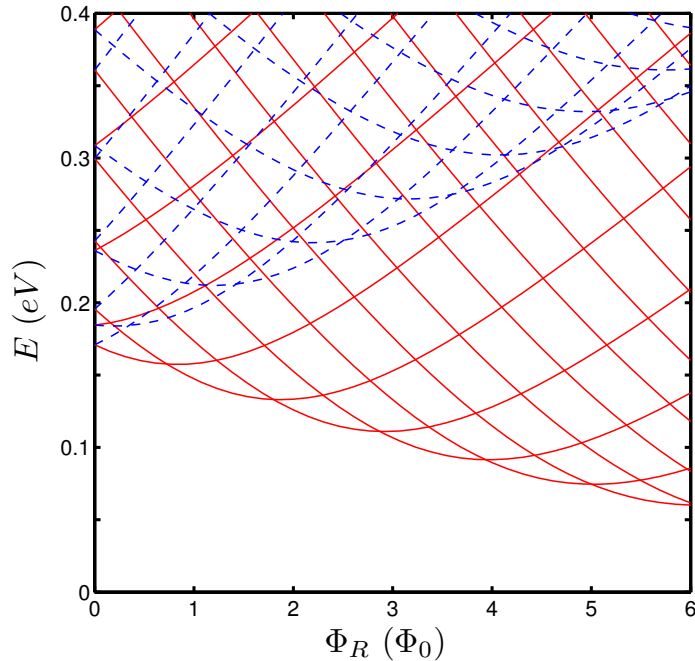


Figure 3.9: Energy spectrum, obtained by the continuum model for K (red solid) and K' (blue dashed), as a function of the magnetic flux for a graphene quantum ring defined by an infinite mass boundary, with the same average radius and width as the ring in Fig. 3.8(b). The spectrum is symmetric with respect to $E = 0$.

3.4.2 Geometry, edge types, and n -fold energy bands

Let us now discuss the energy spectra of graphene rings having different geometries and edge types, which were found to be non-compatible with the results from the Dirac models proposed here, but which display interesting similarities among each other and with previous results, besides exhibiting signatures from the symmetry of the ring, as we will demonstrate further on.

Figure 3.10 shows the energy spectra of zigzag hexagonal rings with $N_E = 15$ and $N_I = 10$ (a) and $N_I = 9$ (b). Depending on the ring width, the spectrum can either exhibit a central six-fold sub-band around $E = 0$, as in Fig. 3.10(a), or two six-fold sub-bands separated by a gap around this energy, as shown in Fig. 3.10(b). A structural difference determines the qualitative behavior of the spectrum: the (former) latter is obtained when the external and internal zigzag edges of the ring are (anti-) aligned, as illustrated in the insets. Contrary to the nanoribbon case, for quantum rings it is the zigzag structure that exhibits an oscillatory behavior as the width changes. This agrees with the fact that the electronic properties of zigzag nanoribbons oriented at 120° with respect to one another, exhibit oscillatory behavior as the width changes, whereas such

junctions made with armchair nanoribbons show no qualitative dependence on the width. [143] This supports the idea that the energy spectra of hexagonal graphene rings are strongly dependent on the electronic properties of their corner junctions.

Such a strong dependence on the edge type, where even the alignment of the edges play an important role, is hard to be described by analytical solutions within the continuum model. Besides, it is clear that both spectra in Fig. 3.10 cannot be obtained from our simplified model. Nevertheless, we can still estimate the period of the energy oscillations observed in Fig. 3.10 by $\Phi_R = n\Phi_0$, using a reasonable value of ring radius, which in the case of Fig. 3.10 is $\approx 29 \text{ \AA}$. As the energy spectrum for the aligned case, shown in Fig. 3.10(b), exhibits a gap around $E = 0$, one could expect that introducing $M \neq 0$ in Eq. (3.9) would lead to the correct energy spectrum. Although the low-lying states of this spectrum resembles qualitatively those in Fig. 3.6(b) for $M = 0.5E_0$, the AB oscillations found by the simplified model exhibit a π -phase shift in comparison to the results in Fig. 3.10(b), so that the ground state for $\Phi_R = 0$ in Fig. 3.6(b) (Fig. 3.10(b)) is double (non) degenerate.

Notice that the energy spectrum of hexagonal graphene rings with zigzag edges has been previously investigated in Ref. [138], but with a different focus. In these previous results, the six-fold energy bands of this system were already pointed out. However, information about the details of the energy spectrum close to the Fermi energy and their dependence on the edges alignment, as well as the possibility of predicting the period of AB oscillations by using the Dirac model, were missing, and are now complemented by the results of the present manuscript.

The energy spectra of rhombus-shaped quantum rings with zigzag edges are shown in Fig. 3.11 as a function of the magnetic flux, for the same value of N_E as in Fig. 3.2 and with N_I (a) 11 and (b) 9. In this case, due to the geometry of the system, it is not possible to construct zigzag rhombus rings having different kinds of edges alignment. In this way, the spectra for different ring widths exhibit the same qualitative behavior, with two-fold energy sub-bands, just like those previously observed for the armchair case in Fig. 3.2. Notice that the states around $E = 0$, that look like zero-energy states, are rather composed by three pairs of oscillating states, with very low energy. As a matter of fact, the two-fold energy bands of this system have been already pointed out by Bahamon *et al.*, [138] therefore, our results complement the findings of this previous paper by providing details of the energy spectrum around $E = 0$, as well as the dependence of the energy spectrum on the ring width.

Figure 3.12 shows the energy spectra for triangular zigzag quantum rings considering two ring sizes: (a) $N_E = 17$, $N_I = 12$ and (b) $N_E = 15$, $N_I = 10$. Just like the zigzag rhombus case, the zigzag triangular rings can only be constructed with aligned edges. The spectra look qualitatively similar to those observed for the zigzag rhombus-shaped ring in Fig. 3.11, but with three-fold oscillating energy bands for higher energy states, instead of the pairs of oscillating states observed in the rhombus-shaped zigzag case.

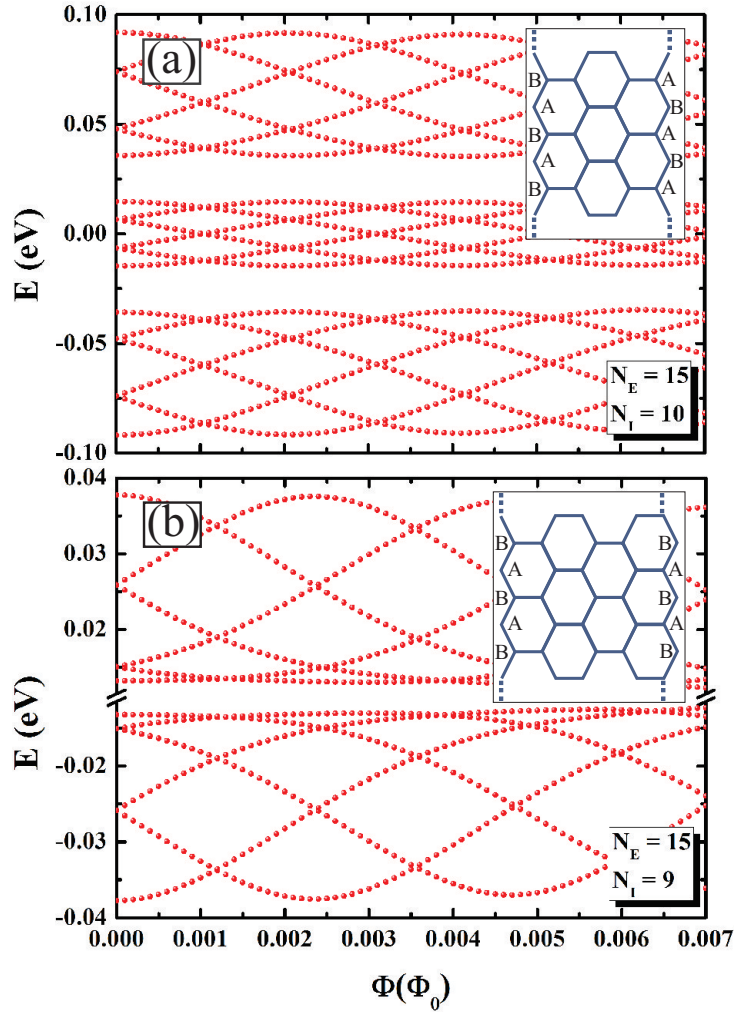


Figure 3.10: Energy levels of zigzag hexagonal quantum rings, schematically shown in Fig. 1(b), as a function of the magnetic flux through a single carbon hexagon for two ring widths: (a) $N_E = 15$, $N_I = 10$ and (b) $N_E = 15$, $N_I = 9$. In the (former) latter the inner and outer zigzag edges are (anti-) aligned, as sketched in the insets.

However, there are two important differences between these two spectra: (i) the zigzag triangular rings, in fact, exhibit zero-energy (edge) states, no matter the length of its sides, whereas zigzag rhombus-shaped rings do not, as shown by the insets of Fig. 3.11 and previously explained in the text; (ii) the first energy state in the zigzag rhombus-shaped ring is always non-degenerate, whereas this state in the zigzag triangular ring is doubly degenerate. Results in previous papers [138] demonstrate that the anti-crossings separating the three-fold energy bands of triangular zigzag quantum rings originate from the coupling between inner and outer edge states.

The magnetic field dependence of the energy levels of armchair triangular quantum rings is shown in Fig. 3.13 for (a) anti-aligned and (b) aligned edges, where the spectra are also composed by three-fold oscillating energies, as in the zigzag case. However, the energy levels are shown to be much more affected by the magnetic field threading the ring

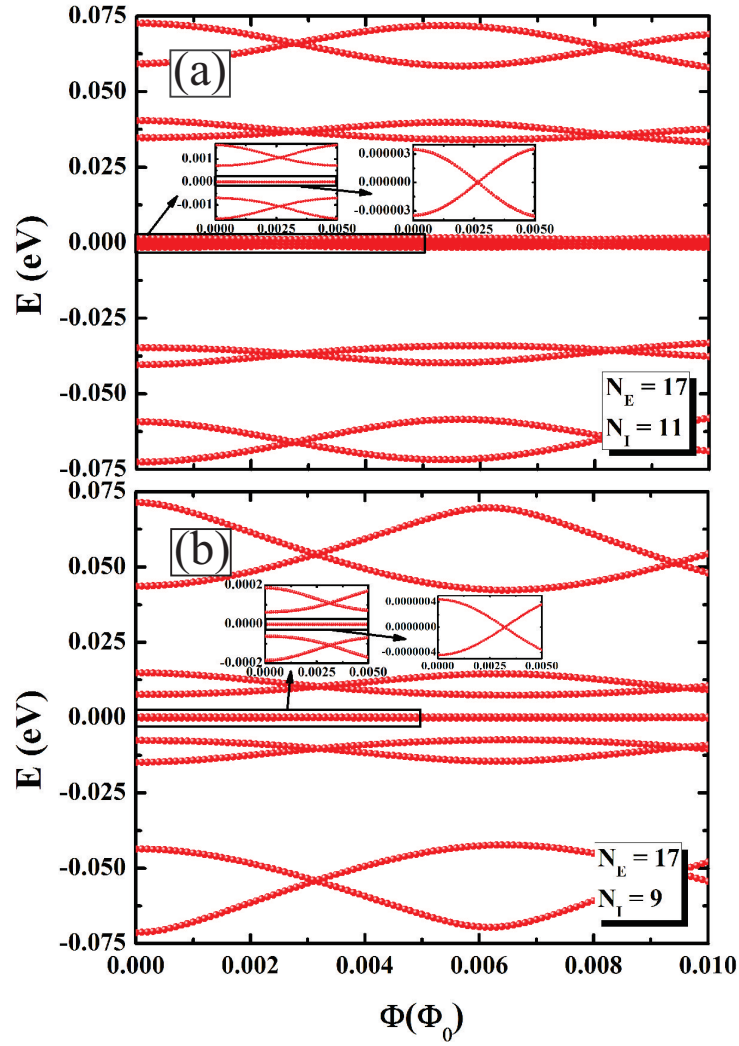


Figure 3.11: Energy levels of zigzag rhombus quantum rings, schematically shown in Fig. 1(f), as a function of the magnetic flux through a single carbon hexagon for two ring widths: (a) $N_E = 17$, $N_I = 11$ and (b) $N_E = 17$, $N_I = 9$. For both widths, the energy spectrum does not have a zero-energy state, they are three pairs of oscillating states as shown in the insets.

in the armchair case and no significant difference on the edges alignment was observed. Another difference as compared to the zigzag triangular rings is the absence of the zero-energy state, which is expected, since the zero energy states are normally related to edge states in zigzag boundaries. [144, 145] The spectra also exhibit a huge gap of $\Delta E > 1$ eV around $E = 0$, which becomes smaller either as the magnetic field increases or as the ring width becomes larger (i. e. as N_I becomes smaller for a fixed N_E).

It is important to emphasize a clear similarity between the results obtained in the previous sub-section for armchair hexagonal (rhombus-shaped) rings in Fig. 3.3 (Fig. 3.2) and those obtained for the zigzag case in Fig. 3.10 (Fig. 3.11): for any edge type or alignment, the energy spectra exhibit six(two)-fold energy bands, with AB oscillations with varying magnetic field. A similar effect is also shared by zigzag and armchair tri-

angular rings, as shown in Figs. 3.12 and 3.13, respectively, where the energy spectra exhibit three-fold bands. These results strongly suggest that the number of energy states composing these bands is related to the symmetry groups of rotation C_6 , C_2 and C_3 , for hexagon, rhombus and triangle, respectively, which are closely related to the number of sides of the polygon formed by the ring.[138]

3.5 Conclusion

We calculated the energy levels of graphene quantum rings with several geometries under an applied magnetic field and observed that the energy spectrum and the AB oscillations for these systems are strongly dependent on their geometry and edge structures.

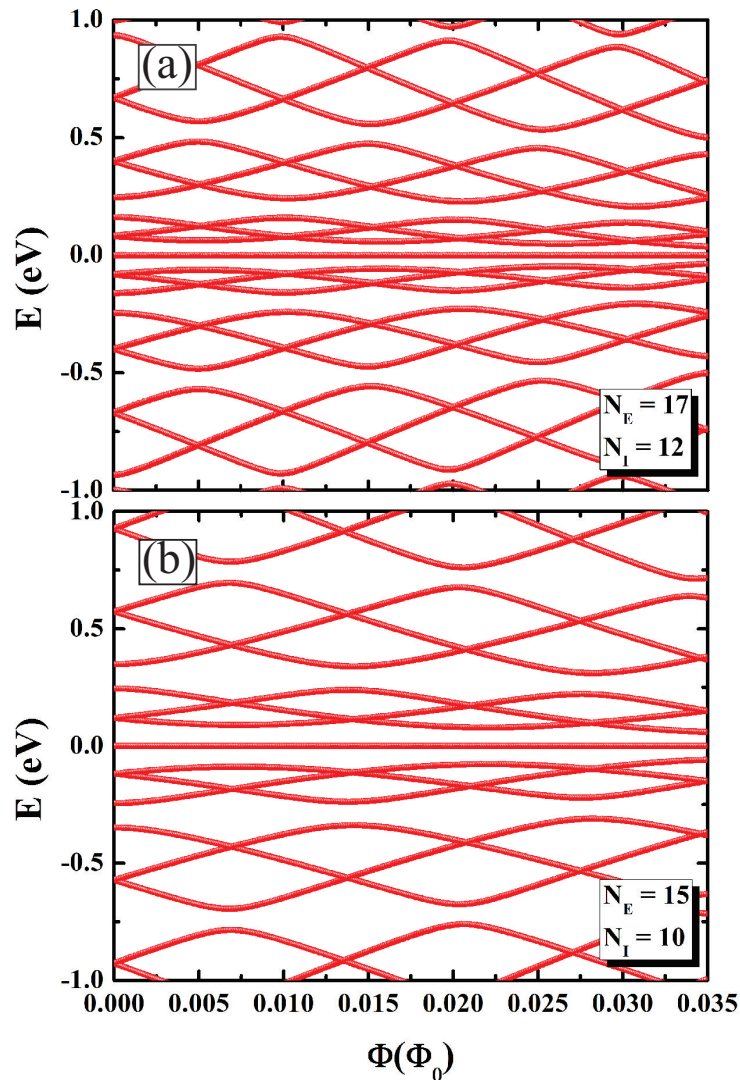


Figure 3.12: Energy levels of zigzag triangular quantum rings, schematically shown in Fig. 1(d), as a function of the magnetic flux through a single carbon hexagon for two ring widths: (a) $N_E = 17$, $N_I = 12$ and (b) $N_E = 15$, $N_I = 10$. For both widths, the energy spectrum has a zero-energy state.

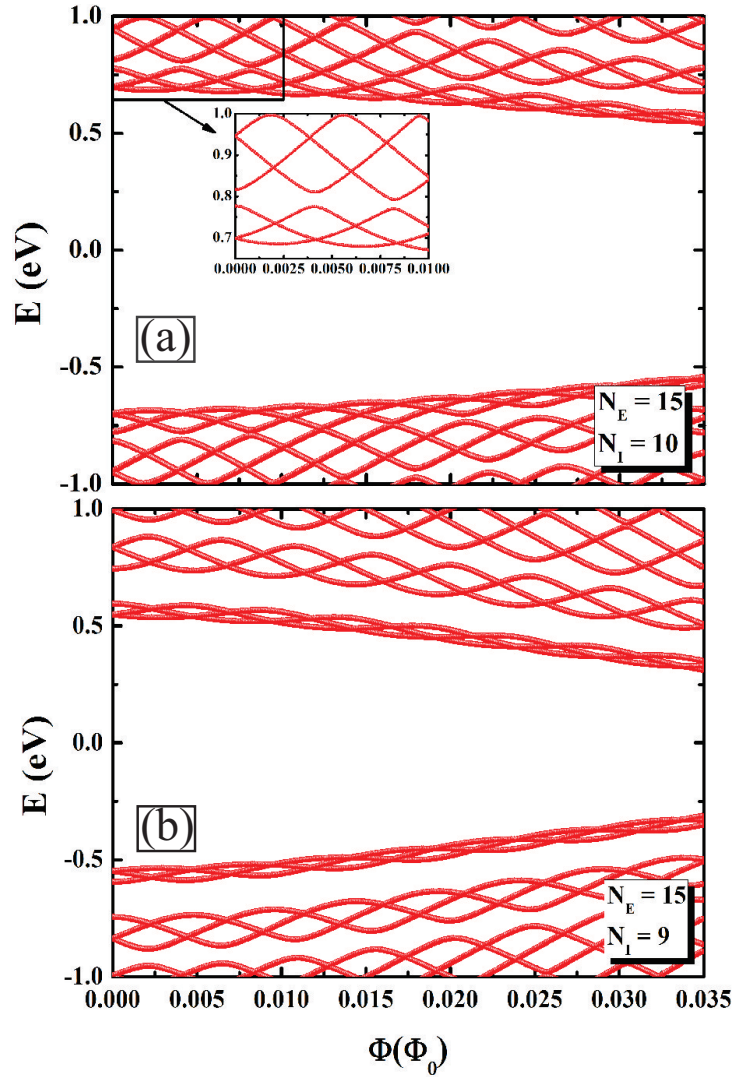


Figure 3.13: Energy levels of armchair triangular quantum rings, schematically shown in Fig. 1(c), as a function of the magnetic flux through a single carbon hexagon for two ring widths: (a) $N_E = 15$, $N_I = 10$ and (b) $N_E = 15$, $N_I = 9$. The spectrum is symmetric with respect to $E = 0$.

For rings with zigzag edges, the TB spectra for each geometry are qualitatively different, showing six-, three- and two-fold energy sub-bands, separated by large gaps, for hexagonal, triangular and rhombus-like rings, respectively. In the hexagonal case, the alignment between inner and outer zigzag edges is demonstrated to play an important role in the formation of the sub-bands, whereas the triangular and rhombus rings have only the aligned edge case due to geometric reasons, presenting similar energy spectra for different sizes. Such a strong dependence of the energy spectrum on the edge structure, specially the observed oscillatory behavior of the spectra with changing ring width, due to the alignment or anti-alignment of the inner and outer edges, is a feature of the quantum ring spectra that can hardly be captured by the continuum models.

The energy spectrum obtained from the TB model for hexagonal quantum rings with

armchair edges exhibits six-fold sub-bands separated by narrow gaps, which become larger as the width of the ring increases. The spectrum does not have $E = 0$ states at zero magnetic field, but exhibits such states for certain values of magnetic flux. Similar features are observed for a rhombus-like ring with armchair edges (except for the six-fold sub-bands which, in this case, are two-fold), but only in the case where the inner and outer edges are anti-aligned. The main features of these energy spectra can be obtained by a simplified model, which considers electrons obeying the Dirac equation for a circular ring with zero width. Despite the different geometry of the actual rings, with such a simple circular model one can (i) estimate the energy levels and the period of AB oscillations or, alternatively, estimate the ring radius by analyzing its energy spectrum as a function of the magnetic field, even in the presence of a substrate induced staggered potential, which appears in the continuum model as a background mass term; (ii) predict the alternating direction of the persistent currents through the ring arms as the magnetic field increases, observed in the TBM; and (iii) predict the almost linearly increasing energy states as a function of the ring radius in the presence of an uniform magnetic field, which is also confirmed by the TBM results. The approximation is better suited for rings with smaller widths and for lower energies and magnetic fields. On the other hand, all the results for the triangular geometry in the armchair case exhibit three-fold sub-bands separated by large energy gaps, which cannot be described by such a simplified model.

We also studied two cases of circular rings within the TB model: in the first one, where the ring is cut from a graphene layer, we observe an energy spectrum composed by pairs of energy states which exhibit AB oscillations as the magnetic field increases. In the second, where the electrons are confined in a ring-like structure by an external staggered site-dependent potential, the energy spectrum exhibits a gap around $E = 0$ and the ground state is doubly degenerate in the absence of a magnetic field. As the magnetic field increases, this degeneracy is lifted, the energy gap is reduced, and AB oscillations are observed in two different branches of energies, one that increases and the other that decreases with magnetic field. Surprisingly, the TBM results for both *circular* cases are very different from those obtained by the simplified continuum model for a *circular* ring, which, in turn, was demonstrated to perfectly describe *hexagonal* and *rhombus-like* armchair rings. On the other hand, our results demonstrate that the spectrum of the staggered potential case can be obtained by the continuum model for a finite width circular ring defined by mass barriers, where one identifies the different energy branches observed in the TBM results as coming from different Dirac cones, demonstrating a magnetic field induced lifting of the valley degeneracy in these systems. However, the mass boundary conditions used here and in Refs. [94], [95] and [117] are shown to describe only the case of a ring defined by a ring-like staggered potential, so that the complicated energy spectrum of the more realistic circular ring cut out of a graphene sheet cannot be described by any of the simplistic boundary conditions or simplified models analyzed here.

We thus summarize our findings with the following general conclusions: 1) rings with a given n -fold symmetry exhibit n -fold energy subbands; 2) edge alignment in zigzag hexagonal rings lead to differences in the six-fold sub-bands distribution around the Fermi level, whereas for armchair rhombus-shaped rings, drastic modifications to the energy spectrum are observed, specially regarding the separation between the two-fold bands; 3) an infinitely thin Dirac ring describes quite well armchair hexagonal and rhombus-shaped (with anti-aligned edges) structures, specially for thin ring widths; and 4) the Dirac model for a ring defined by infinite mass boundaries does not describe rings cut out of a graphene flake, but rather those defined by a ring-shaped staggered potential.

Analytical study of the energy levels in bilayer graphene quantum dots

Using the four-band continuum model we derive a general expression for the infinite-mass boundary condition in bilayer graphene. Applying this new boundary condition we analytically calculate the confined states and the corresponding wave functions in a bilayer graphene quantum dot in the absence and presence of a perpendicular magnetic field. Our results for the energy spectrum show an energy gap between the electron and hole states at small magnetic fields. Furthermore the electron (e) and hole (h) energy levels corresponding to the K and K' valleys exhibit the $E_K^{e(h)}(m) = -E_{K'}^{h(e)}(m)$ symmetry, where m is the angular momentum quantum number.

4.1 Motivation

A considerable number of studies have addressed the electronic properties of quantum dots (QDs) in semiconductors [146, 147]. Such QDs can be used as single photon sources, lasers and are promising candidates for spin qubits and thus for future quantum information technology. However the spin-orbit and electron spin-nuclear spin interactions in conventional semiconductor QDs, i.e. mainly based on GaAs, limit the spin coherence time and thus the functionality of the device.

Very soon after the discovery of graphene [1, 18], theoretical and experimental studies appeared on graphene quantum dots (GQDs). GQDs can be exceptional systems for spintronics applications due to their long spin coherence time which is a consequence of the very weak spin-orbit interaction in graphene. The gapless and linear spectrum of graphene at its Fermi energy in the vicinity of two non-equivalent points in the Brillouin zone, namely K and K' , results in the Klein tunneling effect which prevents electrical confinement of carriers in graphene structures [124]. Therefore, the direct etching of a graphene sheet into small flakes seems to be the only realizable way for fabricating monolayer graphene QDs. In a series of theoretical studies the energy levels of triangular, hexagonal, rectangular and circular QDs have been investigated using both tight-binding

and continuum (i.e. solving the Dirac-Weyl equation) models in the absence and presence of a perpendicular magnetic field [77, 111, 121, 148, 149, 150, 151, 152]. These studies demonstrate that the energy spectrum of graphene QDs are highly dependent on the shapes and edges (which implies different boundary conditions) of the dot.

It has been recognized that two weakly van der Waals coupled sheets of graphene, i.e. known as bilayer graphene (BLG), has very different electronic properties from graphene [79]. Pristine BLG is gapless and exhibits an almost parabolic energy spectrum around the K and K' points in its Brillouin zone. The possibility of opening an energy gap in BLG using a perpendicular electric field, leads to the prediction [125, 153, 154, 155, 156] and realization [157, 158] of gate defined QDs in BLG. In such QDs, the edges are no longer important.

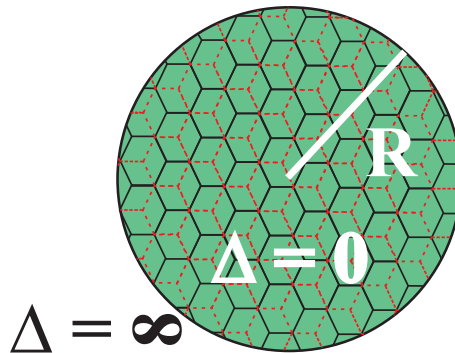


Figure 4.1: An illustration of a circular quantum dot of radius R made of bilayer graphene. The dot is surrounded by an infinity mass potential $\Delta \rightarrow \infty$.

Alternatively, bilayer graphene flakes are another type of QDs which may exhibit very different properties but which have been barely studied. Ref. [159] investigated triangular BLG dots and Ref. [160] showed the energy levels of circular QDs in BLG surrounded with finite flakes within a tight-binding approach.

Using the Dirac-Weyl equation a system very similar to circular GQDs was investigated half a century ago, i.e. many years before the excitement about graphene, by Berry and Mondragon [93] as a theoretical example for the confinement of neutrino's. The main advantage of this model is that: (i) analytic results can be obtained, and (ii) that the results are comparable [111, 121] to the tight-binding results for not too large energies and for particular edge termination. It is very surprising that up to now no equivalent theoretical study has been made for QDs in BLG. The reason for this can be traced back to the non availability of appropriate boundary conditions.

In this paper, by solving the Dirac-Weyl equation, we obtain for the first time analytical results for the energy levels of circular QDs in BLG in the presence of a perpendicular magnetic field. A schematic picture of our system is shown in Fig. 4.1. First we derive novel infinite-mass boundary conditions for BLG. Recent experiments in both monolayer [78, 161, 162] and bilayer [163, 164] graphene report the appearance of an energy gap in the energy spectrum due to the interaction with the substrate that is composed by

a hexagonal atomic lattice, such as hexagonal boron nitride (h-BN) and SiC. This energy gap is a consequence of an effective mass potential induced by the substrate. The virtues of the infinite-mass boundary conditions has been already discussed for monolayer graphene QDs [77, 90, 126]. The results in Ref. [77] for the energy spectrum of graphene QDs with infinite-mass boundary conditions have demonstrated reasonable agreement between theory and experiment. To complement our study, we compare analytical results with the energy levels of a BLG quantum dot surrounded by a mass potential media using the tight-binding approach.

Our paper is organized as follows. In Sec. 4.2, we derive the infinite-mass boundary conditions for BLG which can be applicable for any dot geometry in BLG. In Sec. 4.3, we solve the Dirac-Weyl equation analytically (for both K and K' valleys) and obtain the energy levels of circular QDs in BLG for zero magnetic field and in Sec. 4.4 in the presence of a perpendicular magnetic field. The cyclotron resonance for the system is discussed in Sec. 4.5. We summarize our results in Sec. 4.6.

4.2 Infinite-mass boundary condition

Here we will generalise the infinite-mass boundary condition for monolayer graphene to BLG. Our approach will be based on the formalism discussed in Ref. [165] in which the authors obtain the boundary conditions for the scattering problem of a circular mass barrier in monolayer graphene and extend their work to the case of BLG. The Hamiltonian describing a Dirac electron in the presence of a circular mass barrier in BLG is given by

$$H = \begin{pmatrix} 0 & \pi & t & 0 \\ \pi^\dagger & 0 & 0 & 0 \\ t & 0 & 0 & \pi^\dagger \\ 0 & 0 & \pi & 0 \end{pmatrix} + \begin{pmatrix} \tau\Delta & 0 & 0 & 0 \\ 0 & -\tau\Delta & 0 & 0 \\ 0 & 0 & \tau\Delta & 0 \\ 0 & 0 & 0 & -\tau\Delta \end{pmatrix}, \quad (4.1)$$

where Δ indicates a position-dependent *mass term* [153, 154] and the index $\tau = \pm 1$ distinguishes the two K and K' valleys. $t \sim 400$ meV is the interlayer coupling term, π and π^\dagger are the momentum operators in polar coordinates

$$\pi = -i\hbar v_F e^{i\theta} \left(\frac{\partial}{\partial \rho} + \frac{i}{\rho} \frac{\partial}{\partial \theta} \right), \quad (4.2a)$$

$$\pi^\dagger = -i\hbar v_F e^{-i\theta} \left(\frac{\partial}{\partial \rho} - \frac{i}{\rho} \frac{\partial}{\partial \theta} \right), \quad (4.2b)$$

with $v_F \approx 10^6$ m/s being the velocity of the carriers in BLG. The eigenstates of the Hamiltonian (4.1) are given by the four-component wave function $\Psi = [\psi_A, \psi_B, \psi_{B'}, \psi_{A'}]^T$.

Solving the stationary Schrödinger equation $H\Psi = E\Psi$ we obtain the following system of coupled differential equations

$$\begin{aligned}
e^{i\theta} \left(\frac{\partial}{\partial \rho} + \frac{i}{\rho} \frac{\partial}{\partial \theta} \right) \psi_B &= i [(\epsilon - \tau \Delta') \psi_A - t' \psi_{B'}], \\
e^{-i\theta} \left(\frac{\partial}{\partial \rho} - \frac{i}{\rho} \frac{\partial}{\partial \theta} \right) \psi_A &= i [(\epsilon + \tau \Delta') \psi_B], \\
e^{-i\theta} \left(\frac{\partial}{\partial \rho} - \frac{i}{\rho} \frac{\partial}{\partial \theta} \right) \psi_{A'} &= i [(\epsilon - \tau \Delta') \psi_{B'} - t' \psi_A], \\
e^{i\theta} \left(\frac{\partial}{\partial \rho} + \frac{i}{\rho} \frac{\partial}{\partial \theta} \right) \psi_{B'} &= i [(\epsilon + \tau \Delta') \psi_{A'}],
\end{aligned} \tag{4.3}$$

where the radial coordinate ρ is given in units of the dot radius R . The energy ϵ , the hopping term t' and the mass potential Δ' are in units of $E_0 = \hbar v_F/R$. The circular

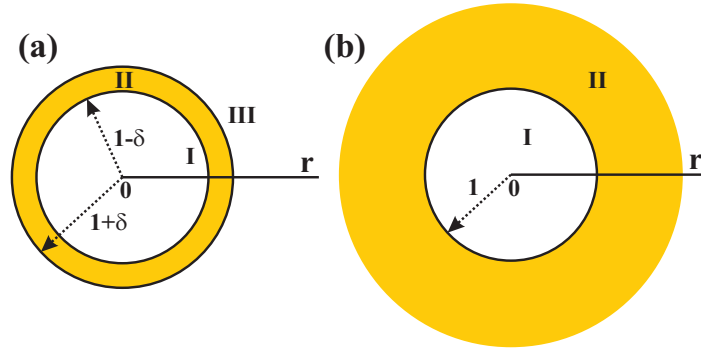


Figure 4.2: Schematic picture of the mass potential profile for a (a) ring-shaped barrier and (b) dot barrier divided into three and two regions, respectively. The width of the barrier, i.e. $\delta \ll 1$, is shown by the yellow region and the radius of the dot and ring is set to 1.

symmetry of our problem allows us to take the following angular dependence of the wave function components:

$$\begin{aligned}
&[\psi_A, \psi_B, \psi_{B'}, \psi_{A'}]^T = \\
&e^{im\theta} [\phi_A(\rho), ie^{-i\theta} \phi_B(\rho), \phi_{B'}(\rho), ie^{i\theta} \phi_{A'}(\rho)]^T,
\end{aligned} \tag{4.4}$$

where the integer value m denotes the angular momentum label. Inserting Eq. (4.4) into the set of differential equations (4.3), we obtain

$$\begin{aligned}
\left[\frac{\partial}{\partial \rho} - \frac{(m-1)}{\rho} \right] \phi_B(\rho) &= (\epsilon - \tau \Delta') \phi_A(\rho) - t' \phi_{B'}(\rho), \\
\left[\frac{\partial}{\partial \rho} + \frac{m}{\rho} \right] \phi_A(\rho) &= -(\epsilon + \tau \Delta') \phi_B(\rho), \\
\left[\frac{\partial}{\partial \rho} + \frac{(m+1)}{\rho} \right] \phi_{A'}(\rho) &= (\epsilon - \tau \Delta') \phi_{B'}(\rho) - t' \phi_A(\rho), \\
\left[\frac{\partial}{\partial \rho} - \frac{m}{\rho} \right] \phi_{B'}(\rho) &= -(\epsilon + \tau \Delta') \phi_{A'}(\rho).
\end{aligned} \tag{4.5}$$

In order to find the infinite-mass boundary condition we consider a Dirac electron interacting with circular barrier structures shown in yellow color in Fig. 4.2. We start by solving the set of differential equations (4.5) in the barrier region (region II) applying the standard boundary condition for the four wave function components on the solid circles shown in Fig. 4.2(a) and take the limit $\Delta' \rightarrow \infty$. We obtain the following system of differential equations for region *II*, i.e. inside the barrier,

$$\begin{aligned}
\frac{\partial}{\partial \rho} \phi_B &= -\tau \Delta' \phi_A - t' \phi_{B'}, \\
\frac{\partial}{\partial \rho} \phi_A &= -\tau \Delta' \phi_B, \\
\frac{\partial}{\partial \rho} \phi_{A'} &= -\tau \Delta' \phi_{B'} - t' \phi_A, \\
\frac{\partial}{\partial \rho} \phi_{B'} &= -\tau \Delta' \phi_{A'},
\end{aligned} \tag{4.6}$$

which has the solution

$$\begin{aligned}
\phi_A &= F e^{\alpha_+(\rho-1)} + G e^{-\alpha_+(\rho-1)} \\
&\quad + H e^{\alpha_-(\rho-1)} + I e^{-\alpha_-(\rho-1)}, \\
\phi_B &= -\frac{\tau}{\Delta'} [\alpha_+ F e^{\alpha_+(\rho-1)} - \alpha_+ G e^{-\alpha_+(\rho-1)} \\
&\quad + \alpha_- H e^{\alpha_-(\rho-1)} - \alpha_- I e^{-\alpha_-(\rho-1)}], \\
\phi_{B'} &= \tau [F e^{\alpha_+(\rho-1)} + G e^{-\alpha_+(\rho-1)} \\
&\quad - H e^{\alpha_-(\rho-1)} - I e^{-\alpha_-(\rho-1)}], \\
\phi_{A'} &= -\frac{1}{\Delta'} [\alpha_+ F e^{\alpha_+(\rho-1)} - \alpha_+ G e^{-\alpha_+(\rho-1)} \\
&\quad - \alpha_- H e^{\alpha_-(\rho-1)} + \alpha_- I e^{-\alpha_-(\rho-1)}].
\end{aligned} \tag{4.7}$$

where $\alpha_{\pm} = \sqrt{\Delta'(\Delta' \pm t')}$. The boundaries of the mass barrier region are determined by $-\delta \leq \rho - 1 \leq \delta$. The above solutions at the different boundaries become

$$\begin{aligned}
\phi_A^I(1 - \delta) &= F e^{-\alpha_+\delta} + G e^{\alpha_+\delta} \\
&\quad + H e^{-\alpha_-\delta} + I e^{\alpha_-\delta}, \\
\phi_B^I(1 - \delta) &= -\frac{\tau}{\Delta'} [\alpha_+ F e^{-\alpha_+\delta} - \alpha_+ G e^{\alpha_+\delta} \\
&\quad + \alpha_- H e^{-\alpha_-\delta} - \alpha_- I e^{\alpha_-\delta}], \\
\phi_{B'}^I(1 - \delta) &= \tau [F e^{-\alpha_+\delta} + G e^{\alpha_+\delta} \\
&\quad - H e^{-\alpha_-\delta} - I e^{\alpha_-\delta}], \\
\phi_{A'}^I(1 - \delta) &= -\frac{1}{\Delta'} [\alpha_+ F e^{-\alpha_+\delta} - \alpha_+ G e^{\alpha_+\delta} \\
&\quad - \alpha_- H e^{-\alpha_-\delta} + \alpha_- I e^{\alpha_-\delta}],
\end{aligned}$$

$$\begin{aligned}
\phi_A^{III}(1+\delta) &= Fe^{\alpha+\delta} + Ge^{-\alpha+\delta} \\
&\quad + He^{\alpha-\delta} + Ie^{-\alpha-\delta}, \\
\phi_B^{III}(1+\delta) &= -\frac{\tau}{\Delta'} [\alpha_+ Fe^{\alpha+\delta} - \alpha_+ Ge^{-\alpha+\delta} \\
&\quad + \alpha_- He^{\alpha-\delta} - \alpha_- Ie^{-\alpha-\delta}], \\
\phi_{B'}^{III}(1+\delta) &= \tau [Fe^{\alpha+\delta} + Ge^{-\alpha+\delta} \\
&\quad - He^{\alpha-\delta} - Ie^{-\alpha-\delta}], \\
\phi_{A'}^{III}(1+\delta) &= -\frac{1}{\Delta'} [\alpha_+ Fe^{\alpha+\delta} - \alpha_+ Ge^{-\alpha+\delta} \\
&\quad - \alpha_- He^{\alpha-\delta} + \alpha_- Ie^{-\alpha-\delta}].
\end{aligned} \tag{4.8}$$

Eliminating the coefficients F , G , H and I the solution in the limit of $\delta \ll 1$ becomes

$$\begin{aligned}
\phi_{A'}^{III}(1) - \phi_{A'}^I(1) &= \tau [\phi_B^{III}(1) - \phi_B^I(1)] \\
&\quad + \frac{\alpha_-}{\Delta'} \tanh(\alpha_- \delta) \{ \phi_A^{III}(1) + \phi_A^I(1) \\
&\quad \quad - \tau [\phi_{B'}^{III}(1) + \phi_{B'}^I(1)] \}, \\
\phi_{B'}^{III}(1) - \phi_{B'}^I(1) &= -\tau [\phi_A^{III}(1) - \phi_A^I(1)] \\
&\quad - \frac{\Delta'}{\alpha_+} \tanh(\alpha_+ \delta) \{ \phi_B^{III}(1) + \phi_B^I(1) \\
&\quad \quad + \tau [\phi_{A'}^{III}(1) + \phi_{A'}^I(1)] \}.
\end{aligned} \tag{4.9}$$

Considering a very thin and very high mass barrier we take the following limits

$$\delta \rightarrow 0, \quad \Delta' \gg t', \quad \tanh(\alpha_{\pm} \delta) = P = \text{const}$$

which allows us to rewrite the set of Eqs. (4.9) as

$$\begin{aligned}
\phi_{A'}^{III}(1) - \phi_{A'}^I(1) &= \tau [\phi_B^{III}(1) - \phi_B^I(1)] \\
&\quad + P \{ [\phi_A^{III}(1) + \phi_A^I(1)] - \tau [\phi_{B'}^{III} + \phi_{B'}^I] \},
\end{aligned} \tag{4.10a}$$

$$\begin{aligned}
\phi_{B'}^{III}(1) - \phi_{B'}^I(1) &= -\tau [\phi_A^{III}(1) - \phi_A^I(1)] \\
&\quad - P \{ [\phi_B^{III} + \phi_B^I] + \tau [\phi_{A'}^{III} + \phi_{A'}^I] \},
\end{aligned} \tag{4.10b}$$

where the parameter P is related to the magnitude of the height of the barrier with the maximum value 1.[165] Equations (4.10a) and (4.10b) correspond to a general form of the boundary conditions for the structure shown in Fig. 4.2(a). These general conditions allow us to write the boundary condition for a dot-shaped mass barrier, as depicted in Fig. 4.2(b). For this case we take the following limits

$$\begin{aligned}
\Delta' &= \infty, \quad P = 1, \\
\phi_A^{III}(1) &= \phi_B^{III}(1) = \phi_{A'}^{III}(1) = \phi_{B'}^{III}(1) = 0,
\end{aligned} \tag{4.11}$$

which results into

$$\phi_{A'}^I(1) - \tau\phi_B^I(1) - \tau\phi_{B'}^I(1) + \phi_A^I(1) = 0, \quad (4.12a)$$

$$\phi_{A'}^I(1) - \tau\phi_B^I(1) + \tau\phi_{B'}^I(1) + \phi_A^I(1) = 0. \quad (4.12b)$$

These are the boundary conditions for a BLG quantum dot surrounded by an infinite-mass potential barrier. Notice that Eqs. (4.12a) and (4.12b) connect the value of the pseudospin components at the boundary of the two sublattices of each layer with each other. Both equations have the same structure, except for a single sign change. However, we can not simply add the two equations in order to reduce the boundary condition to a single equation. The reason is that the general solution of a four band problem is always composed of two coefficients to each of the four pseudospin components. The infinite-mass boundary condition for a monolayer GQD can easily be obtained by removing the second layer, i.e. by putting $\phi_{A'}^I(1) = \phi_{B'}^I(1) = 0$. In the next section we obtain the energy levels of a circular QD in BLG using the boundary conditions (4.12). In order to find the energy spectrum of a BLG quantum dot we need to apply both conditions at the boundaries, which will result in a transcendental equation for the energy levels.

4.3 Energy levels: Zero magnetic field

Now, we consider our main problem and obtain the energy levels of a circular QD in BLG in the absence (in current section) and presence (in Sec. 4) of a perpendicular magnetic field. We will employ the infinite-mass boundary conditions (i.e. Eqs. (4.12a) and (4.12b)).

In the absence of a magnetic field the Hamiltonian of a BLG and the corresponding wave function are respectively given by Eq. (4.1) and Eq. (4.4). Solving $H\Psi = E\Psi$ leads to the set of coupled equations given by Eq. (4.5). We solved these equation for $\Delta' = 0$ (The infinity mass potential will be applied at the boundary). Decoupling the system of differential equations (4.5) we arrive at the ordinary Bessel differential equation

$$\rho^2 \frac{\partial^2 \phi_A(\rho)}{\partial \rho^2} + \rho \frac{\partial \phi_A(\rho)}{\partial \rho} + [\kappa_{\pm}^2 \rho^2 - m^2] \phi_A(\rho) = 0, \quad (4.13)$$

where $\kappa_{\pm} = \sqrt{\epsilon^2 \pm t'|\epsilon|}$. We define the solution inside the dot as [166]

$$\begin{aligned} \phi_A &= C_1 J_m(\kappa_+ \rho) + C_2 J_m(\kappa_- \rho), \\ \phi_B &= -\frac{1}{\epsilon} [C_1 \kappa_+ J_{m-1}(\kappa_+ \rho) + C_2 \kappa_- J_{m-1}(\kappa_- \rho)], \\ \phi_{B'} &= \text{sgn}(\epsilon) [-C_1 J_m(\kappa_+ \rho) + C_2 J_m(\kappa_- \rho)], \\ \phi_{A'} &= \frac{1}{|\epsilon|} [C_1 \kappa_+ J_{m+1}(\kappa_+ \rho) - C_2 \kappa_- J_{m+1}(\kappa_- \rho)], \end{aligned} \quad (4.14)$$

where $J_m(\kappa_{\pm}\rho)$ is the Bessel function of the first kind and sgn is the sign function. It is important to point out that in the range of $|\epsilon| \leq t'$, κ_- is pure complex, such that the Bessel function returns a complex (real) value when m is odd (even), for small values of the Bessel function argument ($k_- \rho$). Based on this we take into account the real (imaginary) part of $J_m(\kappa_- \rho)$ and $\kappa_- J_{m\pm 1}(\kappa_- \rho)$ when κ_- is complex and m is even (odd).

Applying the boundary conditions (4.12a) and (4.12b) we arrive at a system of two algebraic equations. Finding the roots of the determinant of the coefficients, i.e. C_1 and C_2 , we obtain a transcendental equation for the energy levels that we solve numerically.

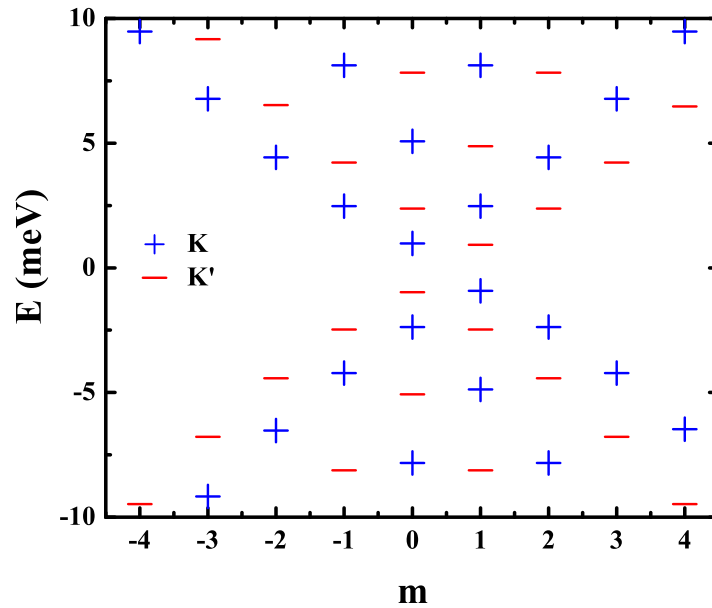


Figure 4.3: Energy levels of a circular BLG quantum dot as a function of angular momentum label m for $R = 70$ nm and in the absence of a magnetic field. The energy levels corresponding to the K and K' valleys are shown by the blue crosses and the red dashed , respectively.

Figure 4.3 shows the energy levels of a QD with radius $R = 70$ nm as function of angular momentum m for zero magnetic field. The results show that the ground state is degenerate and correspond to $m = 0$ and $m = 1$. This can be linked to the geometric phase which shifts the angular momentum labels in the first and third expressions of Eq. (4.5). The electron (e) and hole (h) states in Fig. 4.3 are related by $E_K^e(m) = -E_{K'}^h(m)$ symmetry, corresponding to a reversal of electrons and hole states when going from valley K to K' . Another remarkable symmetry is $E_K^e(m) = E_K^e(-m)$ ($E_{K'}^h(m) = E_{K'}^h(-m)$) between the electron (hole) states of the K (K') valley while the levels corresponding to the K' (K) valley display a shift in energy between negative and positive angular momenta.

Results for the energy levels as a function of the dot radius are shown in Figs. 4.4(a, c,

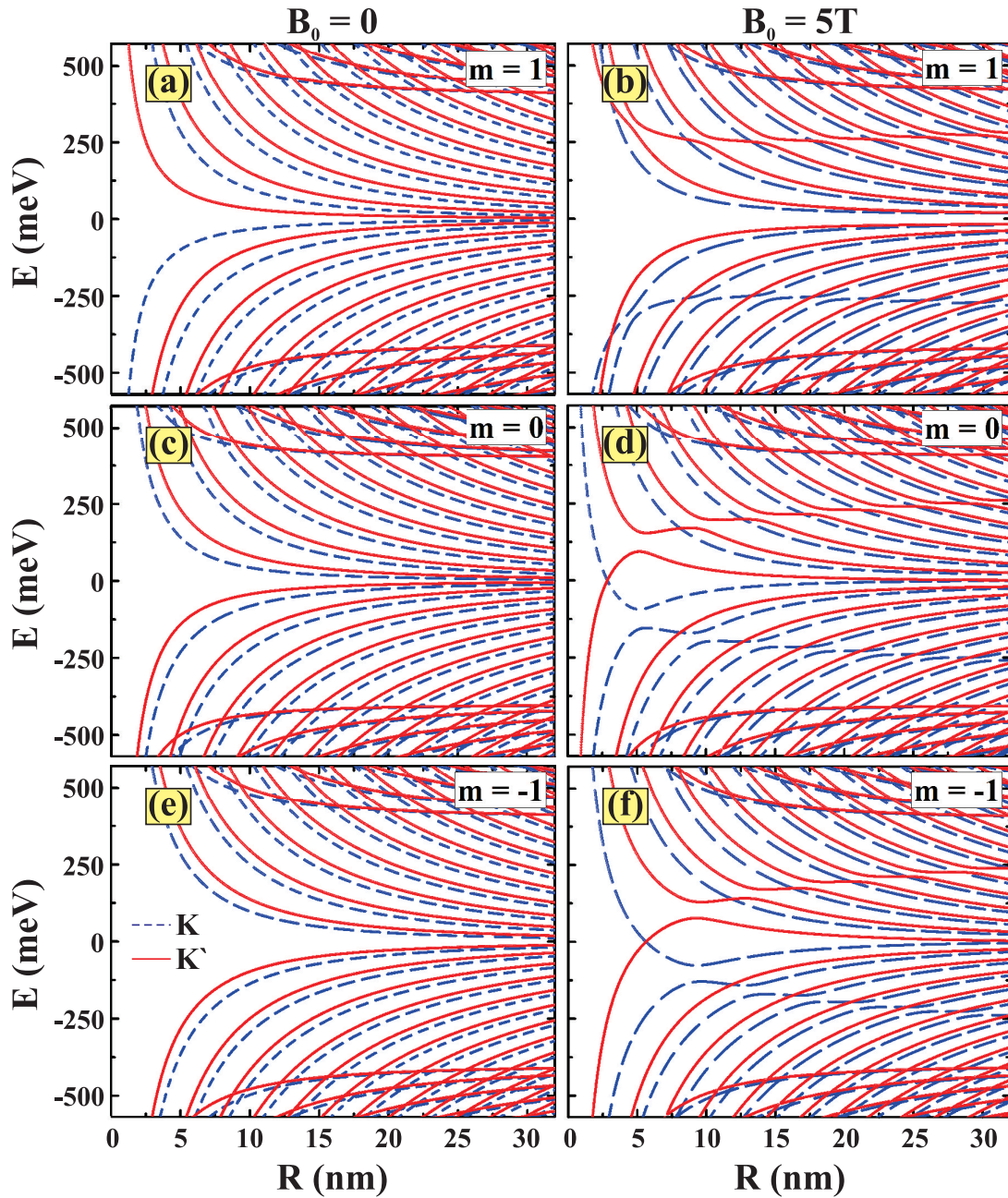


Figure 4.4: Energy levels of a circular BLG quantum dot as a function of the dot radius with $m = 1$ (a, b), $m = 0$ (c, d) and $m = -1$ (e, f). Left and right panels correspond, respectively, to zero magnetic field and $B_0 = 5$ T. The energy levels corresponding to the K and K' valleys are shown by the blue dashed and the red solid curves respectively.

e) for zero magnetic field and $m = 0, \pm 1$. The blue-dashed and red-solid curves correspond respectively to the K and K' valleys. The energy spectrum shows two sets of levels. The upper set of levels approach for large R the inter-layer hopping term in BLG, i.e. $t \approx 400$ meV and is related to the upper band of BLG. For $B_0 = 0$, the spectrum shows a $1/R^2$ dependence for the lowest states and $1/R$ for the states in the upper set. This can be linked to the fact that in BLG the low energy levels are related to a parabolic dispersion $E \sim k^2$ and the higher energies can be approximated with a linear dispersion $E \sim k$.

4.4 Energy levels: Perpendicular magnetic field

In the presence of a perpendicular magnetic field B_0 the momentum operators π and π^\dagger in Hamiltonian (4.1) are defined as

$$\pi = v_F e^{i\theta} \left[-i\hbar \left(\frac{\partial}{\partial r} + \frac{i}{r} \frac{\partial}{\partial \theta} \right) + i \frac{eB_0 r}{2} \right], \quad (4.15a)$$

$$\pi^\dagger = v_F e^{-i\theta} \left[-i\hbar \left(\frac{\partial}{\partial r} - \frac{i}{r} \frac{\partial}{\partial \theta} \right) - i \frac{eB_0 r}{2} \right], \quad (4.15b)$$

where we used the symmetric gauge for the vector potential $\vec{A} = (0, B_0 r/2, 0)$. Acting the Hamiltonian (4.1) on ψ , given by Eq. (4.4) we obtain the following set of coupled differential equations

$$\begin{aligned} \left[\frac{\partial}{\partial \rho} - \frac{(m-1)}{\rho} - \beta \rho \right] \phi_B(\rho) &= \epsilon \phi_A(\rho) - t' \phi_{B'}(\rho), \\ \left[\frac{\partial}{\partial \rho} + \frac{m}{\rho} + \beta \rho \right] \phi_A(\rho) &= -\epsilon \phi_B(\rho), \\ \left[\frac{\partial}{\partial \rho} + \frac{(m+1)}{\rho} + \beta \rho \right] \phi_{A'}(\rho) &= \epsilon \phi_{B'}(\rho) - t' \phi_A(\rho), \\ \left[\frac{\partial}{\partial \rho} - \frac{m}{\rho} - \beta \rho \right] \phi_{B'}(\rho) &= -\epsilon \phi_{A'}(\rho), \end{aligned} \quad (4.16)$$

where $\rho = r/R$, $\epsilon = ER/\hbar v_F$, $t' = tR/\hbar v_F$ and $\beta = eB_0 R^2/2\hbar = R^2/2l_B^2$ are dimensionless, with $l_B = \sqrt{\hbar/eB_0}$ the magnetic length. Decoupling the above equations with respect to ϕ_A we arrive at

$$\begin{aligned} \left[\frac{\partial^2}{\partial \rho^2} + \frac{1}{\rho} \frac{\partial}{\partial \rho} - \frac{m^2}{\rho^2} - 2m\beta - \beta^2 \rho^2 \right] \phi_A(\rho) \\ = \gamma_\pm(\epsilon) \phi_A(\rho), \end{aligned} \quad (4.17)$$

where the eigenvalues are given by $\gamma_\pm(\epsilon) = -\epsilon^2 \pm \sqrt{\epsilon^2 t'^2 + 4\beta^2}$ and $\gamma_\pm(\epsilon) = -2\beta(2n + |m| + m + 1)$, with $n = 0, 1, 2, \dots$. Using the ansatz $\phi_A(\rho) = \rho^{|m|} e^{-\rho^2 \beta/2} \xi(\rho^2)$, Eq. (4.17) yields the confluent hypergeometric ordinary differential equation

$$\begin{aligned} \tilde{\rho} \frac{\partial^2 \xi(\tilde{\rho})}{\partial \tilde{\rho}^2} + [|m| + 1 - \tilde{\rho}] \frac{\partial \xi(\tilde{\rho})}{\partial \tilde{\rho}} \\ - \left[\frac{\gamma_\pm(\epsilon)}{4\beta} + \frac{(|m| + m + 1)}{2} \right] \xi(\tilde{\rho}) = 0, \end{aligned} \quad (4.18)$$

which has the solution $\xi(\tilde{\rho}) = C_1 \widetilde{M}(A_+, B, \tilde{\rho}) + C_2 \widetilde{M}(A_-, B, \tilde{\rho})$ where $\widetilde{M}(A_{\pm}, B, \tilde{\rho})$ is the regularized confluent hypergeometric function with

$$\tilde{\rho} \rightarrow \beta \rho^2 = \beta r^2 / R^2, \quad (4.19a)$$

$$B \rightarrow |m| + 1, \quad (4.19b)$$

$$A_{\pm} \rightarrow \gamma_{\pm}(\epsilon) / 4\beta + (|m| + m + 1) / 2. \quad (4.19c)$$

and C_j 's ($j = 1, 2$) are the normalization coefficients. In order to find ϕ_B , $\phi_{B'}$ and $\phi_{A'}$ we insert the solution for ϕ_A in the differential equations (4.16). Using the properties of the regularized confluent hypergeometric function[167], this results into

$$\begin{aligned} \phi_B(\rho) = & -\frac{\rho^{|m|}}{\epsilon} e^{-\rho^2 \beta / 2} \left\{ \frac{(|m| + m) \xi(\tilde{\rho})}{\rho} \right. \\ & + 2\beta \rho \left[C_1 A_+ \widetilde{M}(A_+ + 1, B + 1, \tilde{\rho}) \right. \\ & \left. \left. + C_2 A_- \widetilde{M}(A_- + 1, B + 1, \tilde{\rho}) \right] \right\}, \end{aligned} \quad (4.20)$$

$$\begin{aligned} \phi_{B'}(\rho) = & \frac{\rho^{|m|}}{\epsilon t'} e^{-\rho^2 \beta / 2} \left\{ 4\beta^2 \rho^2 \left[C_1 A_+ (A_+ + 1) \right. \right. \\ & \times \widetilde{M}(A_+ + 2, B + 2, \tilde{\rho}) + C_2 A_- (A_- + 1) \\ & \times \widetilde{M}(A_- + 2, B + 2, \tilde{\rho}) \left. \right] + 4\beta \left[|m| + 1 \right. \\ & \left. - \beta \rho^2 \right] \left[C_1 A_+ \widetilde{M}(A_+ + 1, B + 1, \tilde{\rho}) \right. \\ & \left. + C_2 A_- \widetilde{M}(A_- + 1, B + 1, \tilde{\rho}) \right] \\ & \left. + \left[\epsilon^2 - 2\beta(|m| + m) \right] \xi(\tilde{\rho}) \right\}, \end{aligned} \quad (4.21)$$

$$\begin{aligned} \phi_{A'}(\rho) = & -\frac{\rho^{|m|}}{\epsilon^2 t'} e^{-\rho^2 \beta / 2} \left\{ 8\beta^3 \rho^3 \left[C_1 A_+ (A_+ + 1) \right. \right. \\ & \times (A_+ + 2) \widetilde{M}(A_+ + 3, B + 3, \tilde{\rho}) + C_2 A_- \\ & \times (A_- + 1)(A_- + 2) \widetilde{M}(A_- + 3, B + 3, \tilde{\rho}) \left. \right] \\ & + 4\beta^2 \rho \left(3|m| - m + 4 - 4\beta \rho^2 \right) \left[C_1 A_+ \right. \\ & \times (A_+ + 1) \widetilde{M}(A_+ + 2, B + 2, \tilde{\rho}) + C_2 A_- \\ & \times (A_- + 1) \widetilde{M}(A_- + 2, B + 2, \tilde{\rho}) \left. \right] + 2\beta \rho \\ & \times \left(\epsilon^2 - 8\beta(|m| + 1) + 4\beta^2 \rho^2 + \frac{2}{\rho^2} (|m| \right. \\ & \left. - m)(|m| + 1) \right) \left[C_1 A_+ \widetilde{M}(A_+ + 1, B + 1, \tilde{\rho}) \right. \\ & \left. + C_2 A_- \widetilde{M}(A_- + 1, B + 1, \tilde{\rho}) \right] + (\epsilon^2 - 2\beta \\ & \times (|m| + m)) \left(\frac{(|m| - m)}{\rho} - 2\beta \rho \right) \xi(\tilde{\rho}) \left. \right\}. \end{aligned} \quad (4.22)$$

After demanding the boundary conditions Eqs. (4.12a) and (4.12b) at $\rho = 1$ we arrive at two algebraic equations from which we find the energy levels by solving them numerically.

Figures 4.4(b, d, f) show the energy levels as a function of radius for $B_0 = 5$ T. For $B_0 \neq 0$ as the size of the dot increases the spectrum becomes weakly dependent on the dot radius and the energy levels approach the Landau levels (LLs) of BLG. As a result, the low-lying states approach $E = 0$, which corresponds to the zeroth LL of BLG. The interplay between the confinement due to the magnetic field and due to the infinite-mass potential leads to the appearance of anti-crossings between the levels of one valley and crossings between the levels of two different valleys.

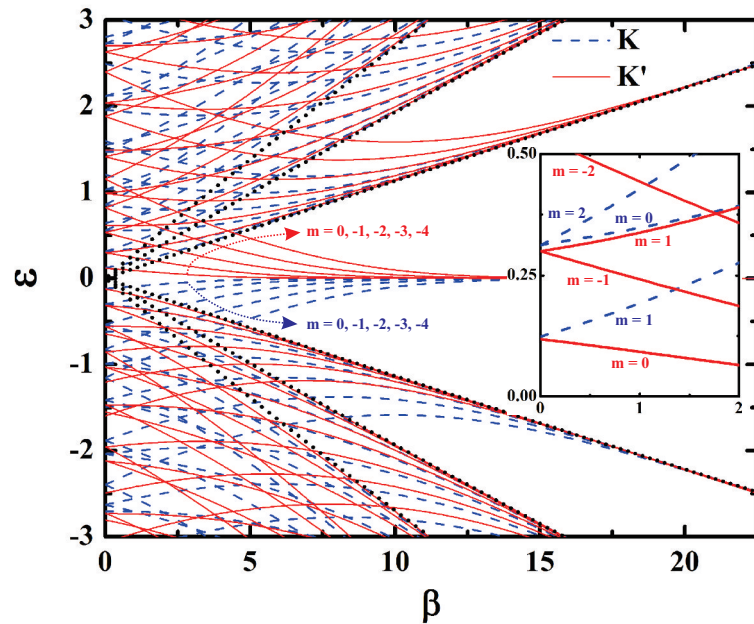


Figure 4.5: Energy spectrum of a circular BLG quantum dot as a function of a perpendicular magnetic field with $R = 70$ nm and for $-4 \leq m \leq 4$. The energy levels corresponding to the K and K' valleys are shown by the blue dashed and the red solid curves, respectively. The black dotted lines are the three first LLs of BLG. The inset shows an enlargement of the low energy levels at small magnetic fields.

Figure 4.5 shows the energy spectrum of a BLG quantum dot as a function of external magnetic field with radius $R = 70$ nm and for $-4 \leq m \leq 4$. The blue dashed and red solid curves respectively show the energy levels for the K and K' valleys. In the inset of Fig. 4.5 we present a zoom of the energy levels at low magnetic fields. At $B = 0$, the two lowest degenerate states, i.e. $E_K(m = 1)$ and $E_{K'}(m = 0)$, belong to different valleys. Notice that the upper set of degenerate levels are pertinent to the same valleys (i.e. $E_K(m = -1) = E_K(m = 1)$ and $E_K(m = 0) = E_K(m = 2)$). This degeneracy is lifted for nonzero magnetic field which is a consequence of the discretization of the energy spectrum when a magnetic field is applied. Furthermore, the spectrum shows the symmetry $E_K^e(m) = -E_{K'}^h(m)$ for the QD system created by an infinite-mass potential at

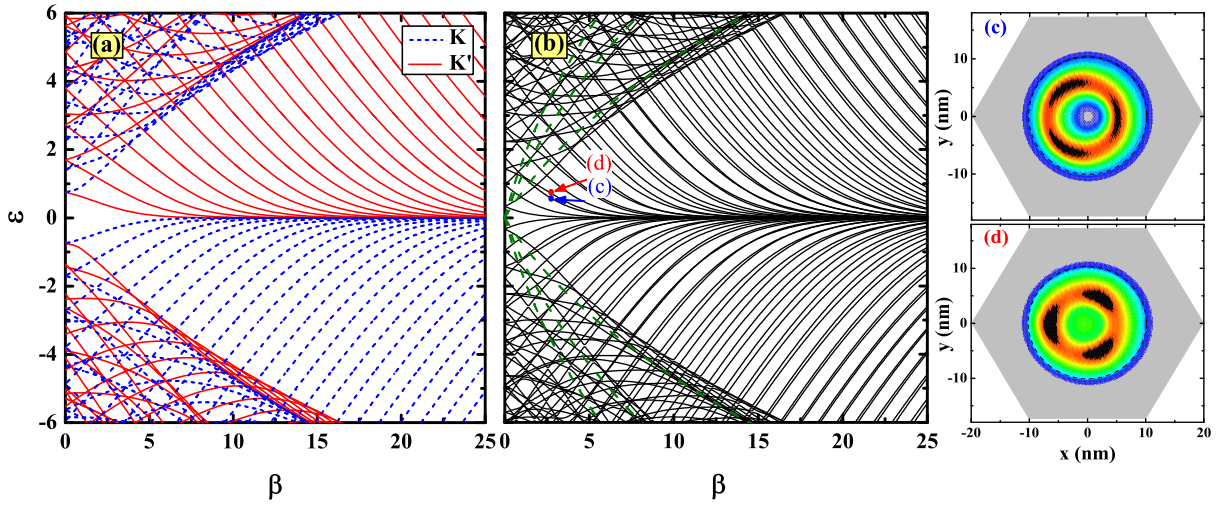


Figure 4.6: Energy spectrum of a circular BLG quantum dot as a function of a perpendicular magnetic field with $R = 10$ nm obtained within (a) the continuum model taking $-22 \leq m \leq 22$ and (b) the tight-binding model. The energy levels corresponding to the K and K' valleys are shown in (a) by the blue dashed and the red solid curves, respectively. The green dashed lines are the three first LLs of bulk BLG. Figures (c) and (d) show the squared total wave function ($|\Psi_{TB}|^2$) for the states indicated by (c) $\epsilon \approx 0.5348$ and (d) $\epsilon \approx 0.6746$ in figure (b), respectively. Blue (red, black) color is low (high, very high) density. The mass potential region is shadowed by the gray color.

the edge. We should emphasize that this symmetry is present in both zero and nonzero magnetic fields. For large magnetic field (i.e. when $l_B \ll R$) the carriers become strongly localized at the center of the dot and the energy levels approach the LLs of a pristine BLG sheet, i.e. $E_n = (\hbar v_F/l_B)\sqrt{2n+1 \pm 1}$ with $n = 0, 1, 2, \dots$. The energy states that approach the LLs of BLG satisfy the condition $m \leq n$ where n denotes the n th LL of BLG. For example those states that approach the zeroth and the first LLs respectively correspond to the $m \leq 0$ and $m \leq 1$ states. This behavior is qualitatively similar to that found in monolayer QDs with infinite-mass potential [111] and in semiconductor QDs [168].

Despite of having the advantage of analytical solutions using the continuum model, it is interesting to obtain the energy spectrum within the tight-binding approach in which we are able to study a QD in BLG with realistic edges. We employ a first-nearest-neighbor tight-binding formalism [111, 149] for circular QDs cut out from BLG and surrounded by a mass potential media where the sublattices A and B in both upper and lower layers are respectively connected to potentials $+V$ and $-V$ with $V = 1$ eV. In order to avoid the influence of outer edges we take a hexagonal structure with armchair edges for the mass potential media. The energy levels of a QD with radius $R = 10$ nm is shown in Figs. 4.6(a) and 4.6(b) respectively obtained using the continuum and tight-binding models.

A circularly cut-out region in bilayer graphene has a combination of both zigzag and armchair edges at the boundaries which mixes the states in the K and K' valleys. This makes the QD more complex system. Therefore, our results presented in Fig. 4.6(b) are only qualitatively comparable with those obtained using the previous continuum model in Fig. 4.6(a). In both cases, the energy levels approach the LLs of bulk BLG as magnetic field increases. The energy levels in both spectra exhibit similar magnetic field dependences. Two interesting features are found within the tight-binding calculations (see Fig. 4.6(b)): (i) the energy levels approach the zeroth LL of BLG in groups of two. This can be linked to the symmetry of the wave functions due to the confinement brought by the zigzag edges of the cut out circular QD. In Figs. 4.6(c) and 4.6(d) we show the electron densities corresponding to the points indicated by (c) and (d) (chosen from one group of energy levels) in Fig. 4.6(b). (ii) Degeneracies are lifted resulting in many more energy levels. This is a consequence of the mixing of the K and K' states due to the presence of armchair and zigzag edges at the circular boundary of the QD.

In Fig. 4.7, we show a contour plot of the probability density, separately for each layer, as a function of the normalized magnetic field and the dot radius for the states corresponding to the K valley and for (a, b) $m = 0$, (c, d) $m = 1$, and (e, f) $m = -1$. Left and right panels show respectively the densities $|\phi_A|^2 + |\phi_B|^2$ and $|\phi_{A'}|^2 + |\phi_{B'}|^2$ which correspond to the charge density in the different layers. As the magnetic field increases the electrons become more localized closer to the center of the dot. Our results clearly show different distributions of the electrons in each layer. This can be traced back to the definition of the infinite-mass boundary conditions in Eqs. (4.12a) and (4.12b) in which the spinor $\phi_{B'}$ has a different sign in the equations. This will influence the density balance in each layer. Another consequence of the boundary condition used in the continuum model is the symmetry between the four wave function components $\phi_{A(A')}^K(m) = \phi_{A(A')}^{K'}(m)$ and $\phi_{B(B')}^K(m) = \phi_{B(B')}^{K'}(m)$.

4.5 Cyclotron resonance

In cyclotron resonance experiments, e.g. see Refs. [169, 170, 171, 172, 173], transitions are induced between the ground state and excited states. We calculated the transition between the state i and j using the relation $|\langle \Psi_i | \rho e^{\pm i\phi} | \Psi_j \rangle|^2$ which dictates the selection rule $\Delta m = \pm 1$. Another selection rule which is due to the valley index in graphene is $\Delta\tau = 0$ implying that transitions between inter-valley states is not allowed [174, 175]. In Figs. 4.8(a) and 4.8(b) we show the transition energies $\Delta\epsilon$ and the corresponding transition rates as function of magnetic field from the two lowest energy states shown in the inset of Fig. 5, i.e. $E_{K'}(m = 0)$, $E_K(m = 1)$. The transitions between the states in K (or K') valley are labelled by $(m \rightarrow m')_{K(K')}$ where m and m' are respectively the angular momentum of the initial and final state. The transition energies for the states that approach the same (different) LLs of BLG decrease (increase) as β increases. Our results

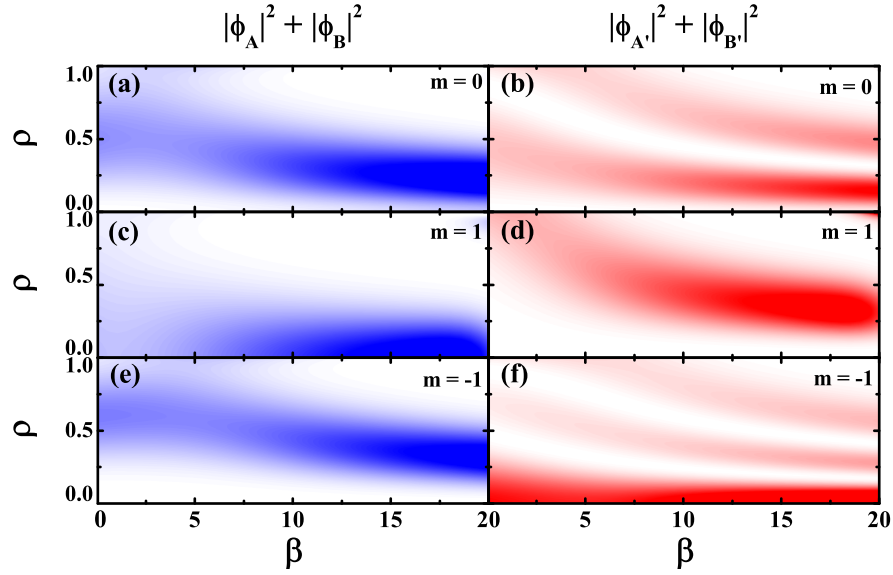


Figure 4.7: Contour plot of the electron probability density as a function of the normalized magnetic field β and the dot radius ρ for the lowest states of the K valley and with (a, b) $m = 0$, (c, d) $m = 1$, and (e, f) $m = -1$. Left and right panels show respectively $|\phi_A|^2 + |\phi_B|^2$ and $|\phi_{A'}|^2 + |\phi_{B'}|^2$ corresponding to the density in the different layers.

in Fig. 4.8(b) show that the transition rates decrease as the magnetic field increases. For large fields, e.g. for $\beta \gtrsim 7$, we found that the rates associated with the $(1 \rightarrow 0)_K$, $(0 \rightarrow 1)_{K'}$, and $(0 \rightarrow -1)_{K'}$ transitions approach each other. These transitions are weaker than that of the $(1 \rightarrow 2)_K$ transition which occurs between the states with higher angular momentums.

4.6 Conclusion

In this paper, we derived novel infinite-mass boundary conditions for BLG. The boundary conditions were obtained from a four-band continuum model. Subsequently, we employed these boundary conditions for a circular QDs in BLG surrounded by an infinite-mass potential. Such a mass potential can be realized experimentally using an appropriate substrate that breaks the sublattice symmetry of BLG resulting in the opening of an energy gap in the band structure of BLG.

Solving the four-band Dirac-Weyl Hamiltonian, in the vicinity of both K and K' valleys, we obtained analytically the energy levels and the corresponding wave functions of a BLG quantum dot. The energy spectrum was calculated in the absence and presence of a perpendicular magnetic field. We demonstrated that the energy spectrum exhibit two sets of states as function of dot radius R . The upper set of levels is related to the upper band of BLG and approach the inter-layer hopping term in BLG, i.e. $t \approx 400$ meV.

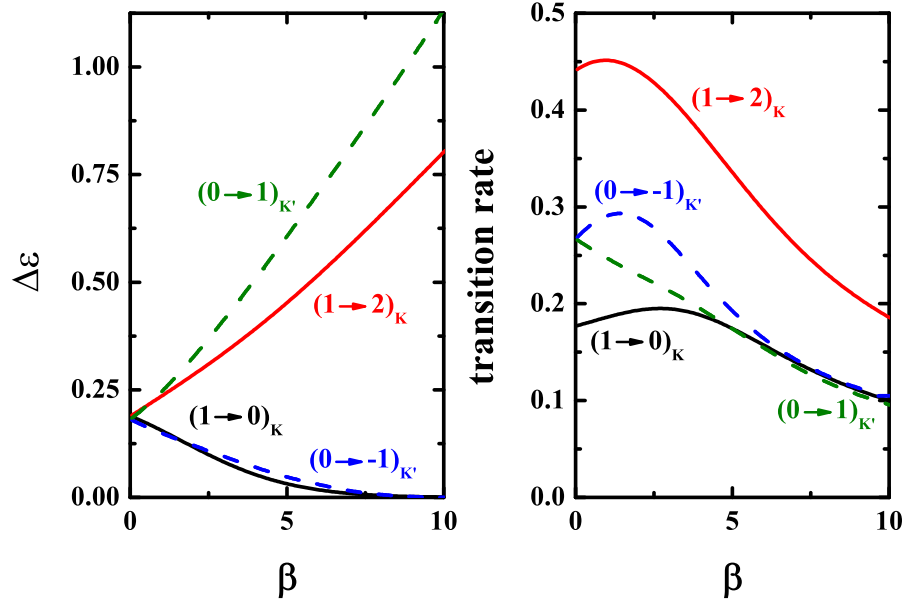


Figure 4.8: (a) Transition energies and (b) the corresponding transition rates as a function of the normalized magnetic field for a QD with radius $R = 70$ nm. The label $(m \rightarrow m')$ indicates the angular momentum of the initial m and the final m' states. The results corresponding to the K and K' valleys are respectively shown by the solid and dashed curves.

At zero magnetic field the spectrum shows a $1/R^2$ dependence for the lowest states and $1/R$ for the states in the upper set.

Our results show that the energy levels approach the LLs of a BLG sheet with increasing magnetic field. The spectrum shows the symmetry $E_K^{e(h)}(m) = -E_{K'}^{h(e)}(m)$ corresponding to a reversal of electron and hole states. This symmetry is present in the absence and presence of a magnetic field and it is a consequence of the confinement due to the infinity mass potential. Within the tight-binding approach, we obtained the energy levels of a BLG quantum dot with actual edges and showed that the results are qualitatively similar to those obtained with the continuum model. Further, we obtained the transition energies and evaluated the corresponding transition rates for the lowest energy levels in a BLG quantum dot.

The QDs we studied in this paper may be realized experimentally by using appropriate substrates containing a circular hole, e.g. hexagonal boron nitride [176], in order to induce an infinity mass potential on BLG.

Monolayer-bilayer graphene quantum dots

Using the tight-binding model, we study the confined states in two different hybrid monolayer - bilayer systems: (i) a hexagonal anti-dot in bilayer graphene under perpendicularly applied electric field and (ii) a hexagonal bilayer graphene dot surrounded by a hexagonal region of monolayer graphene. The behavior of the energy levels as a function of dot size and under an applied external magnetic field is investigated. In the presence of electrostatic bias we find that the energy spectrum for dots formed by zigzag edges presents states inside the gap whose features are marked by dot-localized states, edge states and mixed states coexisting together, whereas for dots with armchair edges one has only dot-localized states. We demonstrate that these dot-localized energy levels inside the gap formed by the potential bias decrease as the dot size increases as already expected for a quantum dot confined state, while edge and mixed states exhibit an opposite behavior. In the presence of both magnetic and electric fields for a zigzag dot we observe topologically protected states inside the gap and the convergence of the energy spectra to the Landau levels in all system configurations.

5.1 Motivation

Quantum dots (QDs) in graphene, a monolayer of graphite [1, 18], and in bilayer graphene are the subject of a considerable number of both theoretical and experimental studies [148, 177, 178] with the hope of benefiting of the exceptional properties of graphene, such as high carrier mobility and long spin coherence time for electronic and particularly spintronic applications. The absence of an energy gap in both monolayer (MLG) and bilayer graphene (BLG) spectrum is the main obstacle preventing straightforward fabrication of graphene QDs. However, BLG is in particular of interest, in which a perpendicular electric field realized by external gate potentials applied to the different layers of BLG can open an energy gap [79]. Recent theoretical [125, 153, 154, 155] and experimental [157, 158] studies demonstrate electron confinement into gate-defined QDs by tailoring the gap in BLG.

QDs in MLG are fabricated by direct etching of a pristine graphene sheet into the small flakes in which the shape and edges of the dot become very important. The electronic and transport properties of such QDs with different shapes and different edges are investigated extensively [77, 96, 111, 121, 149, 150, 151, 152]. There also exist several theoretical studies pertinent to BLG flakes in which, in contrast to the gate-defined QDs in BLG, edge disorder influences the electronic properties of the dot significantly [159, 160].

Realistic few layer graphene samples extracted from graphite often contain patches of both MLG and BLG. Electronic transport measurements demonstrated the importance of monolayer-bilayer interface states in transport and electronic properties of quantum structures fabricated based on such samples [179, 180, 181, 182, 183, 184]. The monolayer-bilayer interface states were theoretically investigated in a system of two semi-infinite MLG and BLG sheets with both zigzag- and armchair-terminated junctions in the absence [185, 186] and presence [187, 188] of an external magnetic field.

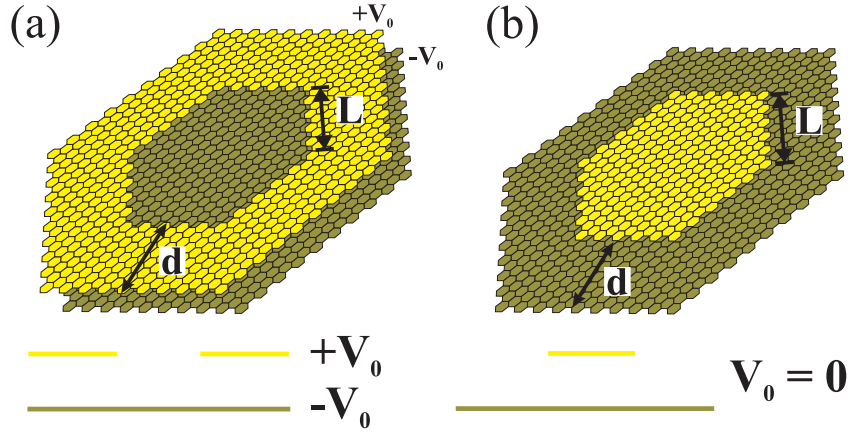


Figure 5.1: (Color online) Sketches of the studied systems in this work composed by hexagonal shaped quantum dots of size L in bilayer graphene created by (a) cutting out atoms in the inner region of the top layer and (b) with the top layer being smaller than the bottom one. In both cases (a) and (b), the outer edges are taken armchair forming a hexagonal dot with a larger size. A cross-section view of the dots are presented at the bottom of each system. The distance between the layers is d , that was taken as $\approx 100 \text{ \AA}$.

The existence of both monolayer and bilayer islands in exfoliated graphene samples, motivated us to propose different types of graphene QDs consisting of both MLG and BLG. In this paper, we study the confined states into two different systems schematically depicted in Figs. 1(a) and 1(b): (i) a hexagonal MLG dot surrounded by a hexagonal biased BLG region, and (ii) a hexagonal BLG dot surrounded by a hexagonal region of MLG. The outer boundaries of the considered systems are terminated by armchair edges in order to avoid the influence of edge states corresponding to the outer hexagonal dot. The found QD states are therefore not influenced by the finite size of the total system and are therefore representative for an infinite system. Using nearest-neighbour tight-binding formalism we obtain the energy levels of these QDs for both zigzag and armchair

terminated monolayer-bilayer interface. We report our results in the absence and presence of a perpendicular magnetic field.

The paper is organized as follows. In Sec. II, we briefly discuss the tight-binding approach used in our numerical calculations. In Sections III(A) and III(B) we present the energy levels of the QDs illustrated in Figs. 5.1(a) and (b), respectively, for zero and external magnetic field. Finally we present concluding remarks in Sec. IV.

5.2 Numerical Method

In order to describe electrons in an AB-stacked bilayer graphene, we work within the tight-binding approximation, whose nearest-neighbor tight-binding Hamiltonian can be written as

$$\begin{aligned}
 H_{TB} = & \sum_{n=1}^2 \sum_i (\epsilon_{n;i} + V_{n;i}) c_{n;i}^\dagger c_{n;i} \\
 & + \sum_{n=1}^2 \sum_{\langle i,j \rangle} \left(\tau_{ij} c_{n;i}^\dagger c_{n;j} + \tau_{ij}^* c_{n;i} c_{n;j}^\dagger \right) \\
 & + \tau_\perp \sum_{i,j} \left(c_{1;i}^\dagger c_{2;j} + c_{1;i} c_{2;j}^\dagger \right),
 \end{aligned} \tag{5.1}$$

where $c_{n;i}$ ($c_{n;i}^\dagger$) annihilates (creates) an electron in site i , with on-site energy ϵ_i . n is the layer index, the sum $\sum_{\langle i,j \rangle}$ is taken only between nearest neighbor sites i and j in each layer and τ_{ij} (τ_\perp) is the (intra-) inter-layer hopping energy. Let us label the bottom layer as layer 1 and the upper layer as layer 2. Thus, the first term of H_{TB} corresponds to the on-site energy and external potential, the second term is related to the Hamiltonian for each layer and the third term describes the interlayer coupling in which we consider only the hopping between the two atoms stacked right on top of each other. The potential in each site i and in each layer n is represented by $V_{n;i}$ and was included only for the system configuration shown in Fig. 5.1(a) where we considered the symmetric situation $V_{1;i} = -V_0$ and $V_{2;i} = V_0$ for the bottom and top layers, respectively. The way that we apply the bias potential is similar as has been done in Ref. [160], where it was assumed opposite potentials applied to the two layers, thereby allowing the conservation of electron-hole symmetry. Note that different works the external gate potential was taken just in one of the layers while keeping the other at a constant value [154]. By applying an external electrical potential, a gap in the energy spectrum is opened. Due to this feature, different kinds of confining structures in bilayer graphene can be achieved [160]. In this perspective quantum dots [154, 155] and rings [121, 156, 166] in bilayer graphene have been already studied analytically by applying appropriate gate potentials. Nowadays, nanostructure fabrication allows for an accurate spatial control of the electrostatic potential and this independent on the top and bottom layer [189, 190] of suspended BLG [157] and in addition in a split and localized way for the bottom [191] and top [192] gates.

The actual outer hexagonal structure used in this work has dimension of $\approx 325,18$ Å which corresponds to a length of ≈ 77 carbon hexagons in each side. The tight-binding approach applied here has been already discussed [79, 80, 193] and used [159, 160] previously, as well as in the theoretical treatment of the interface between MLG and BLG [185, 188].

5.3 Results and discussion

5.3.1 Zero magnetic field

Let us now investigate the energy spectrum for the system configurations Figs. 5.1(a) and 5.1(b) in the absence of a magnetic field and in the presence of a bias voltage for the former case. In both cases we verify the dependence on the type of edge of the inner dot: (i) the inner edge of the top hexagonal anti-dot (for Fig. 5.1(a)) and (ii) the hexagonal bilayer dot in the top layer (for Fig. 5.1(b)). Figure 5.2 shows the energy spectrum as a function of the anti-dot size L for hexagonal BLG quantum dots with zigzag edges as sketched in Fig. 5.1(a). In the bottom (top) layer a potential $-V_0$ ($+V_0$) with $V_0 = 0.1$ eV was applied such that it opens a gap of $2V_0$ in the spectrum, as can be seen in Fig. 5.2. Since the dot has zigzag edges, we obtain many energy levels inside the gap. This characteristic is a signature of the zero energy states observed in MLG quantum dots with zigzag edges [149, 194].

Another important remark about Fig. 5.2 is related to the anti-crossings that appear in the spectrum, as shown in the enlarged region (yellow circle) around $L \approx 110$ Å. The anti-crossing behavior can be better understood when we look at the corresponding electron probability densities for the points (1 to 15) indicated in the zoom. These results for $|\psi|^2 = |\psi_1|^2 + |\psi_2|^2$, where $\psi_{1(2)}$ represents the wave function in the bottom (top) layer, are shown in Fig. 5.3 and they indicate that at the anti-crossing (points 6, 7, 9 and 10) the electrons are confined due to the interplay between edges states corresponding to the zigzag edges and inside the dot owing to bias voltages, as presented in Fig. 5.3(c). The levels with increasing energy indicated by points 1, 2 and 3 and shown in Fig. 5.3(a), correspond to states that are confined at the zigzag edges near the MLG and BLG junction. It was realized that, even though the bottom layer does not present explicit edges close to the middle of the system, the electron feels the edges corresponding to interlayer coupling near to the MLG and BLG junction. The same kind of confinement was observed for the points 8, 13, 14 and 15 as shown in Figs. 5.3(d) and 5.3(e), respectively. Each set of points formed by (a) 1, 2 and 3, and (d) 8, 13 and 14 have the same symmetry and all of them are edges states whose only difference is the fact that they are shifted by $\pi/3$ due to the C_3 symmetry which belongs to the hexagonal geometry. It can be observed that the levels 1, 2 and 3 that are going up are almost degenerated and only one of them (3) keeps increasing and the others two edge states (1 and 2) undergo a transition from a mix

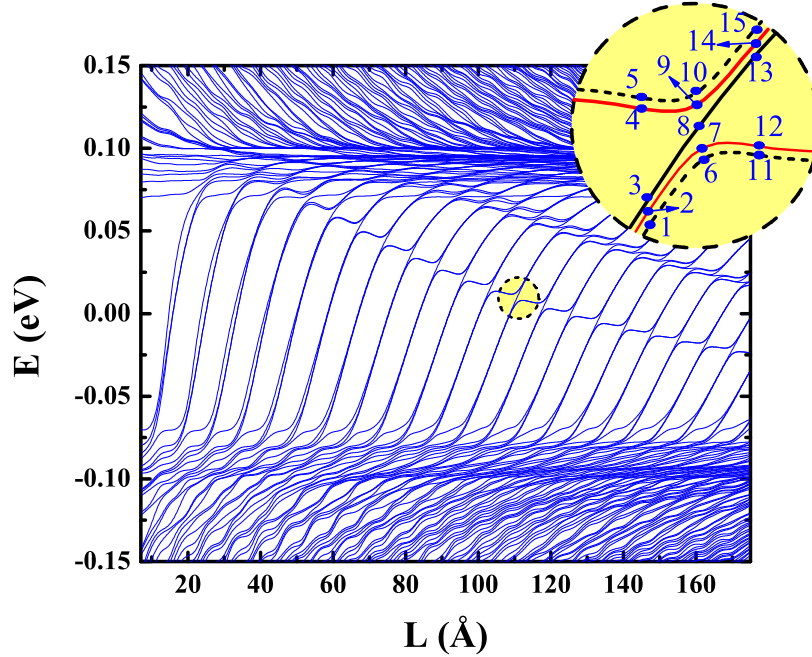


Figure 5.2: (Color online) Energy spectrum of hexagonal BLG quantum dots with zigzag edges as a function of dot size L in the presence of a symmetric electrical bias with $V_0 = 0.1$ eV for the system represented in Fig. 5.1(a). A zoom of the yellow region is shown to emphasize the behaviour around the anti-crossing of different states.

of edge states and states inside the dot (6 and 7) to just states localised inside the dot (11 and 12). The level corresponding to point 3 remains to be an edge state as indicated by points 8 and 13 in the same line, as shown in Fig. 5.3(d). The levels corresponding to states 4, 5, 11 and 12 are states purely inside the dot and they are decreasing as the anti-dot size increases, as shown in Fig. 5.3(b). Thus, it can be summarized that the states inside the gap, for an anti-dot created at the top layer of bilayer graphene and in the presence of a gate potential, are due to the interplay of zigzag edge states that are increasing in energy with L and states completely inside the anti-dot located only on the bottom layer that present decreases in energy with L .

In the quest to obtain an energy spectrum which has a gap, but on the other hand that is not too polluted by other states as observed in the spectrum for anti-dot formed by zigzag edge in bilayer graphene shown in Fig. 5.2, we perform now a study in the case that the cut out bilayer graphene anti-dot is built with armchair edges. The result for the energy levels of armchair anti-dots as a function of the side length L is presented in Fig. 5.4. Note that if we put the spectrum shown in Fig. 5.4 on the top of the spectrum demonstrated in Fig. 5.2, one verifies that they match to a very good agreement, such as all energy levels inside the gap (for energies between $E \in [-V_0, V_0]$) decrease in the same way and with the same slope. These decreasing energies correspond to states that are confined inside the dot created in the bottom layer. It can be seen in Figs. 5.5(a, b, c) for the point 1 ($E \approx 0.03499$ eV and $L \approx 78.10$ Å) in the spectrum of Fig. 5.4 that

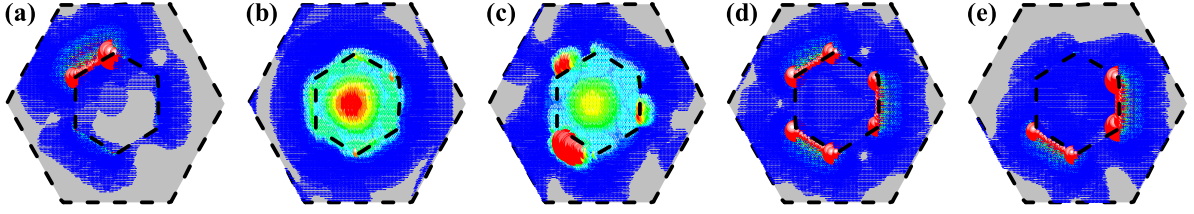


Figure 5.3: (Color online) Squared total wave function ($|\psi|^2 = |\psi_1|^2 + |\psi_2|^2$) for the states labeled in Fig. 5.2 as (a) 1, 2, 3, (b) 4, 5, 11, 12, (c) 6, 7, 9, 10, (d) 8, 13, 14 and (e) 15. The wave functions corresponding to the states represented in each item from (a) to (d) have the same symmetry, but they have a phase difference such that are rotated as related to each other. Small (large) circle with blue (red) color represents low (high) density. The bilayer region is shadowed by the gray color.

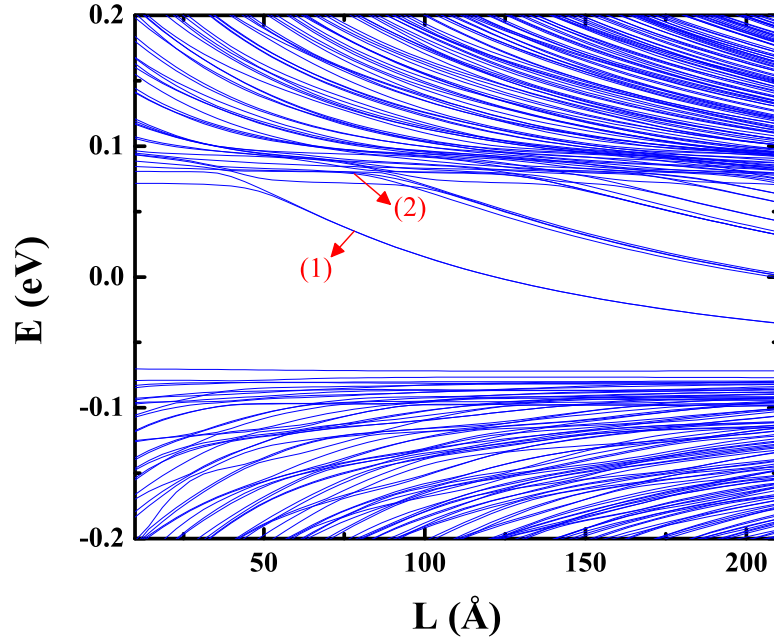


Figure 5.4: (Color online) Energy spectrum of hexagonal BLG quantum dots with armchair edges as a function of dot size L in the presence of electrical bias with $V_0 = 0.1$ eV for the system represented in Fig. 5.1(a).

the probability density is strongly localised (red color) around the center of the dot in the bottom layer (a), whereas (b) in the top layer the electron density is localised around the anti-dot center. It implies that the total probability density is largely localized in the center of the system. Thus, it indicates that most significant difference between the energy spectra for the zigzag (Fig. 5.2) and armchair (Fig. 5.4) edged QDs is the presence of states inside the gap that correspond to edge states localised at the inner zigzag edge. Moreover, as for the zigzag case (Fig. 5.2) the energy levels above ($E > V_0$) and below ($E < -V_0$) the gap region converge to the values V_0 and $-V_0$, respectively. These states are spread out over the bilayer graphene, *i. e.* they are localized on the large hexagonal

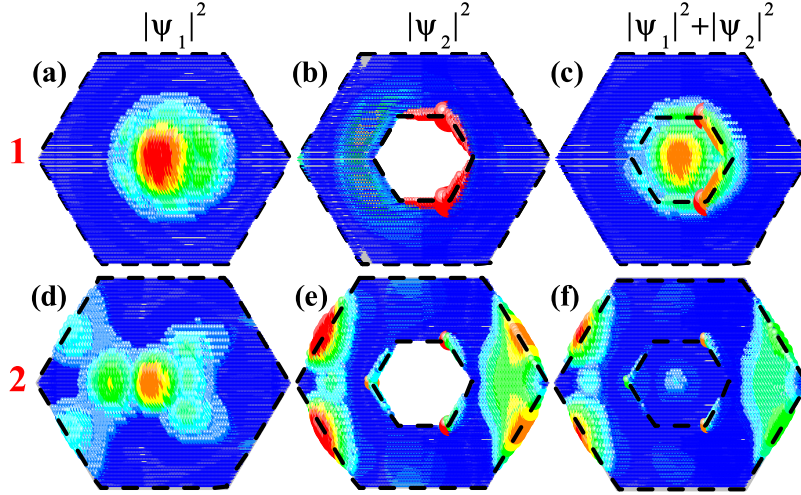


Figure 5.5: (Color online) Squared total wave function $|\psi|^2$ and contribution from each layer: bottom $|\psi_1|^2$ and up $|\psi_2|^2$ for the states indicated by 1 and 2 in Fig. 5.4. Small (large) circle with blue (red) color represents low (high) density. The bilayer region is shadowed by the gray color.

bilayer dot. However, there is a transition between dot-localized states that are inside the gap ($|E| < V_0$) and states that are completely spread along the large hexagonal bilayer dot ($|E| > V_0$). These energy levels can be seen immediately below $E \approx V_0$ and above $E \approx -V_0$. Their dependence on L is almost flat and the counter plot of their density probabilities demonstrate a mix of dot-localized state for the bottom layer and a spread state along the top layer. It is illustrated in Figs. 5.5(d, e, f) for the point 2 indicated in the armchair energy spectrum shown in Fig. 5.4, respectively for (d) bottom layer $|\psi_1|^2$, (e) top layer $|\psi_2|^2$ and (f) the total probability $|\psi_1|^2 + |\psi_2|^2$.

As a suggestion of another kind of confinement structure in bilayer graphene, we shall study the dependence of the energy levels of the system sketched in Fig. 5.1(b) as a function of the flake size L that is surrounded by hexagonal monolayer graphene. This analysis is done in the absence of any external potential, as can be identified in the schematic cross-section view at the bottom part of the system, *i. e.* we assumed that $V_{1(2)} = 0$. A general feature noticed in this kind of system is that the energy spectrum for quantum dots formed by both edges, zigzag and armchair shown in Figs. 5.6(a) and 5.6(b) respectively, does not change for sizes smaller than $\approx 25 \text{ \AA}$ ($\approx 40 \text{ \AA}$) for the zigzag (armchair) case. This invariance, related to the type of edges, is due to the fact that for small size of the dot in the bilayer region the electron does not feel and does not recognize the system as a bilayer, but rather as monolayer graphene. Thus, for small sizes $L \lesssim 25 \text{ \AA}$ (zigzag edge) and $L \lesssim 40 \text{ \AA}$ (armchair edge), the energy spectrum forms plateaus converging to values, that match the same values for both edge configurations, as shown by the black dashed lines in Fig. 5.6. These are the monolayer energy levels, since for both edge termination, systems (a) and (b) have the same size. Notice that in general,

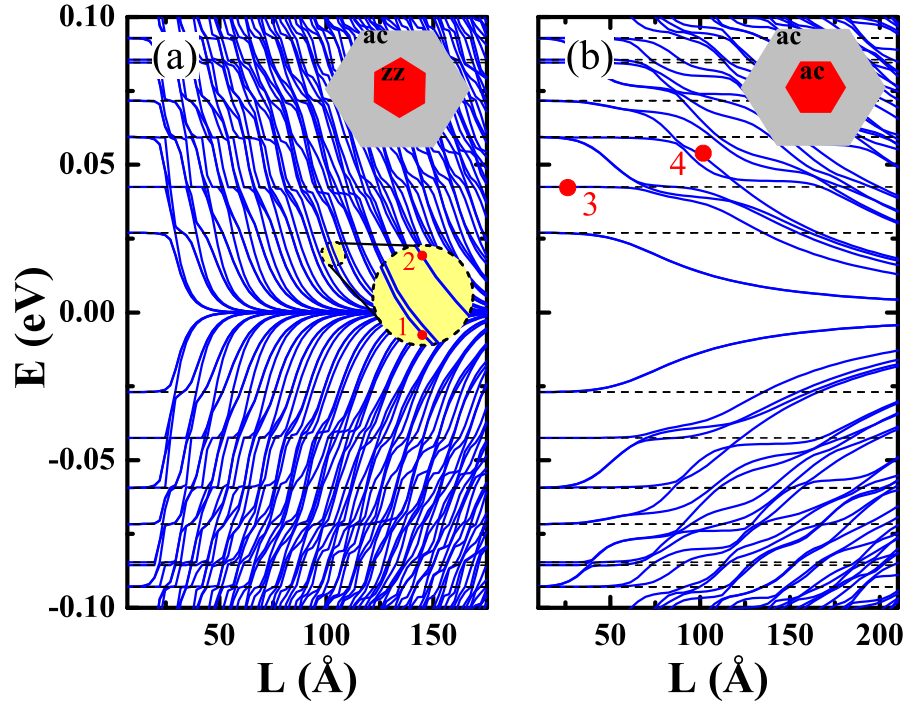


Figure 5.6: (Color online) Energy spectrum of hexagonal BLG quantum dots with (a) zigzag and (b) armchair edges as a function of dot size L for the system represented in Fig. 5.1(b). The dashed lines are the energy levels of the monolayer system that has the same dimension as the bottom layer for the bilayer system sketched in Fig. 5.1(b).

the degeneracy of the energy levels is lifted and the plateaus become less pronounced as one increases the size L , resulting in many more energy levels. An illustration of an exception in the degeneracy breaking is the first state in the spectrum for the armchair dot in Fig. 5.6(b), that remains a degenerate state. For both edge terminations, Fig. 5.6(a) zigzag and 5.6(b) armchair, the energy levels decrease when L increases, being different in two aspects: (i) for the zigzag case, more states are obtained and they decrease with L converging to zero-energy and forming plateaus when E matches the monolayer levels; and (ii) a large gap in the armchair spectrum stays open even for large dot sizes.

To confirm our statements about delocalized states for small L and dot-localized states for large L , we show in Fig. 5.7 the modulus squared of the wave functions for the points 1, 2, 3 and 4 indicated in panels (a) and (b) of spectrum presented in Fig. 5.6. As shown in the zoom on the circular panel of Fig. 5.6(a), there are three states that are going down being two of them approximately degenerate ($E \approx 0.02150$ eV and $E \approx 0.02159$ eV), given by the point 1 located at $L \approx 100.84$ Å. It was verified that these two states come from the same initial plateau, hence their wave functions have the same behavior and type of symmetry, as shown in Fig. 5.7(a). Both levels are essentially edge states and only differ by a rotation of π . The other energy level, point 2 shown in Fig. 5.7(b) with energy $E \approx 0.02556$ eV, is a combination of edge and center localized state. The probability densities for armchair dots are shown in Figs. 5.7(c) and 5.7(d) corresponding

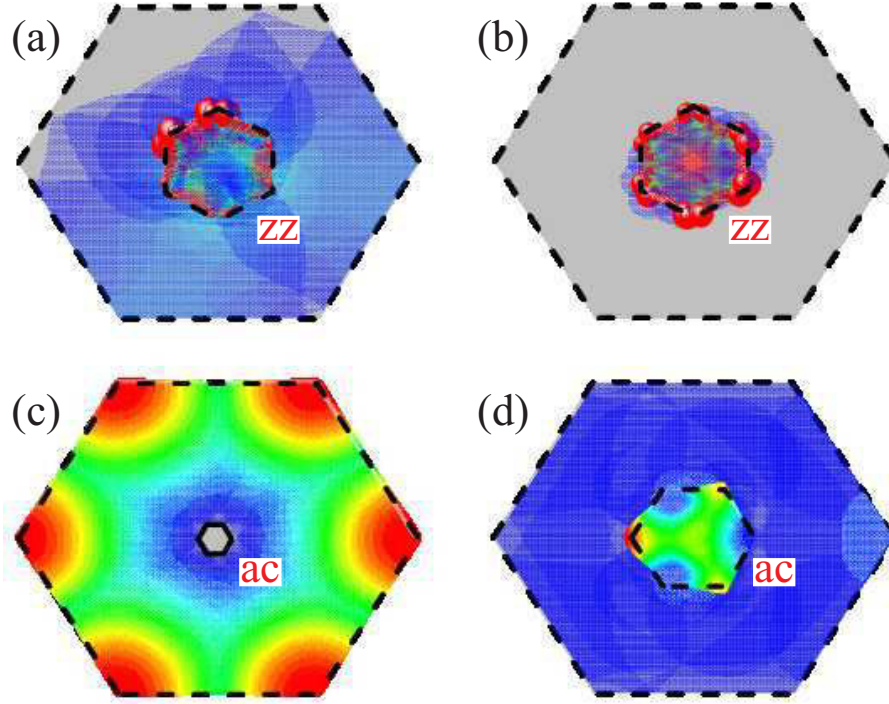


Figure 5.7: (Color online) Squared total wave function $|\psi|^2$ for the states indicated by (a) 1 and (b) 2 in Fig. 5.6(a) for the zigzag (zz) case and (c) 3 and (d) 4 in Fig. 5.6(b) for the armchair (ac) case. Small (large) circle with blue (red) color represents low (high) density. The bilayer region is shadowed by the gray color.

to the points 3 and 4 in Fig. 5.6(b), respectively. The point 3 placed on the plateaus energy range ($L \approx 22, 72 \text{ \AA}$) is an example of a delocalized state that is spread out over only the monolayer graphene. On the other hand, for large dot size, as for example for $L \approx 99.40 \text{ \AA}$ given by point 4, one finds dot-localized state with $|\psi|^2$ located in the middle of the bilayer system. Thus, we can verify that the proposed structure sketched in Fig. 5.1(b) can be used as a confined system for carriers in MLG/BLG junction.

5.3.2 In the presence of a perpendicular magnetic field

In this section, we include an external magnetic field, with possible addition or not of a bias voltage for the system sketched in Fig. 5.1(a). The effect of an external magnetic field is incorporated in the tight-binding model via the Peierls substitution, *i. e.* a phase is included in the inter-layer hopping parameters, such that $\tau_{ij} \rightarrow \tau_{ij} \exp \left[i \frac{e}{\hbar} \int_j^i \vec{A} \cdot d\vec{l} \right]$, where \vec{A} is the vector potential that corresponds to the applied magnetic field. We conveniently choose the Landau gauge $\vec{A} = (0, Bx, 0)$, for a magnetic field perpendicular to graphene $\vec{B} = B\hat{z}$. For the chosen gauge, one has that the Peierls phase is zero and $\exp i \frac{2\pi x}{3a} \frac{\phi}{\phi_0}$ in the x - and y -directions, where $a = 1.42 \text{ \AA}$ is the lattice parameter of graphene, $\phi_0 = h/e$ is the magnetic quantum flux and $\phi = 3\sqrt{3}a^2 B/2$ is the magnetic flux through a carbon hexagon. The magnetic field has no effect on the intra-layer hopping τ_{\perp} .

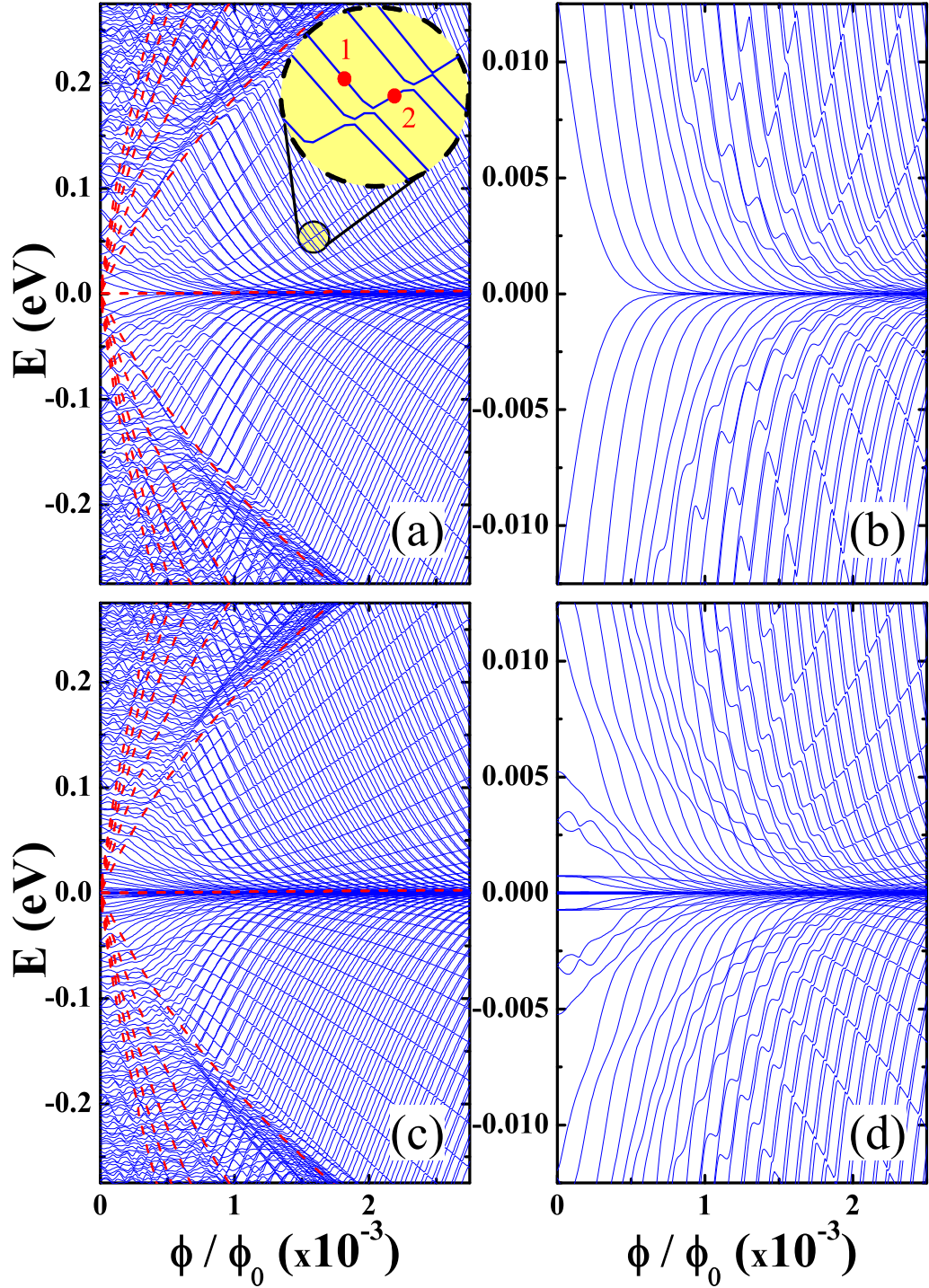


Figure 5.8: (Color online) Energy spectrum of hexagonal BLG quantum dots with (a, b) armchair and (c, d) zigzag edges as a function of magnetic flux in the absence of electrical bias for the system represented in Fig. 5.1(a). The red lines in (a) and (c) correspond to the first six Landau levels of an unbiased bilayer graphene. (b) and (d) show a zoom closer around $E = 0$.

Let us first consider the unbiased case, and investigate the effect of a magnetic field. In Fig. 5.8 we show the results for the energy spectrum of hexagonal bilayer graphene quantum dots with (a, b) armchair and (c, d) zigzag edges as a function of the magnetic flux (ϕ/ϕ_0). In this section, our results for the zigzag and armchair edges are obtained for fixed anti-dot side lengths, respectively $L \approx 49.19 \text{ \AA}$ and $L \approx 52.54 \text{ \AA}$ corresponding to $N = 20$ and $N = 13$ hexagonal carbon rings in each edge. In general, for both edge terminations, as the magnetic flux increases, the energy levels approach the Landau levels of an unbiased bilayer graphene[86, 155], represented by the red lines, and more and more excited states converge to the zeroth Landau level, which naturally produces (anti)-crossings between the excited states, as shown in Figs. 5.8(b) and 5.8(d). Furthermore, these figures clearly demonstrate that the energy spectrum possesses an electron-hole symmetry, *i. e.* $E_h = -E_e$, where h(e) denotes hole (electron). Comparing Figs. 5.8(a, b) and 5.8(c, d), we can realize that the energy levels are almost similar, except at small magnetic flux values in which: (i) the spectrum for zigzag quantum dots exhibits edge states that are not present in armchair dots for the levels near zero energy and (ii) in addition, the spectrum for armchair quantum dots exhibits a gap around $E = 0$. As magnetic flux increases, the degeneracy of the energy levels is lifted resulting in a closing of the energy gap in the spectrum of armchair quantum dots. These two behaviours given by the presence of many zero energy states for zigzag hexagonal dots and by the presence of a gap in the energy spectrum for armchair hexagonal dots for $B = 0$ are also found in zigzag and armchair quantum dots in monolayer graphene under the influence of an external magnetic field, as it has been already studied in Refs. [111], [138] and [194]. These results are comparable between monolayer and bilayer quantum dots, since the confinement created by the system sketched in Fig. 5.1(a) is located mainly in one layer, *i. e.* the bottom one, in this manner the confined states exhibit qualitatively similar behavior as if the system were only composed of one layer. The interplay between confinement by the magnetic field and quantum dot confinement is responsible for the appearance of several crossings and anti-crossings in the energy spectrum for both edge termination cases.

Figure 5.9 depicts the density distribution for the states denoted in the Fig. 5.8(a) that are emphasized in the yellow circular region and shown in the inset by the red points 1 and 2. The points 1 and 2 have respectively energies $E \approx 0.05638 \text{ eV}$ and $E \approx 0.05369 \text{ eV}$ and magnetic flux $\phi/\phi_0 \approx 0.00154$ and $\phi/\phi_0 \approx 0.00159$. As one observes in the inset, the pair of states that have nearby energy they switch their behaviour at the anti-crossing. This kind of feature can only be captured by the tight-binding approach, because in the continuum model these increasing states should be formed by a single state. These seemingly degenerate states become even more separated as the magnetic flux increases, which is related to the lifting of the degeneracy by the magnetic field. Thus, to identify the origin of each tendency we plot the contribution of each layer to the electron density in separated way for the points 1 and 2 corresponding to the states

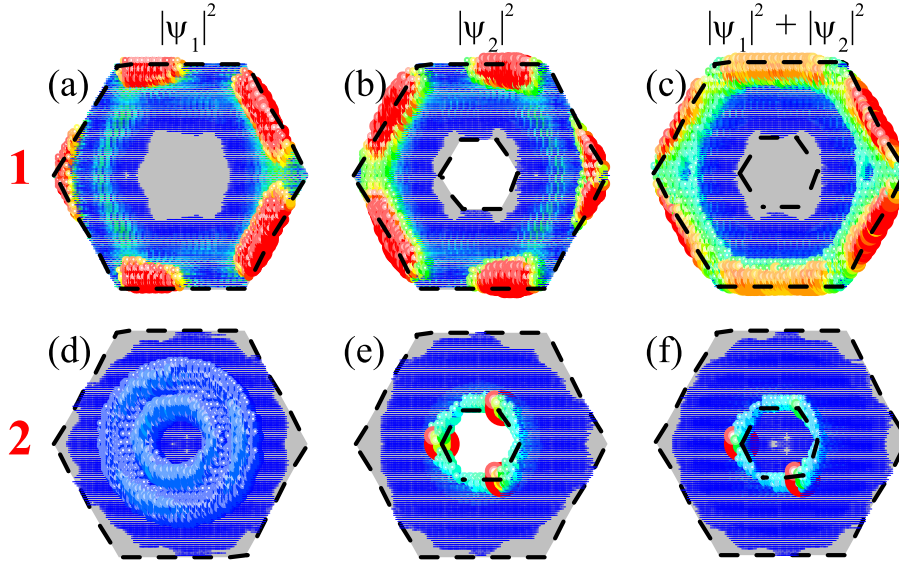


Figure 5.9: (Color online) Squared total wave function $|\psi|^2 = |\psi_1|^2 + |\psi_2|^2$ in each layer: bottom $|\psi_1|^2$ and upper $|\psi_2|^2$ for the states indicated by 1 and 2 in Fig. 5.8(a). Small (large) circle with blue (red) color represents low (high) density. The bilayer region is shadowed by the gray color.

that are respectively decreasing and increasing with B . Figures 5.9(a) and 5.9(b) show respectively the bottom and top layer contribution for the wave function corresponding to the electron states indicated by the point 1, while Figs. 5.9(d) and 5.9(e) are for the wave function of the point 2. The squared total wave function for the points 1 and 2 are shown in Figs. 5.9(c) and 5.9(f). Notice that both group of states are edge states, but located in different regions of the bilayer system. This resembles the inner and outer edge states found in quantum rings made of monolayer graphene [138].

The dependence of the energy levels of hexagonal BLG quantum dots on the magnetic flux for non-zero bias field is shown in Fig. 5.10, respectively for anti-dots with (a, b) arm-chair and (c, d) zigzag edges. The applied bias was $V_0 = 0.1$ eV. As can be seen, the energy spectrum for both edge terminations approaches the Landau levels, that in this case are the Landau levels for biased bilayer graphene with $V_0 = 0.1$ eV, shown by dashed red lines. As has been already reported [86, 195, 196], the Landau levels for biased bilayer graphene is given by $\gamma = [\epsilon - u_0]^2/2 + (\Delta u)^2/8 \pm 1/2\sqrt{\tau'^2[(\epsilon - u_0)^2 - (\Delta u/2)^2] + [\beta - \Delta u(\epsilon - u_0)]^2} = (\beta/2)(2n + |m| + m + 1)$, being $n = 0, 1, 2, 3, \dots$, m is the angular momentum label, $\beta = \frac{4\pi}{3\sqrt{3}a^2} \frac{\phi}{\phi_0}$, $u_1 = -u_2 = -V_0/\hbar v_F$, $\epsilon = E/\hbar v_F$, $\tau' = \tau/\hbar v_F$, v_F is the Fermi velocity, $\Delta u = u_2 - u_1$ and $u_0 = (u_1 + u_2)/2$.

A striking feature of these results is that the energy levels have a non-monotonic dependence on the magnetic field, which is not found for the unbiased case. As one can notice, the vast majority of Landau levels increase as the magnetic flux increases, but there are two states, for electrons and holes, that intersect each other at $E = 0$. In addition,

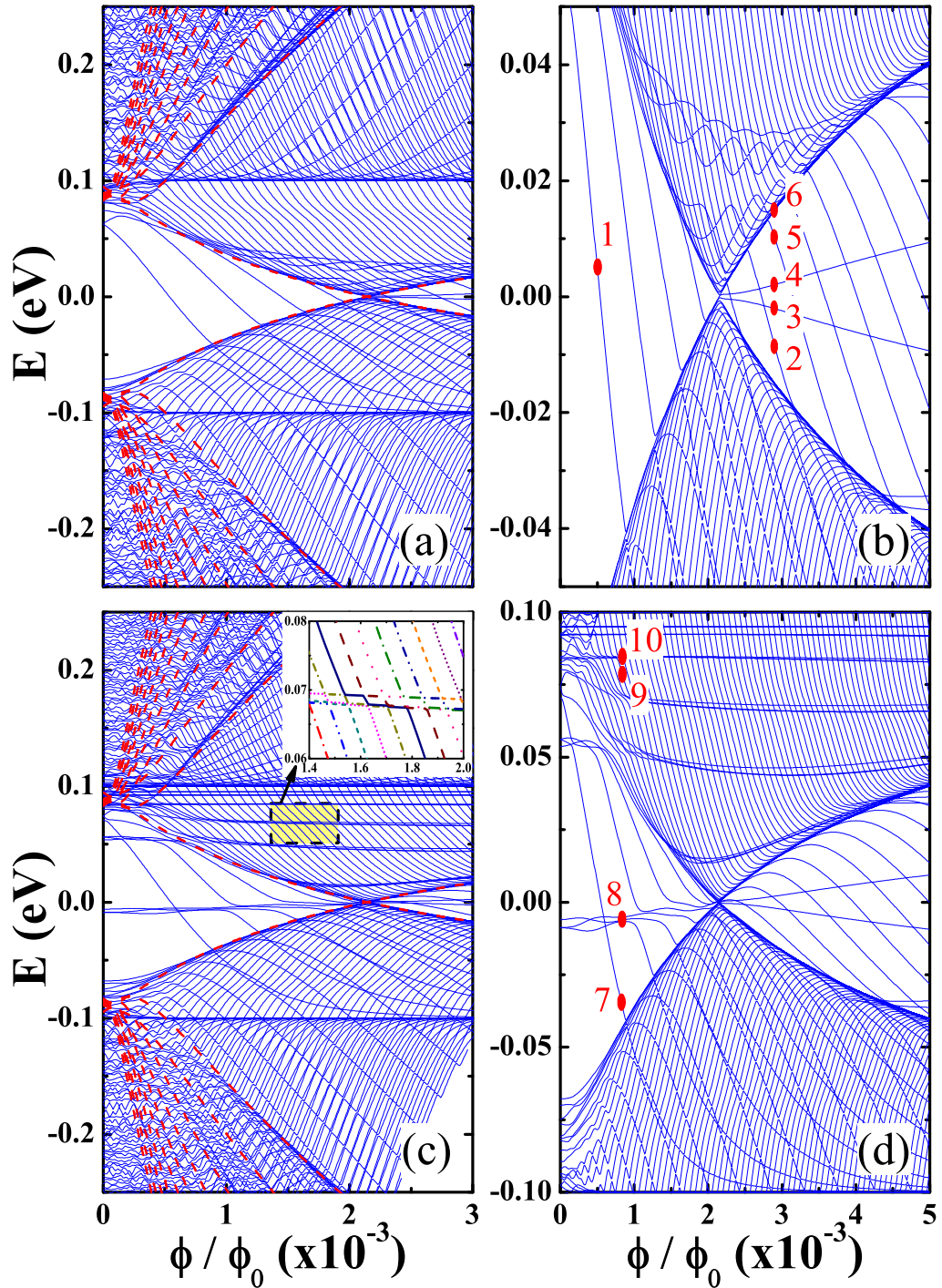


Figure 5.10: (Color online) Energy spectrum of hexagonal BLG quantum dots with (a, b) armchair and (c, d) zigzag edges as a function of magnetic flux in the presence of electrical bias with $V_0 = 0.1$ eV for the system represented in Fig. 5.1(a). The red lines in (a) and (c) correspond to the first six Landau levels of a biased bilayer graphene. (b) and (d) show a zoom closer around $E = 0$ to emphasize the points 1 – 10 and the opening of the energy levels around the zero energy.

another aspect can be observed in the Landau levels of biased BLG and, consequently, in the energy spectrum calculated here, is the appearance of crossings at very small values of ϕ/ϕ_0 . As already studied in Ref. [86], the crossings between the Landau levels for a biased bilayer graphene in each branch (positive and negative levels) occur at larger values of the magnetic field as the potential difference increases. These two features arise from the potential difference between the layers and can be explained by taking into account the non-parabolicity of the band structure of biased bilayer graphene, which displays a mexican hat shape that becomes more pronounced as the potential difference becomes larger.

One important consequence of the combination of the magnetic field together with the presence of an electrostatic confinement is that it breaks the inversion symmetry of the bilayer, *i. e.* the spectrum is now electron-hole asymmetric $E_h \neq -E_e$. Furthermore, one can notice from Fig. 5.10 that: (i) for small values of ϕ/ϕ_0 the spectrum for both edge termination possesses a large gap around $E = 0$ that becomes less pronounced as the magnetic flux increases; (ii) two different bands can be recognized, one for the levels inside the gap between $E \in [-V_0, V_0]$ and the other for the highest states that converge to the $E = \pm V_0$ axes defined by the value of the bias; (iii) similarly as in the unbiased case, *i. e.* Fig. 5.8, pairs of states with nearby energy values are decreasing together and end up converging to the $E = \pm V_0$ axis in the present case and to the zeroth Landau level in the former case, but here for instance they seem to cross each other in the same magnetic field range; (iv) the positive part of the spectrum that forms the band located inside the gap has a different characteristic as compared with the negative part of the spectrum, in which the negative part presents many crossings that are not present in positive one; and (v) states that do not change with the magnetic field are observed only for zigzag BLG quantum dots, and can be associated with topologically protected (edge) states, since their properties are preserved even when some external parameter varies. These topologically protected states are observed only for the positive part of the zigzag quantum dot spectrum inside the gap and, according to the inset shown in Fig. 5.10(c), which presents a zoom of the yellow rectangle around $\phi/\phi_0 \approx 1.7 \times 10^{-3}$, one can realize that these topological states in fact are composed not really by a single state, but rather by a band of curves that has a flat behaviour for the same specific magnetic flux values.

Let us now investigate the density distribution for some states inside the gap region, as denoted by points 1–6 and 7–10, respectively for armchair and zigzag edge terminations in the presence of both magnetic field and a gate voltage, as shown in Figs. 5.10(b) and 5.10(d). We first analyze the wave functions for anti-dots formed by inner armchair edges, whose plots are shown in Fig. 5.11 for the points 1–6. As already expected, and similar to Figs. 5.5(a)–5.5(c) corresponding to the armchair anti-dot case in Sec. 5.3.1, the decreasing states inside the gap are dot-localized states, as observed for the state shown in Fig. 5.11(a) corresponding to the point 1 in the spectrum given by Fig. 5.10(b). All the decreasing states inside the gap region and before the crossing between

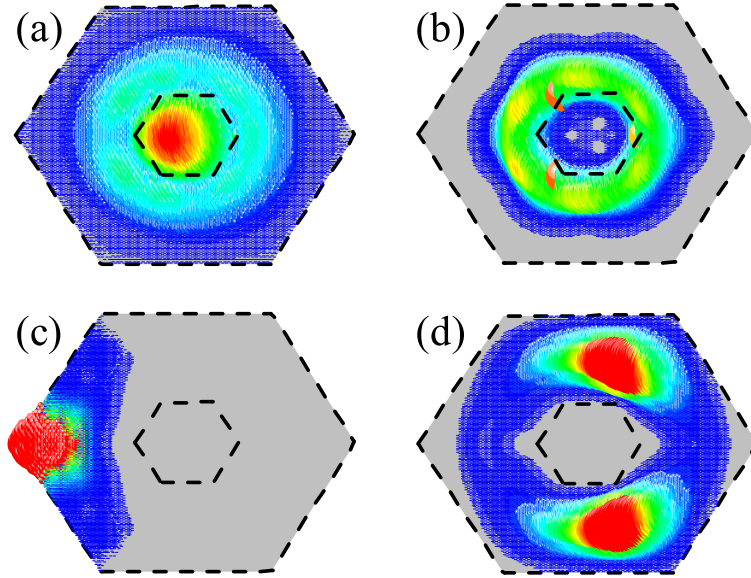


Figure 5.11: (Color online) Squared total wave function $|\psi|^2$ for the states indicated in Fig. 5.10(b) for the system sketched in Fig. 5.1(a) with armchair edges, such as the points 1 – 6 correspond to the plots (a) 1, (b) 2 and 5, (c) 3 and 4 and (d) 6. Small (large) circle with blue (red) color represents low (high) density. The bilayer region is shadowed by the gray color.

the two zeroth biased Landau levels have the same feature as the one for the point 1, but the same behaviour does not occur for the states with higher magnetic flux after the Landau levels crossing. As one can notice from Figs. 5.11(b)-5.11(d) these states are spread out over the whole bilayer system. The wave functions for the pairs of points 2 and 5 (Fig. 5.11(b)) and 3 and 4 (Fig. 5.11(c)) have the same kind of symmetry differing only by a phase rotation of π . It is easily to understand the difference between the wave function symmetries for these two pairs of points 2 – 5 and 3 – 4, since they come from the energy levels that possess the same feature. The energy levels for the points 2 and 5 have a decreasing tendency, while the points 3 and 4 are related to states that are split in energy. For the states with larger energy, more peaks are observed in the delocalized wave function, as already expected and as shown in Fig. 5.11(d) for the point 6 located close to the upper zeroth Landau level and that presents two peaks.

Just like in the armchair anti-dot case, the wave functions for the energy levels of the zigzag anti-dot inside the gap that exhibit a decreasing behaviour as the magnetic flux increase are dot-localized states, as demonstrated by Fig. 5.12(a) for the point 7 in the energy spectrum given by Fig. 5.10(d). In fact, the energy levels that appear intercepting the decreasing dot-localized states are edge states, as demonstrated by Fig. 5.12(b) for point 8. The three energy levels marked by point 8 have the same symmetry being just rotated by a phase of $\pi/3$ due to the fact that a hexagon presents a C_3 symmetry rotation group. Let us now check the total contribution $|\psi_1|^2 + |\psi_2|^2$ for the points 9 and 10 to find

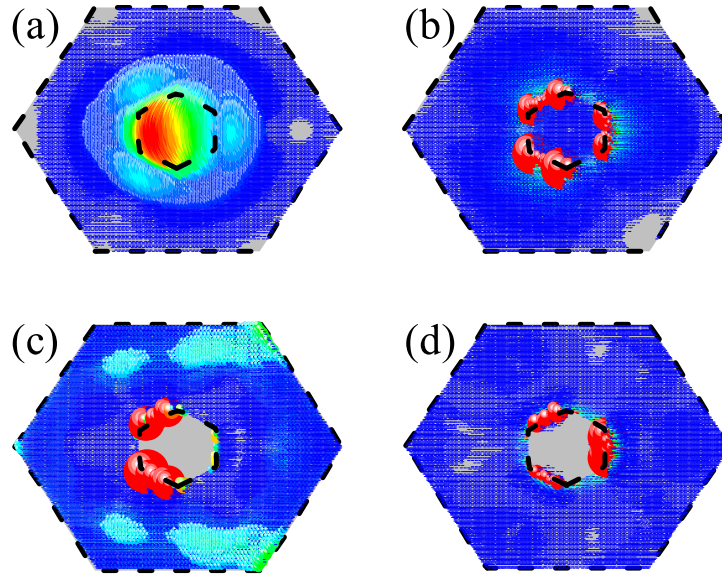


Figure 5.12: (Color online) Squared total wave function $|\psi|^2$ for the states indicated in Fig. 5.10(d) for a system sketched in Fig. 5.1(a) with zigzag edges, such as the points 7 – 10 correspond to the plots (a) 7, (b) 8, (c) 9 and (d) 10. Small (large) circle with blue (red) color represents low (high) density. The bilayer region is shadowed by the gray color.

the origin of the topological protected states as emphasized in the yellow zoom region in Fig. 5.10(c). The point 9 corresponds to a state that decreases in energy with B , whereas the point 10 is located on the flat part for the same energy level. Just looking at the squared modules of the wave functions for these two points, we can see that one of them is a mixed state of an edge state and a spread state, as given by Fig. 5.12(c) for the point 9, while the wave function for the flat state denoted by 10 is only an edge state. Moreover, although it was not shown for the zigzag edge case, one can observe also that the energy levels that approach the zeroth Landau levels that cross each other around energy $E = 0$ correspond to states that are spread out throughout the whole bilayer system, as shown for the armchair case in Fig. 5.11(d).

5.4 Conclusion

We proposed two different type of QD systems composed of nanostructured bilayer graphene. We presented a theoretical study of the energy levels within the tight-binding approach. The two proposed system are hexagonal bilayer quantum dots created by (i) cutting out atoms in the inner region of the top layer forming, in this way, an hexagonal bilayer anti-dot and (ii) a hexagonal flake at the top layer surrounded by a hexagonal region of monolayer graphene at the bottom. We have obtained results for the energy

spectra for both quantum dots with armchair and zigzag edges and discussed localization of carriers in these MLG/BLG quantum dots, analyzing the energy spectra in the presence of a perpendicular magnetic field and a gate potential. Our numerical calculations also allow us to find the density probability and thus to check which states are dot-localized and which are localized outside the middle of the system.

In the absence of magnetic field we computed the energy levels as a function of the side length of the top hexagonal (anti-)dot for the (first) second proposed system. For the anti-dot case, we considered the application of an external bias potential that opens a gap in the energy spectrum only for the bilayer region. Two different sets of energy levels are observed in this case, one of them inside the gap $E \in [-V_0, V_0]$ and the other for high energy values $|E| < -V_0$. The latter decreases with the dot size, converging to the energies $E = V_0$ and $E = -V_0$ for positive and negative region of the spectrum, respectively. The former depends on the edge termination, such that it has a mix of decreasing and increasing levels with increasing size of the anti-dot with zigzag edges and only decreasing energy levels for the armchair case. We showed that the energy levels inside the gap that decrease as the dot size increases are dot-localized states for the both edge terminations, so that they are localized essentially on the bottom layer. In addition, in zigzag anti-dot case we obtained many more states inside the gap region that are increasing as the dot size also increases. These states correspond to edge states related to the anti-dot zigzag edges. Another feature observed in the zigzag system is the appearance of anti-crossings in the spectrum, related to the interplay between edges states in the zigzag edges near the MLG and BLG junction and states inside the dot confined by bias voltage.

The second proposed structure can be used as a type of hybrid MLG/BLG system to confine carriers. Even in the absence of external bias potential, it presents a strong localization in the middle of the system, as well as for smaller dot sizes the energy levels converge to flat states that correspond to the monolayer energy levels, such that the electron probability density is spread out along only the monolayer graphene flake.

In the presence of a perpendicular magnetic field we observed that the energy levels approach to the Landau levels in the both edge termination and also for both cases considering or not the effect of an applied bias potential. Similar way to hexagonal monolayer graphene dots, we demonstrated that the energy spectrum as a function of the magnetic flux possesses a gap for smaller values of magnetic flux in the armchair dot case and many zero energies in the zigzag case that correspond to edge states. Furthermore, the energy spectrum for the unbiased case presents (i) an electron-hole symmetry and (ii) the appearance of several crossing and anti-crossings for both edge terminations that can be linked to the interplay between the magnetic field confinement and the quantum dot confinement. For the biased quantum dot case, we found some states that exhibit behaviour similar to topologically protected states, since that the properties of these state do not change as the magnetic flux changes. We showed that these states are edge states

and they preserve this symmetry even when the magnetic flux increases. Other important consequence of the combination of magnetic field and an electrostatic confinement is that it breaks the inversion symmetry of the bilayer such as the electron-hole symmetry is not preserved in the energy spectrum.

Wave packet scattering on graphene edges in the presence of a (pseudo) magnetic field

The scattering of a Gaussian wave packet in armchair and zigzag graphene edges is theoretically investigated by numerically solving the time dependent Schrödinger equation for the tight-binding model Hamiltonian. Our theory allows to investigate scattering in reciprocal space, and depending on the type of graphene edge we observe scattering within the same valley, or between different valleys. In the presence of an external magnetic field, the well know skipping orbits are observed. However, our results demonstrate that in the case of a pseudo-magnetic field, induced by non-uniform strain, the scattering by an armchair edge results in a non-propagating edge state.

6.1 Motivation

Due to its unique electronic properties, graphene has become a topic of intensive study in recent years. Within the low energy approximation for the tight-binding Hamiltonian of graphene, electrons behave as massless Dirac fermions, with a linear energy dispersion. [1] This leads to a plethora of interesting physical phenomena, ranging from Klein tunneling and other quasi-relativistic effects [124, 197] to the existence of new types of electron degrees of freedom, namely, the pseudo-spin, related to the distribution of the wave function over the carbon atoms belonging to the different triangular sublattices composing the graphene hexagonal lattice, and the presence of two inequivalent electronic valleys, usually labeled as K and K', in the vicinity of the gapless points of the energy spectrum of graphene.

Recent papers studied the scattering of electrons by edges [198] and defects [199] in graphene, both theoretically [165] and experimentally [200]. Armchair and zigzag are the two types of edges which are most frequently considered in the study of graphene ribbons, although other types of terminations exist due to edge reconstruction, which has been demonstrated both theoretically [201] and experimentally [202, 203, 204]. Even so, the edge reconstruction effect strongly depends on how the nanoribbon is made: normally, it

occurs when the technique used to fabricate the nanoribbon is based on a mechanism that drives the system to thermodynamic equilibrium. According to the continuum (Dirac) model, armchair edges in finite graphene samples lead to a boundary condition that mixes the wavefunctions of K and K' valleys, whereas a zigzag edge appears in the Dirac theory of graphene as a separate boundary condition for the wavefunctions of each valley. [90, 96] This suggests that electrons reflected by a graphene edge would exhibit inter-valley scattering only in the armchair case, whereas reflection by a zigzag edge would produce scattering inside the same Dirac valley. This prediction was confirmed by recent experiments, [205] where inter-valley scattering by armchair edges was even shown to be very robust in the presence of defects. The inter- and intra-valley scattering possibilities are schematically illustrated in Fig. 6.1(a), which shows K and K' Dirac cones in the reciprocal space of graphene.

Besides its singular electronic properties, graphene also exhibits interesting mechanical properties, as it can support strong elastic stretch. This provides us with the new possibility to tune the electron properties in graphene through strain engineering. [74, 206, 207, 208, 209, 210, 211, 212, 213, 214] In fact, it has been demonstrated recently that electrons in a strained graphene lattice behave as if they were under an external magnetic field, which points towards opposite directions in the K and K' valleys, so that the time reversal symmetry of the system as a whole is preserved. [215, 216] Such fields were experimentally observed recently, when measurements of the energy states in a graphene bubble revealed a Landau level-like structure corresponding to an external magnetic field of ≈ 300 T. [217] By designing non-uniform strain fields in a graphene sheet, one is able to produce a uniform pseudo-magnetic field for electrons. [218]

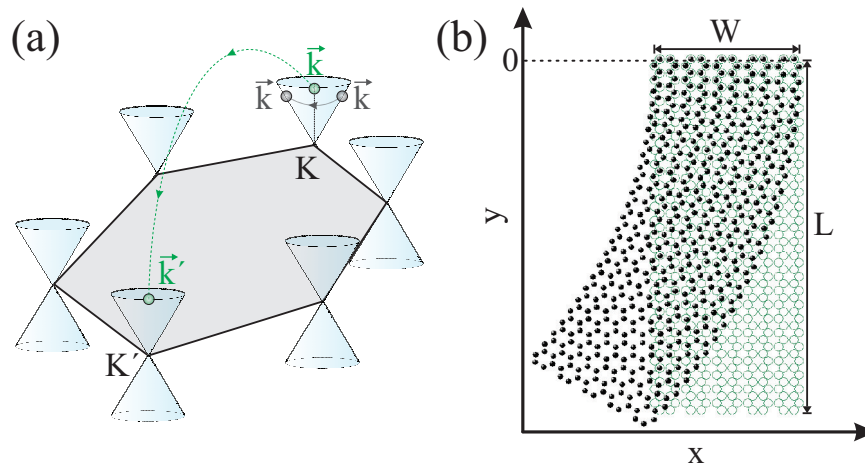


Figure 6.1: (a) Dirac cones of graphene, along with an illustrative scheme of the inter- (green circles) and intra- (gray circles) valley scattering. (b) Sketch of the strained graphene sample considered in this work, where the (open green) full black circles represent the (un)strained case. The upper boundary is set as the $y = 0$ axis for convenience.

The aim of this chapter is two fold - we use wave packet dynamics calculations: (i) to

investigate electron reflection by armchair and zigzag edges in a finite graphene sample, assumed to be made by cutting a graphene monolayer, such that no edge reconstruction is expected to occur at room temperature, where our results demonstrate the possibilities of inter- and intra-valley scattering, depending on the type of edge, and (ii) to study the influence of an external magnetic field and a non-uniform strain distribution on the electron trajectories in these systems. We compare the features observed for electrons under a perpendicular external magnetic field with those seen with a pseudo-magnetic field. Fig. 6.1(b) shows a sketch of the graphene flake considered in our calculations, where the open (green) circles illustrate the unstrained sample and the closed (black) circles illustrate the strained one. Such a non-uniform strain field was suggested by Guinea *et al.* [218] and was shown to exhibit an almost uniform pseudo-magnetic field.

All the calculations were done within the tight-binding description of graphene, using the time-evolution method developed in Ref. [131] and in the Chapter 2 of this thesis. As we are not restricting ourselves to a single Dirac cone in our model, the scattering between Dirac cones by armchair edges will appear naturally. Notice that Fig. 6.1(b) is just an illustrative scheme of our system, where the number of atoms was reduced in order to help its visualization. Besides, the sample shown in Fig. 6.1(b) is a ribbon, which improves the visualization of the strained case. However, the actual flake considered in our calculations has 1801×2000 atoms, which looks more like a rectangle, rather than a ribbon and corresponds to a flake with dimensions of about $426 \times 221 \text{ nm}^2$. Such a large flake is necessary to isolate each reflection of the wave packet on a single edge, as we need to consider a large packet in order to avoid dispersion. [131, 219]

6.2 Edge-dependent scattering

Let us first analyze the wave packet reflection by zigzag and armchair edges in a plain graphene sample, *i.e.* in the absence of magnetic fields and strain. The initial wave packet $\Psi(x, y)$ is taken as a circularly symmetric gaussian distribution of width d , multiplied by a plane wave with wave vector $\vec{k} = (k_x, k_y)$ and a pseudo-spinor $\sigma = (A, B)^T$

$$\Psi(\vec{r}) = \frac{1}{d\sqrt{2\pi}} \begin{pmatrix} A \\ B \end{pmatrix} \times \exp \left[-\frac{(x - x_0)^2 + (y - y_0)^2}{2d^2} + i\vec{k} \cdot \vec{r} \right]. \quad (6.1)$$

The pseudo-spinor in our model is simulated by defining a multiplication factor in the wave function, which assumes different values for sites belonging to the A and B sublattices. Notice that for low energy electrons in graphene, the tight-binding Hamiltonian can be approximated as $H = v_F \hbar \vec{k} \cdot \vec{\sigma}$, where v_F is the Fermi velocity, so that the propagation velocity vector in the Heisenberg picture is given by $d\vec{x}/dt = -[\vec{x}, H]i/\hbar = v_F \vec{\sigma}$. Hence, the pseudo-spin polarization of the wave packet plays an important role in defining the

direction of propagation. As the upper and right edges of the flake are of armchair and zigzag type, respectively, we consider $\sigma = (1, i)^T$, *i.e.* propagation in the y -direction, in order to observe wave packet scattering on the upper armchair edge, and $\sigma = (1, 1)^T$, *i.e.* propagation in the x -direction, for scattering on the right zigzag edge. The initial wave vector \vec{k} is taken in the vicinity of the Dirac point $\vec{K} = (0, 4\pi/3\sqrt{3}a)$, where $a = 1.42\text{\AA}$ is the inter-atomic distance. At each time step, we calculate the average values $\langle x \rangle = \int_{-\infty}^{\infty} x |\Psi|^2 dx dy$ and $\langle y \rangle = \int_{-\infty}^{\infty} y |\Psi|^2 dx dy$, in order to track the wave packet trajectory in real space. Besides, a fast Fourier transform (FFT) of the wave packet is taken at each time step, in order to track its scattering in reciprocal space.

The average positions $\langle x \rangle$ (black solid) and $\langle y \rangle$ (red dashed) are shown in Fig. 6.2 as a function of time, for a wave packet propagating in the x (y) direction, towards the

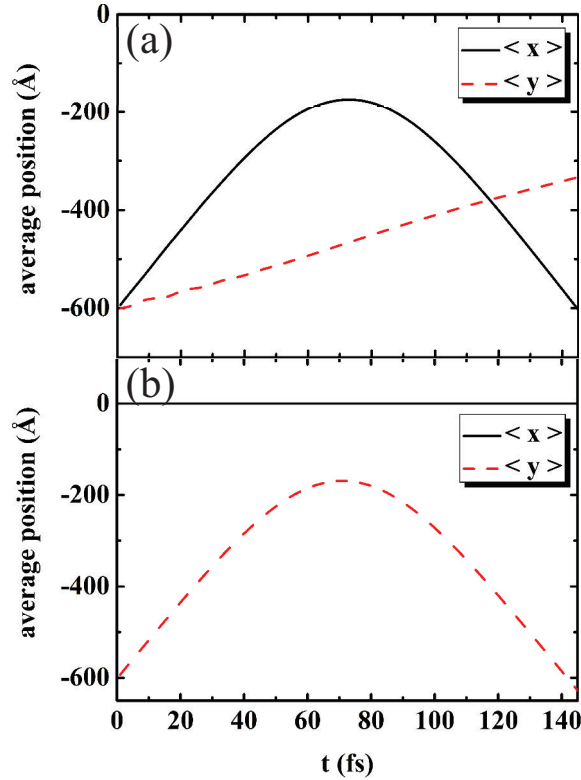


Figure 6.2: Average position of a gaussian wave packet of width $d = 300 \text{\AA}$ in an unstrained graphene flake, in the absence of external magnetic fields, as a function of time. (a) Horizontal propagation of a wave packet with $\vec{k} = (0.03\text{\AA}^{-1}, 4\pi/3\sqrt{3}a)$, and its consequent reflection by a zigzag edge. In this case the origin of the system is shifted, so that the right zigzag edge is set as the $x = 0$ axis. The wave packet starts at $(x_0, y_0) = (-600\text{\AA}, -600\text{\AA})$, and exhibits also a slow drag towards the upper edge, due to Zitterbewegung effects. (b) Vertical propagation of a wave packet with $\vec{k} = (0, 4\pi/3\sqrt{3}a + 0.02\text{\AA}^{-1})$, starting at $(0, -600\text{\AA})$, exhibiting reflection by the upper armchair border. In this case, the sample is not shifted, *i.e.* the upper edge is at the $y = 0$ axis, as sketched in Fig. 6.1(b).

right zigzag (upper armchair) edge of the sample, and being reflected by this edge back to its initial position. Figs. 6.2(a) and (b) correspond to zigzag and armchair reflections, respectively. The wave packet starts at 600 \AA from the sample edge and reaches the edge at $t \approx 70 \text{ fs}$ in both cases. Due to the finite width of the packet ($d = 300 \text{ \AA}$), its center of mass never reaches the border [131], so that $\langle x \rangle$ or $\langle y \rangle$ start to exhibit backscattering when they are still $\approx 150 \text{ \AA}$ far from the edge. Notice that the motion in the y -direction shown in Fig. 6.2(b) is perfectly vertical, *i.e.* $\langle x \rangle = 0$ during the whole propagation. However, this is not the case for propagation in the x -direction as apparent in Fig. 6.2(a), which is not perfectly horizontal, *i.e.* $\langle y \rangle$ does not stay the same, as the wave packet slowly drags towards larger y during propagation. This effect is a manifestation of the zitterbewegung, as discussed in detail in Ref. [131]. Although we did not manage to construct a wave packet that propagates perfectly horizontal, avoiding such a vertical drag, this effect does not interfere in our results and conclusions, as our analysis of scattering on the zigzag edge depends only on the horizontal component of motion.

Once we know the instant when the wave packet is reflected by the graphene edge in real space, at that moment we analyze what happens in reciprocal space. Fig. 6.3(a) shows the lines (red dashed) in reciprocal space along which we will take the wave functions. The contour plots in Fig. 6.3(b) illustrate the wave function along the horizontal line (i) – (ii) depicted in Fig. 6.3(a) in reciprocal space, as time elapses, in the case of x -direction propagation and, consequently, zigzag edge reflection. For such a propagation direction, we assumed the initial wave vector as $\vec{k} = (0.03 \text{ \AA}^{-1}, 4\pi/3\sqrt{3}a)$. Therefore, the initial wave packet (at $t = 0$) has a peak around $k_x^{i-ii} = 0.03 \text{ \AA}^{-1}$. This peak is conserved until the wave packet starts to be reflected by the right zigzag edge, when interference patterns start to show up. At $\approx 70 \text{ fs}$, a peak at $k_x^{i-ii} = -0.03 \text{ \AA}^{-1}$ starts to appear, while the former peak at $k_x^{i-ii} = 0.03 \text{ \AA}^{-1}$ smoothly decays. This is indeed the instant when the wave packet is reflected by the zigzag edge in real space, as shown in Fig. 6.2(a). As time elapses, the wave packet ends up only around $k_x^{i-ii} = -0.03 \text{ \AA}^{-1}$. This is direct evidence of intra-valley scattering as schematically illustrated in Fig. 6.1(a).

Figs. 6.3(c) and (d) show the wave function in reciprocal space taken along the vertical line (iii) – (iv) depicted in Fig. 6.3(a) as time elapses, for vertical propagation and, consequently, armchair edge reflection. For propagation in the y -direction, we consider $\vec{k} = (0, 4\pi/3\sqrt{3}a + 0.02 \text{ \AA}^{-1})$, so that the wave packet initially exhibits a peak around $\approx 1.723 \text{ \AA}^{-1}$, as shown in Fig. 6.3(c). This peak is preserved up to $t \approx 70 \text{ fs}$, when the wave packet is scattered by the upper armchair edge (see Fig. 6.2(b)) and the amplitude of the peak starts to decrease. Meanwhile, another peak appears around $k_y^{iii-iv} \approx -1.723 \text{ \AA}^{-1}$, which is located in the K' valley, as shown in Fig. 6.1(a). The inter-valley scattering situation is illustrated by the green circles in Fig. 6.1(a) which is clearly observed in reciprocal space.

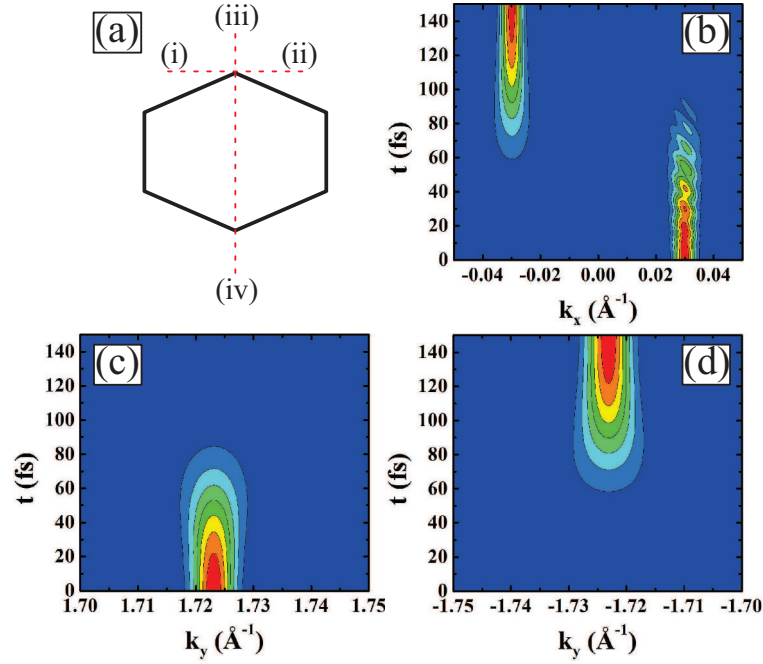


Figure 6.3: Time evolution of the wave packet in reciprocal space corresponding to the situations shown in Fig. 6.2. (a) Illustrative scheme of the lines in reciprocal space along which Fourier transform of the wave functions are taken. For the propagation in the horizontal direction (see Fig. 6.2(a)), we consider $\vec{k} = (0.03\text{\AA}^{-1}, 4\pi/3\sqrt{3}a)$. The time evolution of the wave function along the (i) – (ii) line of reciprocal space is shown in (b) as contour plots. For vertical propagation (see Fig. 6.2(b)), we consider $\vec{k} = (0, 4\pi/3\sqrt{3}a + 0.02\text{\AA}^{-1})$. The time evolution of the wave function along the (iii) – (iv) line of reciprocal space is shown as contour plots in (c) and (d), corresponding to different ranges of k_y^{iii-iv} .

6.3 Skipping orbits

Let us now investigate the trajectory of a wave packet in the presence of an external magnetic field, while it undergoes reflection at the edges of our rectangular graphene flake. We consider the same conditions as in Fig. 6.2(a), *i.e.* the wave packet in this case moves to the right, being thus pushed to the upper armchair edge by the Lorentz force due to the perpendicular magnetic field. The trajectory drawn by $\vec{r} = (\langle x \rangle, \langle y \rangle)$ for such a packet in the xy -plane after a $t = 2000$ fs propagation, under a ≈ 5 T field, is shown in Fig. 6.4(a), where skipping orbits are clearly observed, [220] coming from the successive reflections at the borders of the system, followed by cyclotronic semi-circles, as one would expect from such a scattering problem. The arrows indicate the direction of propagation, and the edges of the figure are set to be exactly at the position of the edges of the graphene flake. In order to help their analysis, the trajectories were divided into four regions, labeled from (I) to (V). Fig. 6.4(b) shows $\langle x \rangle$ and $\langle y \rangle$ separately as a function of time, where one verifies *e.g.* the attachment of the packet to the upper edge ($\langle y \rangle$ close to $y = 0$ in region

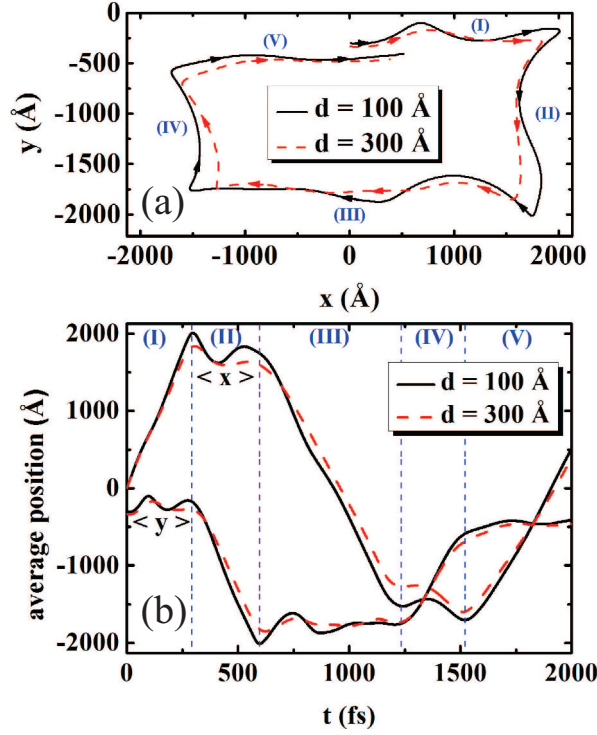


Figure 6.4: Trajectories drawn by $\langle x \rangle$ and $\langle y \rangle$ for a gaussian wave packet in the presence of an external magnetic field ≈ 5 T, propagating close to the edges in a rectangular graphene flake, within a $t = 2000$ fs propagation time. The arrows indicate the direction of propagation. Different values of the initial wave packet width d are considered. The edges of this panel are placed at the positions of the actual edges of the sample. (b) Average values of the wave packet position $\langle x \rangle$ and $\langle y \rangle$ as a function of time for the trajectories drawn in (a). Different parts of the trajectory in (a) were labeled from (I) to (V), and the time intervals where they occur are delimited by the vertical lines in (b).

(I), followed by a decrease in $\langle y \rangle$, when it attaches to the right edge ($\langle x \rangle$ close to $x = 2100$ Å, in region (II)), and its further attachment to the bottom edge of the sample ($\langle y \rangle$ close to $y = -2100$ Å in region (III)). As previously mentioned, due to the finiteness of the packet width, the trajectory as described by ($\langle x \rangle, \langle y \rangle$) does not reach the edges of the system. Besides, the wave packet disperses as time elapses, which distorts the trajectory as compared to the one obtained by classical ballistic motion. [131] Even so, the main conclusion one draws from this result is quite clear: as well as in ordinary systems with confined Schrödinger particles, [221] electrons in graphene under external magnetic fields exhibit a skipping orbit pattern when propagating close to the edges of the sample. We performed calculations for different wave packet widths $d = 100$ Å and 300 Å, and the results lead to the same qualitative conclusion, differing only by the distance the wave packet may reach the edge. There is, however, an important difference between these skipping orbits and those in ordinary Schrödinger systems, namely, the wave packet in this case may scatter not only between momentum states with opposite signs within the same valley, as usual, but they can also scatter from one valley to another, depending on

the type of edge, as we demonstrated in Fig. 6.3. Nevertheless, the effect of an external magnetic field on electron states belonging to both valleys is the same, therefore, there is no detectable manifestation of inter-valley scattering in this situation. This is not the case when, instead of an external magnetic field, we consider a strain induced pseudo-magnetic field, as we will demonstrate in what follows.

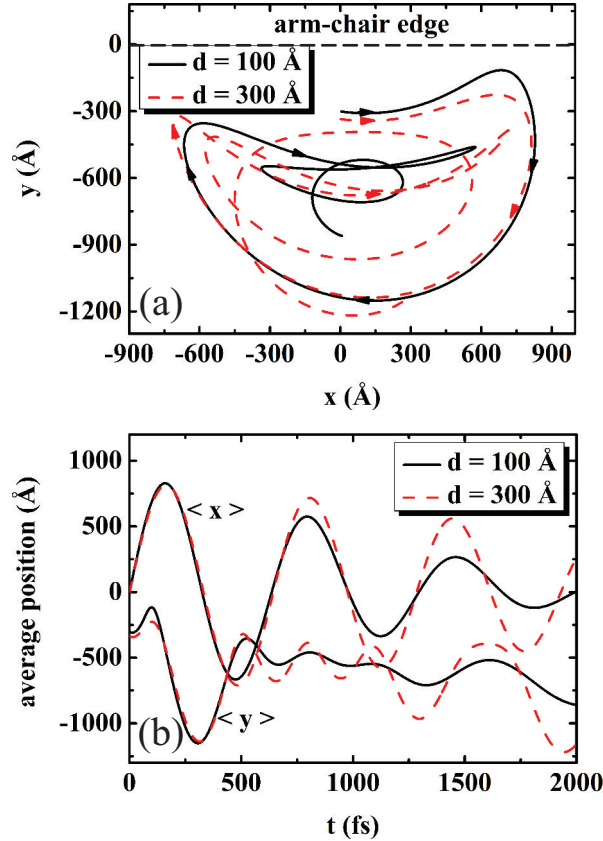


Figure 6.5: (a) Trajectories drawn by $\langle x \rangle$ and $\langle y \rangle$ for a $t = 2000$ fs time evolution of a wave packet, which propagates close to the upper (armchair) border of a bent rectangular graphene sample, for two values of wave packet width d . The radius of the circular distortion is $R = 10^4$ Å, corresponding to an almost uniform ≈ 5 T pseudo-magnetic field. The horizontal dashed line represents the upper edge of the sample. (b) Average values of the wave packet position $\langle x \rangle$ and $\langle y \rangle$ as a function of time for the trajectories drawn in (a).

For a circularly strained graphene flake, like that sketched in Fig. 6.1(b), electrons in the sample behave as if they were in an almost uniform magnetic field perpendicular to the plane. In order to produce such a strain, our 1801×2000 atoms sample is distorted into a semi-circle of radius $R = 10^4$ Å, leading to a pseudo-magnetic field ≈ 5 T, *i.e.* close to the value considered for the external magnetic field in Fig. 6.4. The presence of such a pseudo-magnetic field when electrons move close to the edge are expected to result in skipping orbits, similar to those in Fig. 6.4. Surprisingly, Fig. 6.5(a) shows this is not really the case: after performing a semi-circular trajectory due to the Lorentz force coming

from the pseudo-magnetic field, the packet, which started in the K valley, is reflected by the upper armchair edge and scatters to the K' valley, where the pseudo-magnetic field points in the opposite direction. The semi-circular trajectory now travels in the opposite direction until the packet reaches the edge again, being scattered back to its former Dirac cone at the K valley. This procedure occurs several times until the packet is so strongly dispersed that it, eventually, does not reach any of the edges, and performs only circular trajectories in the middle of the graphene flake. The series of reflections by the armchair border obtained in the strained case suggests the existence of a quasi-bound state at this edge, which is clearly seen by the time-dependence of the average coordinates $\langle x \rangle$ and $\langle y \rangle$, shown in Fig. 6.5(b). As time elapses, both $\langle x \rangle$ and $\langle y \rangle$ simply oscillate around $x = 0$ and close to the upper border of the sample, respectively. Notice that differently from Fig. 6.4(a), the lateral and bottom borders of the panel in Fig. 6.5(a) do not match the edges of the sample, in order to help the visualization of the trajectory, which in this case is localized in a small region of the sample. One can also observe that the results for different wave packet widths d are qualitatively the same, differing only by the amplitudes of the $\langle x \rangle$ and $\langle y \rangle$ oscillations in time.

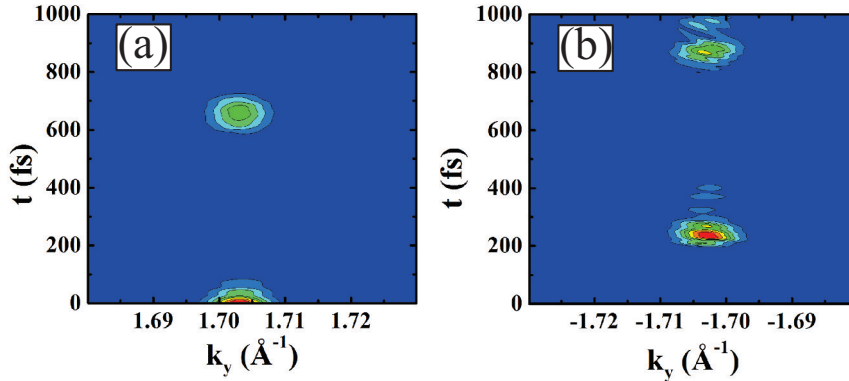


Figure 6.6: Contour plots of the time evolution of the wave packet in reciprocal space corresponding to the propagation shown in Fig. 6.5, *i.e.* for a strained graphene sample. The Fourier transform of the wave packet is taken in the vicinity of the (a) K and (b) K' points of the reciprocal space illustrated in Fig. 6.3(a), along the $k_x = -0.06 \text{ \AA}^{-1}$ ($k_x = 0.045 \text{ \AA}^{-1}$) vertical axis for K (K').

The sequence of scatterings between K and K' valleys suggested by the trajectories observed in Fig. 6.5 is confirmed by a direct observation of the wavefunction in reciprocal space. This is illustrated by Fig. 6.6, which shows the Fourier-transformed wavefunction (contour plots) as a function of the vertical component of the wave vector k_y as function of time t , similar to Figs. 6.3 (c) and (d). Since the initial wave packet in this case is at $\vec{k} = (-0.06 \text{ \AA}^{-1}, 4\pi/3\sqrt{3}a)$, in the vicinity of the K point, the k_y in Fig. 6.6(a) is taken for a fixed $k_x = -0.06 \text{ \AA}^{-1}$, *i.e.* in the center of the initial wave packet. One clearly sees that the peak of the wave packet in reciprocal space oscillates between the K (a) and K' (b) regions in Fig. 6.6 as time elapses, as a consequence of the successive inter-valley

scatterings by the upper armchair edge of the system, as observed in Fig. 6.5. Indeed, the first peak in the K' cone (Fig. 6.6(b)), for instance, starts to appear at $t \approx 200$ fs, which is the same time when $\langle x \rangle$ and $\langle y \rangle$ start to decrease in Fig. 6.5(b), after the wave packet is scattered by the edge for the first time. It is important to point out that we had to take the $k_x = 0.045 \text{ \AA}^{-1}$ vertical axis in order to observe the K' propagation in Fig. 6.6(b), instead of the $k_x = 0.06 \text{ \AA}^{-1}$ that would be expected from the value of the wave vector in our initial wave packet. In fact, one cannot expect that the K and K' points in the strained case remain vertically aligned in reciprocal space, as illustrated in Fig. 6.3(a), due to the distortion of the Dirac cones caused by the strain. [217] Also, we observe that the scattered wave packets are no longer gaussian, as they start to exhibit interference patterns due to the scattering by the edges. Even so, the conclusions drawn from the results in Fig. 6.6 are not affected by this fact, while Fig. 6.6 gives us a clear demonstration that the successive K to K' scatterings are indeed strongly related to the non-propagating edge states found for the strained case in Fig. 6.5.

6.4 Probability density current calculations

The trajectories illustrated in Figs. 6.4 and 6.5 have a direct effect on the probability density currents, which are numerically calculated based on the method developed in Ref. [222]. Since we can define the probability current j in terms of the continuity equation, then the discrete current centered on site n can be written as

$$j_n - j_{n+1} = a \frac{\partial}{\partial t} \rho_{n,n}, \quad (6.2)$$

where $\rho_{n,n} = \langle n | \hat{\rho} | n \rangle$ are the matrix elements of the density matrix operator $\hat{\rho} = |\Psi\rangle\langle\Psi|$, and the time derivative is determined by the equation of motion for $\hat{\rho}$

$$\frac{\partial}{\partial t} \rho_{nm} = \frac{i}{\hbar} \sum_m (\Psi_n \Psi_m^* H_{mn} - H_{nm} \Psi_m \Psi_n^*) \quad (6.3)$$

where $\Psi_n = \langle n | \Psi \rangle$. We will limit ourselves to the case of nearest-neighbor interaction, *i.e.* $H_{n,m} = 0$ when $|m - n| > 1$, from which we obtain

$$\begin{aligned} \frac{\partial}{\partial t} \rho_{nn} &= \frac{i}{\hbar} [(\Psi_n \Psi_{n+1}^* H_{n+1,n} - H_{n,n+1} \Psi_{n+1} \Psi_n^*)] \\ &\quad + \frac{i}{\hbar} [\Psi_n \Psi_{n-1}^* H_{n-1,n} - H_{n,n-1} \Psi_{n-1} \Psi_n^*], \end{aligned} \quad (6.4)$$

which is easily rewritten in the form

$$\begin{aligned} \frac{\partial}{\partial t} \rho_{nn} &= -\frac{2}{\hbar} \Im [\Psi_n \Psi_{n+1}^* H_{n+1,n}] \\ &\quad + \frac{2}{\hbar} \Im [\Psi_{n-1} \Psi_n^* H_{n,n-1}]. \end{aligned} \quad (6.5)$$

By comparing Eqs. (6.2) and (6.5), one easily identifies the local current in n as

$$j_n = \frac{2a}{\hbar} \Im [\Psi_n^* \Psi_{n-1} H_{n,n-1}]. \quad (6.6)$$

Notice that Eq. (6.6) was developed without taking into account any specific lattice and the presence of magnetic fields. However, a generalization to arbitrary discrete lattice is straightforward, and the presence of a magnetic field is included simply by the Peierls substitution of the hopping parameters. [223] As graphene is a hexagonal lattice, the current components in x and y directions have different forms and are site dependent. Defining the sites location through their line (n) and column (m) positions in the lattice (see Ref. [131]), one obtains

$$j_x(n, m) = \pm \frac{a}{\hbar} \left\{ 2\Im [\Psi_{n,m} \Psi_{n,m\pm 1}^* \tau_{n,m\pm 1}] - \Im [\Psi_{n,m} \Psi_{n-1,m}^* \tau_{n-1,m}] - \Im [\Psi_{n,m} \Psi_{n+1,m}^* \tau_{n+1,m}] \right\} \quad (6.7)$$

and

$$j_y(n, m) = \frac{\sqrt{3}a}{\hbar} \left\{ \Im [\Psi_{n,m} \Psi_{n+1,m}^* \tau_{n+1,m}] - \Im [\Psi_{n,m} \Psi_{n-1,m}^* \tau_{n-1,m}] \right\} \quad (6.8)$$

where the \mp sign in j_x will be positive (negative) if the (n, m) -site belongs to the sublattice A (B), and $\tau_{n,m}$ is the hopping parameter which, in the presence of a magnetic field, includes an additional phase according to the Peierls substitution $\tau_{n,m} \rightarrow \tau_{n,m} \exp \left[i \frac{e}{\hbar} \int_m^n \vec{A} \cdot d\vec{l} \right]$, where \vec{A} is the vector potential describing the magnetic field.

The probability density currents calculated by Eq. (6.6) are integrated in space and plotted as a function of time in Fig. 6.7 for the situations proposed in Figs. 6.4 and 6.5, *i.e.* (a) in the presence of an external 5 T magnetic field, and (b) in a strained graphene sample, which produces an almost uniform ≈ 5 T pseudo-magnetic field. As in the other results discussed previously, the results obtained for the two different values of wave packet width considered in this case, $d = 100$ Å (black solid - circles) and $d = 300$ Å (red dashed - triangles), exhibit similar qualitative features, differing only in a quantitative way. In Fig. 6.7(a), for an external field, one observes a total current flow in the x -direction oscillating around a positive value in the region I, whereas j_y oscillates around zero in this region. This is a manifestation of the propagation of the wave packet through the upper edge of the sample, by means of skipping orbits, as illustrated in Fig. 6.4(a). What follows can also be understood by analyzing Fig. 6.4(a): In regions II and IV (III and V), where the wave packet propagates along the vertical (horizontal) edges, the component of the current in the $y(x)$ -direction oscillates around a non-zero value, indicating an electron propagation through the sample by the skipping orbits mechanism. This is not the case when we consider a strain-induced pseudo-magnetic field: Fig. 6.7(b) shows that both j_x and j_y always oscillating around zero, confirming that there is no net current in the system and that the skipping orbits near the armchair edge in this case are non-propagating states.

The results found in our work have observable consequences in experiments. For example, the edge propagation of electrons through skipping orbits in an ordinary system

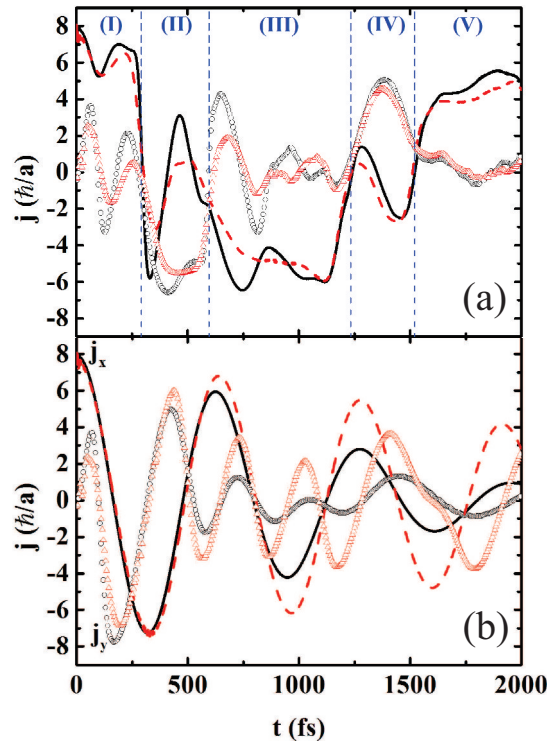


Figure 6.7: Integrated probability density currents as a function of time for the situations proposed in Figs. 6.4 and 6.5, namely, (a) for an unstrained graphene sample in the presence of an external 5 T magnetic field, and (b) in a circularly bent graphene sample, which produces an almost uniform ≈ 5 T pseudo-magnetic field. The curves (symbols) represent the component of the current in the x (y)-direction, *i.e.* j_x (j_y). Two different values of wave packet width are considered: $d = 100$ Å (black solid - circles) and 300 Å (red dashed - triangles) The regions delimited in (a) are the same as in Fig. 6.4.

under an external magnetic field plays an important role in electron transport in the direction parallel to the edge. [221] Our results demonstrate that these skipping orbits are still present in a graphene ribbon under an external magnetic field, but they are not observed in the case of pseudo-magnetic fields in the direction parallel to an armchair border of graphene. This is a clear example that the pseudo-magnetic field has different consequences as compared to a real magnetic field. Therefore, in a strained armchair graphene ribbon, edge electrons should not propagate along the ribbon, so that the transport in these systems must be dominated only by electrons propagating far from the edge. Moreover, the non-propagating state found at the armchair edge of a strained sample is a consequence of periodic inter-valley scattering processes, and this type of scattering has an important effect on Raman spectroscopy. [224] Therefore, the successive electron reflections at the armchair edge of a strained sample would manifest itself as an intense peak in Raman experiments taken close to the border of the graphene sample.

6.5 Conclusion

In summary, we investigated the reflection of a wave packet on zigzag and armchair edges of a graphene ribbon. Our results demonstrate the scattering of the wave packet from K to K' Dirac cones in the case of armchair edges, whereas scattering from positive to negative average momentum inside the same cone is observed in the zigzag case, which is in agreement with predictions from mean field (Dirac) theory of graphene and with recent experimental results. [205] In the presence of an external magnetic field, skipping orbits are observed. However, for a strain induced pseudo-magnetic field, our numerical results demonstrate that the incoming and scattered wave packets perform orbits in opposite directions in the armchair case. This effect is easy to be understood if one considers the combination between two events, both already predicted by the Dirac theory of graphene: (i) the K to K' scattering by armchair edges and (ii) the opposite sign of the pseudo-magnetic field in the different cones. This result points directly to the possibility of observing non-propagating edge states in an armchair terminated strained graphene sample under pseudo-magnetic fields, which is completely different from the external magnetic fields case, where the skipping orbit states are always propagating. The effects predicted by our theoretical work are expected to have important consequences in future experiments on strained graphene samples.

Valley filtering using electrostatic potentials in bilayer graphene

Propagation of an electron wave packet through a quantum point contact (QPC) defined by electrostatic gates in bilayer graphene is investigated. The gates are set as to provide a bias between the layers, in order to produce an energy gap. If the gates on both sides of the contact produce the same bias, steps in the electron transmission probability are observed, as in an usual QPC. However, if the bias is inverted on one of the sides of the QPC, only electrons belonging to one of the Dirac valleys are allowed to pass, which provides a very efficient valley filtering.

7.1 Motivation

The unique band structure of graphene has brought the possibility of developing devices based on different degrees of freedom, other than charge (electronics) and spin (spintronics), namely, using its different pseudo-spin states (pseudo-spintronics) and electronic valleys (valleytronics). Valley filtering in graphene has been pursued by many researchers, as a path to use the valley degree of freedom of electrons in this material as the basis for future valley-tronics. Previous theoretical proposals for valley filtering demand a high control of the atomic structure of the graphene layer, either by cutting it in specific directions as to produce uniform zigzag edges [225], or by applying stress in a specific manner in order to obtain an almost uniform pseudo-magnetic field [131, 226, 227], or even by taking advantage of the valley filtering process that occurs when an electron propagates through a line of heptagon-pentagon defects on the honeycomb lattice.[199, 228, 229]

Monolayer graphene is gapless and therefore its usage in electronic devices is unfavourable. [1] In bilayer graphene on the other hand, a gap may be opened by applying a bias between the two layers.[79] Therefore, in bilayer graphene, it is possible to produce electrostatic confined structures, such as quantum wires, dots and rings.[121, 154, 155, 156, 160, 166] A special case of quantum wire confinement occurs when one applies opposite bias on the different sides of the quantum wire potential: in this case, one dimensional

uni-directional chiral states are created, whose subband structures along the free direction for K and K' valleys are mirror symmetric. [230, 231, 232] In the present chapter we will use the latter property to propose a novel valley filter, which is solely based on the use of electrostatic potentials and we do not require any complicated tailoring of the graphene lattice as needed in previous proposed filters.

In this chapter, we demonstrate that a quantum point contact (QPC) defined by electrostatic gates in bilayer graphene, as sketched in Fig. 7.1(a), exhibits steps in its transmission probabilities as the energy of the incident electron increases, just like in an ordinary point contact. On the other hand, valley polarized current is predicted when the sides of the point contact have opposite bias, as sketched in Fig. 7.1(b). The specific conditions for such polarization are discussed in detail in Sec. 7.3. In Sec. 7.2 we present our technique to solve the time-dependent Schrödinger equation based on a tight-binding model. The numerical results are presented in Sec. 7.3 and we summarize our discussion giving the main conclusions in Sec. 7.4.

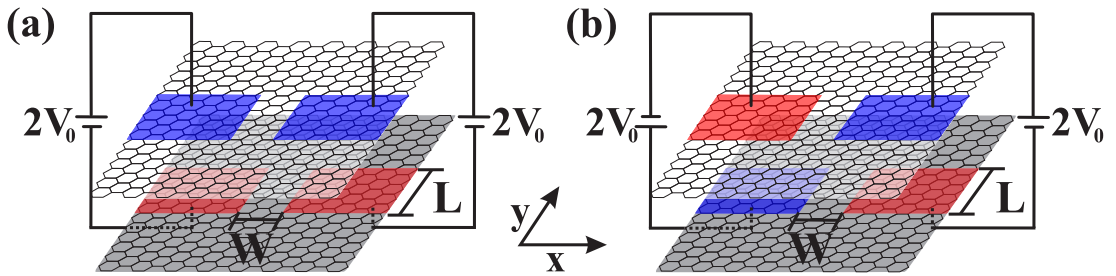


Figure 7.1: Sketch of the QPC structure, forming a channel with length L and width W , with (a) aligned and (b) anti-aligned bias. The actual sample used in our numerical calculation is rectangular with 3601×1000 atoms in each layer that corresponds to a size $\approx 213 \times 443 \text{ nm}^2$.

7.2 Split-operator technique for the bilayer graphene Hamiltonian

In this section we present the theoretical tools for the carrier time evolution in bilayer graphene. In order to do so, we solve the time-dependent Schrödinger equation for the tight-binding Hamiltonian of bilayer graphene in order to investigate the time evolution of a wave packet describing an electron propagating through a quantum point contact.

The time evolution of a quantum state is described by the time-dependent Schrödinger equation given by

$$\Psi(\vec{r}, t) = \hat{U}(t, t_0)\Psi(\vec{r}, t_0), \quad (7.1)$$

where $\hat{U}(t, t_0)$ is known as the time evolution operator. For the case in which the Hamiltonian does not explicitly depend on time, this operator can be written as $\hat{U}(t, t_0) =$

$\exp[-\frac{i}{\hbar}H(t-t_0)]$. Different techniques to expand this exponential operator are found in the literature, for example iterative methods based on the Crank-Nicholson scheme and the Chebyshev polynomials method. Furthermore for systems with moderate space dimensions there is the possibility to solve this problem by brute force, using full diagonalisation [233]. Here, we opted for the split-operator technique [131].

Our approach is based on the tight-binding model for the description of an electron in bilayer graphene. We consider respectively n and m as the row and column indexes to locate a particular site in the lattice, and $l = \{1, 2\}$ index corresponds to bottom and top layers, respectively. The basis vector state is defined as $|n, m, l\rangle$. So, the tight-binding Hamiltonian reads

$$\begin{aligned} H_{TB}|n, m, l\rangle &\cong (E_{n,m,l} + V_{n,m,l})|n, m, l\rangle \\ &+ \tau_{n-1,m}|n-1, m, l\rangle + \tau_{n+1,m}|n+1, m, l\rangle \\ &+ \tau_{n,m-1}|n, m-1, l\rangle + \tau_{n,m+1}|n, m+1, l\rangle \\ &+ \Delta_{n,m}|n, m, l+1\rangle + \Delta_{n,m}|n, m, l-1\rangle, \end{aligned} \quad (7.2)$$

where $\tau_{n,m-1}$ and $\Delta_{n,m}$ are the intra- and inter-layer hopping energies between the sites, respectively. The tight-binding Hamiltonian for bilayer graphene in matrix form is now represented by two pentadiagonal matrices in blocks, connected by two diagonal matrices. To numerically simplify the problem, which is important when dealing with large systems, we first rewrite Eq. (7.2) as follows

$$H_{TB}|n, m, l\rangle = H_{n,l}|n, m, l\rangle + H_{m,l}|n, m, l\rangle + H_{n,m}|n, m, l\rangle, \quad (7.3)$$

where the operators $H_{n,l}$, $H_{m,l}$ and $H_{n,m}$ are defined as

$$\begin{aligned} H_{n,l}|n, m, l\rangle &= \left(\frac{\epsilon_{n,m,l} + V_{n,m,l}}{2} \right) |n, m, l\rangle \\ &+ \tau_{n,m-1}|n, m-1, l\rangle + \tau_{n,m+1}|n, m+1, l\rangle, \end{aligned} \quad (7.4)$$

$$\begin{aligned} H_{m,l}|n, m, l\rangle &= \left(\frac{\epsilon_{n,m,l} + V_{n,m,l}}{2} \right) |n, m, l\rangle \\ &+ \tau_{n-1,m}|n-1, m, l\rangle + \tau_{n+1,m}|n+1, m, l\rangle \end{aligned} \quad (7.5)$$

and

$$H_{n,m}|n, m, l\rangle = \Delta_{n,m}|n, m, l+1\rangle + \Delta_{n,m}|n, m, l-1\rangle. \quad (7.6)$$

In doing so, we split the Hamiltonian and thus transform the problem of pentadiagonal matrices in blocks into a series of calculations involving only products of tridiagonal matrices, which are much easier to handle with known computational routines.

Subsequently, the time evolution operator is expanded as follows

$$\begin{aligned} e^{-(i/\hbar)H_{TB}\Delta t} &= e^{-(i/2\hbar)H_{n,m}\Delta t} e^{-(i/2\hbar)H_{m,l}\Delta t} e^{-(i/\hbar)H_{n,l}\Delta t} \\ &\times e^{-(i/2\hbar)H_{m,l}\Delta t} e^{-(i/2\hbar)H_{n,m}\Delta t} + \mathcal{O}(\Delta t^3), \end{aligned} \quad (7.7)$$

and we neglect terms of order $\mathcal{O}(\Delta t^3)$ which correspond to the non-commutativity between the operators $H_{n,l}$, $H_{m,l}$ and $H_{n,m}$. Higher accuracy is realised by considering a smaller time step. Here, we took $\Delta t = 0.1$ fs. Using the well-known property of the Pauli matrices

$$\exp[-i\vec{A} \cdot \vec{\sigma}] = \cos(A)\mathbf{I} - i\frac{\sin(A)}{A} \begin{pmatrix} A_z & A_x - iA_y \\ A_x + iA_y & -A_z \end{pmatrix}, \quad (7.8)$$

for any vector \vec{A} , where $A = |\vec{A}|$ and \mathbf{I} is the identity matrix, and realising that the $H_{n,m}$ operator for each n and m fixed is just a 2×2 matrix with zero-diagonal elements described by $\Delta_{n,m}\sigma_x$, we have that the exponential of $H_{n,m}$ is given exactly by

$$e^{-(i/2\hbar)\Delta_{n,m}\sigma_x\Delta t} = \begin{pmatrix} \cos(A_x) & -i\sin(A_x) \\ -i\sin(A_x) & \cos(A_x) \end{pmatrix} = \mathcal{M}_l, \quad (7.9)$$

where $A_x = \Delta_{n,m}\Delta t/2\hbar$.

The wave function at time step $t + \Delta t$ is then given by

$$\begin{aligned} |\Psi_{n,m,l}\rangle_{t+\Delta t} &\cong e^{-(i/2\hbar)H_{n,m}\Delta t} e^{-(i/2\hbar)H_{m,l}\Delta t} e^{-(i/\hbar)H_{n,l}\Delta t} \\ &\times e^{-(i/2\hbar)H_{m,l}\Delta t} e^{-(i/2\hbar)H_{n,m}\Delta t} |\Psi_{n,m}\rangle_t, \end{aligned} \quad (7.10)$$

that can be developed in five steps

$$\eta_{n,m,l} = e^{-(i/2\hbar)H_{n,m}\Delta t} |\Psi_{n,m,l}\rangle_t, \quad (7.11)$$

$$\xi_{n,m,l} = e^{-(i/2\hbar)H_{m,l}\Delta t} \eta_{n,m,l}, \quad (7.12)$$

$$\chi_{n,m,l} = e^{-(i/\hbar)H_{n,l}\Delta t} \xi_{n,m,l}, \quad (7.13)$$

$$\varrho_{n,m,l} = e^{-(i/2\hbar)H_{m,l}\Delta t} \chi_{n,m,l}, \quad (7.14)$$

$$|\Psi_{n,m,l}\rangle_{t+\Delta t} = e^{-(i/2\hbar)H_{n,m}\Delta t} \varrho_{n,m,l}, \quad (7.15)$$

where at each step we use the Cayley equation for the exponentials [234], such that

$$\begin{aligned} \eta_{n,m,l} &= \mathcal{M}_l |\Psi_{n,m,l}\rangle_t, \\ \left(1 + \frac{i\Delta t}{4\hbar} H_{m,l}\right) \xi_{n,m,l} &= \left(1 - \frac{i\Delta t}{4\hbar} H_{m,l}\right) \eta_{n,m,l}, \\ \left(1 + \frac{i\Delta t}{2\hbar} H_{n,l}\right) \chi_{n,m,l} &= \left(1 - \frac{i\Delta t}{2\hbar} H_{n,l}\right) \xi_{n,m,l}, \\ \left(1 + \frac{i\Delta t}{4\hbar} H_{m,l}\right) \varrho_{n,m,l} &= \left(1 - \frac{i\Delta t}{4\hbar} H_{m,l}\right) \chi_{n,m,l}, \\ |\Psi_{n,m,l}\rangle_{t+\Delta t} &= \mathcal{M}_l \varrho_{n,m,l}. \end{aligned} \quad (7.16)$$

The problem is now strongly simplified because now we have to deal only with tridiagonal matrices. We propagate a Gaussian wave packet following this numerical procedure and calculate the transmission probability by integrating the squared modulus of the wave

packet only in the region of the bilayer which is after the QPC. The initial Gaussian wave packet is defined as:

$$\Psi_0(\vec{r}) = \frac{1}{d\sqrt{2\pi}} \begin{pmatrix} A \\ B \\ A' \\ B' \end{pmatrix} \times \exp \left[-\frac{(x-x_0)^2 + (y-y_0)^2}{2d^2} + i\vec{k} \cdot \vec{r} \right]. \quad (7.17)$$

The coefficients $A(A')$ and $B(B')$ in the pseudospinor are related to the probability of finding the electron in each triangular sublattice $A(A')$ and $B(B')$ of the graphene lattice in a given layer. For the bilayer case, we choose the same pseudospinor for both layers, since the total wave function is composed of two Gaussian wave packets, one in each layer, with the same properties, as initial momentum, initial energy and initial position of Gaussian center $\vec{r}_0 = (x_0, y_0)$ in real space. The pseudospinor is characterised by the pseudospin polarization angle θ , such as $(1, e^{i\theta})^T$. Thus the pseudospin polarization has a conceptual connection with the direction of propagation of the wave packet in the tight-binding model and the choice of the angle θ depends also on which Dirac valley the initial wave packet is taken[130, 131]. We take $\theta = 0(\pi)$ for an initial wave packet starting from $K(K')$ valley, since we want it to propagate in the y -direction. The initial wave vector is $\vec{k} = (k_x^0, k_y^0) + \bar{K}$, which is shifted with respect to the Dirac points, where \bar{K} represents the two non-equivalent K and K' points that are located at $(0, \pm 4\pi/3\sqrt{3}a)$, with $a = 0.142$ nm being the in plane inter-atomic distance. For our numerical calculations, the initial wave packet energy E is set by k , the modulus of the wave vector, once that the bottom of the low-energy bands may be approximated by[79] $E = -(\tau_\perp/2) \left(\sqrt{1 + 4(v_F\hbar k/\tau_\perp)^2} - 1 \right)$, in bilayer graphene, where $\tau_\perp \approx 0.4$ eV is the interlayer coupling corresponding to perpendicular hopping between the Bernal stacked layers and $v_F \approx 10^6$ m/s is the Fermi velocity. The width of the Gaussian wave packet was taken as $d = 20$ nm and its initial position as $(x_0, y_0) = (0, -42)$ nm.

An important remark concerning the wave packet dynamics is about the oscillatory behavior of the velocity, *i.e.* the zitterbewegung manifestation on the wave packet motion [131, 197]. We shall show that it can not be avoided for motion of an electron in bilayer graphene that propagates in the y -direction. To understand how this affects the velocity in the y -direction, we use the Dirac Hamiltonian for electrons in bilayer graphene in the vicinity of the K point[79]

$$H_D^{BI} = \begin{pmatrix} 0 & v_F\pi & \tau_\perp & 0 \\ v_F\pi^\dagger & 0 & 0 & 0 \\ \tau_\perp & 0 & 0 & v_F\pi^\dagger \\ 0 & 0 & v_F\pi & 0 \end{pmatrix}, \quad (7.18)$$

where $\pi = p_x + ip_y$ and $\pi^\dagger = p_x - ip_y$ are the momentum operators in Cartesian coordinates, and calculate the commutator $[H_D^{BI}, v_y^{BI}]$. According to the Heisenberg picture,

the velocity in the y -direction is given by

$$v_y = \frac{dy}{dt} = \frac{1}{i\hbar} [H_D, y]. \quad (7.19)$$

Replacing H_D^{BI} into Eq. (7.19) and using the well-known commutation relation $[x_i, p_j] = i\hbar\delta_{ij}$ we find

$$v_y^{BI} = \begin{pmatrix} 0 & iv_F & 0 & 0 \\ -iv_F & 0 & 0 & 0 \\ 0 & 0 & 0 & -iv_F \\ 0 & 0 & iv_F & 0 \end{pmatrix}. \quad (7.20)$$

Now we shall verify whether v_y^{BI} is a constant of motion or not, and if there is any situation where the velocity is not affected by the zitterbewegung in the y -direction. Evaluating $[H_D^{BI}, v_y^{BI}]$ by making use of Eqs. (7.18) and (7.20), one obtains

$$[H_D^{BI}, v_y^{BI}] = \begin{pmatrix} -2iv_F^2 p_x & 0 & 0 & -i\tau_{\perp} v_F \\ 0 & 2iv_F^2 p_x & i\tau_{\perp} v_F & 0 \\ 0 & i\tau_{\perp} v_F & 2iv_F^2 p_x & 0 \\ -i\tau_{\perp} v_F & 0 & 0 & -2iv_F^2 p_x \end{pmatrix}, \quad (7.21)$$

suggesting that even if $p_x = 0$, one has $[H_D^{BI}, v_y^{BI}] \neq 0$, implying that v_y is not a constant of motion, because we are still left with non-zero off-diagonal terms. Conversely, in the monolayer case, we obtain that the velocity in the y -direction is expressed by $v_y^{MO} = -v_F \sigma_y$, where σ_y is the y Pauli matrix and with the monolayer Hamiltonian being $H_D^{MO} = v_F \vec{\sigma} \cdot \vec{p}$. Following the same procedure as for bilayer graphene, we obtain

$$[H_D^{MO}, v_y^{MO}] = \begin{pmatrix} -2iv_F^2 p_x & 0 \\ 0 & 2iv_F^2 p_x \end{pmatrix}, \quad (7.22)$$

and thus $[H_D^{MO}, v_y^{MO}] = 0$ if $p_x = 0$. Therefore, there is no way to avoid the trembling motion at small times for the wave packet propagation in bilayer graphene - even for motion in the y -direction, *i. e.* $k_x^0 = 0$ and $k_y^0 \neq 0$, the wave packet will also move in the x -direction. For this reason, all presented results in this chapter are normalized for the maximum transmission obtained for the case in the absence of any potential.

7.3 Results and discussion

In order to better understand our tight-binding results, let us first investigate the energy dispersions in a BLG quantum wire defined by aligned (Fig. 7.1(a)) and anti-aligned (Fig. 7.1(b)) potential barriers, as obtained by the Dirac approximation for BLG, using the 4×4 Hamiltonian. [79] These spectra are shown in Figs. 7.2(a) and 7.2(b), respectively, for different values of well width. Only states with energy below the barrier height ($V_0 = 200$ meV) are shown. Notice the qualitative difference between the two

spectra. The energy dispersion in the former case exhibits symmetry with respect to positive and negative values of the wave vector in the propagation direction k_y . As the propagation velocity is obtained from $v_g = \partial E / \partial p_y$, with $p_y = \hbar k_y$, this spectrum suggests that wave packets may propagate towards either positive or negative y -direction, provided the average wave vector k_y of the wave packet is in a region of positive or negative derivative of the spectrum, respectively. On the other hand, the spectra for the anti-aligned case does not exhibit the same symmetry. Besides, low energy electrons in this system can only exhibit positive velocity of propagation, since the derivative of the spectrum around $E = 0$ is positive for any value of k_y . In fact, this spectrum is obtained for the BLG Dirac Hamiltonian for electrons around the K point of the first Brillouin zone. The spectrum for K' is obtained just by replacing k_y by $-k_y$ in Fig. 7.2(b), or, equivalently by inverting the polarization of all gates in Fig. 7.1(b).

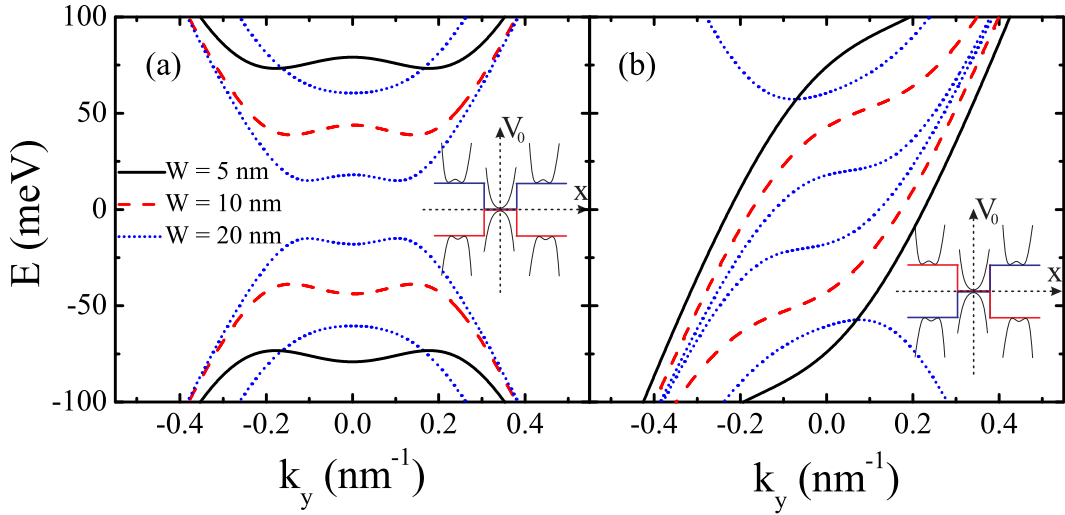


Figure 7.2: Band structure for the two potential configurations sketched in Fig. 7.1, namely, (a) aligned and (b) anti-aligned potential barriers. Results are presented for $V_0 = 200$ meV and three values for the quantum well width $W = 5$ (black solid), 10 (red dashed) and 20 nm, (blue dotted).

Due to the fact that the low energy spectra for the aligned bias case in K and K' points have the $E_{K(K')}(k_x, k_y) = E_{K(K')}(-k_x, k_y)$ and $E_K(k_x, k_y) = E_{K'}(k_x, -k_y)$ symmetries, the transmission probabilities are the same no matter if the wave packet started in K or K' valley. This is verified in Fig. 7.3, which shows the transmission probability as a function of the wave packet energy, for different configurations of the channel defined by aligned potentials, as sketched in Fig. 7.1(a). Results for K and K' valleys in this case are exactly the same. Steps are observed in the transmission probabilities as the wave packet energy increases. This is a well known feature of any QPC, which is related to the existence of quantized energy levels inside the channel - whenever the energy crosses one of the energy levels, a step is produced. In fact, although not shown in the Fig. 7.3, we verify that increasing W moves the steps to lower E , just as expected for an usual QPC, once that

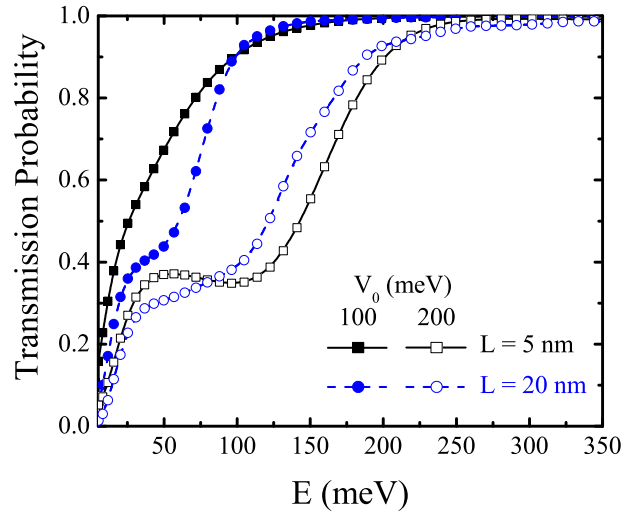


Figure 7.3: Transmission probability as a function of wave packet energy for aligned potentials with $V_0 = 100$ meV (closed symbols) and $V_0 = 200$ meV (open symbols). The value for width of the QPC was considered $W = 10$ nm. The square and circular symbols correspond to the lengths $L = 5$ and 20 nm, respectively.

the energy of the quantized states of the channel decreases as W increases. The figure shows that as L varies the position of the step does not change, but for smaller L , the steps are less pronounced.

Similar features are observed in the anti-aligned case, though with a fundamental difference - results for K and K' in this case are very different, as one can verify by comparing Figs. 7.4(a) and 7.4(b), respectively. This is a clear manifestation of the lack of inter-valley symmetry exhibited by the band structure shown in Fig. 7.2(b). Such a difference between transmission probabilities in different valleys suggests the use of this system as a valley filter. However, in order to do so, we should seek for the best configuration of the system that enhances valley polarization.

Figure 7.5 shows the transmission probabilities (upper panels) and the valley polarization (lower panels) for the anti-aligned system of Fig. 7.1(b) as a function of the bias potential V_0 , for different values of W and L , considering a wave packet energy $E = 30$ meV. Once the wave packet is initially injected in the lowest subband of the energy spectrum (Fig. 7.2), then we limit ourselves to the lowest QPC steps. Valley polarization is defined as $P = 1 - T_{K'}/T_K$, where $T_{K(K')}$ is the transmission probability for a wave packet starting at the $K(K')$ Dirac points, so that $P = 1$ (0) means a wave packet completely (un)polarized in K after the QPC. Transmission probabilities in all cases are reduced as V_0 increases, which is expected, since the existence of a barrier leads to stronger reflection of the tails of the wave packet that are outside the channel region. A very weak oscillation is observed in each curve, which is due to an interference related to the path difference between electrons that go straight through the channel and those that are reflected at

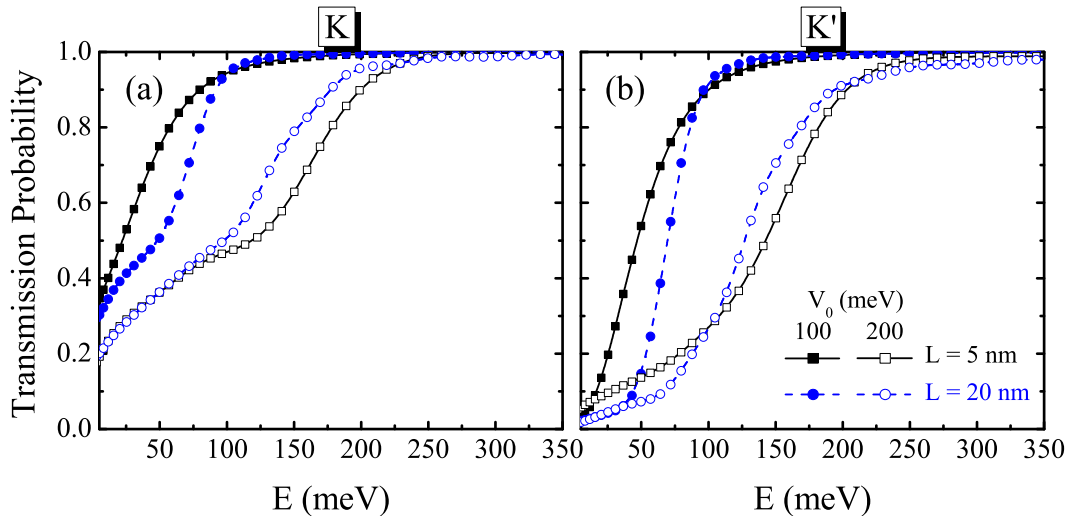


Figure 7.4: The same as Fig. 7.3, but for anti-aligned potentials and with initial wave packet in K valley (a) and in K' valley (b).

the exit and entrance of the channel. Results in Figs. 7.5 (b, d, f) show a polarization that increases up to 1 for higher values of L and V_0 , in particular for small W . For larger W , however, the electron starts to see a larger unbiased area in the channel, thus reducing the polarization effect. This polarization reduction for large W becomes even more significant for wave packets with higher energy. Indeed, extra energy bands with higher energy appear as W increases (see Fig. 7.1(b), blue dotted curves). These bands exhibit states with negative velocities, which, consequently, harness the polarization effect proposed here, which relies on bands with a single direction of the propagation velocity. The results in Fig. 7.4 demonstrate that as the initial energy of the wave packet E increases, high transmission probabilities are reached for wave packets starting in both valleys (K and K') and thus a suppression of the polarization effect is expected in this case, which is due to the low screening of the packet by the barriers for a fixed range of bias potential. It is also clear that increasing the channel length improves the valley polarization.

As already mentioned, even such almost perfect polarization for large L can be destroyed by increasing W . This is clarified in Fig. 7.6, which shows transmission probabilities (upper panels) and polarization (lower panels) as a function of the well width W in an anti-aligned QPC. In the case of $L = 20$ nm (dotted blue line), polarization stays around $\approx 100\%$ for smaller W , but starts to decrease for $W > 10$ nm and 13 nm, in the cases of $V_0 = 100$ meV and 200 meV, respectively.

In summary, our results demonstrate that an almost perfect valley filtering can be realised, provided (i) the electron energy is sufficiently low, (ii) the channel length is sufficiently long, and (iii) the channel width is narrow enough.

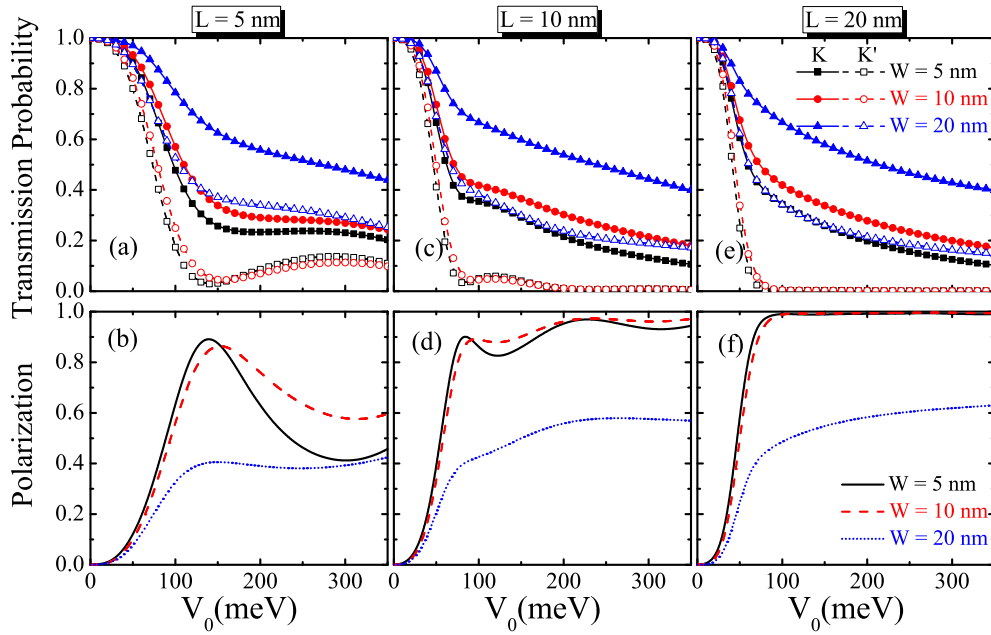


Figure 7.5: Transmission probability (top panels) and valley polarization (bottom panels) as a function of the electrostatic bias V_0 in the case of anti-aligned potentials with initial wave packet energy $E = 30$ meV and three different values of L : (a, b) 5 nm, (c, d) 10 nm and (e, f) 20 nm. The opened (closed) square-like, circular and triangular symbols correspond to $W = 5, 10$ and 20 nm, for the K (K') valley, respectively in panels (a), (c) and (e). The black solid, red dashed and blue dotted lines show the polarization for $W = 5, 10$ and 20 nm, respectively in panels (b), (d) and (f).

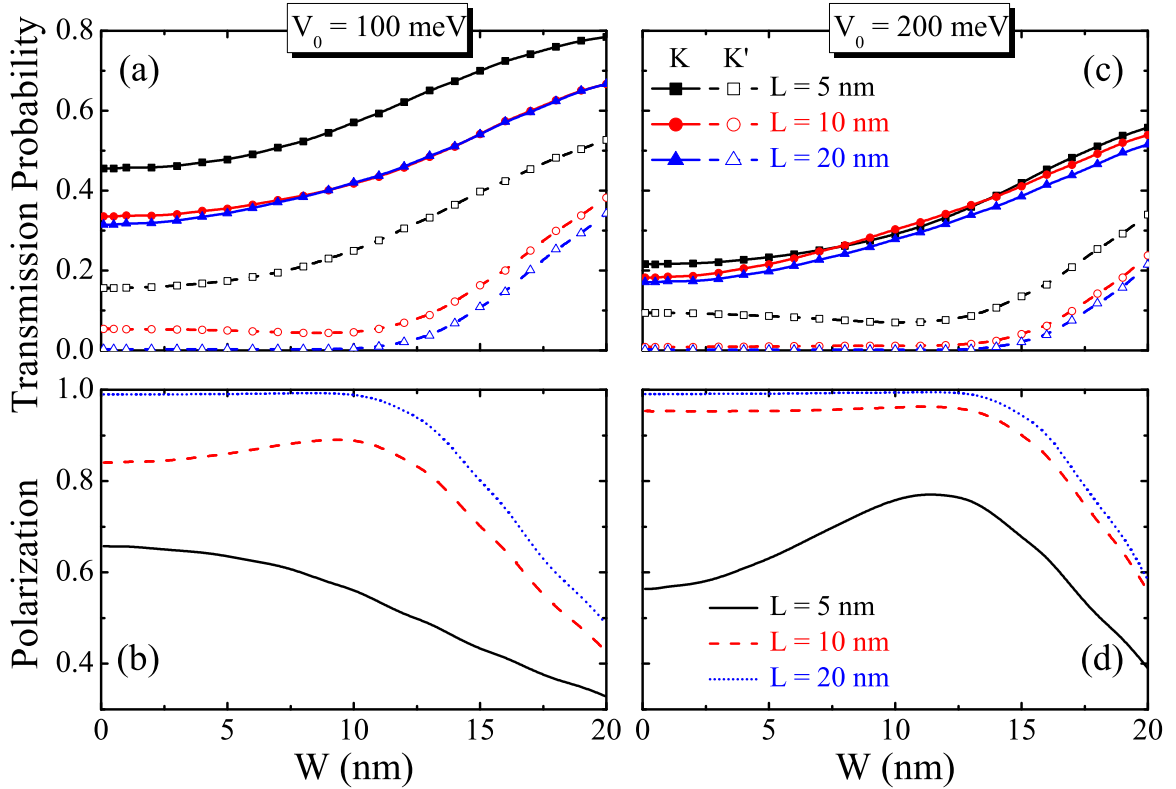


Figure 7.6: (a, c) Transmission probability and (b, d) the polarization as a function of width W of the QPC for anti-aligned potentials with $V_0 = 100$ meV (left side panels) and $V_0 = 200$ meV (right side panels). The average wave packet energy was $E = 30$ meV. The opened (closed) square-like, circular and triangular symbols correspond to $L = 5, 10$ and 20 nm, for the K (K') valley, respectively in Figs. (a) and (c). The black solid, red dashed and blue dotted curves show the polarization for $L = 5, 10$ and 20 nm, respectively in Figs. (b) and (d).

7.4 Conclusion

We calculated the transmission probabilities of a Gaussian wave packet through a quantum point contact defined by electrostatic gates in bilayer graphene. Our results demonstrate that, if one uses the energy gaps introduced by a bias between upper and lower layers in order to define the channel in the point contact, transmission plateaus are observed as the energy of the packet increases, which reflects the discrete eigenstate spectrum in the channel, just like in a conventional QPC. On the other hand, if the bias in the left and right sides of the channel are opposite to each other, although still forming the same energy gap at both sides, a special situation of energy dispersion is obtained, where electrons in each valley have only one possible direction of propagation. In this case, the QPC works as an efficient valley filter, where valley polarization may reach ≈ 1 with increasing gate potential. Such a valley filtering device can have an important impact on future graphene valley-tronics, as it can be relatively easily achieved just by depositing electrostatic gates on graphene[235], with no need either to control edge types, or to produce strain or non-zero mass regions, in contrast to the valley filters previously proposed in the literature.

Conclusions and perspectives

In this thesis, we studied and developed computationally the Split-operator technique for tight-binding and Dirac Hamiltonians in order to investigate electronic properties of carbon nanostructures formed by one or two graphite layers. Further, we also investigated the electronic properties of confined systems formed by monolayer, bilayer and hybrid mono-bilayer graphene using both continuum model and tight-binding approach.

We made a comparison between the energy levels obtained by tight-binding and Dirac models in order to identify which graphene ring structures can be described, to a good accuracy by the continuum model. Different shapes and edge terminations were considered, and a graphene ring defined by a staggered potential was investigated as well. Our results demonstrated that the energy levels of graphene quantum rings show a strong dependence on the ring geometry and the edge termination. Under an applied magnetic field these energy spectra presented the AB oscillations and in general rings with n -fold symmetry exhibited a formation of subbands with n -fold energies. Furthermore, we obtained that infinitely thin Dirac rings describe quite well two ring structures: armchair hexagonal and rhombus-shaped rings.

Further on, we obtained a general expression for the infinite-mass boundary condition in bilayer graphene that can be used for any kind of circular geometry. It was derived using the 4×4 Dirac-Weyl Hamiltonian in the vicinity of both K and K' points. Some electric properties for the bilayer graphene quantum dots defined by this new boundary condition were calculated, such as the energy spectrum as a function of the dot size, of the perpendicular magnetic field intensity and the cyclotron resonance. Our results for the energy spectrum presented an electron(e)-hole(h) symmetry $E_K^{e(h)}(m) = -E_{K'}^{h(e)}(m)$ that is kept for both cases, under the presence or absence of magnetic field. In absence of magnetic field, the energy spectrum exhibits two sets of states that correspond to the upper and lower bilayer energy bands. The lowest states demonstrated a $1/R^2$ dependence, while the upper set that approaches the inter-layer hopping parameter exhibited $1/R$ behavior. Furthermore, the energy spectrum obtained via continuum model was compared with the results calculated within the tight-binding approach for a circular quantum dot with actual edges and showed a good qualitative similarity.

Using the tight-binding approach, we numerically investigated the confined states in two different hybrid monolayer-bilayer systems. In order to understand the energy spectrum for these two hybrid structures, we calculated the influence of an external perpendicular magnetic field as well of different dot sizes on the spectra. Our results allowed us to identify which states are dot-localized states, edge states and mixed states in the energy spectrum. In the presence of the magnetic field, the energy levels approached to the Landau levels in the both zigzag and armchair edge terminations of the bilayer anti-dot and they exhibited an electron-hole symmetry. Both suggested monolayer-bilayer graphene quantum dot were demonstrated to be reasonable systems to confine carriers in graphene nanostructures. The confinement occurs due to the fact that: (i) a gap was opened just in bilayer region for the anti-dot case when it was considered an applied bias gate, whereas (ii) for the case of a bilayer graphene dot surround by a hexagonal region of monolayer graphene, even in the absence of a bias voltage the bilayer energies are lower than energy levels of the monolayer graphene.

Afterwards, we numerically studied the scattering, in the reciprocal and real spaces, of a Gaussian wave packet propagating close to graphene edges. Using the tight-binding model and the Split-operator technique we demonstrated the inter- and intra-valley scattering between K to K' Dirac cones for the reflections close respectively to the zigzag and armchair edges. Under the presence of an external magnetic field we verified the so called skipping orbits due to the scattering of the electron nearby the edge of the sample. On the other hand, for a pseudo-magnetic field induced by non-uniform strain our numerical results demonstrated that scattered wave packet behaved as a non-propagating edge state for the armchair terminated strained graphene.

Finally, we demonstrated that a quantum point contact defined by electrostatic gates in bilayer graphene can be used as a valley filtering device, being this way a very simple form to build valleytronic devices as compared to the already suggested structures proposed in the literature. Two kinds of the gate alignments were investigated using the tight-binding model and the Split-operator techniques in order to compute the transport properties for these systems. For the aligned case, plateaus in the transmission probability as a function of the initial wave packet energy were observed, suggesting a behaviour just like in a conventional quantum point contact. But if the bias are opposite in each side of the device, then the situation is favorable for valley filtering, because in this case the energy dispersion is not symmetric anymore. The chiral states are by this way responsible for allowing only certain direction of propagation in each valley. Our results provided the parameters that improve the efficiency of proposed bilayer system as a valley filter, such as length, width and amplitude of the applied potential. By our simulations, we observed that the almost perfect efficiency can be achieved for a long length and a narrow width of the channel formed between the bias gates.

Regarding the study of charge carriers dynamics in multi-layer graphene-related systems using the wave packet propagation or by a wavefront and for the works concerned

with electronic states in graphene, we propose some interesting problems to be investigated and to be developed in the near future. So, as a short-term perspective, we intend to address a study about the following problems:

- the wave packet scattering on bilayer graphene edges in order to check how much of the incident wave packet is spread to each one of the valleys K and K' in the reciprocal space [130];
- valley filtering in graphene due to substrate-induced potential: in this system, the mass potential is generated by a staggered potential, such that a spacial constriction for the electron in a certain region of monolayer is performed. Thus, we will investigate in which situations there will be a greater percentage of the transmission probability coefficient, leading to a valley filtering effect [127];
- the effect of a periodic potential induced by strain in the graphene eigenenergies: we will investigate which situations present opening of a gap in the energy spectrum. The pseudo-magnetic field induced by strain in our tight-binding model will not be introduced by artificially introducing a vector potential to the Peierls phase [216, 218], but rather by changing the interatomic distances of the carbon atoms of the lattice;
- the scattering of a Gaussian wave packet by an interface between monolayer and bilayer graphene formed by a single and a double boundary with zigzag or arm-chair edges. In this work, we shall demonstrate the dependence of the transmission probability related to the incident angle and also we shall present different features depending on the edge type of interface between monolayer and bilayer graphene, the K and K' Dirac cones considered and also on the alignment of the atomic bounds at monolayer / bilayer interface [186, 236, 237, 238, 239].

Appendix A

Multilayer graphene in AA stacking

An effective two-component Hamiltonian may be derived under some approximations for a n -layer graphene, in a similar way as for graphite. This 2×2 Hamiltonian is described in the low energy limit, *i. e.* in the limit such that the energy is much smaller than the hopping energy t_{\perp} between the parallel layers $E \ll t_{\perp}$, where the upper bands of the energy spectrum of the n -layer graphene are neglected. Thus, in a two-band approximation, one can write the 2×2 Hamiltonian for n coupled layers in rhombohedral stacking as [81]

$$H_n(k) = \frac{(\hbar v_F k)^n}{t_{\perp}^{n-1}} \begin{pmatrix} 0 & e^{-in\varphi_k} \\ e^{+in\varphi_k} & 0 \end{pmatrix}, \quad (8.1)$$

where $k = \sqrt{k_x^2 + k_y^2}$ and $\varphi_k = \tan^{-1}(k_y/k_x)$. The corresponding eigenenergy and wavefunction of the lowest (highest) conduction (valence) band are

$$E_{k,s,n} = \frac{s(\hbar v_F k)^n}{t_{\perp}^{n-1}}, \quad \Psi_{k,s,n} = \frac{1}{\sqrt{2}} \begin{pmatrix} 1 \\ -s e^{in\varphi_k} \end{pmatrix}, \quad \text{with } s = \pm 1, \quad (8.2)$$

where the sign of s refers to the conduction (+) or valence (−) bands, respectively.

Note that for n -layer graphene $E \propto k^n$. This approximation is valid for small energies and the quantitative deviation of this approximation gets more significant as the n increases.



Appendix B

Publications related to this thesis

- D. R. da Costa, M. Zarenia, A. Chaves, G. A. Farias, and F. M. Peeters. *Analytical study of the energy levels in bilayer graphene quantum dots*. Carbon **78**, 392 (2014). DOI: <http://dx.doi.org/10.1016/j.carbon.2014.06.078>

CARBON 78 (2014) 392–400

Available at www.sciencedirect.com
ScienceDirect
journal homepage: www.elsevier.com/locate/carbon

Analytical study of the energy levels in bilayer graphene quantum dots

D.R. da Costa ^{a,b}, M. Zarenia ^{b,*}, Andrey Chaves ^a, G.A. Farias ^a, F.M. Peeters ^{b,a}

^a Departamento de Física, Universidade Federal do Ceará, Caixa Postal 6030, 60455-900 Fortaleza, Ceará, Brazil
^b Department of Physics, University of Antwerp, Groenenborgerlaan 171, B-2020 Antwerp, Belgium

ARTICLE INFO **ABSTRACT**

Article history:
Received 5 March 2014
Accepted 29 June 2014
Available online 16 July 2014

Using the four-band continuum model we derive a general expression for the infinite-mass boundary condition in bilayer graphene. Applying this new boundary condition we analytically calculate the confined states and the corresponding wave functions in a bilayer graphene quantum dot in the absence and presence of a perpendicular magnetic field. Our results for the energy spectrum show an energy gap between the electron and hole states at small magnetic fields. Furthermore the electron (*e*) and hole (*h*) energy levels corresponding to the *K* and *K'* valleys exhibit the $E_{\pm}^{(n)}(m) = -E_{\mp}^{(n)}(m)$ symmetry, where *m* is the angular momentum quantum number.

© 2014 Elsevier Ltd. All rights reserved.

1. Introduction

A considerable number of studies have addressed the electronic properties of quantum dots (QDs) in semiconductors [1,2]. Such QDs can be used as single photon sources, lasers and are promising candidates for spin qubits and thus for future quantum information technology. However the spin-orbit and electron spin–nuclear spin interactions in conventional semiconductor QDs, i.e. mainly based on GaAs, limit the spin coherence time and thus the functionality of the device.

Very soon after the discovery of graphene [3,4], theoretical and experimental studies appeared on graphene quantum dots (GQDs). GQDs can be exceptional systems for spintronics applications due to their long spin coherence time which is a consequence of the very weak spin–orbit interaction in graphene. The gapless and linear spectrum of graphene at its Fermi energy in the vicinity of two non-equivalent points in the Brillouin zone, namely *K* and *K'*, results in the Klein tunneling effect which prevents electrical confinement of carriers in graphene structures [5]. Therefore, the direct etching of a

graphene sheet into small flakes seems to be the only realizable way for fabricating monolayer graphene QDs. In a series of theoretical studies the energy levels of triangular, hexagonal, rectangular and circular QDs have been investigated using both tight-binding and continuum (i.e. solving the Dirac–Weyl equation) models in the absence and presence of a perpendicular magnetic field [6–13]. These studies demonstrate that the energy spectrum of graphene QDs are highly dependent on the shapes and edges (which implies different boundary conditions) of the dot.

It has been recognized that two weakly van der Waals coupled sheets of graphene, i.e. known as bilayer graphene (BLG), has very different electronic properties from graphene [14]. Pristine BLG is gapless and exhibits an almost parabolic energy spectrum around the *K* and *K'* points in its Brillouin zone. The possibility of opening an energy gap in BLG using a perpendicular electric field, leads to the prediction [15–19] and realization [20,21] of gate defined QDs in BLG. In such QDs, the edges are no longer important.

Alternatively, bilayer graphene flakes are another type of QDs which may exhibit very different properties but which

* Corresponding author.
E-mail address: mohammad.zarenia@uantwerpen.be (M. Zarenia).
<http://dx.doi.org/10.1016/j.carbon.2014.06.078>
0008-6223/© 2014 Elsevier Ltd. All rights reserved.

- D. R. da Costa, A. Chaves, M. Zarenia, J. M. Pereira Jr., G. A. Farias, and F. M. Peeters. *Geometry and edge effects on the energy levels of graphene quantum rings: a comparison between tight-binding and simplified Dirac models*. Physical Review B **89**, 075418 (2014). DOI: 10.1103/PhysRevB.89.075418

PHYSICAL REVIEW B **89**, 075418 (2014)

Geometry and edge effects on the energy levels of graphene quantum rings: A comparison between tight-binding and simplified Dirac models

D. R. da Costa,^{1,2,*} Andrey Chaves,^{1,†} M. Zarenia,² J. M. Pereira Jr.,¹ G. A. Farias,^{1,‡} and F. M. Peeters^{1,2}

¹*Departamento de Física, Universidade Federal do Ceará, Caixa Postal 6030, Campus do Pici, 60455-900 Fortaleza, Ceará, Brazil*

²*Department of Physics, University of Antwerp, Groenenborgerlaan 171, B-2020 Antwerp, Belgium*

(Received 17 October 2013; revised manuscript received 30 January 2014; published 18 February 2014)

We present a systematic study of the energy spectra of graphene quantum rings having different geometries and edge types in the presence of a perpendicular magnetic field. Results are obtained within the tight-binding (TB) and Dirac models and we discuss which features of the former can be recovered by using the approximations imposed by the latter. Energy levels of graphene quantum rings obtained by diagonalizing the TB Hamiltonian are demonstrated to be strongly dependent on the rings geometry and the microscopical structure of the edges. This makes it difficult to recover those spectra by the existing theories that are based on the continuum (Dirac) model. Nevertheless, our results show that both approaches (i.e., TB and Dirac model) may provide similar results, but only for very specific combinations of ring geometry and edge types. The results obtained by a simplified model describing an infinitely thin circular Dirac ring show good agreement with those obtained for hexagonal and rhombus armchair graphene rings within the TB model. Moreover, we show that the energy levels of a circular quantum ring with an infinite mass boundary condition obtained within the Dirac model agree with those for a ring defined by a ring-shaped staggered potential obtained within the TB model.

DOI: 10.1103/PhysRevB.89.075418

PACS number(s): 81.05.U–, 71.10.Pm, 03.65.Ta

I. INTRODUCTION

Graphene, a two-dimensional lattice of carbon atoms [1], has been a subject of great interest during the past few years. This interest is not only due to its possible future technological applications, but also because it provides the possibility to probe interesting phenomena predicted by quantum field theories. Several of the exotic properties originate from the fact that low energy electrons in graphene obey the zero mass Dirac equation (for a review see, e.g., Ref. [2]).

Previous works have demonstrated interesting features coming from ringlike and dotlike confinement in graphene [3–9]. Theoretical studies have predicted Aharonov-Bohm (AB) oscillations in both the conductance [10] and the energy spectrum [11] of graphene quantum rings. In fact, AB conductance oscillations were observed in recent experiments on several circular rings fabricated in few-layer graphene [12]. Luo *et al.* [13] demonstrated theoretically that the energy spectrum of armchair quantum rings exhibits signatures of an effective time-reversal symmetry breaking, where a gap around zero energy, which can be removed by applying an external magnetic field, is observed.

From the point of view of the continuum model, where electrons are described as massless Dirac fermions, several models have been suggested for studying the confined states of graphene quantum rings. For instance, Recher *et al.* [14] have used the Dirac model to show that the combined effects of a ring-shaped mass-related potential and an external magnetic field can be used to break the valley degeneracy in graphene. A similar effect was also found by Wurm *et al.* [15], where it was theoretically demonstrated that the splitting of the valley degeneracy by a magnetic field in such a system can

also be observed in the transport properties of rings that are weakly coupled to leads. The analytical solution for the graphene ring proposed in Ref. [14] was used later by Abergel *et al.* [16] to study the interplay between valley polarization and electron-electron interactions on some measurable quantities in such a structure, where they observe, e.g., extra steps in the persistent current as a function of an external magnetic field. A recent paper [17] proposed a simplified model for obtaining energy levels in graphene quantum rings, based on an idea widely used for semiconductor quantum rings [18], where the radial component of the momentum of the confined particle is assumed to be zero, so that the effective Hamiltonian of the system depends only on the angular coordinate. This model has been recently used, e.g., for the study of wave packet revivals in monolayer and bilayer graphene rings [19].

Notice that the continuum model for graphene is developed by considering a periodic honeycomb lattice of carbon atoms of infinite size and by analyzing only the low energy sector of the corresponding tight-binding Hamiltonian. However, the experimentally obtained graphene quantum rings reported in the literature are normally fabricated by cutting out the graphene flake into a finite size ring-shaped structure. In order to take the finite size effects into account within the Dirac theory, the above mentioned previous papers have usually considered either infinite mass boundary conditions, or a “frozen” radial motion of the particles. But it is questionable that these conditions are really sufficient in order to describe a real graphene ring sample. If so, what are the limits of such approximations? Answering these questions is the main purpose of this paper, where we use the tight-binding model (TBM) to calculate the energy spectrum of graphene quantum rings with different geometries and different types of edges. We then discuss the main qualitative features of the obtained spectra in terms of the continuum (Dirac) approximation, making a comparison between the results obtained by such an approximation and those obtained by the TBM. Our results from tight-binding calculations show that the energy spectra

*diego_rabelo@fisica.ufc.br

†andrey@fisica.ufc.br

‡gil@fisica.ufc.br

- D. R. da Costa, A. Chaves, G. A. Farias, L. Covaci, and F. M. Peeters. *Wave-packet scattering on graphene edges in the presence of a pseudomagnetic field*. Physical Review B **86**, 115434 (2012). DOI:10.1103/PhysRevB.86.115434

PHYSICAL REVIEW B **86**, 115434 (2012)**Wave-packet scattering on graphene edges in the presence of a pseudomagnetic field**D. R. da Costa,¹ A. Chaves,¹ G. A. Farias,¹ L. Covaci,² and F. M. Peeters^{1,2}¹*Universidade Federal do Ceará, Departamento de Física, Caixa Postal 6030, 60455-760 Fortaleza, Ceará, Brazil*²*Department of Physics, University of Antwerp, Groenenborgerlaan 171, B-2020 Antwerp, Belgium*

(Received 2 July 2012; published 21 September 2012)

The scattering of a Gaussian wave packet in armchair and zigzag graphene edges is theoretically investigated by numerically solving the time-dependent Schrödinger equation for the tight-binding model Hamiltonian. Our theory allows us to investigate scattering in reciprocal space, and depending on the type of graphene edge we observe scattering within the same valley, or between different valleys. In the presence of an external magnetic field, the well-known skipping orbits are observed. However, our results demonstrate that in the case of a pseudomagnetic field, induced by nonuniform strain, the scattering by an armchair edge results in a nonpropagating edge state.

DOI: 10.1103/PhysRevB.86.115434

PACS number(s): 81.05.ue, 73.63.-b, 73.50.Pz

I. INTRODUCTION

Due to its unique electronic properties, graphene has become a topic of intensive study in recent years. Within the low-energy approximation for the tight-binding Hamiltonian of graphene, electrons behave as massless Dirac fermions, with a linear energy dispersion.¹ This leads to a plethora of interesting physical phenomena, ranging from Klein tunneling and other quasirelativistic effects^{2,3} to the existence of new types of electron degrees of freedom, namely, the pseudospin, related to the distribution of the wave function over the carbon atoms belonging to the different triangular sublattices composing the graphene hexagonal lattice, and the presence of two inequivalent electronic valleys, usually labeled as K and K' , in the vicinity of the gapless points of the energy spectrum of graphene.

Recent papers studied the scattering of electrons by edges⁴ and defects⁵ in graphene, both theoretically⁶ and experimentally.⁷ Armchair and zigzag are the two types of edges which are most frequently considered in the study of graphene ribbons, although other types of terminations exist due to edge reconstruction, which has been demonstrated both theoretically⁸ and experimentally.^{9–11} Even so, the edge reconstruction effect strongly depends on how the nanoribbon is made: Normally, it occurs when the technique used to fabricate the nanoribbon is based on a mechanism that drives the system to thermodynamic equilibrium. According to the continuum (Dirac) model, armchair edges in finite graphene samples lead to a boundary condition that mixes the wave functions of K and K' valleys, whereas a zigzag edge appears in the Dirac theory of graphene as a separate boundary condition for the wave functions of each valley.^{12,13} This suggests that electrons reflected by a graphene edge would exhibit intervalley scattering only in the armchair case, whereas reflection by a zigzag edge would produce scattering inside the same Dirac valley. This prediction was confirmed by recent experiments,¹⁴ where intervalley scattering by armchair edges was even shown to be very robust in the presence of defects. The inter- and intravalley scattering possibilities are schematically illustrated in Fig. 1(a), which shows K and K' Dirac cones in the reciprocal space of graphene.

Besides its singular electronic properties, graphene also exhibits interesting mechanical properties, as it can support

strong elastic stretch. This provides us with the new possibility to tune the electron properties in graphene through strain engineering.^{15–25} In fact, it has been demonstrated recently that electrons in a strained graphene lattice behave as if they were under an external magnetic field, which points towards opposite directions in the K and K' valleys, so that the time reversal symmetry of the system as a whole is preserved.²⁶ Such fields were experimentally observed recently, when measurements of the energy states in a graphene bubble revealed a Landau-level-like structure corresponding to an external magnetic field of ≈ 300 T.²⁷ By designing nonuniform strain fields in a graphene sheet, one is able to produce a uniform pseudomagnetic field for electrons.²⁸

The aim of this paper is twofold. We use wave-packet dynamics calculations (i) to investigate electron reflection by armchair and zigzag edges in a finite graphene sample, assumed to be made by cutting a graphene monolayer, such that no edge reconstruction is expected to occur at room temperature, where our results demonstrate the possibilities of inter- and intravalley scattering, depending on the type of edge, and (ii) to study the influence of an external magnetic field and a nonuniform strain distribution on the electron trajectories in these systems. We compare the features observed for electrons under a perpendicular external magnetic field with those seen with a pseudomagnetic field. Figure 1(b) shows a sketch of the graphene flake considered in our calculations, where the open (green) circles illustrate the unstrained sample and the closed (black) circles illustrate the strained one. Such a nonuniform strain field was suggested by Guinea *et al.*²⁸ and was shown to exhibit an almost uniform pseudomagnetic field.

All the calculations were done within the tight-binding description of graphene, using the time-evolution method developed in Ref. 29. As we are not restricting ourselves to a single Dirac cone in our model, the scattering between Dirac cones by armchair edges will appear naturally. Notice that Fig. 1(b) is just an illustrative scheme of our system, where the number of atoms was reduced in order to help its visualization. Besides, the sample shown in Fig. 1(b) is a ribbon, which improves the visualization of the strained case. However, the actual flake considered in our calculations has 1801×2000 atoms, which looks more like a rectangle, rather than a ribbon, and corresponds to a flake with dimensions of

Bibliography

- [1] A. H. Castro Neto, F. Guinea, N. M. R. Peres, K. S. Novoselov, and A. K. Geim. *The electronic properties of graphene*. Reviews of Modern Physics **81**, 109 (2009).
- [2] M. J. Allen, V. C. Tung, and R. B. Kaner. *Honeycomb carbon: a review of graphene*. Chemical Reviews **110**, 132 (2010).
- [3] R. E. Peierls. *Quelques proprietes typiques des corps solides*. Annales de l'É. H. Poincaré **5**, 177 (1935).
- [4] L. D. Landau. *Zur theorie der phasenumwandlungen II*. Physikalische Zeitschrift der Sowjetunion **11**, 26 (1937).
- [5] L. D. Landau and E. M. Lifshitz. *Statistical Physics. Part I*. Pergamon, Oxford (1980).
- [6] N. D. Mermin. *Crystalline order in two dimensions*. Physical Review **176**, 250 (1968).
- [7] M. I. Katsnelson. *Graphene: carbon in two dimensions*. Material Today **10**, 20 (2007).
- [8] A. K. Geim and K. S. Novoselov. *The rise of graphene*. Nature Materials **6**, 183 (2007).
- [9] H. W. Kroto, J. R. Heath, S. C. O'Brien, R. F. Curl, and R. E. Smalley. *C-60 - Buckminsterfullerene*. Nature **318**, 162 (1985).
- [10] The official website of the Nobel prize. *The nobel prize in chemistry 1996*. Available in: http://www.nobelprize.org/nobel_prizes/chemistry/laureates/1996/. Accessed on: August 21, 2013.
- [11] S. Iijima. *Helical microtubules of graphitic carbon*. Nature **354**, 56 (1991).

- [12] S. Iijima and T. Ichihashi. *Single-shell carbon nanotubes of 1 nm diameter*. Nature **363**, 603 (1993).
- [13] D. S. Bethune, C. H. Kiang, M. S. Devries, G. Gorman, R. Savoy, J. Vazquez, and R. Beyers. *Cobalt-catalyzed growth of carbon nanotubes with single-atomic films*. Nature **363**, 605 (1993).
- [14] P. R. Wallace. *The band theory of graphite*. Physical Review **71**, 622 (1947).
- [15] Interview with A. K. Geim in The Science Watch. *U. Manchester's Andre Geim: sticking with graphene*. Available in: <http://archive.sciencewatch.com/inter/aut/2008/08-aug/08augSWGeim/>. Accessed on: August 21, 2013.
- [16] Interview with K. Novoselov in The Science Watch. *Konstantin Novoselov: from the special topic of graphene*. Available in: <http://archive.sciencewatch.com/ana/st/graphene/09febSTGraNovo/>. Accessed on: August 21, 2013.
- [17] Interview with C. A. dos Santos in Ciência hoje. *Uma história de sorte e sagacidade*. Available in: <http://cienciahoje.uol.com.br/colunas/do-laboratorio-para-a-fabrica/uma-historia-de-sorte-e-sagacidade>. Accessed on: August 21, 2013.
- [18] K. S. Novoselov, A. K. Geim, S. V. Morozov, D. Jiang, Y. Zhang, S. V. Dubonos, I. V. Grigorieva, and A. A. Firsov. *Electric field effect in atomically thin carbon films*. Science **306**, 666 (2004).
- [19] The official website of the Nobel prize. *The nobel prize in physics 2010*. Available in: http://www.nobelprize.org/nobel_prizes/physics/laureates/2010/. Accessed on: August 21, 2013.
- [20] R. Van Noorden. *The trials of new carbon*. Nature **469**, 14 (2011).
- [21] K. S. Novoselov, A. K. Geim, S. V. Morozov, D. Jiang, M. I. Katsnelson, I. V. Grigorieva, S. V. Dubonos, and A. A. Firsov. *Two-dimensional gas of massless Dirac fermions in graphene*. Nature **438**, 197 (2005).
- [22] A. K. Geim and P. Kim. *Carbon wonderland*. Scientific American **298**, 90 (2008).
- [23] F. Schedin, A. K. Geim, S. V. Morozov, E. W. Hill, P. Blake, M. I. Katsnelson, and K. S. Novoselov. *Detection of individual gas molecules adsorbed on graphene*. Nature Materials **6**, 652 (2007).
- [24] S. H. R. de Sena. *Electronic properties of trilayer graphene and strained carbon nanoribbons*. Doctor thesis. Universidade Federal do Ceará, Fortaleza, (2012).

- [25] A. K. Geim and I. V. Grigorieva. *Van der waals heterostructures*. Nature **499**, 419 (2013).
- [26] Programs by David Manthey: Orbital Viewer. Available in: <http://www.orbitals.com/programs/index.htm>. Accessed on: August 16, 2013.
- [27] R. Saito, G. F. Dresselhaus, and M. S. Dresselhaus. *Physical properties of carbon nanotubes*. Imperial College Press, London (1998).
- [28] T. W. Graham Solomons and Craig B. Fryhle. *Organic Chemistry*. 10th edition, John Wiley & Sons, New York (2011).
- [29] M. Scarselli, P. Castrucci, and M. De Crescenzi. *Electronic and optoelectronic nano-devices based on carbon nanotubes*. Journal of Physics: Condensed Matter **24**, 313202 (2012).
- [30] A. Jorio, M. S. Dresselhaus, R. Saito, and G. F. Dresselhaus. *Raman spectroscopy in graphene related systems*. Wiley-VCH, Weinheim (2011).
- [31] M. O. Goerbig and J.-N. Fuchs. *Introduction to the physical properties of graphene*. Lecture Notes (2008).
- [32] M. O. de Castro. *Síntese de grafeno pelo método CVD*. Master thesis. Universidade Federal do Ceará, Fortaleza, (2011).
- [33] C. Soldano, A. Mahmood and E. Dujardin. *Production, properties and potential of graphene*. Carbon **48**, 2127 (2010).
- [34] Presentation of A. K. Geim. *Random walk to graphene: story behind*. Available in: http://www.nobelprize.org/nobel_prizes/physics/laureates/2010/geim-lecture-slides.pdf. Accessed on: August 21, 2013.
- [35] C. Riedl, C. Coletti and U. Starke. *Structural and electronic properties of epitaxial graphene on SiC(0001): a review of growth, characterization, transfer doping and hydrogen intercalation*. Journal of Physics D: Applied Physics **43**, 374009 (2010).
- [36] B. L. VanMil, R. L. Myers-Ward, J. L. Tedesco, C. R. Eddy, G. G. Jernigan, J. C. Culbertson, P. M. Campbell, J. M. McCrate, S. A. Kitt, and D. K. Gaskill. *Graphene formation on SiC substrates*. Materials Science Forum **615**, 211 (2009).
- [37] C. Berger, Z. M. Song, T. B. Li, X. B. Li, A. Y. Ogbazghi, R. Feng, Z. T. Dai, A. N. Marchenkov, E. H. Conrad, P. N. First, and W. A. de Heer. *Ultrathin epitaxial graphite: 2D electron gas properties and a route toward graphene-based nanoelectronics*. The Journal of Physical Chemistry B **108**, 19912 (2004).

- [38] C. Coletti, C. Riedl, D. S. Lee, B. Krauss, L. Patthey, K. von Klitzing, J. H. Smet, and U. Starke. *Charge neutrality and band-gap tuning of epitaxial graphene on SiC by molecular doping*. Physical Review B **81**, 235401 (2010).
- [39] K. S. Kim, Y. Zhao, H. Jang, S. Y. Lee, J. M. Kim, K. S. Kim, J.-H. Ahn, P. Kim, J.-Y. Choi, and B. H. Hong. *Large-scale pattern growth of graphene films for stretchable transparent electrodes*. Nature **457**, 706 (2009).
- [40] C. Mattevi, H. Kima and M. Chhowalla. *A review of chemical vapour deposition of graphene on copper*. Journal of Materials Chemistry **21**, 3324 (2010).
- [41] M. E. Schmidt. *Plasma enhanced chemical vapor deposition of nanocrystalline graphene and device fabrication development*. Doctoral thesis. University of Southampton, Southampton, (2012).
- [42] A. Reina, S. Thiele, X. Jia, S. Bhaviripudi, M. Dresselhaus, J. Schaefer, and J. Kong. *Growth of large-area single- and bi-layer graphene by controlled carbon precipitation on polycrystalline Ni surfaces*. Nano Research **2**, 509 (2009).
- [43] A. Reina, X. Jia, J. Ho, D. Nezich, H. Son, V. Bulovic, M. S. Dresselhaus, and J. Kong. *Large area, few-Layer graphene films on arbitrary substrates by chemical vapor deposition*. Nano Letters **9**, 30 (2009).
- [44] D. Kondo, S. Sato, K. Yagi, N. Harada, M. Sato, M. Nihei, and N. Yokoyama. *Low-Temperature synthesis of graphene and fabrication of top-gated field effect transistors without using transfer processes*. Applied Physics Express **3**, 025102 (2010).
- [45] X. Li, W. Cai, J. An, S. Kim, J. Nah, D. Yang, R. Piner, A. Velamakanni, I. Jung, E. Tutuc, S. K. Banerjee, L. Colombo, and R. S. Ruoff. *Large-area synthesis of high-quality and uniform graphene films on copper foils*. Science **324** (5932), 1312 (2009).
- [46] X. Li, C. W. Magnuson, A. Venugopal, R. M. Tromp, J. B. Hannon, E. M. Vogel, L. Colombo, and R. S. Ruoff. *Large-area graphene single crystals grown by low-pressure chemical vapor deposition of methane on copper*. Journal of the American Chemical Society **133** (9), 28169 (2011).
- [47] P. W. Sutter, J. Flege, and E. A. Sutter. *Epitaxial graphene on ruthenium*. Nature **7** (5), 406 (2008).
- [48] I. Pletikosić, M. Kralj, P. Pervan, R. Brako, J. Coraux, A. T. N'Diaye, C. Busse, and T. Michely. *Dirac cones and minigaps for graphene on Ir(111)*. Physical Review Letters **102** (5), 056808 (2009).
- [49] N. Savage. *Super carbon*. Nature (London) **483**, S30 (2012).

- [50] ParisTech Review. *Is graphene to replace silicon?* Available in: <http://www.paristechreview.com/2013/09/30/graphene-replace-silicon/>. Accessed on: October 20, 2014.
- [51] A. Hudson. *Is graphene a miracle material?* BBC news, published on May 21th (2011). Available in: http://news.bbc.co.uk/2/hi/programmes/click_online/9491789.stm. Accessed on: October 20, 2014.
- [52] F. Bonaccorso, Z. Sun, T. Hasan, and A. C. Ferrari. *Graphene photonics and optoelectronics*. *Nature Photonics* **4**, 611 (2010).
- [53] S.-H. Bae, O. Kahya, B. K. Sharma, J. Kwon, H. J. Cho, B. Ozyilmaz, and J.-H. Ahn. *Graphene-P(VDF-TrFE) Multilayer Film for Flexible Applications*. *ACS Nano* **7**, 3130 (2013).
- [54] S. Bae, H. Kim, Y. Lee, X. Xu, J.-S. Park, Y. Zheng, J. Balakrishnan, T. Lei, H. R. Kim, Y. I. Song, Y.-J. Kim, K. S. Kim, B. Özyilmaz, J.-H. Ahn, B. H. Hong, and S. Iijima. *Roll-to-roll production of 30-inch graphene films for transparent electrodes*. *Nature Nanotechnology* **5**, 574 (2010).
- [55] J.-H. Ahn and B. H. Hong. *Graphene for displays that bend*. *Nature Nanotechnology* **9**, 737 (2014).
- [56] G. Jo, M. Choe, S. Lee, W. Park, Y. H. Kahng, and T. Lee. *The application of graphene as electrodes in electrical and optical devices*. *Nanotechnology* **23**, 112001 (2012).
- [57] S. Böhm. *Graphene against corrosion*. *Nature Nanotechnology* **9**, 741 (2014).
- [58] D. J. F. Gordon, T. Harding, S. Böhm, and W. Li. *Environmentally friendly protective coatings for metal substrate*. Patent no. WO/2011069663 (2011).
- [59] N. T. Kirkland, T. Schiller, N. Medhekar, and N. Birbilis. *Exploring graphene as a corrosion protection barrier*. *Corrosion Science* **56**, 1 (2012).
- [60] R. V. Dennis, L. T. Viyannalage, A. V. Gaikwad, T. K. Rout, and S. Banerjee. *Graphene nanocomposite coatings for protecting low-alloy steels from corrosion*. *American Ceramic Society Bulletin* **92**, 18 (2013).
- [61] S. Chen, L. Brown, M. Levendorf, W. Cai, S.-Y. Ju, J. Edgeworth, X. Li, C. W. Magnuson, A. Velamakanni, R. D. Piner, J. Kang, J. Park, and R. S. Ruoff. *Oxidation Resistance of Graphene-Coated Cu and Cu/Ni Alloy*. *ACS Nano* **5**, 1321 (2011).

- [62] F. Xia, T. Mueller, Y.-m. Lin, A. Valdes-Garcia, and P. Avouris. *Ultrafast graphene photodetector*. *Nature Nanotechnology* **4**, 839 (2009).
- [63] T. Mueller, F. Xia, and P. Avouris. *Graphene photodetectors for high-speed optical communications*. *Nature Photonics* **4**, 297 (2010).
- [64] F. Xia, T. Mueller, R. Golizadeh-Mojarad, M. Freitag, Y.-m. Lin, J. Tsang, V. Perebeinos, and P. Avouris. *Photocurrent imaging and efficient photon detection in a graphene transistor*. *Nano Letters* **9**, 1039 (2009).
- [65] J. Ryu, Y. Kim, D. Won, N. Kim, J. S. Park, E.-K. Lee, D. Cho, S.-P. Cho, S. J. Kim, G. H. Ryu, H.-A.-S. Shin, Z. Lee, B. H. Hong, and S. Cho, *Fast Synthesis of High-Performance Graphene Films by Hydrogen-Free Rapid Thermal Chemical Vapor Deposition*. *ACS Nano* **8**, 950–956 (2014).
- [66] J. Kang, D. Shin, S. Baea, and B. H. Hong. *Graphene transfer: key for applications*. *Nanoscale* **4**, 5527–5537 (2012).
- [67] S. J. Kim, J. Ryu, S. Son, J. M. Yoo, J. B. Park, D. Won, E.-K. Lee, S.-P. Cho, S. Bae, S. Cho, and B. H. Hong. *Simultaneous Etching and Doping by Cu-Stabilizing Agent for High-Performance Graphene-Based Transparent Electrodes*. *Chemistry of Materials* **26**, 2332–2336 (2014).
- [68] C. Yan, K-S. Kim, S.-K. Lee, S.-H. Bae, B. H. Hong, J.-H. Kim, H.-J. Lee, and J.-H. Ahn. *Mechanical and Environmental Stability of Polymer Thin-Film-Coated Graphene*. *ACS Nano* **6**, 2096–2103 (2012).
- [69] J. Park, W. H. Lee, S. Huh, S. H. Sim, S. B. Kim, K. Cho, B. H. Hong, and K. S. Kim. *Work-Function Engineering of Graphene Electrodes by Self-Assembled Monolayers for High-Performance Organic Field-Effect Transistors*. *The Journal Physical Chemistry Letters* **2**, 841–845 (2011).
- [70] A. Zurutuza and C. Marinelli. *Challenges and opportunities in graphene commercialization*. *Nature Nanotechnology* **9**, 730 (2014).
- [71] J. Ribeiro-Soares and M. S. Dresselhaus. *News and Views: Perspectives on Graphene and Other 2D Materials Research and Technology Investments*. *Brazilian Journal of Physics* **44**, 278 (2014).
- [72] Q. Tannock. *Exploiting carbon flatland*. *Nature Materials* **11**, 2 (2012).
- [73] Andrey Chaves. *Dinâmica de pacotes de onda em semicondutores e grafeno e de vórtices em supercondutores*. Doctor Thesis. Universidade Federal do Ceará, Fortaleza, (2010).

- [74] V. M. Pereira and A. H. Castro Neto. *Strain Engineering of Graphene's Electronic Structure*. Physical Review Letters **103**, 046801 (2009).
- [75] M. A. H. Vozmediano, M. I. Katsnelson, and F. Guinea. *Gauge fields in graphene*. Physics Reports **496**, 109 (2010).
- [76] V. M. Pereira, A. H. Castro Neto, and N. M. R. Peres. *Tight-binding approach to uniaxial strain in graphene*. Physical Review B **80**, 045401 (2009).
- [77] S. Schnez, K. Ensslin, M. Sigrist, and T. Ihn. *Analytic model of the energy spectrum of a graphene quantum dot in a perpendicular magnetic field*. Physical Review B **78**, 195427 (2008).
- [78] S. Y. Zhou, G. -H. Gweon, A. V. Fedorov, P. N. First, W. A. de Heer, D. -H. Lee, F. Guinea, A. H. Castro Neto, and A. Lanzara. *Substrate-induced bandgap opening in epitaxial graphene*. Nature Materials **6**, 770 (2007).
- [79] E. McCann, M. Koshino. *The electronic properties of bilayer graphene*. Reports on Progress in Physics **76**, 056503 (2013)
- [80] E. McCann, D. S. L. Abergel, and V. I. Falkó. *Electrons in bilayer graphene*. Solid State Communications **143**, 110 (2007).
- [81] S. B. Kumar and Jing Guo. *Chiral tunneling in trilayer graphene*. Applied Physics Letters **100**, 163102 (2012).
- [82] G. B. Arfken and H. J. Weber. *Mathematical methods for physicists*. Sixth edition. California: Elsevier Academic Press, (2005).
- [83] G. Li and E. Y. Andrei. *Observation of Landau levels of Dirac fermions in graphite*. Nature Physics **3**, 623 (2007).
- [84] M. L. Sadowski, G. Martinez, M. Potemski, C. Berger, and W. A. de Heer. *Landau Level Spectroscopy of Ultrathin Graphite Layers*. Physical Review Letters **97**, 266405 (2006).
- [85] Z. Jiang, E. A. Henriksen, L. C. Tung, Y.-J. Wang, M. E. Schwartz, M. Y. Han, P. Kim, and H. L. Stormer. *Infrared Spectroscopy of Landau Levels of Graphene*. Physical Review Letters **98**, 197403 (2007).
- [86] J. M. Pereira, Jr., F. M. Peeters, and P. Vasilopoulos. *Landau levels and oscillator strength in a biased bilayer of graphene*. Physical Review B **76**, 115419 (2007).
- [87] E. McCann and V. I. Falkó. *Symmetry of boundary conditions of the Dirac equation for electrons in carbon nanotubes*. Journal of Physics: Condensed Matter **16**, 2371 (2004).

- [88] L. Brey and H. A. Fertig. *Electronic states of graphene nanoribbons studied with the Dirac equation*. Physical Review B **73**, 235411 (2006).
- [89] L. Brey and H. A. Fertig. *Edge state and quantized Hall effect in graphene*. Physical Review B **73**, 195408 (2006).
- [90] A. R. Akhmerov and C. W. J. Beenakker. *Boundary conditions for Dirac fermions on a terminated honeycomb lattice*. Physical Review B **77**, 085423 (2008).
- [91] J. Wurm. *Dirac fermions in graphene nanostructures: edges effects on spectral density and quantum transport*. Doctor thesis. Universität Regensburg, Regensburg - Germany, (2011).
- [92] G. Giovannetti, P. A. Khomyakov, G. Brocks, P. J. Kelly, and J. van den Brink. *Substrate-induced band gap in graphene on hexagonal boron nitride: Ab initio density functional calculations*. Physical Review B **76**, 073103 (2007).
- [93] M. V. Berry and R. J. Mondragon. *Neutrino Billiards: Time-Reversal Symmetry-Breaking Without Magnetic Fields*. Proceedings of the Royal Society London, Ser. A **412**, 53 (1987).
- [94] P. Recher, B. Trauzettel, A. Rycerz, Ya. M. Blanter, C. W. J. Beenakker, and A. F. Morpurgo. *Aharonov-Bohm effect and broken valley degeneracy in graphene rings*. Physical Review B **76**, 235404 (2007).
- [95] D. S. L. Abergel, V. M. Apalkov, and T. Chakraborty. *Interplay between valley polarization and electron-electron interaction in a graphene ring*. Physical Review B **78**, 193405 (2008).
- [96] M. Zarenia, A. Chaves, G. A. Farias, and F. M. Peeters. *Energy levels of triangular and hexagonal graphene quantum dots: A comparative study between the tight-binding and Dirac equation approach*. Physical Review B **84**, 245403 (2011).
- [97] J. J. Sakurai. *Modern Quantum Mechanics*. Revised Edition. Massachusetts: Addison-Wesley Publishing Company, (1994).
- [98] J. P. M. Braga. *Técnica Split Operator em coordenadas generalizadas*. Master thesis. Universidade Federal do Ceará, Fortaleza, (2010).
- [99] M. H. Degani. *Stark ladders in strongly coupled GaAs-AlAs superlattices*. Applied Physics Letters **59**, 57 (1991).
- [100] M. H. Degani and J. P. Leburton. *Single-electron states and conductance in lateral-surface superlattices*. Physical Review B **44**, 10901 (1991).
- [101] M. H. Degani. *Competition between shallow-impurity and T-shaped quantum-wire states*. Physical Review B **66**, 233306 (2002).

- [102] C. L. N. de Oliveira, J. S. de Sousa, J. A. K. Freire, G. A. Farias, V. N. Freire, and M. H. Degani. *Lifetime of quasi-bound states in open semiconductor quantum structures*. *Physica Status Solidi (c)* **2**, 3031 (2005).
- [103] M. Suzuki. *Fractal decomposition of exponential operators with applications to many-body theories and Monte Carlo simulations*. *Physics Letters A* **146**, 319 (1990).
- [104] William H. Press, Brian P. Flannery, Saul A. Teukolsky, and William T. Vetterling. *Numerical recipes in Fortran 77: The art of scientific computing*. 2nd Edition. Cambridge University Press, United States of America, (1992).
- [105] Andrey Chaves, G. A. Farias, F. M. Peeters, and B. Szafran. *Wave packet dynamics in semiconductor quantum rings of finite width*. *Physical Review B* **80**, 125331 (2009).
- [106] Kh Yu Rakhimov, Andrey Chaves, G. A. Farias, and F. M. Peeters. *Wavepacket scattering of Dirac and Schrödinger particles on potential and magnetic barriers*. *Journal of Physics: Condensed Matter* **23**, 275801 (2011).
- [107] G. Grosso and G. P. Parravicini. *Solid state physics*. San Diego: Academic Press, (2003).
- [108] C. Kittel. *Introdução à física do estado sólido*. 8th edition. Rio de Janeiro: LTC, (2006).
- [109] R. L. Liboff. *Introductory quantum mechanics*. 4th edition. San Francisco: Addison-Wesley Publishing Company, (2003).
- [110] Z. Wu, Z. Z. Zang, K. Chang, and F. M. Peeters. *Quantum tunneling through graphene nanorings*. *Nanotechnology* **21**, 185201 (2010).
- [111] M. Grujić, M. Zarenia, A. Chaves, M. Tadić, G. A. Farias, and F. M. Peeters. *Electronic and optical properties of a circular graphene quantum dot in a magnetic field: Influence of the boundary conditions*. *Physical Review B* **84**, 205441 (2011).
- [112] P. Hewageegana and V. Apalkov. *Electron localization in graphene quantum dots*. *Physical Review B* **77**, 245426 (2008).
- [113] C. A. Downing, D. A. Stone, and M. E. Portnoi. *Zero-energy states in graphene quantum dots and rings*. *Physical Review B* **84**, 155437 (2011).
- [114] J. Schelter, B. Trauzettel, and P. Recher. *How to Distinguish between Specular and Retroconfigurations for Andreev Reflection in Graphene Rings* *Physical Review Letters* **108**, 106603 (2012).

- [115] S. Zhang, H. Chen, E. Zhang, and D. Liu. *The Aharonov-Anandan current induced by a time-dependent magnetic flux in graphene rings*. Europhysics Letters **103**, 58005 (2013).
- [116] J. Schelter, D. Bohr, and B. Trauzettel. *Interplay of the Aharonov-Bohm effect and Klein tunneling in graphene*. Physical Review B **81**, 195441 (2010).
- [117] C.-H. Yan and L.-F. Wei. *Size effects in Aharonov-Bohm graphene rings*. Journal of Physics: Condensed Matter **22**, 295503 (2010).
- [118] S. Russo, J. B. Oostinga, D. Wehenkel, H. B. Heersche, S. S. Sobhani, L. M. K. Vandersypen, and A. F. Morpurgo. *Observation of Aharonov-Bohm conductance oscillations in a graphene ring*. Physical Review B **77**, 085413 (2008).
- [119] T. Luo, A. P. Iyengar, H. A. Fertig, and L. Brey. *Effective time-reversal symmetry breaking and energy spectra of graphene armchair rings*. Physical Review B **80**, 165310 (2009).
- [120] J. Wurm, M. Wimmer, H. U. Baranger, and K. Richter. *Graphene rings in magnetic fields: Aharonov-Bohm effect and valley splitting*. Semiconductor Science and Technology **25**, 034003 (2010).
- [121] M. Zarenia, J. M. Pereira, A. Chaves, F. M. Peeters, and G. A. Farias. *Simplified model for the energy levels of quantum rings in single layer and bilayer graphene*. Physical Review B **81**, 045431 (2010).
- [122] F. E. Meijer, A. F. Morpurgo, and T. M. Klapwijk. *One-dimensional ring in the presence of Rashba spin-orbit interaction: Derivation of the correct Hamiltonian*. Physical Review B **66**, 033107 (2002); B. Molnár, F. M. Peeters, and P. Vasilopoulos. *Spin-dependent magnetotransport through a ring due to spin-orbit interaction*. Physical Review B **69**, 155335 (2004).
- [123] T. García, S. Rodríguez-Bolívar, N. A. Cordero, and E. Romera. *Wavepacket revivals in monolayer and bilayer graphene rings*. Journal of Physics: Condensed Matter **25**, 235301 (2013).
- [124] M. I. Katsnelson, K. S. Novoselov, and A. K. Geim. *Chiral tunnelling and the Klein paradox in graphene*. Nature Physics **2**, 620 (2006).
- [125] A. Matulis and F. M. Peeters. *Quasibound states of quantum dots in single and bilayer graphene*. Physical Review B **77**, 115423 (2008).
- [126] J. Wurm, A. Rycerz, I. Adagideli, M. Wimmer, K. Richter, and H. U. Baranger. *Symmetry Classes in Graphene Quantum Dots: Universal Spectral Statistics, Weak Localization, and Conductance Fluctuations*. Physical Review Letters **102**, 056806 (2009).

- [127] M. Zarenia, O. Leenaerts, B. Partoens, and F. M. Peeters. *Substrate-induced chiral states in graphene*. Physical Review B **86**, 085451 (2012).
- [128] R. E. Peierls. *Zur Theorie des Diamagnetismus von Leitungselektronen*. Zeitschrift für Physik **80**, 763 (1933).
- [129] J. M. Luttinger. *The Effect of a Magnetic Field on Electrons in a Periodic Potential*. Physical Review **84**, 814(1951).
- [130] D. R. da Costa, A. Chaves, G. A. Farias, L. Covaci, and F. M. Peeters. *Wave-packet scattering on graphene edges in the presence of a pseudomagnetic field*. Physical Review B **86**, 115434 (2012).
- [131] A. Chaves, L. Covaci, Kh. Yu. Rakhimov, G. A. Farias, and F. M. Peeters. *Wave-packet dynamics and valley filter in strained graphene*. Physical Review B **82**, 205430 (2010).
- [132] J. M. Pereira, A. Chaves, G. A. Farias, and F. M. Peeters. *Klein tunneling in single and multiple barriers in graphene*. Semiconductor Science and Technology **25**, 033002 (2010).
- [133] In the K' point, substituting $\vec{\sigma} \rightarrow \vec{\sigma}^*$ (see e. g. Ref.[1]), one obtains the same energy spectrum, but for $l \rightarrow l + 1$.
- [134] G. Paz. *On the connection between the radial momentum operator and the Hamiltonian in n dimensions*. European Journal of Physics **22**, 337 (2001).
- [135] A. G. Aronov and Y. B. Lyanda-Geller. *Spin-orbit Berry phase in conducting rings*. Physical Review Letters **70**, 343 (1993).
- [136] Y. S. Yi, T. Z. Qian, and Z. B. Su. *Spin precession and time-reversal symmetry breaking in quantum transport of electron through mesoscopic rings*. Physical Review B **55**, 10631 (1997).
- [137] T. Choi, S. Y. Cho, C. M. Ryu, and C. K. Kim. *Quantum transport by nonadiabatic Aharonov-Casher phase in mesoscopic rings*. Physical Review B **56**, 4825 (1997).
- [138] D. A. Bahamon, A. L. C. Pereira, and P. A. Schulz. *Inner and outer edge states in graphene rings: A numerical investigation*. Physical Review B **79**, 125414 (2009).
- [139] G. A. Farias, M. H. Degani, J. A. K. Freire, J. Costa e Silva, and R. Ferreira. *Impurities and geometrical effects on the electron energy spectrum of quantum rings*. Physical Review B **77**, 085316 (2008).
- [140] A. C. A. Ramos, A. Chaves, G. A. Farias, and F. M. Peeters. *Electronic states above a helium film suspended on a ring-shaped substrate*. Physical Review B **77**, 045415 (2008).

- [141] A. Chaves, J. Costa e Silva, J. A. K. Freire, and G. A. Farias. *The role of surface roughness on the electron confinement in semiconductor quantum rings*. *Microelectronics Journal* **39**, 455 (2008).
- [142] E. A. de Andrada e Silva. *Probability current in the tight-binding model*. *American Journal of Physics* **60**, 753 (1992).
- [143] A. Iyengar, T. Luo, H. A. Fertig, and L. Brey. *Conductance through graphene bends and polygons*. *Physical Review B* **78**, 235411 (2008).
- [144] P. Potasz, A. D. Guclu, O. Voznyy, J. A. Folk, and P. Hawrylak. *Electronic and magnetic properties of triangular graphene quantum rings*. *Physical Review B* **83**, 174441 (2011).
- [145] P. Potasz, A. D. Guclu, and P. Hawrylak. *Zero-energy states in triangular and trapezoidal graphene structures*. *Physical Review B* **81**, 033403 (2010).
- [146] T. Chakraborty. *Quantum Dots: A Survey of the Properties of Artificial Atoms*. Amsterdam: Elsevier Science (1999); L. Jacak, P. Hawrylak, A. Wjs. *Quantum dots*. Berlin: Springer-Verlag (1998).
- [147] S. M. Reimann and M. Manninen. *Electronic structure of quantum dots*. *Rev Mod Phys* **74**, 1283-1342 (2002).
- [148] A. V. Rozhkov, G. Giavaras, Y. P. Bliokh, V. Freilikher, and F. Nori. *Electronic properties of mesoscopic graphene structures: Charge confinement and control of spin and charge transport*. *Physics Reports* **503**, 77 (2011).
- [149] D. R. da Costa, A. Chaves, M. Zarenia, J. M. Pereira Jr., G. A. Farias, and F. M. Peeters. *Geometry and edge effects on the energy levels of graphene quantum rings: A comparison between tight-binding and simplified Dirac models*. *Physical Review B* **89**, 075418 (2014).
- [150] A. V. Rozhkov and F. Nori. *Exact wave functions for an electron on a graphene triangular quantum dot*. *Physical Review B* **81**, 155401 (2010).
- [151] H. P. Heiskanen, M. Manninen, and J. Akola. *Electronic structure of triangular, hexagonal and round graphene flakes near the Fermi level*. *New Journal of Physics* **10**, 103015 (2008).
- [152] M. Ezawa. *Metallic graphene nanodisks: Electronic and magnetic properties*. *Physical Review B* **76**, 245415 (2007).
- [153] P. Recher, J. Nilsson, G. Burkard, and V. Trauzettel. *Bound states and magnetic field induced valley splitting in gate-tunable graphene quantum dots*. *Physical Review B* **79**, 085407 (2009).

- [154] J. M. Pereira, Jr., P. Vasilopoulos, and F. M. Peeters. *Tunable Quantum Dots in Bilayer Graphene*. Nano Letters **7**, 946 (2007).
- [155] J. M. Pereira, Jr., F. M. Peeters, P. Vasilopoulos, R. N. Costa Filho, and G. A. Farias. *Landau levels in graphene bilayer quantum dots*. Physical Review B **79**, 195403 (2009).
- [156] M. Zarenia, J. M. Pereira, Jr., F. M. Peeters, and G. A. Farias. *Electrostatically confined quantum rings in bilayer graphene*. Nano Letters **9**, 4088 (2009).
- [157] M. T. Allen, J. Martin, and A. Yacoby. *Gate-defined quantum confinement in suspended bilayer graphene*. Nature communications **3**, 934 (2012).
- [158] A. M. Goossens, S. C. M. Driessen, T. A. Baart, K. Watanabe, T. Taniguchi, and L. M. K. Vandersypen. *Gate-Defined Confinement in Bilayer Graphene-Hexagonal Boron Nitride Hybrid Devices*. Nano Letters **12**, 4656 (2012).
- [159] A. D. Güçlü, P. Potasz, and P. Hawrylak. *Electric-field controlled spin in bilayer triangular graphene quantum dots*. Physical Review B **84**, 035425 (2011).
- [160] D. P. Zebrowski, E. Wach, and B. Szafran. *Confined states in quantum dots defined within finite flakes of bilayer graphene: Coupling to the edge, ionization threshold, and valley degeneracy*. Physical Review B **88**, 165405 (2013).
- [161] G. Giovannetti, P. A. Khomyakov, G. Brocks, P. J. Kelly, and J. van den Brink. *Substrate-induced band gap in graphene on hexagonal boron nitride: Ab initio density functional calculations*. Physical Review B **76**, 073103 (2007).
- [162] R. Quhe, J. Zheng, G. Luo, Q. Liu, R. Qin, J. Zhou, D. Yu, S. Nagase, W.-N. Mei, Z. Gao, and J. Lu. *Tunable and sizable band gap of single-layer graphene sandwiched between hexagonal boron nitride*. NPG Asia Materials **4**, e6 (2012).
- [163] W. Zhang, C.-T. Lin, K.-K. Liu, T. Tite, C.-Y. Su, C.-H. Chang, Y.-H. Lee, C.-W. Chu, K.-H. Wei, J.-L. Kuo, and L.-J. Li. *Opening an electrical band gap of bilayer graphene with molecular doping*. ACS Nano **5**, 7517 (2011).
- [164] A. Ramasubramanian, D. Naveh, and E. Towe. *Tunable band gaps in bilayer graphene-BN heterostructures*. Nano Letters **11**, 1070 (2011).
- [165] M. Ramezani Masir, A. Matulis, and F. M. Peeters. *Scattering of Dirac electrons by circular mass barriers: Valley filter and resonant scattering*. Physical Review B **84**, 245413 (2011).
- [166] L. J. P. Xavier, J. M. Pereira, Jr., Andrey Chaves, G. A. Farias, and F. M. Peeters. *Topological confinement in graphene bilayer quantum rings*. Applied Physics Letters **96**, 212108 (2010).

- [167] In our calculation we used the relation $d\widetilde{M}(A, B, \widetilde{\rho})/d\widetilde{\rho} = A\widetilde{M}(A + 1, B + 1, \widetilde{\rho})$.
- [168] C. S. Lent. *Edge states in a circular quantum dot*. Physical Review B **43**, 4179 (1991).
- [169] G. Janssen, E. Goovaerts, A. Bouwen, B. Partoens, B. Van Daele, N. Žurauskienė, P. M. Koenraad, and J. H. Wolter. et al. *Observation of cyclotron resonance in an InAs/GaAs wetting layer with shallowly formed quantum dots*. Physical Review B **68**, 045329 (2003).
- [170] P. W. Fry, I. E. Itskevich, D. J. Mowbray, M. S. Skolnick, J. J. Finley, J. A. Barker, E. P. O'Reilly, L. R. Wilson, I. A. Larkin, P. A. Maksym, M. Hopkinson, M. Al-Khafaji, J. P. R. David, A. G. Cullis, G. Hill, and J. C. Clark. *Inverted electron-hole alignment in InAs-GaAs self-assembled quantum dots*. Physical Review Letters **84**, 733 (2000).
- [171] Z. Jiang, E. A. Henriksen, L. C. Tung, Y.-J. Wang, M. E. Schwartz, M. Y. Han, P. Kim, and H. L. Stormer. *Infrared spectroscopy of landau levels of graphene*. Physical Review Letters **98**, 197403 (2007).
- [172] R. S. Deacon, K.-C. Chuang, R. J. Nicholas, K. S. Novoselov, and A. K. Geim. *Cyclotron resonance study of the electron and hole velocity in graphene monolayers*. Physical Review B **76**, 081406(R) (2007).
- [173] E. A. Henriksen, Z. Jiang, L.-C. Tung, M. E. Schwartz, M. Takita, Y.-J. Wang, P. Kim, and H. L. Stormer. *Cyclotron resonance in bilayer graphene*. Physical Review Letters **100**, 087403 (2008).
- [174] D. S. L. Abergel and V. I. Fal'ko. *Optical and magneto-optical far-infrared properties of bilayer graphene*. Physical Review B **75**, 155430 (2007).
- [175] M. Zarenia, B. Partoens, T. Chakraborty, and F. M. Peeters. *Electron-electron interactions in bilayer graphene quantum dots*. Physical Review B **88**, 245432 (2013).
- [176] C. R. Dean, A. F. Young, I. Meric, C. Lee, L. Wang, S. Sorgenfrei, K. Watanabe, T. Taniguchi, P. Kim, K. L. Shepard, and J. Hone. *Boron nitride substrates for high-quality graphene electronics*. Nature Nanotechnology **5**, 722 (2010).
- [177] W.-d. Sheng, M. Korkusinski, A. D. Güçlü, M. Zielinski, P. Potasz, E. S. Kadantsev, O. Voznyy, and P. Hawrylak. *Electronic and optical properties of semiconductor and graphene quantum dots*. Frontiers of Physics **7**, 328 (2012).
- [178] F. Molitor, J. Güttinger, C. Stampfer, S. Dröscher, A. Jacobsen, T. Ihn, and K. Ensslin, J. Phys.: Condens. Matter **23**, 243201 (2011).

- [179] Y. Kobayashi, K. I. Fukui, T. Enoki, K. Kusakabe, and Y. Kaburagi. *Observation of zigzag and armchair edges of graphite using scanning tunneling microscopy and spectroscopy*. Physical Review B **71**, 193406 (2005).
- [180] Y. Niimi, T. Matsui, H. Kambara, K. Tagami, M. Tsukada, and H. Fukuyama. *Scanning tunneling microscopy and spectroscopy of the electronic local density of states of graphite surfaces near monoatomic step edges*. Physical Review B **73**, 085421 (2006).
- [181] C. P. Puls, N. E. Staley, and Y. Liu. *Interface states and anomalous quantum oscillations in hybrid graphene structures*. Physical Review B **79**, 235415 (2009).
- [182] A. Iagallo, Sh. Tanabe, S. Roddaro, M. Takamura, Y. Sekine, H. Hibino, V. Misikis, C. Coletti, V. Piazza, F. Beltram, and S. Heuniar. *Bilayer-induced asymmetric quantum Hall effect in epitaxial graphene*. aXiv:1410.2024 (2014).
- [183] Y. Nam, J. Sun, N. Lindvall, S. J. Yang, D. Kireev, Ch. R. Park, Y. W. Park, and A. Yurgens. *Quantum Hall effect in graphene decorated with disordered multilayer patches*. Applied Physics Letters **103**, 233110 (2013).
- [184] F. Giannazzo, I. Deretzis, A. La Magna, F. Roccaforte, and R. Yakimova. *Electronic transport at monolayer-bilayer junctions in epitaxial graphene on SiC*. Physical Review B **86**, 235422 (2012).
- [185] E. V. Castro, N. M. R. Peres, and J. M. B. Lopes dos Santos. *Localized states at zigzag edges of multilayer graphene and graphite steps*. Europhysics Letters **84**, 17001 (2008).
- [186] T. Nakanishi, M. Koshino, and T. Ando. *Transmission through a boundary between monolayer and bilayer graphene*. Physical Review B **82**, 125428 (2010).
- [187] M. Koshino, T. Nakanishi, and T. Ando. *Interface Landau levels in graphene monolayer-bilayer junctions*. Physical Review B **82**, 205436 (2010).
- [188] Z.-x. Hu, W. Ding. *Edge states at the interface between monolayer and bilayer graphene*. Physics Letters A **376**, 610 (2012).
- [189] S. Dröscher, J. Güttinger, T. Mathis, B. Batlogg, T. Ihn, and K. Ensslin. *High-frequency gate manipulation of a bilayer graphene quantum dot*. Applied Physics Letters **101**, 043107 (2012).
- [190] J. Velasco, L. Jing, W. Bao, Y. Lee, P. Kratz, V. Aji, M. Bockrath, C. N. Lau, C. Varma, R. Stillwell, D. Smirnov, F. Zhang, J. Jung, and A. H. MacDonald. *Transport spectroscopy of symmetry-broken insulating states in bilayer graphene*. Nature Nanotechnology **7**, 156 (2012).

- [191] A. L. Grushina, D.-K. Ki, and A. F. Morpurgo. *A ballistic pn junction in suspended graphene with split bottom gates*. Applied Physics Letters **102**, 223102 (2013).
- [192] A. Müller, B. Kaestner, F. Hohls, T. Weimann, K. Pierz, and H. W. Schumacher. *Bilayer graphene quantum dot defined by topgates*. Journal of Applied Physics **115**, 233710 (2014).
- [193] E. V. Castro, N. M. R. Peres, J. M. B. Lopes dos Santos, A. H. Castro Neto, and F. Guinea. *Localized States at Zigzag Edges of Bilayer Graphene*. Physical Review Letters **100**, 026802 (2008).
- [194] Z. Z. Zhang, Kai Chang, and F. M. Peeters. *Tuning of energy levels and optical properties of graphene quantum dots*. Physical Review B **77**, 235411 (2008).
- [195] L. M. Zhang, M. M. Fogler, and D. P. Arovas. *Magnetoelectric coupling, Berry phase, and Landau level dispersion in a biased bilayer graphene*. Physical Review B **84**, 075451 (2011).
- [196] D. Wang and G. Jin. *Combined effect of magnetic and electric fields on Landau level spectrum and magneto-optical absorption in bilayer graphene*. Europhysics Letters **92**, 57008 (2010).
- [197] G. M. Maksimova, V. Ya. Demikhovskii, and E. V. Frolova. *Wave packet dynamics in a monolayer graphene*. Physical Review B **78**, 235321 (2008).
- [198] H. Yang, A. J. Mayne, M. Boucherit, G. Comtet, G. Dujardin, and Young Kuk. *Quantum interference channeling at graphene edges*. Nano Letters **10**, 943 (2010).
- [199] D. Gunlycke and C. T. White. *Graphene valley filter using a line defect*. Physical Review Letters **106**, 136806 (2011).
- [200] Jian-Hao Chen, W. G. Cullen, C. Jang, M. S. Fuhrer, and E. D. Williams. *Defect Scattering in Graphene*. Physical Review Letters **102**, 236805 (2009).
- [201] J. A. M. Van Ostaay, A. R. Akhmerov, C. W. J. Beenakker, and M. Wimmer. *Dirac boundary condition at the reconstructed zigzag edge of graphene*. Physical Review B **84**, 195434 (2011).
- [202] P. Koskinen, S. Malola, and H. Häkkinen. *Self-passivating edge reconstructions of graphene*. Physical Review Letters **101**, 115502 (2008).
- [203] P. Koskinen, S. Malola, and H. Häkkinen. *Evidence for graphene edges beyond zigzag and armchair*. Physical Review B **80**, 073401 (2009).
- [204] P. Rakyta, A. Kormányos, J. Cserti, and P. Koskinen. *Exploring the graphene edges with coherent electron focusing*. Physical Review B **81**, 115411 (2010).

- [205] C. Park, H. Yang, A. J. Mayne, G. Dujardin, S. Seo, Y. Kuk, J. Ihm, and G. Kim. *Formation of unconventional standing waves at graphene edges by valley mixing and pseudospin rotation*. Proceedings of the National Academy of Sciences of the United States of America **108**, 18622 (2011).
- [206] E. J. G. Santos, A. Ayuela, S. B. Fagan, J. Mendes Filho, D. L. Azevedo, A. G. Souza Filho, and D. Sánchez-Portal. *Switching on magnetism in Ni-doped graphene: Density functional calculations*. Physical Review B **78**, 195420 (2008).
- [207] A. T. N'Diaye, R. van Gastel, A. J. Martinez-Galera, J. Coraux, H. Hattab, D. Wall, F. -J. M. Zu Heringdorf, M. H. Hoegen, J. M. Gomez-Rodríguez, B. Poelsema, C. Busse and T. Michely. *In situ observation of stress relaxation in epitaxial graphene*. New Journal of Physics **11**, 113056 (2009).
- [208] F. M. D. Pellegrino, G. G. N. Angilella, and R. Pucci. *Strain effect on the optical conductivity of graphene*. Physical Review B **81**, 035411 (2010).
- [209] C. Metzger, S. Reemi, M. Liu, S. V. Kusminskiy, A. H. Castro Neto, A. K. Swan, and B. B. Goldberg. *Biaxial Strain in Graphene Adhered to Shallow Depressions*. Nano Letters **10**, 6 (2010).
- [210] G. Cocco, E. Cadelano and L. Colombo. *Gap opening in graphene by shear strain*. Physical Review B **81**, 241412 (2010).
- [211] F. M. D. Pellegrino, G. G. N. Angilella, and R. Pucci. *Dynamical polarization of graphene under strain*. Physical Review B **82**, 115434 (2010).
- [212] O. Cretu, A. V. Krasheninnikov, J. A. Rodríguez-Manzo, L. Sun, R. M. Nieminen, and F. Banhart. *Migration and Localization of Metal Atoms on Strained Graphene*. Physical Review Letters **105**, 196102 (2010).
- [213] L. Covaci and F. M. Peeters. *Superconducting proximity effect in graphene under inhomogeneous strain*. Physical Review B **84**, 241401 (2011).
- [214] E. J. G. Santos, A. Ayuela, and D. Sanchez-Portal. *Strain-tunable spin moment in Ni-doped graphene*. The Journal of Physical Chemistry C **116**, 1174 (2012).
- [215] F. Guinea, M. I. Katsnelson, and A. K. Geim. *Energy gaps and a zero-field quantum Hall effect in graphene by strain engineering*. Nature Physics **6**, 30 (2010).
- [216] T. Low and F. Guinea. *Strain-induced pseudomagnetic field for novel graphene electronics*. Nano Letters **10**, 3551 (2010).
- [217] N. Levy, S. A. Burke, K. L. Meaker, M. Panlasigui, A. Zettl, F. Guinea, A. H. Castro Neto, and M. F. Crommie. *Strain-induced pseudo-magnetic fields greater than 300 Tesla in graphene nanobubbles*. Science **30**, 544 (2010).

- [218] F. Guinea, A. K. Geim, M. I. Katsnelson, and K. S. Novoselov. *Generating quantizing pseudomagnetic fields by bending graphene ribbons*. Physical Review B **81**, 035408 (2010).
- [219] T. M. Rusin and W. Zawadzki. *Zitterbewegung of electrons in graphene in a magnetic field*. Physical Review B **78**, 125419 (2008).
- [220] R. J. Haug. *Edge-state transport and its experimental consequences in high magnetic fields*. Semiconductor Science and Technology **8**, 131 (1993).
- [221] T. Usuki, M. Saito, M. Takatsu, R. A. Kiehl, and N. Yokoyama. *Numerical analysis of ballistic-electron transport in magnetic fields by using a quantum point contact and a quantum wire*. Physical Review B **52**, 8244 (1995).
- [222] E. A. de Andrada e Silva. *Probability current in the tight-binding model*. American Journal of Physics **60**, 753 (1992).
- [223] M. Governale and C. Ungarelli. *Gauge-invariant grid discretization of the Schrödinger equation*. Physical Review B **58**, 7816 (1998).
- [224] L. M. Malard, M. A. Pimenta, G. Dresselhaus, and M. S. Dresselhaus. *Raman spectroscopy in graphene*. Physics Reports **473**, 51 (2009).
- [225] A. Rycerz, J. Tworzydło, and C. W. J. Beenakker. *Valley filter and valley valve in graphene*. Nature Physics **3**, 172 (2007).
- [226] Y. Jiang, T. Low, K. Chang, M. I. Katsnelson, and F. Guinea. *Generation of Pure Bulk Valley Current in Graphene*. Physical Review Letters **110**, 046601 (2013).
- [227] T. Low and F. Guinea. *Strain-Induced Pseudomagnetic Field for Novel Graphene Electronics*. Nano Letters **10**, 3551 (2010).
- [228] D. Gunlycke and C. T. White. *Valley and spin polarization from graphene line defect scattering*. Journal of Vacuum Science & Technology B **30**, 03D112 (2011).
- [229] Yang Liu, Juntao Song, Yuxian Li, Ying Liu, and Qing-Feng Sun. *Controllable valley polarization using graphene multiple topological line defects*. Physical Review B **87**, 195445 (2013).
- [230] I. Martin, Ya. M. Blanter, and A. F. Morpurgo. *Topological Confinement in Bilayer Graphene*. Physical Review Letters **100**, 036804 (2008).
- [231] H. Schomerus. *Helical scattering and valleytronics in bilayer graphene*. Physical Review B **82**, 165409 (2010).

- [232] M. Zarenia, J. M. Pereira, Jr., G. A. Farias, and F. M. Peeters. *Chiral states in bilayer graphene: Magnetic field dependence and gap opening*. Physical Review B **84**, 125451 (2011).
- [233] H. Fehske, J. Schleede, G. Schubert, G. Wellein, V. S. Filinov, and A. R. Bishop. *Numerical approaches to time evolution of complex quantum systems*. Physics Letters A **373**, 2182 (2009).
- [234] N. Watanabe and M. Tsukada. *Fast and stable method for simulating quantum electron dynamics*. Physical Review E **62**, 2914 (2000).
- [235] C. J. Chua, M. R. Connolly, A. Lartsev, T. Yager, S. Lara-Avila, S. Kubatkin, S. Kopylov, V. I. Fal'ko, R. Yakimova, R. Pearce, T. J. B. M. Janssen, A. Ya. Tzalenchuk, and C. G. Smith. *Quantum Hall Effect and Quantum Point Contact in Bilayer-Patched Epitaxial Graphene*. Nano Letters **14**(6), 3369 (2014).
- [236] J. W. González, H. Santos, M. Pacheco, L. Chico and L. Brey. *Electronic transport through bilayer graphene flakes*. Physical Review B **81**, 195406 (2010).
- [237] Johan Nilsson, A. H. Castro Neto, F. Guinea and N. M. R. Peres. *Transmission through a biased graphene bilayer barrier*. Physical Review B **76**, 165416 (2007).
- [238] Y. Hasegawa and M. Kohmoto. *Electric-field-induced penetration of edge states at the interface between monolayer and bilayer graphene*. Physical Review B **85**, 125430 (2012).
- [239] J. Ruseckas, A. Mekys, G. Juzeliūnas and I. V. Zozoulenko. *Electron transmission through graphene monolayer-bilayer junction: an analytical approach*. Lithuanian Journal of Physics **52**, 70 (2012).

Index

- acetylene, 40
- Aharonov-Bohm, 91, 99
- allotropes of carbon, 34, 35, 45, 46
- amorphous, 45, 46
- armchair, ix, xi, 62, 79–82, 90–94, 96–104, 108–110, 112–114, 127, 128, 131, 132, 135–147, 149–154, 156–161, 174–176
- Bernal stacking, 68, 69, 166
- bilayer graphene, xi, xii, 54, 62, 63, 68–73, 76, 78, 79, 91, 115, 116, 128, 131–133, 135–137, 140–144, 146, 162–164, 166, 167, 173–176
- carbon materials, 34, 35
- carbon nanotube, 35, 45–47
- carbyne, 45
- coating, 55, 56, 59
- corrosion, 55, 56
- CVD, 47, 50–54
- diamond, 34, 43, 45–47
- Dirac, xi, xii, 36, 50, 62–68, 75, 76, 79–84, 86, 88, 90–92, 95, 96, 99, 101, 105, 107, 108, 113, 114, 116, 117, 119, 129, 149–152, 157, 158, 161, 162, 166–169, 174–176
- epitaxial growth, 47, 49, 52
- ethylene, 41
- ethyne, 50
- Fermi energy level, 50, 65, 80, 108, 114, 115
- Fermi velocity, 67, 95, 142, 151, 166
- fiber, 45, 56
- film, 35, 36, 49–55, 59
- fullerene, 35, 45–47
- Gaussian, xi, 63, 149, 151, 152, 155, 158, 165, 166, 173, 175, 176
- graphene, xi, 34–36, 41, 45–71, 74–76, 78–81, 83, 84, 86, 87, 90–96, 101, 106–108, 111, 113–117, 128, 131, 132, 137, 139, 141, 142, 146, 147, 149–157, 159–163, 166, 173–177
- graphite, 34–36, 41, 45–50, 52
- hopping, 65, 68–71, 76, 78, 86, 92, 94, 118, 124, 129, 133, 139, 159, 164, 166
- hybridization, 34, 37–47
- insulating, 45, 98
- insulator, 47
- lattice, xi, 34, 35, 46, 47, 64–66, 69, 74, 79–82, 86, 87, 90–94, 117, 139, 149, 150, 159, 162–164, 166, 176
- LCD, 53
- metal, 45, 47, 50–52, 55–57
- methane, 43, 50
- nanoribbon, 79, 98, 107, 108, 149, 150

- Peierls transformation, 65, 92, 94, 139, 159
photodetector, 56, 57, 59
polyacetylene, 41
- quantum dot, xii, 62, 65, 82, 84, 92, 115–
117, 121–123, 126, 127, 129–138, 140–
144, 146, 147, 175
- quantum ring, xi, 62, 65, 82, 84, 90–92, 95–
99, 101–109, 111, 112, 142, 174
- semiconductor, 37, 45, 56, 70, 72, 80, 82, 86,
91, 99, 115, 127
- semimetal, 45
- Split-operator, xi, 62, 64, 84, 85, 87, 88, 163,
164, 174, 175
- staggered potential, 65, 72, 82, 83, 90, 92–
95, 113, 114, 174, 176
- sublattice, 64, 65, 67–69, 71, 75, 76, 79, 81,
82, 84, 92–95, 121, 127, 129, 149,
151, 159, 166
- tight-binding, ix–xiii, 62, 64, 65, 68–70, 79,
81, 82, 86, 87, 90–92, 96, 115–117,
127, 128, 130–134, 139, 141, 146,
149, 151, 163, 164, 166, 167, 174–
176
- zigzag, ix, xi, 62, 79–82, 92–94, 101, 107–
112, 114, 128, 131, 132, 134–147,
149–153, 161, 162, 175, 176